

NASA Contractor Report 191012

P-3-1

Tank Pressure Control in Low Gravity by Jet Mixing

(NASA-CR-191012) TANK PRESSURE
CONTROL IN LOW GRAVITY BY JET
MIXING Final Report (Boeing
Defense and Space Group) 201 p

N95-28001

Unclassified

63/28 0051309

Michael D. Bentz
Boeing Defense & Space Group
P.O. Box 3999
Seattle, WA 98124

March 1993

Prepared for
National Aeronautics and Space Administration
Lewis Research Center
Contract Number NAS3-25363



NASA Contractor Report 191012

Tank Pressure Control in Low Gravity by Jet Mixing

Michael D. Bentz
Boeing Defense & Space Group
P.O. Box 3999
Seattle, WA 98124

March 1993

Prepared for
National Aeronautics and Space Administration
Lewis Research Center
Contract Number NAS3-25363

Date for general release: March 1995.

FOREWORD

This final report documents the technical effort conducted by Boeing Defense and Space Group under Contract NAS3-25363 up to and including the first flight of the apparatus aboard the Space Transportation System. It does not cover the effort for subsequent flight(s) of the experiment. The period of performance covered by this report is November 1988 through September 1992. The project was funded by the National Aeronautics and Space Administration's (NASA) In-Space Technology Experiments Program (In-STEP), and the contract was administered by NASA Lewis Research Center.

NASA Project Manager:

Richard H. Knoll

Key NASA Personnel:

Todd Tofil	Deputy Project Manager
John Aydelott	Science Advisor
Dr. M. Mojibul Hasan	Project Scientist
Dr. Chin-Shun Lin	Project Scientist

Boeing Program Manager:

Dr. Jere S. Meserole

Boeing Principal Investigator:

Michael D. Bentz

Key Boeing Personnel:

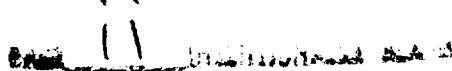
Dan Luterman	mechanical design
Glenn Sikkema	electronics design
Donald Skene	technician
Gary Frankfurt	technician
Gary Brown	software

Data are presented in *System Internationale* (SI) units, with English units also given where appropriate.

The complete set of video imagery obtained on this effort is available as an adjunct to this final report through the NASA Lewis Research Center videotape library. A request form for this video supplement is shown on the last page.

CONTENTS

FOREWORD	i
CONTENTS	iii
SYMBOLS	v
SUMMARY	1
INTRODUCTION	3
BACKGROUND	7
OBJECTIVES	13
EXPERIMENT APPROACH AND REQUIREMENTS	15
General	15
Instrumentation	18
EXPERIMENT APPARATUS AND OPERATION	21
STS Accommodations	21
Structure	24
Fluid System	27
Power Supply	32
Controls and Data Storage	33
Instrumentation	34
Photography	35
Operating Timeline	37
LOW-G AIRCRAFT TEST	39
Aircraft Test Objectives and Approach	39
Aircraft Test Results and Conclusions	40
IN-SPACE TEST	43
Payload Performance	43
Data Summary	47
ANALYSIS AND DISCUSSION	63
Flow Patterns	63
Mixing Times	66
Comparison With Mixing Models	74
Heater Plate Convection	80
Heating Phase Effects	81
CONCLUSIONS	83
REFERENCES	85
APPENDIX A	A-1



SYMBOLS

A	liquid/vapor interface area
B_0	Bond number of jet at liquid/vapor interface, $\rho g D_j^2 / \sigma$
c_{pl}	liquid specific heat
D_j	jet diameter at liquid/vapor interface
D_o	jet diameter at nozzle exit (nozzle inside diameter)
D_{tank}	tank diameter
F	flow characterization parameter (see equation 6)
g	acceleration
gpm	gallons per minute
h	convective heat transfer coefficient
h_b	jet submergence (distance from nozzle exit to liquid/vapor interface)
ID	inside diameter
k_l	liquid thermal conductivity
l	liters
l/min	liters per minute
m	mass
N	dimensionless buoyancy parameter
Nu	Nusselt number based on heater length
P	tank pressure
P_{nc}	sum of partial pressures of noncondensable gases
Pr_l	liquid Prandtl number, $c_{pl}\mu_l/k_l$
Q	volumetric flow rate
Re_j	jet Reynolds number, $V_o D_o / \nu_l$
T	fluid temperature
T_{sat}	saturation temperature
ΔT	maximum fluid temperature spread
t	time
t_{mix}	time required to mix fluid (see pages 5-6 for specific definitions of mixing times)
V	ullage volume
V_{liquid}	volume of bulk liquid
V_o	jet velocity at nozzle exit
W	watts
We_j	Weber number of jet at liquid/vapor interface, $\rho_l V_o^2 R_o^2 / \sigma D_j$
Z_b	liquid level (distance from liquid/vapor interface to mixer-end of tank)
λ	latent heat of evaporation
μ_l	liquid dynamic viscosity
ν_l	liquid kinematic viscosity
ρ	ullage density
ρ_l	liquid density
σ	surface tension
τ	time constant for exponential decay of temperature and pressure



SUMMARY

The Tank Pressure Control Experiment (TPCE) is a space experiment designed to develop an essential cryogenic fluid management technology: control of storage tank pressures in the absence of gravity by forced-convective mixing. Axial-jet recirculation mixers are candidates for controlling pressure rise in cryogenic fluids stored for future long-duration missions, such as in an orbiting propellant depot. Positive control of tank pressure under all fluid orientations and conditions is critical, but the addition of excessive energy to the fluid from such devices must be minimized to avoid vehicle disturbances and cryogen boiloff losses.

The objectives of TPCE were to characterize the fluid dynamics of axial-jet-induced mixing in low gravity, to evaluate the validity of empirical mixing models, and to provide data for use in developing and validating computational fluid dynamic models of mixing processes. The experiment used refrigerant-113 as the test fluid, at near-saturation conditions, with the equilibrium pressure approximately 4.2 kPa (0.6 psi) above the vapor pressure. This simulates the fluid dynamic and thermodynamic behavior of subcritical cryogenic fluids in space that are stored at or near their boiling points. The 13.7-liter, 25-cm-diameter tank was filled to an 83% fill fraction. Immersed heaters created pressure increases and thermal gradients. A 1.0-cm-diameter nozzle produced an axial jet that was turned on to mix the fluid and return the pressure to a near-equilibrium level. Video cameras recorded the liquid/vapor interface shapes and flow patterns produced as a function of mixer flow rate, while temperatures and pressures were recorded to assess the mixing and pressure control effectiveness. The experiment was packaged as a Complex Autonomous Payload utilizing the Get-Away Special container in the Shuttle payload bay as its carrier.

TPCE accomplished all of its objectives in flight on the Space Transportation System (STS) in August 1991. Two of the flow patterns observed generally agreed with prior drop tower test observations and correlations. The jet penetrated the ullage and formed a symmetrical recirculating flow pattern at jet Weber numbers of approximately 4.8 and above. Weber numbers of 1.4 or less produced a symmetrical, nonpenetrating pattern. Mixing was found to be effective at both of these flow patterns, in terms of the ability to produce pressure collapse and thermal equilibration. The penetrating jet provided the most rapid pressure reduction and equilibration. Jet Weber numbers between 1.4 and 4.8 resulted in asymmetric flows which were less consistent in their mixing effectiveness. A closed-form equation derived from a simple thermodynamic model was found to provide an approximate prediction of the pressure reduction time as a function of mixer parameters, tank size, and fluid thermophysical properties.

A low-energy axial jet mixer was found to be effective and consistent at mixing, enhancing heat and mass transfer between the phases, and controlling tank pressure. Active mixing—which offers increased predictability and controllability in space cryogenic systems compared with passive pressure control designs—was demonstrated to be possible using a low kinetic energy jet that incurs no significant boiloff penalty.

INTRODUCTION

Reliable control of tank pressure is essential to the storage and handling of cryogenic fluids in space. A number of candidate future missions will require the use of large quantities of cryogenic fluids and advanced concepts for storing and handling them. Applications such as reusable space transfer vehicles, manned Mars stages, and orbital propellant depots will require the storage of cryogenic fluids for greater lengths of time than has been demonstrated to date.

Any tank of cryogenic liquid stored in space is subject to heat addition from its environment, often at varying rates and with a nonuniform distribution around the tank. These heat inputs raise the tank pressure by evaporating liquid and/or warming the vapor. The absence of strong gravity-driven natural convection can lead to nonuniform distribution of the heat in the liquid. As the pressure in a closed tank rises in response to the heating, its rate of increase depends strongly on the distribution of the heat within the fluid. A nonuniform temperature distribution results in higher pressure than would be found with an isothermal fluid. Localized "hot spots" in the fluid drive the pressure up faster and to higher levels because the tank pressure is strongly driven by the vapor pressure of the warmest liquid in the tank. If the heat input is instead distributed uniformly throughout the fluid, then the pressure rise is minimized. The pressure rise rate in a tank of well-mixed cryogen can be more than an order of magnitude lower than that in a tank of cryogen that is not in equilibrium.

The near-absence of gravity not only reduces natural convection, but also makes it difficult to relieve the resulting pressure increase by the conventional venting of vapor since the locations of the liquid and vapor are not generally known with certainty. For long-term storage, pressure must therefore be controlled by thermodynamic means such as a refrigerator or a thermodynamic vent system (TVS). A TVS, which is essentially an open-loop refrigeration cycle, provides cooling by expanding a small amount of liquid or vapor through an expansion valve, passing it through a heat exchanger to absorb heat from the remaining fluid, and then venting the warmed vapor overboard. The effectiveness of either a TVS or a refrigerator depends on the distribution of cooling to all regions of the tank. To accomplish this, either system can be coupled with a mixer using a compact heat exchanger that is integral to the mixer device, as illustrated schematically in figure 1. An internal heat exchanger employing forced convection offers lower mass than a passive system using only an external TVS-cooled shield that relies on conduction and natural convection.

For short-term storage periods (such as the several days that might elapse between the launching of an upper stage to orbit and the firing of its engines), mixing alone could be an adequate means of controlling pressures. A relatively small amount of induced liquid motion may be sufficient to break up the hot spots and provide forced-convection heat transfer at a rate many times higher than that for free convection and conduction in low gravity.

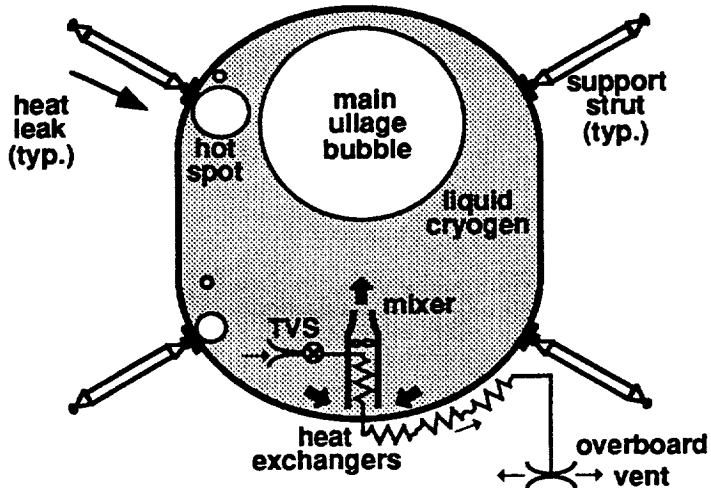


Figure 1: Pressure Control System Using Mixer

The benefits of active mixing to space cryogenic systems are that it:

1. *Reduces pressure-rise-rate in a nonvented tank.* This allows systems to be designed that can store cryogen for longer periods without venting or refrigeration.
2. *Enables the use of compact heat exchangers.* Forced convective mixing increases the effectiveness of a refrigerator or TVS and allows the use of an internal compact heat exchanger, thus reducing weight compared with a passive system.
3. *Can serve as a backup for passive cooling systems.* If cooled external shields are used by a TVS or refrigerator to intercept heat leaks, rather than an internal heat exchanger, the ability of such a system to cool the fluid depends primarily on heat conduction. An active mixer can be added as a backup to this passive system to increase confidence in its ability to provide positive control of tank pressure.
4. *May reduce on-orbit fluid transfer time.* The rate of a non-vented fill depends on the rate at which vapor can be condensed, which in turn depends on the rate of dissipation of the heat of compression and condensation away from the liquid/vapor interface. Although the incoming liquid stream will induce some circulation, under some circumstances additional forced circulation could speed the condensation and thereby reduce the fill time or increase the final liquid fill level that is attainable.
5. *Ensures delivery of uniform-temperature liquid to engines.* For propellant tanks, mixing can provide a more uniform propellant supply to the engines, which potentially reduces pressurization requirements and residual propellant mass.
6. *Makes the fluid state predictable.* Periodic mixing reduces or eliminates the potential for sudden pressure rise or drop due to nonequilibrium fluid states when the fluid is subjected to sudden motions.

The problem is not whether mixing systems can be built that provide adequate circulation, but how to mix efficiently as well as reliably. Mixers have been designed for use in previous cryogenic space systems (the Saturn S-IVB stage and the cancelled Shuttle/Centaur stage [ref. 1]) based on extensive ground testing. These, however, had to be designed conservatively to compensate for the lack of certainty about low-g mixing behavior.

One penalty for conservatism is that a high-velocity mixing jet could result in fluid frothing and in undesirable vehicle disturbances, particularly for applications in which propellant is a large percentage of the vehicle mass. Another penalty is that the energy used by the device eventually dissipates as heat in the fluid, resulting in an increase in propellant boiloff. Thus there is a need to minimize the kinetic energy added by the mixer.

For example, the Shuttle/Centaur hydrogen tank mixer is rated at 15W total power input while operating (ref. 1). Of this 15W, the jet kinetic energy rate is approximately 0.4W and the rest is due to pressure losses in the TVS, mixer inefficiency, and motor losses. In long-term storage applications, a mixer dissipating even 0.4W would represent a significant heat addition, resulting in 25 kg (55 lbm) per year additional boiloff of hydrogen or 60 kg (132 lbm) per year of oxygen. Previous mixer performance models indicate that this energy input could be reduced at least one order of magnitude by using a larger jet diameter and lower jet velocity. Low-kinetic-energy jet mixing, however, was unproven in its effectiveness with a low-g fluid orientation prior to the present effort. Without adequate low-g data, mixers would continue to be designed conservatively (i.e., with higher-velocity flow) resulting in both mass and power penalties.

Many investigators over the past twenty-five years have recognized the need for understanding mixing in space-vehicle tanks. Their studies have included small- and large-scale thermal tests in one g with a number of test fluids, plus low-g mixing simulations and drop tower tests. Several analytical models and empirical correlations were developed, as described in the following background section, and valuable conclusions and understandings emerged from these efforts. However, because of the complexity of the fluid dynamic problem and the difficulty of studying it in a normal-gravity environment, there has been no validated model of low-g mixing behavior.

The following sections describe the objectives of the TPCE space experiment, the technical approach and requirements for meeting these objectives, the experimental apparatus and operating sequence, the results of preliminary low-g testing on an aircraft, and finally the results of a 25.3 hour test on board the Space Shuttle Atlantis (mission STS-43). The observed flow patterns and the measured mixing effectiveness are discussed and compared with the prior correlations, and a simplified thermodynamic model of pressure control effectiveness is derived and compared with the flight data. The complete set of digital data is presented in graphical form in Appendix A, and instructions for obtaining a copy of the video data are given.

BACKGROUND

In 1968 Poth *et al.* (ref. 2) evaluated a variety of mixing concepts for low-g cryogenic pressure control devices. Concepts such as paddlewheels, dielectrophoresis, radial jets, axial jets, and other devices were studied. The desired capabilities of a mixer included:

1. The ability to provide thorough mixing with minimal kinetic energy addition.
2. The ability to disrupt (penetrate) the ullage, to reach all regions of the tank with the mixer flow, and to sweep the tank walls.
3. The ability to provide effective mixing at all fill levels.
4. The avoidance of swirling motions and non-symmetrical forces exerted on the tank walls, to avoid disturbances to the vehicle.
5. The ability to operate intermittently (non-continuous operation) if desired.
6. Compatibility with liquid hydrogen.

The mixing device also should be compact, lightweight, and capable of being integrated with a compact heat exchanger. Based on all of these evaluation criteria, the axial liquid jet was found by Poth to be most suitable for spacecraft propellant tank pressure control.

Most prior work to predict low-g mixer performance has been based on analysis and on normal-gravity experiments. An industrial mixing equation, published in 1948 by Fossett and Prosser (ref. 3), uses a nondimensional correlation of the time required to blend liquids:

$$\frac{t_{\text{mix}} V_0 D_0}{D_{\text{tank}}^2} = 9 \quad (1)$$

Here t_{mix} is defined as the time required to distribute a chemical species throughout a liquid. V_0 and D_0 are the velocity and diameter of the jet, respectively, at the outlet of the mixer nozzle, and D_{tank} is the diameter of the vessel. A later correlation by Fox and Gex (ref. 4) incorporates more parameters including the kinematic viscosity of the liquid, ν , and the liquid level, Z_b . Their correlation can be rearranged in terms of the same dimensionless grouping for comparison:

$$\frac{t_{\text{mix}} V_0 D_0}{D_{\text{tank}}^2} = (118) \sqrt{Z_b} \left[\frac{V_0 D_0 \nu}{g} \right]^{1/6} \frac{1}{D_{\text{tank}}} \quad (\text{Re} > 2,000) \quad (2)$$

The dependence on viscosity and velocity in the right-hand side of this equation is weak, and if Z_b , D_0 , and D_{tank} scale together then the dependence on tank size is also weak. This equation, however, can lead to predicted mixing times for large liquid hydrogen tanks that are an order of magnitude greater than those predicted by equation (1).

Whereas equations (1) and (2) were derived for the mixing of various industrial chemical compounds, Poth and Van Hook (refs. 5, 6) conducted a series of axial jet stratification-reduction tests with heated water in tanks 0.3 m (1 ft) and 3 m (10 ft) in diameter. The same dimensionless grouping was used to present mixing time, defined as the time required for the axial jet mixer to bring all liquid temperatures measured to within ten percent of each other (results were also given for 20% and 5% convergence

times, as well as pressure collapse times). The results of these normal gravity tests were presented in terms of a dimensionless buoyancy parameter N:

$$\frac{t_{\text{mix}} V_0 D_0}{D_{\text{tank}}^2} = f(N) \quad (3)$$

As the buoyancy parameter N (which accounts for the thickness of the stratified layer as well as its buoyancy) approaches zero, the function $f(N)$ approaches a constant, having a value between approximately 1 and 4 (for 10% temperature convergence).

Wollen (ref. 7) tested jet mixing in simulated low gravity by observing the time required for an acid/base mixture to become homogeneous enough for a pH-indicator dye to become colorless. He reported a constant value of the same dimensionless mixing time, for sufficiently high Reynolds numbers:

$$\frac{t_{\text{mix}} V_0 D_0}{D_{\text{tank}}^2} = 3.46 \quad (\text{Re} > 5,000) \quad (4)$$

Meserole *et. al.* (ref. 8) measured thermal mixing times in refrigerant-11 in normal gravity in a 25-cm diameter tank with varying nozzle diameters. At flow rates high enough to overcome the retarding effect of buoyancy (i.e. at Reynolds numbers greater than 15,000) the dimensionless mixing time agreed with the value reported by Wollen.

Dominick (ref. 9) tested a side-mounted jet in refrigerants 11 and 113 in one-g, measuring steady-state condensation rates at the liquid/vapor interface rather than transient pressure reduction rates. He found that the submerged jet, when impinging on the surface, increased ullage condensation rates by a factor of seven over those obtained with no mixing in normal gravity.

Bullard (ref. 10) and Sterbentz (ref. 11) successfully demonstrated the effectiveness of a compact TVS combined with an axial mixing jet in controlling the pressure of liquid hydrogen in normal gravity. These tests, using 1.04-m (41-in) and 2.8-m (110-in) tanks, also confirmed that the axial jet is more effective than a side-mounted jet. Pressure decay rates were controlled by the rate of heat transfer in the heat exchanger, and were approximately predicted by a simple one-lump thermodynamic model.

The above experiments had a one-g liquid/vapor configuration; that is, a flat interface. Mixing is inherently different in low gravity because of the liquid/vapor orientation. Under conditions having sufficient orbital drag with minimal disturbances, such as large-diameter tanks at low orbital altitudes (e.g., a propellant depot), the liquid will tend to be settled at one region of the tank, but its interface will be highly curved by surface tension forces. Under other conditions the liquid position will be highly variable and affected by acceleration noise ("g-jitter") and boiling. Experiments using heated (non-isothermal) fluids in one-g are also strongly affected by buoyancy, which stratifies the fluid and retards mixing.

In an early low-gravity mixing experiment Berenyi, *et al.* (ref. 12) conducted drop-tower tests of jet mixing in 10-cm (4-in) and 20-cm (8-in) spherical tanks. The objective of these experiments was to determine the jet velocity required to penetrate all bubbles and provide complete circulation in the tank.

Aydelott (refs. 13, 14, 15) tested an axial jet mixer in several 10-cm (4-in) diameter tanks of ethanol during freefall in the NASA Lewis Research Center 5-second drop

tower facility. Dye was added to the jet and the mixing time, defined as the time required to distribute the dye throughout the bulk liquid, was determined visually. Mixing times were correlated by:

$$\frac{t_{\text{mix}} Q}{V_{\text{liquid}}} = (0.09) + (0.01) \ln(F) \quad (5)$$

where Q is the volumetric flow rate, V_{liquid} is the volume of the bulk liquid, and F is a flow characterization parameter defined (for completely turbulent jets) as

$$F = \frac{(1.6)We_j - (0.5)}{(1) + (0.6)Bo_j} \quad (\text{Re} > 1,250) \quad (6)$$

Aydelott defines the jet Weber number, We_j , and Bond number, Bo_j , as the values at the zone where the jet meets the liquid/vapor interface, using the diameter of the jet at the interface, D_j , as the characteristic dimension:

$$We_j = \frac{\rho_1 V_o^2 R_o^2}{\sigma D_j} \quad (7)$$

$$Bo_j = \frac{\rho_1 g D_j^2}{\sigma} \quad (8)$$

The jet Weber number defined here is the ratio of jet momentum to the surface tension force that resists jet penetration at the liquid/vapor interface. The jet Bond number is the ratio of the force of gravity or acceleration on the jet geyser to that of surface tension.

The left-hand side of equation (5) is a different nondimensionalization of the mixing time than in the first four equations. This correlation was not intended to encompass a tank-to-jet diameter ratio other than 25:1 and, in comparison with other test data, would not be expected to properly reflect the effect of jet diameter on mixing time. However for a constant ratio of tank-to-nozzle diameter and for a given tank shape and fill level the parameter is essentially proportional to the dimensionless mixing time parameter shown in equations (1) through (4). This supports the use of $(t_{\text{mix}} V_o D_o / D_{\text{tank}}^2)$ as a correlator of fluid mixing time, at sufficiently-high Reynolds numbers, for a wide range of fluids and tank sizes.

It may be observed that this parameter, $(t_{\text{mix}} V_o D_o / D_{\text{tank}}^2)$, is related to the square root of the jet momentum rate, $(\pi/4)\rho V_o^2 D_o^2$, rather than to the kinetic energy rate, $(\pi/8)\rho V_o^3 D_o^2$. This would indicate that mixing effectiveness is determined by the rate of addition of momentum (the jet's thrust), rather than by the rate of addition of kinetic energy (the jet's power). Therefore it appears to be most efficient to design a jet mixer with minimum kinetic energy but with sufficient momentum, or $(V_o D_o)^2$, to produce the desired pressure control effectiveness. This would imply that the velocity of the jet should be minimized while the diameter, and therefore the volumetric flow rate, should be increased accordingly. (In designing a system, the diminishing return as the diameter is increased would be traded off against the size and mass of the device.)

Aydelott (ref. 13-15) identified four jet flow patterns from his tests. Low-g Flow Pattern I is defined as dissipation of the jet in the bulk liquid region without breaking the interface (this is the regime most similar to one-g experiments). In Flow Pattern II the jet penetrates and forms a geyser, and in Pattern III the geyser reaches the opposite end of the tank and collects there. Flow Pattern IV is defined as flow of the jet over the

opposite end of the tank and along the walls back to the bulk liquid region, giving complete circulation throughout the tank. Pattern I was observed at values of F less than 0.4 (the transition between patterns I and II ranges from $0.4 < F < 1.0$). Flow Pattern IV was found at $F > 2.5$. The correlation of his mixing time parameter with the flow parameter given in equation (5) was valid only for Patterns I and IV. Patterns II and III were observed to be irregular and less effective at mixing and therefore are considered to be undesirable flow conditions (although this observation is based on very short-duration tests).

Since the Weber number defined in equation (7) is proportional to the jet momentum, normalized by dividing it by a surface tension force, We_j may be a useful parameter for predicting both flow pattern and mixing times. Aydelott's flow characterization parameter F successfully correlated data at varying g-levels including one g, but it is essentially proportional to We_j for cases in which the jet Bond number, Bo_j , is much less than one (as will usually be the case in low g). Since the use of equations (5) and (6) causes difficulties at low values of We_j which give negative values of F , one can equivalently use We_j to correlate flow patterns at sufficiently small Bo_j values. Considering only the subset of Aydelott's data in which Bo_j is small, Flow Pattern I and the borderline Pattern I/II are seen at We_j values between 0.31 and 1.11, Patterns II and III are observed at $1.16 < We_j < 2.04$, and Pattern IV is seen at We_j values of 1.33 to over 200 (note that there is some overlap between the Pattern III and Pattern IV ranges).

Sterbentz and Bullard (ref. 11) give an analytic prediction of the jet momentum required to penetrate the ullage, using an assumed 9° jet spread half-angle. This prediction was reported to agree approximately with Berenyi's (ref. 12) drop tower results. The penetration criterion, which is based on a simple force balance at the meniscus, can be rearranged in terms of We_j as:

$$We_{j, \text{critical}} = 1 \quad (9)$$

Figure 2 depicts the zone of interaction between the jet and the liquid/vapor interface. Poth (ref. 2) gives a more detailed jet penetration analysis that accounts for the effect of eddy viscosity on the jet velocity profile. The resulting criterion is:

$$\frac{V_o^2 D_o^2 \rho}{\sigma g_c} \geq (1.055) h_b \quad (10)$$

which when rearranged in terms of We_j is:

$$We_{j, \text{critical}} = (0.26) \frac{h_b}{D_j} \quad (11)$$

If one assumes, as did Aydelott, that a completely turbulent jet ($Re > 1250$) spreads at approximately 7° for the first 6.2 outlet diameters and thereafter at 11° , the Poth criterion reduces, for $(D_o/h_b) \ll 1$, to:

$$We_{j, \text{critical}} = 0.69 \quad (12)$$

Thus this analytical prediction of the jet momentum required to penetrate the ullage is in agreement with the low-g experimental data of Aydelott (ref. 15).

Computational fluid dynamics modelling of submerged axial jets with free surfaces has more recently been performed by Hochstein *et al.* (ref. 16), Wendl (ref. 17), and Wendl *et al.* (ref. 18). Predictions of the critical jet velocity required to penetrate the

ullage, made for the TPCE geometry under a subcontract to the present effort (ref. 17), agreed well with the predictions of Aydelott (ref. 15). The numerical codes, which are still under development, could ultimately predict three-dimensional flow patterns and the thermodynamic response to mixing (i.e., pressure and temperature) for a tank of arbitrary size and with any cryogenic fluid. Further code development and validation will require low-g fluid dynamic and thermodynamic data for comparison with the predictions.

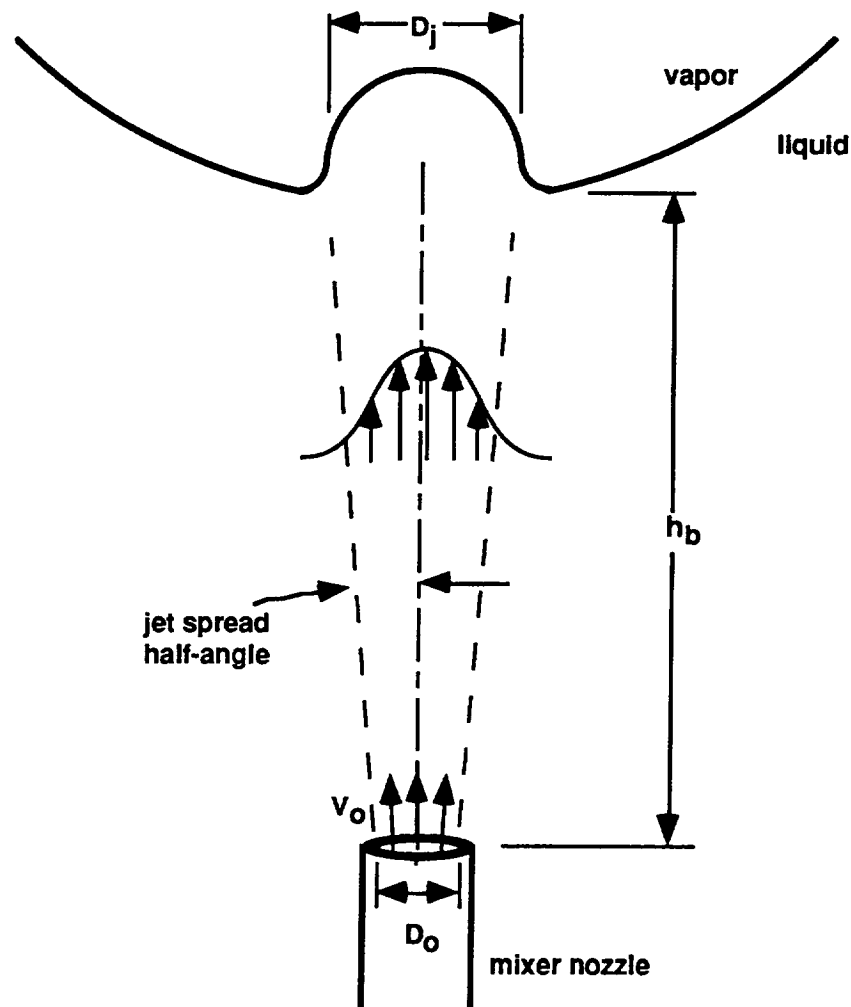


Figure 2: Zone of Interaction Between Jet and Liquid/Vapor Interface

OBJECTIVES

The experimental work described in the preceding section was subject to the inherent limitations of ground-based testing. Gravity constrained the liquid/vapor geometry and caused buoyancy effects in the one-g tests. The low-g drop tower tests were limited to small size tanks and very short test durations.

The next step toward a complete understanding of pressure control in low g is to test axial jet mixing of a non-isothermal fluid in a realistic low-g environment. To be realistic, the gravity level of the test environment must be low enough that the fluid is dominated by capillary and inertial forces rather than acceleration forces, and the duration must be sufficient to observe both the fully-developed flow patterns and the complete pressure collapse. Except with extremely small scale test tanks, these conditions can only be met by an in-space experiment.

The objectives of the TPCE project are to measure the effectiveness of an axial jet mixer at pressure control in low g, to evaluate existing mixing models, and to provide data for developing and validating future models. Specifically, the experiment objective is to determine the effectiveness of jet mixing as a function of flow rate, where effectiveness is defined by:

- a. the ability of the jet to disrupt the vapor and reach all regions of the tank,
- b. the rate at which mixing equilibrates temperatures in the fluid, and
- c. the rate at which mixing reduces the pressure in the tank.

EXPERIMENT APPROACH AND REQUIREMENTS

General

The Tank Pressure Control Experiment is designed to be carried as a Shuttle secondary payload within a Get-Away Special (GAS) canister. This constrains the experiment to the use of a noncryogenic simulant fluid. Refrigerant-113 (trichlorotrifluoroethane) was chosen because of its benign physical characteristics and because of its moderate vapor pressure over the range of temperatures expected during flight. In addition to the higher boiling point, the thermophysical properties of this test fluid differ from those of cryogenic propellants in several important ways, particularly in the liquid's thermal diffusivity and Prandtl number. Also, the scale of the experiment and the scope of the project do not permit a thermodynamically-scaled experiment. For instance, the important ratio of tank thermal mass to volume cannot be held constant, nor can a realistic tank thermal environment be reproduced without compromising the ability to view the fluid through the tank walls. Therefore the emphasis of TPCE is on the fluid dynamics. An understanding of the fluid dynamic behavior is of primary importance. Any model of pressure control processes will be strongly driven by the predicted flow patterns and liquid/vapor interface areas, since these control the rates of heat and mass transfer. However, thermodynamic data (temperatures and pressure) are acquired in TPCE to allow an assessment of relative mixing effectiveness and to obtain data for comparison with models.

To simulate cryogenic propellants that are stored at or near their boiling point, the test fluid is also near its saturation point. As a goal the total tank pressure (at equilibrium) is equal to the vapor pressure of the mixed fluid, plus a minimum excess pressure which is required to prevent pump cavitation in the absence of gravitational head pressure. This excess pressure is referred to as the total partial pressure of noncondensable gases, or P_{nc} . Complete cavitation suppression requires a P_{nc} of approximately 7 kPa (1 psi) for TPCE's fluid system, as determined by developmental testing. To provide this amount with minimum effect on the ullage thermal capacitance it was desired that the P_{nc} consist primarily of helium gas. Thus the refrigerant was to be as free of other dissolved gases as possible, with approximately 7-14 kPa (1-2 psi) partial pressure of helium. (As will be discussed in the Payload Performance section, the actual composition of P_{nc} in flight was somewhat different than this goal.)

The GAS container allows a total payload volume of 0.14 m^3 (5 ft^3) and mass of 91 kg (200 lbm). This constrains the geometry of the experiment's fluid tank. The geometry of the tank was chosen based on a review of the propellant tank dimensions proposed in several studies of space transfer vehicles and propellant depots. A tank geometry was chosen that is representative of liquid hydrogen tanks in these applications. This is a cylinder with hemispherical ends, having a length-to-diameter (L/D) ratio of 1.4. (Typical hydrogen tank L/D's range from 1.0 to 2.5 in the literature, while oxygen tank L/D's range from 0.7 to 1.0.) These considerations resulted in a 13.7-liter (0.485-ft^3) tank with a 25.4-cm (10-in) inside diameter, as shown in figure 3. This is approximately a 5% to 7% scale model (by linear dimension) of a typical space transfer vehicle hydrogen tank.

A jet nozzle is positioned along the tank's major axis near one end of the tank. The nozzle outlet is displaced 6.3 cm (2.5 in) from the end of the tank to represent the geometry of a combined mixer/TVS in an application. The mixer pumps are located outside of the tank due to the difficulties of developing a scale-model internal pump that

meets STS safety requirements. These external pumps are supplied with liquid from the tank by a liquid acquisition device (LAD) so that the jet will not contain vapor.

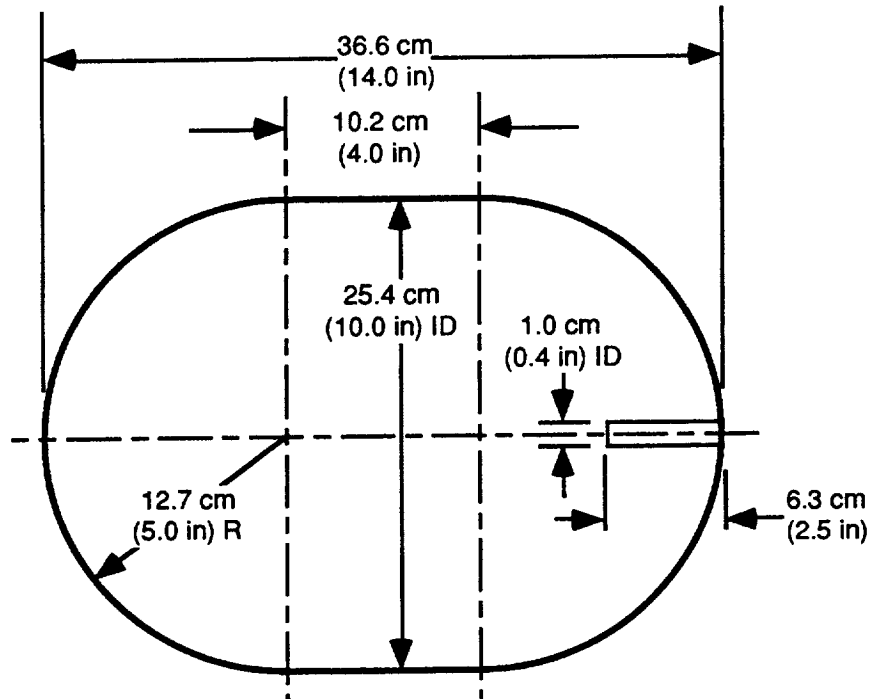


Figure 3: TPCE Test Tank Geometry

The jet nozzle is a straight tube with a 1-cm (0.40-in) inside diameter. This diameter was chosen so that the tank-to-jet diameter ratio is 25, for similarity to several prior experiments. Aydelott's tests (refs. 13 and 15) used a tank-to-jet diameter ratio of 25, and Sterbentz's (ref. 11) used a ratio of 21. In practice, the jet diameter could be optimized by trading the kinetic energy reduction associated with a larger-diameter nozzle against the mass and volume of the device, but a diameter ratio of 25 is expected to be representative of the optimum range for most cases.

The fill fraction chosen for the experiment is approximately 85%, representing a nearly full propellant tank (the actual fill fraction as flown was 83%). Ideally a variable fill fraction would be tested, but for simplicity, reliability, safety, and practicality a single fill level had to be selected, and 85% was chosen to represent a nearly-full condition. A high fill level (75% to 95%) may be a critical design condition for pressure control systems for several reasons: (1) the rate of pressure rise is greatest with a small ullage volume, for a given rate of heat input to the ullage and/or rate of evaporation; (2) the greater the fill fraction is, the further the liquid jet may have to travel to reach the ullage, therefore the greater the required flow rate to produce a given jet Weber number (or mixing effectiveness); and (3) for a non-vented fill of a tank in low-g, the nearly-full condition is probably the fill rate-limiting condition because the interfacial areas available for ullage cooling and condensation are small, hence the effectiveness of the mixing could strongly control the fill time and/or the final achievable fill level.

The experiment operation consists of a series of test runs in which the pressure is raised by addition of a fixed amount of heat and then is reduced by mixing. This intermittent mixer operation is to simulate an on-demand pressure control system, which could be activated whenever the pressure in a storage tank rises to a predetermined level and

operated until the pressure falls back below the fixed control band. However, TPCE uses a fixed duration for each heating and mixing phase, for simplicity and reliability, rather than operating "on-demand". Each run consists of a ten-minute pressure rise period (unless the pressure increases by 21 kPa [3 psi], in which case the heating phase is terminated early for safety reasons). This is followed by a fifteen-minute pressure reduction (mixing) phase. Another fifteen minutes with no activity is added to each run to allow fluid motions to damp out, and the equilibrium liquid/vapor interface shape to be reestablished, before beginning the next run.

Heat leaks into the fluid, and the resulting temperature gradients, are simulated by two heaters immersed in the fluid. The heating rate is high enough to create a significant pressure rise within a short time for each test run, but low enough (<25 watts) to avoid potential in-flight hazards associated with overheating the refrigerant vapor. To help meet safety requirements the heaters are designed to have sufficient thermal mass to avoid the possibility of their reaching the decomposition temperature in ten minutes of operation at 25W. A surface area of approximately 130 cm^2 (20 in^2) is chosen (see the Experiment Apparatus and Operation section for the actual values) to provide a heat flux of up to 0.2 W/cm^2 (1.25 W/in^2). This heat flux is below the expected burnout heat flux of 0.5 W/cm^2 (3.5 W/in^2) at $10^{-6}g$ (calculated from an equation by Zuber, ref. 19), so that film boiling is not expected to be encountered (film boiling would reduce the amount of heat added to the fluid due to its lower heat transfer coefficients, so nucleate boiling was desired). At a 25W heating rate, a maximum pressure rise of 14 to 21 kPa (2 to 3 psi) over a ten-minute heating period in low g was predicted by a lumped thermodynamic model of the fluid that accounts for evaporation, condensation, and heat conduction.

Each heater is near a tank wall but offset at least 0.6 cm (0.25 in) so that the majority of the heat flows into the fluid rather than out of the tank. One heater, designated heater A, is at the end of the tank opposite the mixer nozzle. The second heater, heater B, is located off the tank major axis along the side of the tank. Heater B's location is intended to produce an asymmetric initial condition (i.e., the bubble(s) and the temperature gradient are not centered on the path of the mixing jet) so that the effects of a realistic asymmetric, three-dimensional initial condition can be assessed. Heater B is also offset a greater distance from the tank wall to ensure that it, and any boiling activity, is visible in the photography.

A range of mixer flow rates is selected that spans a ten-to-one range, to include both penetrating and nonpenetrating flow regimes. The flow pattern correlation of Aydelott (ref. 15) was used in selecting the values in the test matrix, given in figure 4. The figure shows the flow rates chosen along with the corresponding flow patterns predicted by Aydelott's correlation. Four "primary" flow rates are the highest priority: two Pattern IV points, one Pattern I point, and zero flow (to assess self-mixing, or the pressure decay rate without forced circulation). Each primary test point is run three times with each of the two heaters to assess the repeatability of the results, and is also run once with both heaters on (with the heaters connected in series so that the total heat input is one-half the normal rate, and one-quarter the normal heat flux). Five "secondary" flow rates are chosen to extend the range above and below the primary points and to test intermediate values for which Patterns II and III are predicted. Each of these is run once with each heater. There are thus 38 total test runs: 24 primary and 14 secondary. The runs are arranged in a pre-planned randomized order, with the primary runs being executed first. Each run lasts for approximately 40 minutes, for a total test duration of 25.3 hours.

		Mixer Flow Rate:								
(gallons/min):	0.00	0.08	0.15	0.20	0.30	0.40	0.50	0.70	1.00	
(liters/min):	0.00	0.30	0.57	0.76	1.14	1.51	1.89	2.65	3.79	
Flow Pattern:	-	I	I	I/II	II	IV	IV	IV	IV	
Heater A	3 runs	1 run	3 runs	1 run	1 run	3 runs	1 run	3 runs	1 run	
Heater B	3 runs	1 run	3 runs	1 run	1 run	3 runs	1 run	3 runs	1 run	
Heaters A/B	1 run		1 run			1 run		1 run		

Figure 4: Test Matrix and Predicted Flow Patterns

The acceleration requirements for the experiment operation are consistent with normal STS orbital operations. Steady-state g-levels of 10^{-4} g or less are sufficient to produce a capillary force dominated fluid orientation, and are low enough to have a negligible effect on the jet geyser. This g-level also is low enough that buoyancy-driven free convection is negligible. It is desirable that for some of the test runs the liquid be settled at the mixer end of the tank and the ullage bubble at the opposite end—this axisymmetric fluid configuration is most similar to previous experimentation, most amenable to analysis, and of interest for those applications in which orbital drag will keep the liquid settled at one end of the tank. This initial condition is provided by orienting the experiment tank with the nozzle end aft, such that the launch and OMS insertion burns will position the liquid at that end. Furthermore, a period of "tail-first" Orbiter orientation is specified so that on-orbit atmospheric drag tends to settle the liquid at the aft end (a period of eight or more hours of tail-first time was requested; nearly 12 hours was actually provided on STS-43 as will be discussed later). In addition to this tail-first attitude, the more typical "nose-first" orientation and other attitudes were also desired for portions of the test timeline to assess the effect of initial fluid orientation on the results.

Orbiter reaction control system (RCS) thruster firings, crew activities, and other events can impart brief acceleration levels of up to 10^{-2} g. This noise, above and beyond the steady-state acceleration due to drag, can induce significant transient motions in the fluid and the interface. If their duration is sufficient, these events can cause the fluid to be reoriented. The level of noise has been shown in previous flights to be greatly dependent on the phase of the mission and the activities of the crew and other payloads. Operation of the experiment over at least a 24-hour period provides some data during periods of high activity and some during a sleeping period. This provides an indication of the effect of acceleration disturbances on pressure control system performance, including self-mixing.

Instrumentation

The primary data to be obtained are visual: the fluid orientations and the jet flow patterns as functions of flow rate. These are recorded by video cameras that photograph the fluid through transparent tank walls. In each run the first two minutes of the heating stage are photographed, so that the fluid initial conditions and the onset of boiling can be observed. The camera is then turned off until the beginning of the mixing stage, when it is turned on again for four minutes of photography. There is therefore a total of nearly four hours of real-time video (the maximum capacity of the tapes used). As aids in correlating the video data with the experiment timeline and digital data, brief periods of

camera operation without lamps provide separation of the runs and of the heating and mixing stages, and two light-emitting diodes (LEDs) flash a code at the beginning of each run that identifies the run number. The LEDs also flash once per second during photography to aid in timing any events seen on the videotapes.

Quantitative data taken are the tank pressure, the mixer flow rate, the temperature at four locations in the fluid, the temperature of each heater plate, the temperature of the fluid in the mixer flow, the heater power, and the acceleration in each of three axes. The purpose of measuring accelerations is to characterize the relative noisiness of different portions of the test, and to record the timing, magnitude, and duration of acceleration events that may influence the experimental results and possibly explain behavior seen in the video or pressure data. Determination of the precise value of the orbital drag acceleration is not a requirement of the experiment because, except for its effect on the initial ullage location, the steady-state g-level is not high enough to affect mixing phenomena (whereas the acceleration spikes could).

Specifics on the instrumentation (range, resolution, and accuracy) are given in the following sections.

EXPERIMENT APPARATUS AND OPERATION

STS Accommodations

The Tank Pressure Control Experiment is installed aboard the Space Transportation System (STS) in a Get-Away Special (GAS) carrier system. The GAS (or Small Self-Contained Payload) carrier provides standardized interfaces with the STS and can facilitate flight manifesting, integration, and safety. Payloads using the GAS carrier must be self-contained and autonomous, requiring no Orbiter power or data services and minimal crew control.

TPCE weighs 84 kg (186 lbm) and fills the 0.14 m³ (5 ft³) GAS canister. For the STS-43 mission the experiment was mounted on the port side of the payload bay, on the sill, approximately one-third of the way aft of the forward end of the bay. TPCE's GAS canister is purged and sealed, and contains one atmosphere of dry nitrogen gas throughout the flight. The experiment is controlled by a microcomputer that activates pumps, heaters, lamps, and instrumentation in a pre-programmed sequence. The computer also records data and stores it in solid-state memory. All payload power is from internal alkaline batteries.

Figure 5 is a photograph of the payload being installed in a GAS canister. Figure 6 is a sectional drawing of TPCE within the canister showing major elements of the apparatus (most details are omitted or simplified in this drawing for clarity).

Operation of the payload is initiated by a baroswitch, which is GAS-standard equipment. The baroswitch senses the depressurization of the payload bay during launch and closes a relay which connects the payload's battery pack. Operation of the experiment is autonomous after that point. As a backup to the baroswitch, the STS-43 crew checked the status of the relay to ensure that it was closed. After allowing sufficient time for the experiment to complete its planned sequence, the crew opened the relay via the autonomous payload controller (APC) in the aft flight deck, removing power from the payload. The baroswitch, power control relays, and APC interfaces are contained in the GAS electronics area visible in figure 6.

A moderate thermal attitude was provided during the operating time of TPCE. This included a predominantly bay-toward-Earth orientation, with brief excursions toward the sun and deep space. The GAS canister is well insulated, and the payload itself is thermally isolated from the canister, so the thermal environment for the experiment was stable and benign. A "tail-first" Orbiter attitude was requested for at least eight hours during experiment operation so that orbital atmospheric drag would tend to settle the liquid at the aft end of the tank. Nearly twelve hours of this attitude were actually provided, which included the first sleeping period.

PREGEDING PAGE BLANK NOT FILMED

20

ORIGINAL PAGE
BLACK AND WHITE PHOTOGRAPH

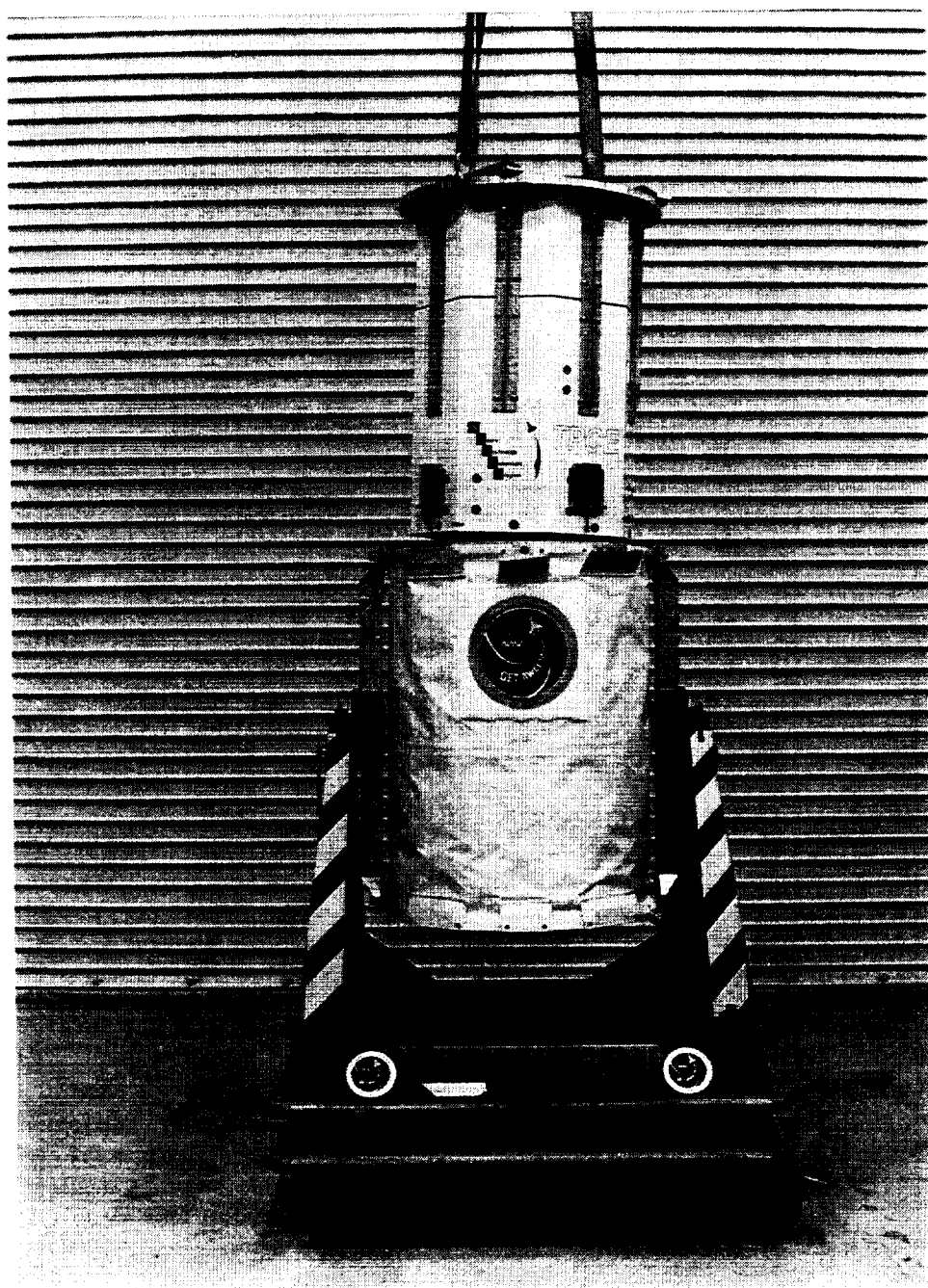


Figure 5: TPCE and Get-Away Special Carrier

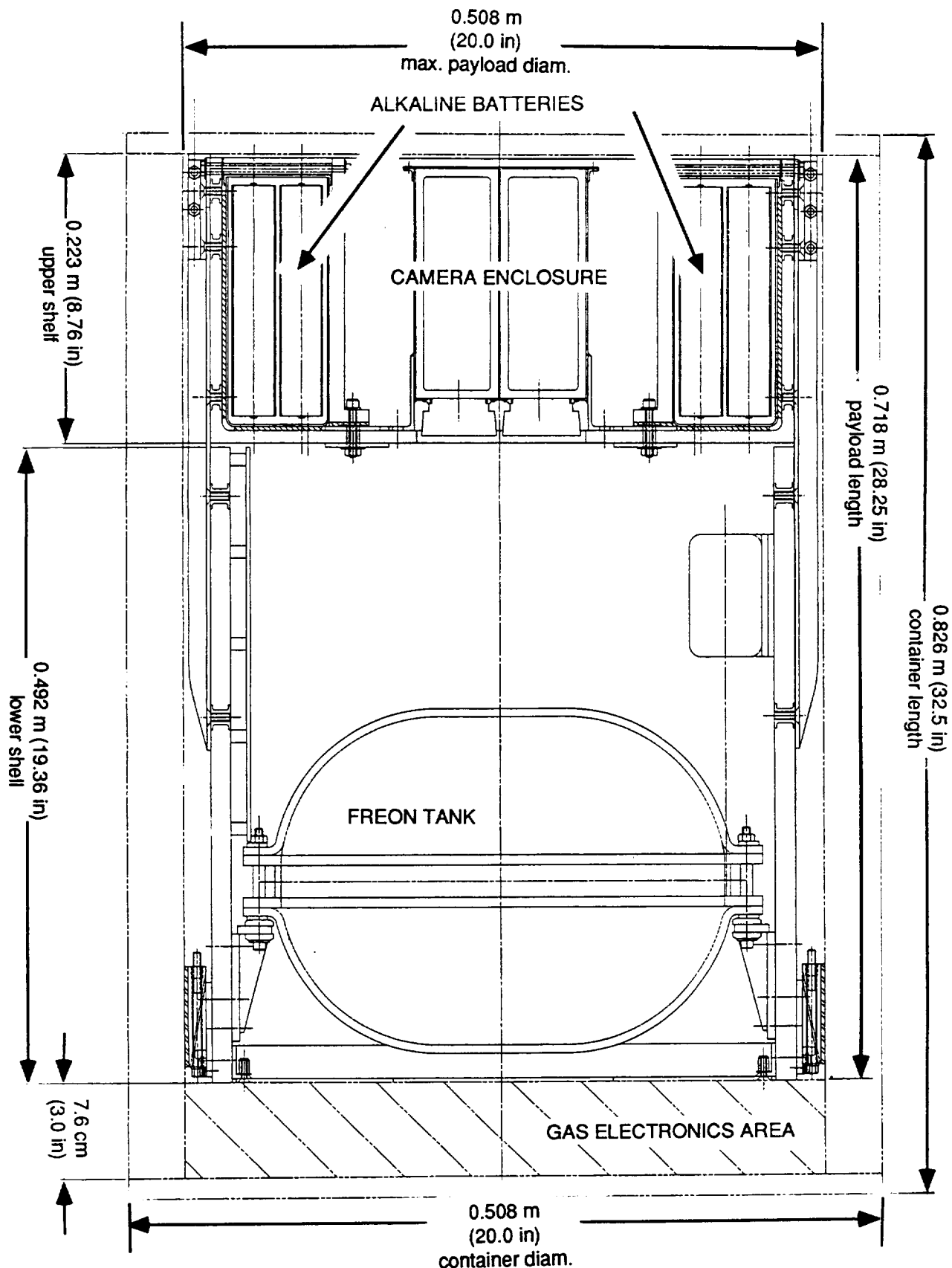


Figure 6: Sectional View of Major Payload Components

Structure

All components of the payload are mounted inside a composite shell. The composite, a foam-fiberglass-epoxy sandwich, provides high strength and stiffness plus low thermal conductance to the environment. It is lightweight and low-cost, and allows flexibility for mounting components during assembly. The shell has an octagonal cross section and is constructed in two pieces: a main "lower" section, and an "upper" tray. The two sections are mounted to each other and to the GAS canister's upper plate by eight tie bars, as shown in figure 7. Four equally-spaced adjustable bumpers carry lateral loads to the inside of the GAS canister at the lower end.

The fluid tank, the heaviest assembly in the payload, is mounted to six aluminum brackets via neoprene grommets. The grommets provide further isolation of the tank from heat conduction, vibration, and stresses. The aluminum brackets are attached to the lower section of the composite shell. Figure 8 is a photograph of the lower end of the payload that shows some of these details. For this photograph the end panel was removed—normally this panel closes off the bottom of the payload and provides a reflective interior surface for lighting. Figure 9 is a drawing showing the installation of the tank as viewed from the "upper" end of the payload (the camera's viewpoint). It also shows the locations of the bumpers and of some of the fluid system components.

The upper composite tray contains the battery pack, computer, and video cameras. It is removable for access to the fluid system, memory modules, and electronics contained in the lower section.

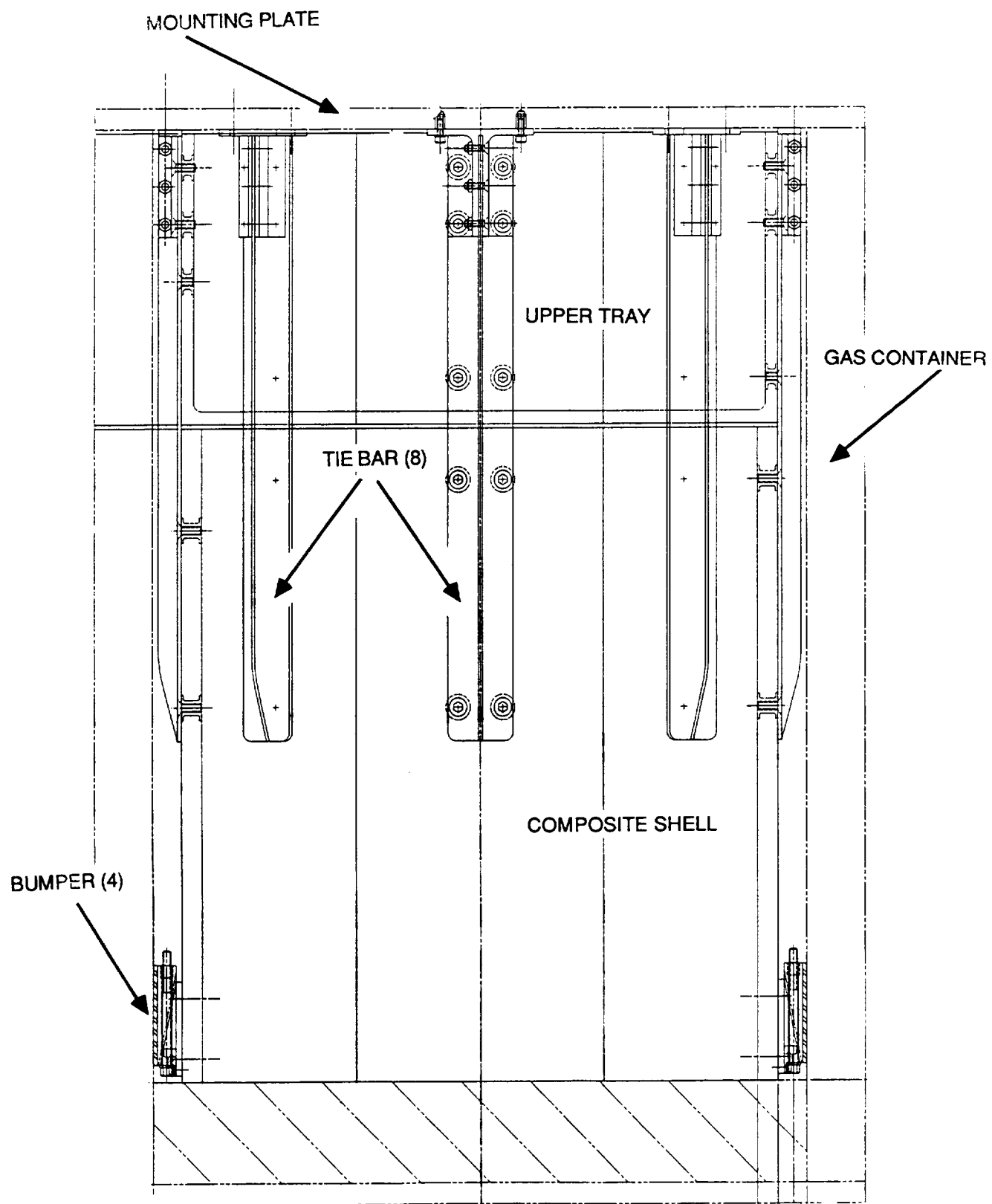


Figure 7: Structural Design

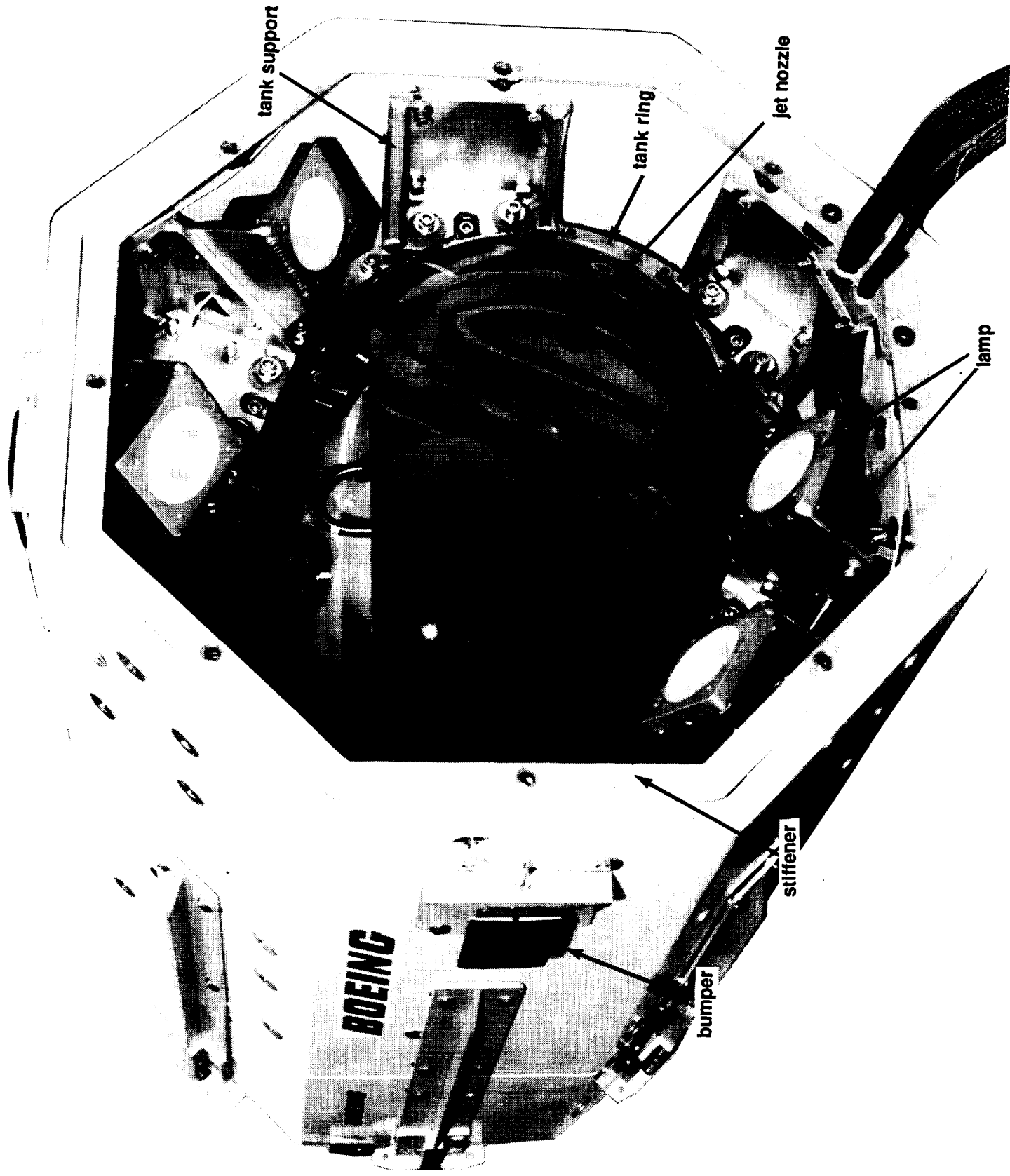


Figure 8: End View of Payload (Reflective Panel Removed)

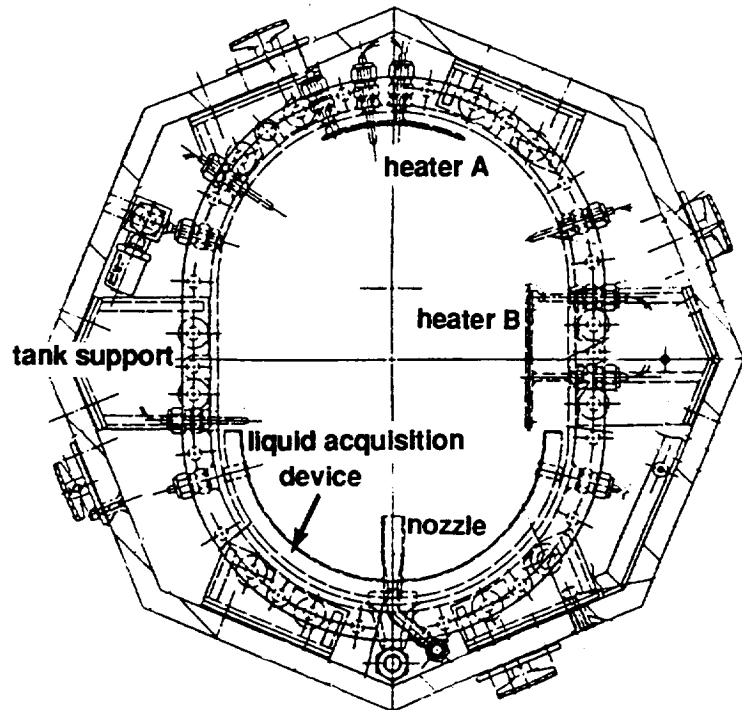


Figure 9: Tank Mounting Orientation

Fluid System

In accordance with the technical requirements stated previously, the tank is constructed in the approximate shape of a 25.4-cm (10-inch) diameter cylinder with hemispherical ends and a total inside length of 35.6 cm (14 inches). Its total calculated volume is 13.7 liters (0.485 ft^3). Its capacity was measured to be $21.8 +/- 0.5 \text{ kg}$ ($48 +/- 1.0 \text{ lbm}$) of refrigerant 113, or 13.9 liters (0.49 ft^3). This measured capacity includes the volume of fluid contained in the pumped loop but not the small volume of the pressure transducer manifold.

The tank itself is constructed in three main pieces: two transparent domes and a stainless steel oval-shaped center ring. The two domes are thermoformed from 0.1-cm (0.25-in) original thickness sheets of a crazing-resistant grade of acrylic plastic. They are bolted to the steel ring and are sealed against it with buna-N O-rings. The gaps between the flange bend radius and the flat surfaces of the steel ring are filled with epoxy, as shown in figure 10. The epoxy filler provides a smooth, rounded surface to avoid flow disturbances. All attachments and penetrations to the tank are made through the steel ring, including plumbing, thermistor probes, heater supports and feedthroughs, and LAD mounts. Figure 11 is a photograph of the tank assembly, and figure 12 shows its installation in the payload from the point of view of the cameras. All three fluid tubes leading to the tank are flexible metal hose which, in addition to the neoprene tank mounting grommets, provides strain relief and reduces transmission of vibrations to the fluid.

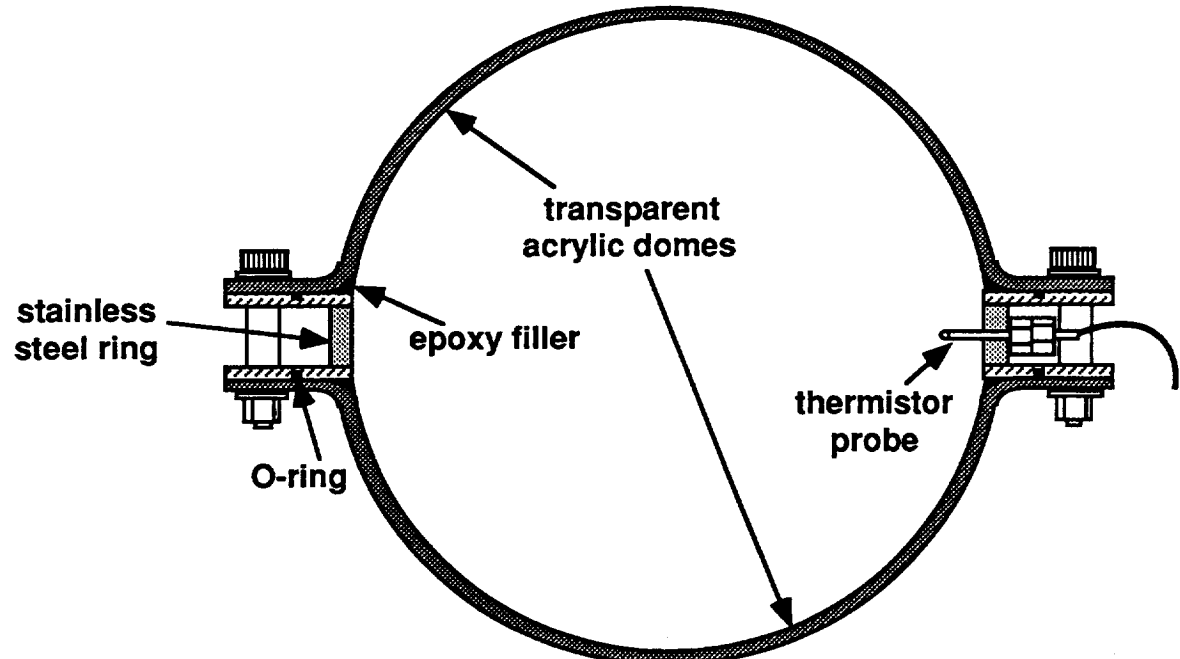


Figure 10: Tank Construction (not to scale)

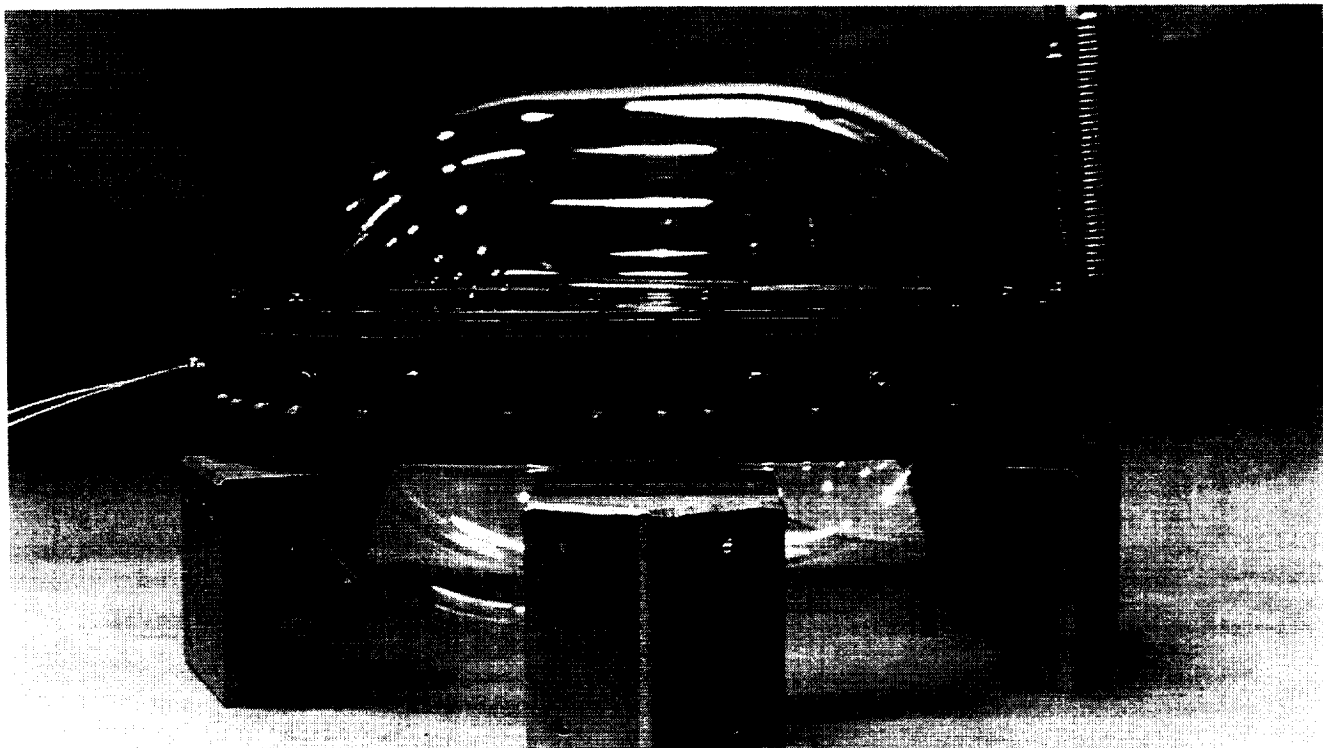


Figure 11: Tank Assembly

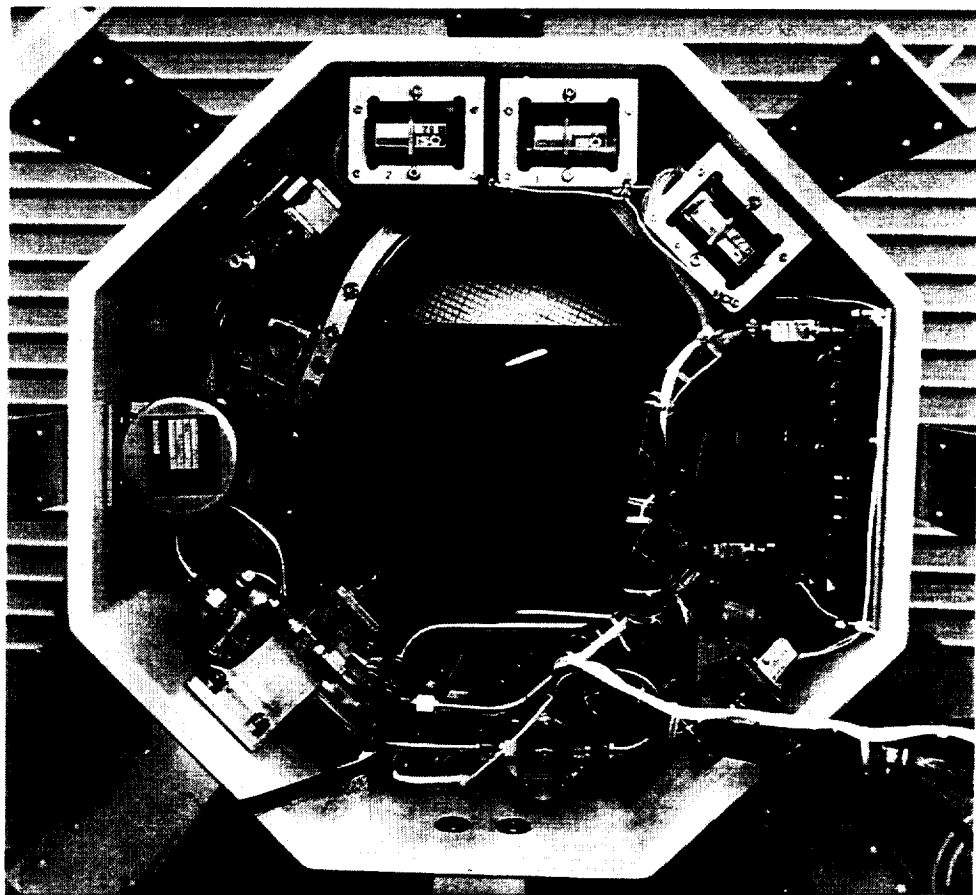


Figure 12: Fluid System Installation

Figure 13 is a schematic of the fluid system. The tank contains six temperature probes consisting of thermistors encapsulated in stainless steel sheaths. Thermistors T2, T4, and T5 reach $2.54 +/ - 0.15$ cm ($1.0 +/ - 0.06$ in) from the inside wall of the tank, and thermistor T1 extends $1.27 +/ - 0.15$ cm ($0.5 +/ - 0.06$ in). Thermistors T3 and T6 are attached to heaters A and B. Thermistor T7 is another probe inserted into the mixer flow downstream from the flow meter. A pressure transducer is connected to the tank via a small manifold and tube.

Also connected to the manifold are a pressure relief valve and a pressure switch. A second relief valve is mounted directly to the side of the tank. The computer is programmed to turn the heaters off if the pressure reaches 157 kPa absolute (22.8 psia), which in the nominally 103-kPa (15-psi) GAS canister environment equates to 54 kPa gage (7.8 psig). As a backup, the pressure switch is a safety device to interrupt power to the heaters in the case the pressure rises above 62 kPa gage (9.0 psig). In addition, the relief valves prevent any potential for tank rupture by venting fluid if the pressure reaches 69 kPa gage (10.0 psig). The tank's maximum design pressure is 86.1 kPa (12.5 psig), with a design ultimate safety factor of 2.5. (Under normal operating conditions the tank was not expected to reach a positive differential pressure at any time during the STS-43 mission, and this proved to be the case.)

Two pumps plumbed in parallel are used to provide the mixing flow. A single pump is used at lower flow rates (with the capability of switching to the other pump in case the first pump fails to deliver flow). Both are operated in the runs requiring higher flow rates. To reduce the net positive suction head requirements, the pump suction line and inlet ports are designed for minimum pressure loss.

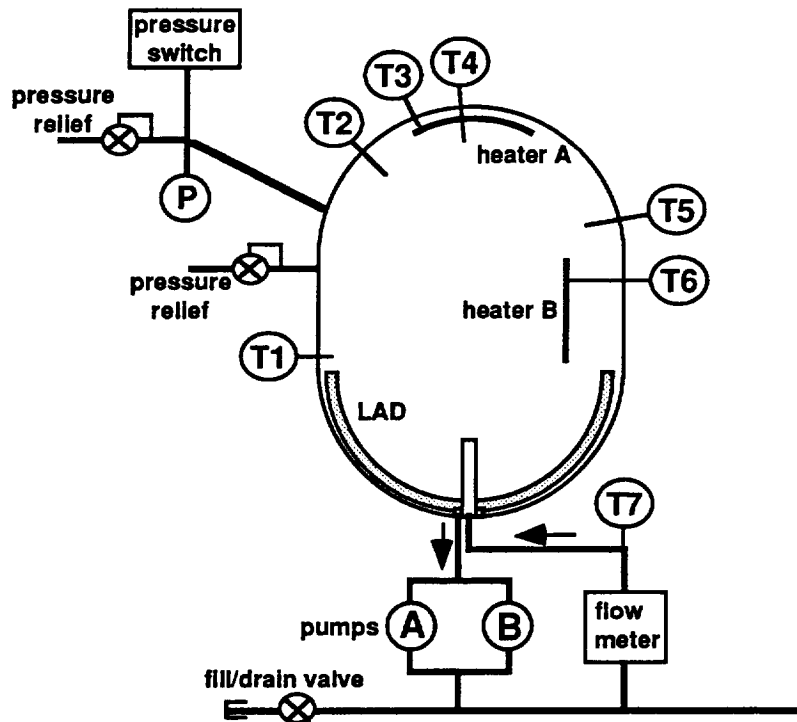


Figure 13: Fluid System Schematic

The pumps are supplied with vapor-free liquid at all times by the LAD, which is a semicircular channel made of stainless steel plate. The side of this channel facing the tank wall is micro-etched with 0.38-mm (0.015-in) diameter perforations and has a 21% open area fraction. The gap width between this porous surface and the tank wall is 0.6 cm (1/4 in).

Two heaters are immersed in the fluid. Heater A is located 0.5 cm (0.2 in) from one end of the tank (at its maximum distance), and heater B is located off the tank centerline approximately 2.5 cm (1.0 in) from the side wall. Heater A is bent to a 12.1-cm (4.75-in) radius to follow the curvature of the tank wall, while heater B is flat. The two heaters are constructed of an etched-foil element encased in silicone rubber insulation, which is sandwiched between two 304L stainless steel plates as shown in figure 14. The perimeter of the sandwich is welded to seal the element from the fluid. The heating element is a 9.6 cm by 6.6 cm (3.8 by 2.6 in) rectangle with a 0.64-cm (0.25-in) circular cutout so that thermistor probe T4 can pass through the heater. Each steel plate has a thickness of 0.191 cm (0.075 in), narrowing to 0.089 cm (0.035 in) near the perimeter weld. The outside dimensions of the assembly are 10.46 by 7.42 cm (4.12 by 2.92 in), for an overall surface area (both sides included) of 155 cm² (24.1 in²). This area includes the small perimeter flange that extends 0.30 to 0.41 cm (0.12 to 0.16 in) beyond the element. The heater assembly is welded to a standoff tube which supports the assembly and contains the leads. Additional support is provided by a thermistor probe bonded (using thermally-conductive epoxy) onto a small area of greater thickness. The total mass of each heater, excluding the standoff tube and thermistor, is 0.214 kg (0.472 lbm), and the thermal capacitance is estimated to be 0.10 kJ/K. Figure 15 is a photograph of the two heaters.

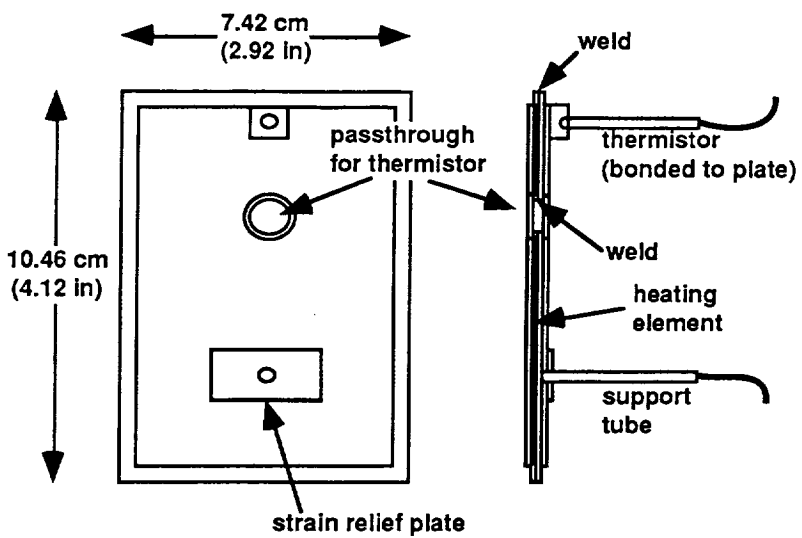


Figure 14: Heater Construction (not to scale)

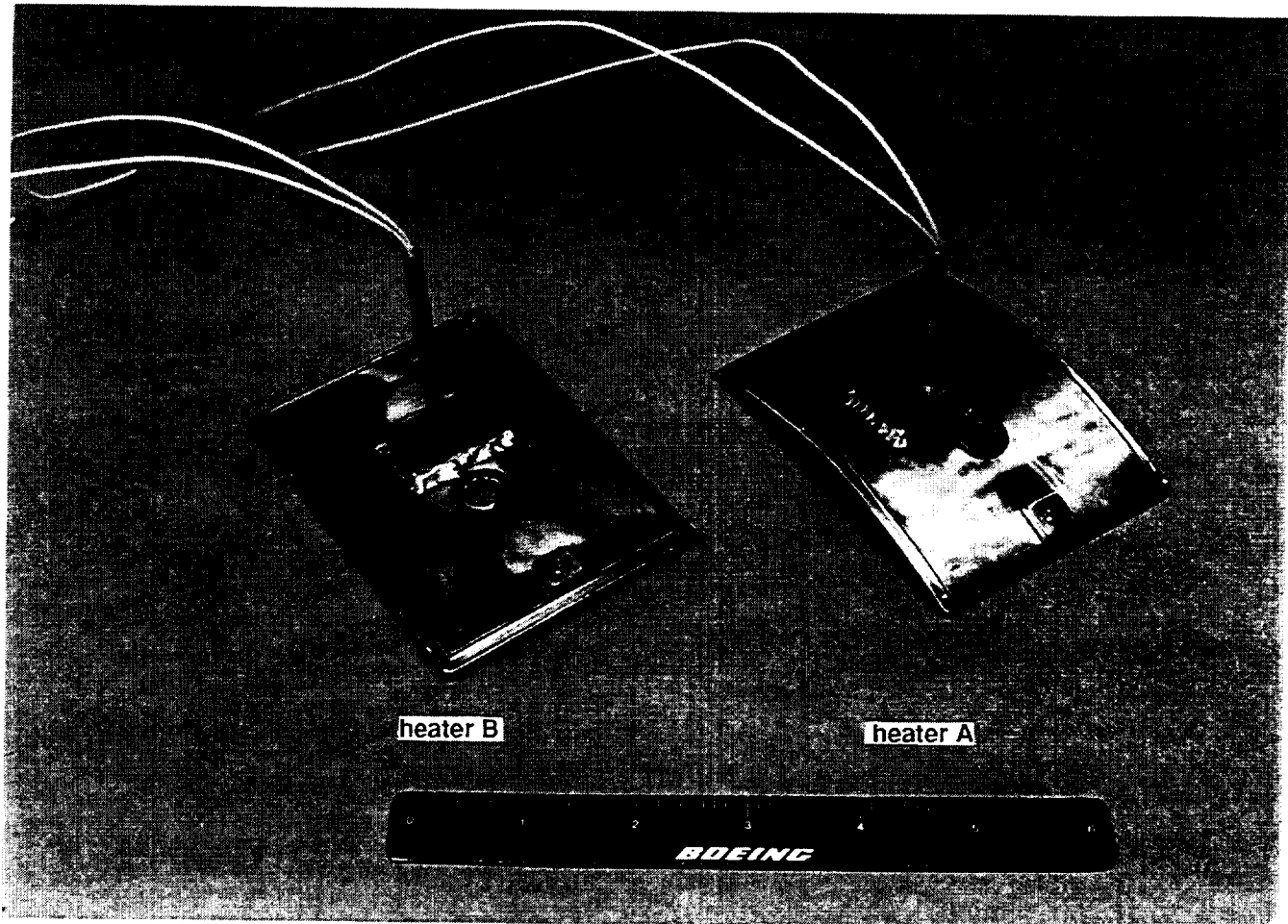


Figure 15: Heaters

Power Supply

The payload is powered by an internal battery pack consisting of 96 F-size alkaline (non-rechargeable) cells. The cells are connected in a series-parallel arrangement that provides 12 and 18 volt (nominal) outputs. The total battery pack capacity is 2000 watt-hours under constant drain rates, which is approximately three times the energy required by the payload under normal conditions. The extra capacity provides voltage stability under peak drain rates, better low-temperature performance, and reserve capacity in case of partial battery failure or other payload failures. The cells are packaged into 48 two-cell stacks which are glued into a rigid polyurethane foam block inside a fiberglass shell. This forms a mechanically strong block with minimum internal void volume. A small volume at the top of the pack, containing the wiring, fuses, and protective diodes, is packed with absorbent insulating felt material and covered with a fiberglass lid. The pack is designed to contain any liquid electrolyte that might leak in the event of damage, but without containing any gases that might be evolved. At 22 kg (48 lbm), the battery pack is a large portion of the payload mass. Figure 16 shows the battery pack installed in the upper tray along with the computer and camera enclosure.

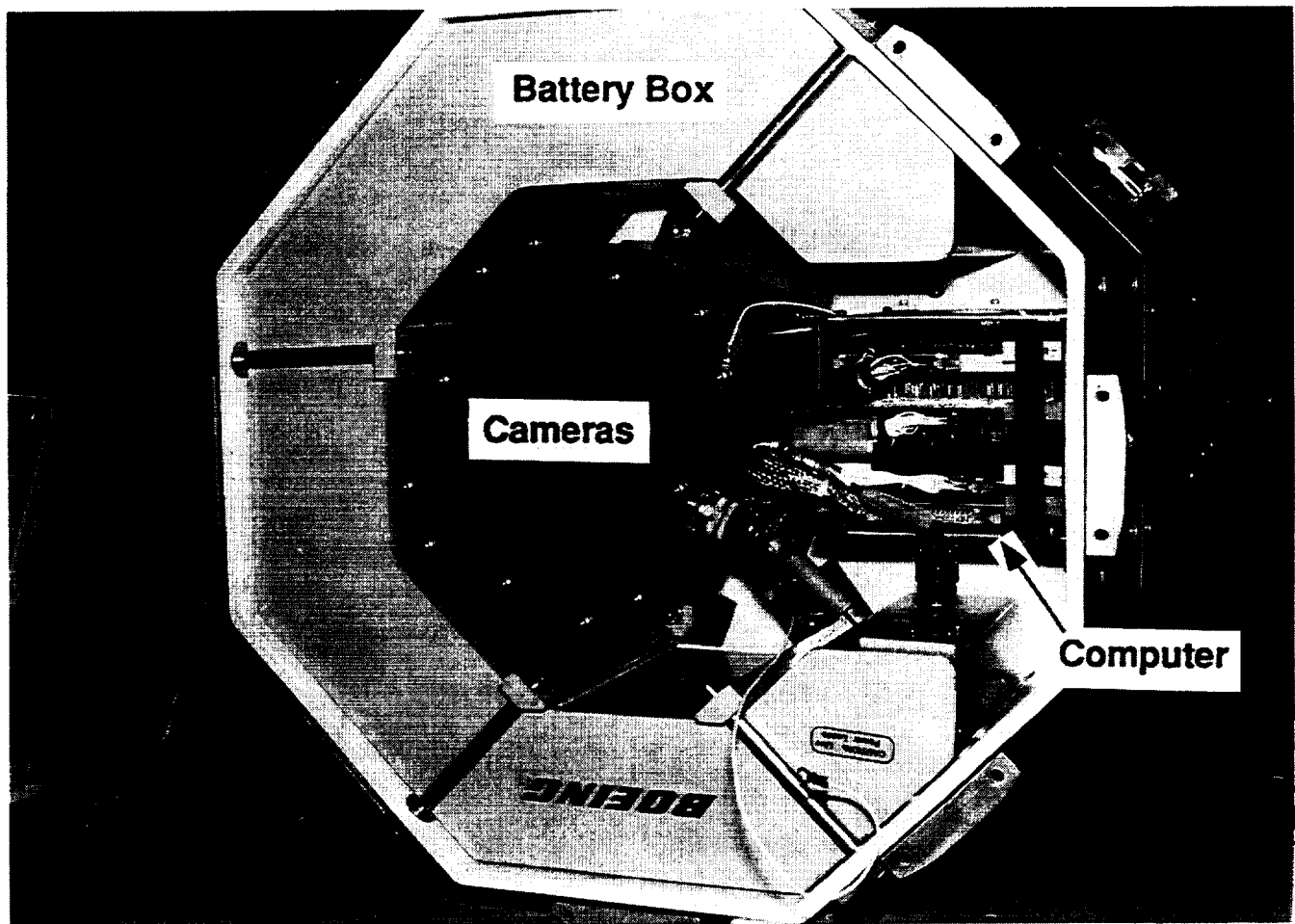


Figure 16: View of Payload Showing Battery Pack, Computer, Cameras

The ground terminal of the battery pack is connected to the GAS container, which is grounded to the Orbiter. The 12V and 18V power leads are connected to the payload via the GAS power relays so that all payload power is controlled by these relays. Payload lamps and cooling fans are supplied with unregulated 12V DC power, and the pumps and heaters use unregulated 18V DC. The mixing pumps are controlled by a pulse-modulation circuit that also compensates for the declining voltage as the batteries discharge, to produce the desired pump speed and flow rate for each test run. Voltage regulators also supply regulated power at +15, -15, +5, +6, and +8 volts to the computer, instrumentation, and video cameras. The power regulating circuits and other components that dissipate significant amounts of heat are located on a circuit board in the main compartment of the payload. Two small cooling fans circulate the nitrogen purge gas in the payload to provide forced-convective cooling of these components.

Controls and Data Storage

A microcomputer mounted in the upper tray controls the payload operation and records the output of the instruments. The computer, visible in figure 16, is based on the ultra-low-power C-44 bus. It uses mostly off-the-shelf complementary metal oxide semiconductor (CMOS) boards having low energy consumption (and consequently low heat dissipation). Four of these circuit boards are housed in a card cage: (1) the central processing unit (CPU) board which uses the 80C85 processor, (2) a 16-channel analog-to-digital converter board, (3) a custom-built output control and equipment interface board, and (4) a memory interface and control board. Figure 17 is a block diagram of the control system. A custom-built circuit board, called the conditioner board, contains the interfaces between the computer and the instrumentation (amplifiers, voltage dividers, pulse counter, filters, and other signal conditioning circuitry) as well as some of the output interfaces and voltage regulators.

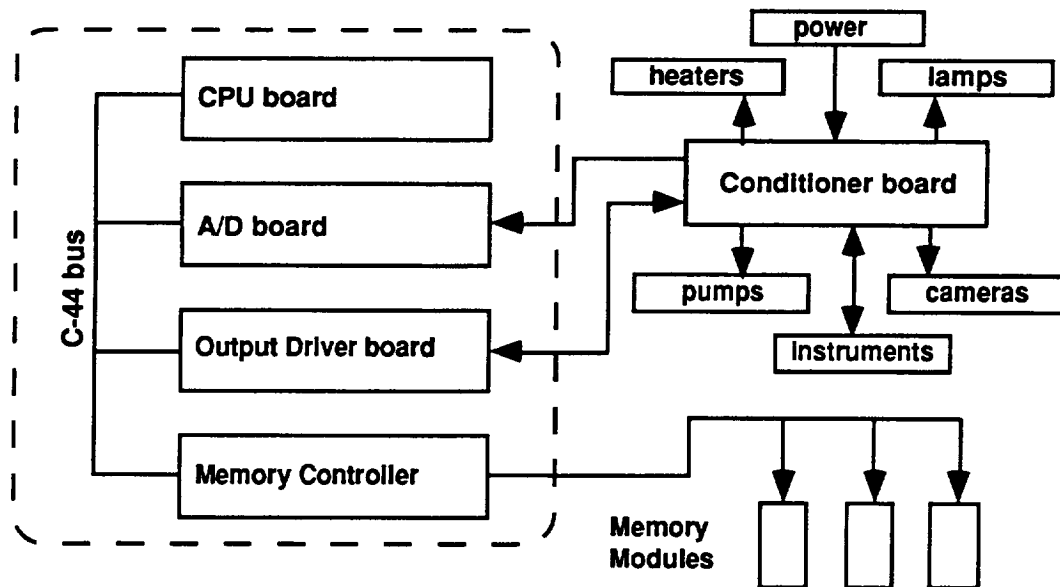


Figure 17: Controls and Data Storage Block Diagram

Software for the controller is written in 8085 assembly language. The code is stored in a non-erasable, fusible-link type of read-only memory so that the instructions cannot be altered by cosmic radiation. Since CMOS devices are known to be susceptible to upset by the radiation environment within a GAS canister in flight, critical variables that must be stored in random access memory during operation are stored in redundant locations.

This makes it possible to recover proper data values (such as the program counter) in the event that a value is erased or altered by radiation.

The memory interface board has its own CPU to control the storage of digital data. It is connected to three solid-state memory modules, each of which stores one megabyte of data on nonvolatile erasable programmable read-only memory (EPROM) chips. These three memory modules are mounted in the payload's lower section and are removable for extraction of the data. Nearly three megabytes of data are stored during execution of a normal mission. Following the mission or a mission simulation test the data is downloaded to a mainframe computer for reduction into engineering units, application of calibration data, and plotting.

Instrumentation

The primary experiment instruments include a flow meter downstream of the pumps, a pressure transducer, the seven fluid temperature sensors (thermistors) discussed previously, and three accelerometers. Figure 18 summarizes the range and accuracy of each instrument, plus the rate at which data are taken during each stage of a test run. The accuracy figures are estimated based on the manufacturers' stated accuracies and on their performance in flight and during pre- and post-flight tests. The pressure transducer, which measures absolute pressure, was found in post-flight testing to have a shifted bias value, i.e. all readings were offset by a small constant value. All pressure data were subsequently corrected for this bias shift, which was likely caused by torque on the transducer fitting during installation. Each "thermistor" is actually a set of three matched thermistors, packaged together in the tip of the probe, that are read in such a way as to have a linear output. Self-heating errors are minimized by applying current to each thermistor only during the brief period that a reading is taken.

INSTRUMENT	RANGE	RESO-LUTION	ACCURACY	SAMPLE RATE		
				stage 2	stage 3	stage 4
pressure transducer (absolute)	0 to 173 kPa (0 to 25 psia)	0.04 kPa (0.006 psi)	0.35 kPa (0.05 psia)	3/sec	3/sec	1/sec
thermistors (7)	-20 to +70°C (-4 to +158°F)	0.02°C (0.036°F)	0.1°C (0.18°F)	1/sec	1/sec	1/min
flow meter	0 to 3.8 l/min (0 to 1.0 gpm)	0.02 l/min (0.005 gpm)	0.04 l/min (0.01 gpm)	-	1/sec	-
heater power	0 - 30 W	0.1 W	0.1 W	1/sec	-	-
accelerometers (3)	+/- 0.01g	2.4×10^{-6} g	5×10^{-4} g abs. 1.2×10^{-5} g rel.	3/sec	3/sec	3/sec

Figure 18: Instrumentation Summary

The accuracy of the three accelerometers is given for absolute readings and relative readings. The bias (zero-point) reading of these units is subject to drift over time and to temperature effects, altering the absolute readings. The scale factor, which governs relative readings such as the magnitude of the acceleration produced by a thruster firing versus the background level, is less susceptible to these errors. The X-axis

accelerometer, being of highest interest for axial jet mixing, is thermally modelled so that its output is adjusted in the post-flight data reduction for changes in both its bias value and scale factor as functions of temperature. The outputs of all three accelerometers are filtered, prior to sampling by the computer's analog-to-digital converters, to remove high-frequency components of the signal. The analog filter used has a time constant of 0.375 seconds.

Other data recorded, for diagnostics and to perform the temperature compensation of the X-accelerometer, are two additional temperatures: (1) inside the X-axis accelerometer, and (2) on the analog-to-digital circuit board in the main computer housing. These have accuracies of approximately 2°C (3.6°F) and are recorded once per run. Voltage-divider circuits are also used to sense the heater power and the battery voltages. The voltage at the 18V nominal battery terminal is recorded once per minute with an accuracy of approximately 0.18V. The 12V level is also measured once per minute to determine that the cells are not overdischarging, but this data is not recorded.

The three accelerometers are installed on one of the tank supports such that their axes are aligned with the STS Orbiter coordinates. Figure 19 shows the TPCE acceleration axes with respect to the fluid tank, to the Orbiter, and to the picture visible when viewing the videotapes.

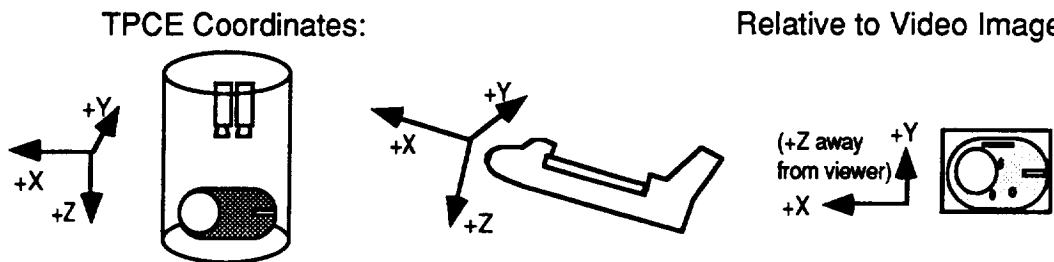


Figure 19: Accelerometer Axes

Photography

Video photography and recording is accomplished with two modified commercial camera/recorder devices. These compact consumer-type 8mm format camcorders provide two hours of photography each. They are modified to use payload power (supplied at 8.0 volts) with computer control of their functions. Certain portions of the cameras are removed and several switches are locked into position. They are mounted in a stainless-steel enclosure with approximately 0.6 cm (0.25 in) of foam padding on all sides and are allowed to "float" inside it for their protection from vibration and shock during launch. Wide-angle adaptor lenses are mounted on the enclosure, which is airtight to eliminate concerns about outgassing of lubricants and other materials in the camcorders. Figure 20 is a photograph of the enclosure.

The cameras view the tank through an opening in the upper tray. Their fields of view are similar, with lines of sight parallel to the centerline of the payload, except that the right-hand camera image is shifted slightly towards heater B to ensure that boiling phenomena on the heater plate are visible.

Four 12-watt halogen incandescent lamps provide illumination of the tank. Their light is directed at the panel at the lower end of the payload. This panel is reflective (a glass-beaded aluminum finish) with a 0.64-cm (0.25-in) square black grid painted on it. The grid's purpose is to enhance visualization of the liquid/vapor interface—the difference

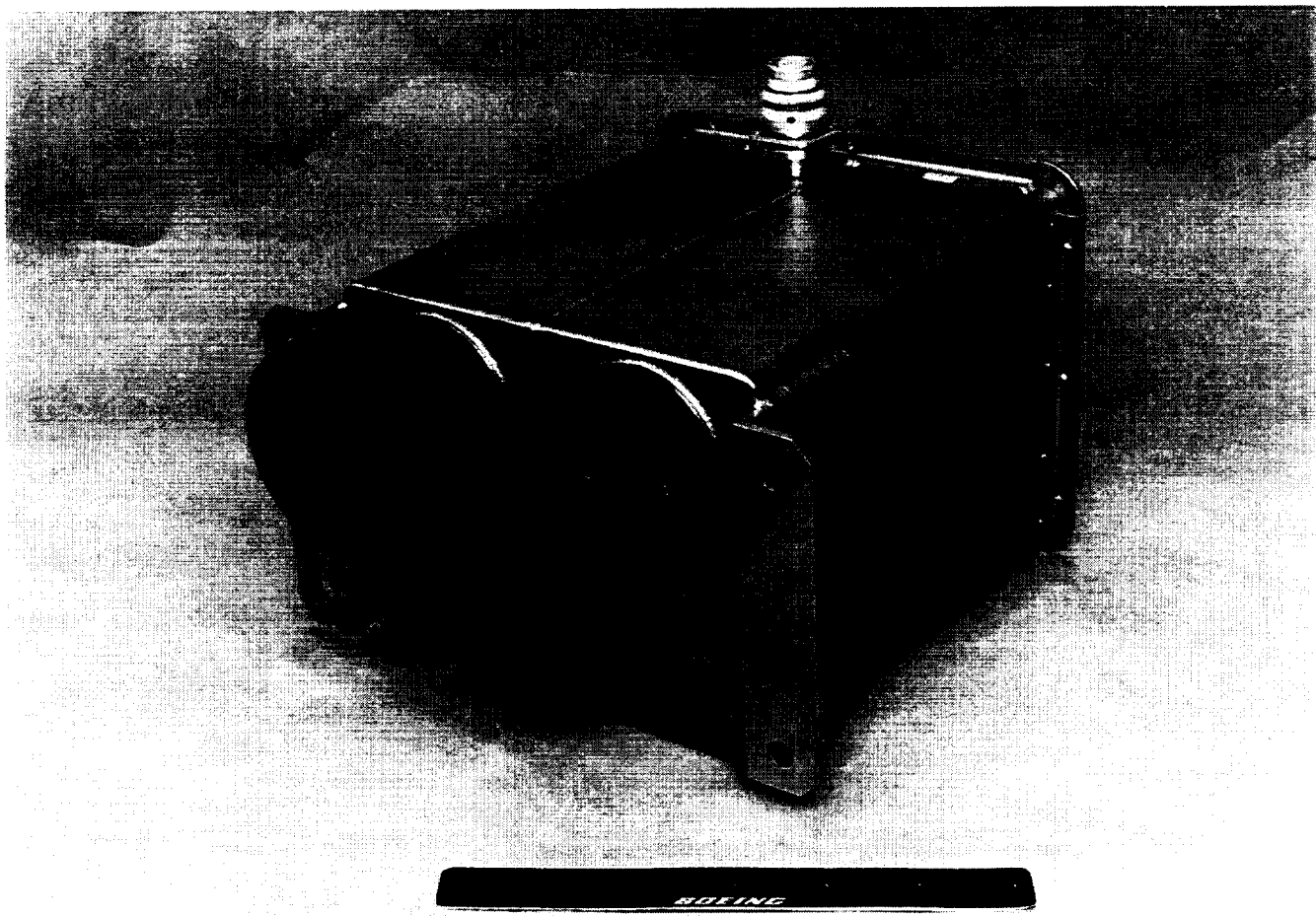


Figure 20: Video Camera/Recorder Assembly

between the refractive indices of the phases produces discontinuities in the grid lines at the liquid/vapor interfaces. The fluid is tinted with a trace amount (<0.5 ppm) of orange dye (Sudan IV) to further aid in discriminating liquid from vapor in the picture.

The lamps are sealed with glass plates (which are frosted to diffuse the light), preventing contact between the hot bulbs and any leaked refrigerant, which could create a decomposition hazard. Each bulb assembly is mounted to an aluminum bracket which blocks most direct viewing of the tank by the bulb and which also acts as a heat sink to minimize radiative heating of the fluid. Each bracket is mounted to a tank support, providing a further heat sink, and the negative electrical lead of each bulb (which is connected to the hot filament) is thermally shorted to the heat sink using a large-diameter ground wire.

Operating Timeline

Depressurization of the Orbiter payload bay during ascent causes the baroswitch to activate the payload approximately one minute after lift-off. At this time the computer begins to operate and starts a six-hour delay period. This delay allows orbit to be achieved and the payload bay doors to be opened before starting the experiment. After this delay period the computer turns on power to the instruments, allows a four-minute warmup period, and performs a ten-second startup health test. After checking for low fluid pressure, which would cause execution of a fluid warmup contingency operation, and for high fluid pressure, which would trigger a high-pressure contingency, the test matrix of thirty-eight runs is begun.

Figure 21 shows the order of the tests and the camera, pump, and heater assigned to each. A run begins by first checking for excessively high pressure and, if found, attempting to reduce it before turning on the heater(s). This is identified as Stage 1 and its duration is one-third second unless the high pressure contingency is encountered. Stage 2 is the heating stage and its total duration is ten minutes, unless the pressure rises more than 21 kPa (3.0 psi) before that time. Data-taking begins at the start of this stage, and video photography begins at approximately six seconds. First a code is flashed on the two LEDs to identify the run number, then the lamps are turned on at 13.33 seconds from start of the run. One second later the heater is turned on. The lamps and camera are turned off at two minutes, and at 10:00.33 the heater is turned off.

Stage 3 is the mixing stage. At 10:02.33 the camera is again turned on and, after allowing a brief period of black picture (to distinguish the stages in the video), the lamps are turned on at 10:06.33. Two seconds later the pump(s) is turned on. The camera is turned off after four minutes, and the pump(s) remains on until 25:00.33, the end of Stage 3. Stage 4, the recovery phase, runs for fifteen minutes with data taken at a reduced frequency (except for accelerometer data, which is recorded at 3 Hz continuously). No heating, mixing, or photography occurs during Stage 4. The entire duration of each run is 40:01, and the next run begins immediately afterward.

The complete sequence of test runs lasts over 25 hours (25:20:38), not including the six-hour initial delay and warmup period. The test matrix concludes at approximately 31.5 hours after lift-off. At this time the computer removes power from most of the payload components and puts itself into a low-power sleep mode. The STS-43 crew turned off the power relay two days after launch, which allowed sufficient time for this nominal sequence plus all of the programmed contingencies.

Run No.	Heater	Design Flow Rate		Pump	Camcorder	Start Time (minutes)
		liters/min.	gallons/min.			
1	B	0.00	0.00		Right	0.00
2	B	2.65	0.70	A&B	Left	40.02
3	B	0.57	0.15	A	Right	80.03
4	B	1.51	0.40	A	Left	120.05
5	B	2.65	0.70	A&B	Right	160.07
6	B	0.00	0.00		Left	200.08
7	B	1.51	0.40	B	Right	240.10
8	A	0.57	0.15	B	Left	280.12
9	A	0.00	0.00		Right	320.13
10	A	2.65	0.70	A&B	Left	360.15
11	A	0.57	0.15	A	Right	400.17
12	A	1.51	0.40	A	Left	440.18
13	A	2.65	0.70	A&B	Right	480.20
14	A	0.00	0.00		Left	520.22
15	A	1.51	0.40	B	Right	560.23
16	A	0.57	0.15	B	Left	600.25
17	B	2.65	0.70	A&B	Right	640.27
18	B	0.00	0.00		Left	680.28
19	B	1.51	0.40	A	Right	720.30
20	B	0.57	0.15	B	Left	760.32
21	A	0.00	0.00		Right	800.33
22	A	2.65	0.70	A&B	Left	840.35
23	A	0.57	0.15	A	Right	880.37
24	A	1.51	0.40	B	Left	920.38
25	B	0.30	0.08	A	Right	960.40
26	B	1.14	0.30	B	Left	1000.42
27	B	0.76	0.20	A	Right	1040.43
28	B	1.89	0.50	B	Left	1080.45
29	A	1.14	0.30	A	Right	1120.47
30	A	1.89	0.50	A	Left	1160.48
31	A	0.76	0.20	B	Right	1200.50
32	A	0.30	0.08	B	Left	1240.52
33	A&B	0.57	0.15	A	Right	1280.53
34	A&B	1.51	0.40	B	Left	1320.55
35	A&B	0.00	0.00		Right	1360.57
36	A&B	2.65	0.70	A&B	Left	1400.58
37	B	3.79	1.00	A&B	Right	1440.60
38	A	3.79	1.00	A&B	Left	1480.62

Figure 21: Order and Characteristics of Test Runs

LOW-G AIRCRAFT TEST

Aircraft Test Objectives and Approach

A prototype payload was constructed for a low-gravity test on the NASA Lewis Research Center Learjet prior to assembly of the STS payload. Up to 30 seconds at a time of reduced gravity are obtained during parabolic flights of this aircraft. The purpose of this test was to reduce technical risk for the STS test by performing a comprehensive systems checkout in a low-g flight environment.

The general objective of the aircraft flight test was to verify the overall operation of the payload inside a GAS canister in a low-g flight environment. It was intended to uncover any possible unexpected performance problems that are not seen in normal gravity testing. In addition, the test would provide experience in shipping the payload, integrating it with the GAS canister, deintegrating, and extracting data after the flight. Five specific objectives were identified for the aircraft flight test:

1. *Flow Patterns.* The flow rates for TPCE were selected using a correlation that is based on subscale drop tower tests. Confirmation that these flow rates will span the desired range of flow patterns was desirable to maximize the value of the data returned from the STS flight.
2. *Cavitation.* Proper operation of the pumps in the absence of a gravitational head pressure was a concern. The low-g test would verify that pump cavitation is suppressed when 7-14 kPa (1-2 psi) of noncondensable gas is added to the ullage to provide net positive suction pressure (NPSP).
3. *Fluid Foaming.* Another concern was the possibility that the jet mixer would cause excessive bubble formation, particularly at the highest flow rates, resulting in foaming and frothing of the fluid in the tank. If the froth were to persist, rather than coalesce, subsequent test runs would be compromised. There was insufficient experience with bubble coalescence and collapse times in low g to completely exclude this possibility without a test.
4. *Heater Operation.* Observation of the heaters was desired to possibly determine whether nucleate boiling is obtained at their heat flux in low g. This could indicate whether the heaters are capable of providing the desired pressure rise during the heating phase of the experiment. (It was recognized however that the short duration of low-g time available might not permit boiling to be established in the aircraft test.)
5. *Photographic Coverage.* Because the liquid and the tank walls refract light, the field of view and the ability to see detail in the tank are highly affected by the liquid/vapor orientation. Since a low-g fluid orientation, particularly a curved interface, is difficult to achieve in the laboratory, it was necessary to test the adequacy of the video photography optical design and lighting on the aircraft.

The prototype payload was installed inside a GAS canister and hard-mounted to the cabin floor of the Learjet. The payload was controlled in real time by on-board experimenters via a small laptop control box. A simplified version of the flight software was installed in the payload computer which caused it to record data at a constant rate

while permitting manual control of the pumps, heaters, lamps, and cameras. The payload was powered by its internal battery pack, and it recorded data into its internal memory for post-flight extraction, although several channels were monitored during the flight via test ports on the control box. Both video cameras operated continuously during each flight test. The payload was oriented so that the tank's longitudinal axis was vertical during level flight, with the mixer nozzle and LAD at the bottom. This ensured that the mixer pump was supplied with liquid during the parabola entry maneuver and that the LAD was initially filled with liquid.

Twenty-four parabolas were flown during four flights. During the first 12 runs the tank was pressurized with helium gas to a total NPSP of 15-21 kPa (2.2-3 psi). For the last 12 runs the NPSP was reduced to approximately 6 kPa (1 psi). Each of the flow rates, including primary and secondary points, from the STS test matrix was tested several times. In each run the heater was turned on during level flight, and the pump(s) was adjusted to produce the desired indicated flow rate and then turned off. Several seconds after entering the low-g portion of the maneuver the pump(s) was turned on and was left on until the 2.5g pull-up began. In the last three runs the pump(s) was turned on prior to low-g entry and left on throughout the parabola.

Aircraft Test Results and Conclusions

The payload operated well throughout all four flights. All flight data were extracted and reviewed. It was discovered that in the first flight (the first six test runs) the pilot's display of the target acceleration, which is used for pitch control during the parabola, was inadvertently set for 0.05g rather than 0g. This resulted in a flat liquid/vapor interface with no observed jet penetration during those six runs. The remaining flights provided acceleration levels which were approximately centered around 0g in all three axes. However there were significant excursions from 0g which frequently reached full-scale on the accelerometers (+/-0.01g) in all runs. Figure 22 shows typical accelerometer readings from the three channels. (In this plot, positive "X" is toward the starboard wing, or away from heater B; positive "Y" is toward the nose of the aircraft, or toward the cameras; and positive "Z" is "up" during level flight, parallel to the direction of jet flow out of the nozzle.)

In reviewing the video data it was evident that aircraft tests cannot substitute for in-space operation of an experiment of this kind. The quality of the acceleration environment was inadequate to produce a surface-tension-dominated fluid orientation, and there was insufficient time in each parabola for the liquid motions induced by the pull-up (and amplified by the g-level reduction) to damp out. Significant velocities remained in the liquid in each run and made it difficult to establish a mixer flow pattern. However, it was determined that the highest flow rates occasionally appeared to penetrate the ullage, and the lowest flow rates did not appear to be capable of penetrating the surface. Since the planned test matrix therefore appeared to span the desired range of flow patterns, it was concluded that the matrix was validated.

Boiling was not observed at the heaters in any run. With the significant residual fluid velocities present during the maneuvers, the low heat flux was insufficient to overcome the forced-convection heat transfer at the heater plates. Consequently specific objective number 4 was determined to be unobtainable with this kind of test.

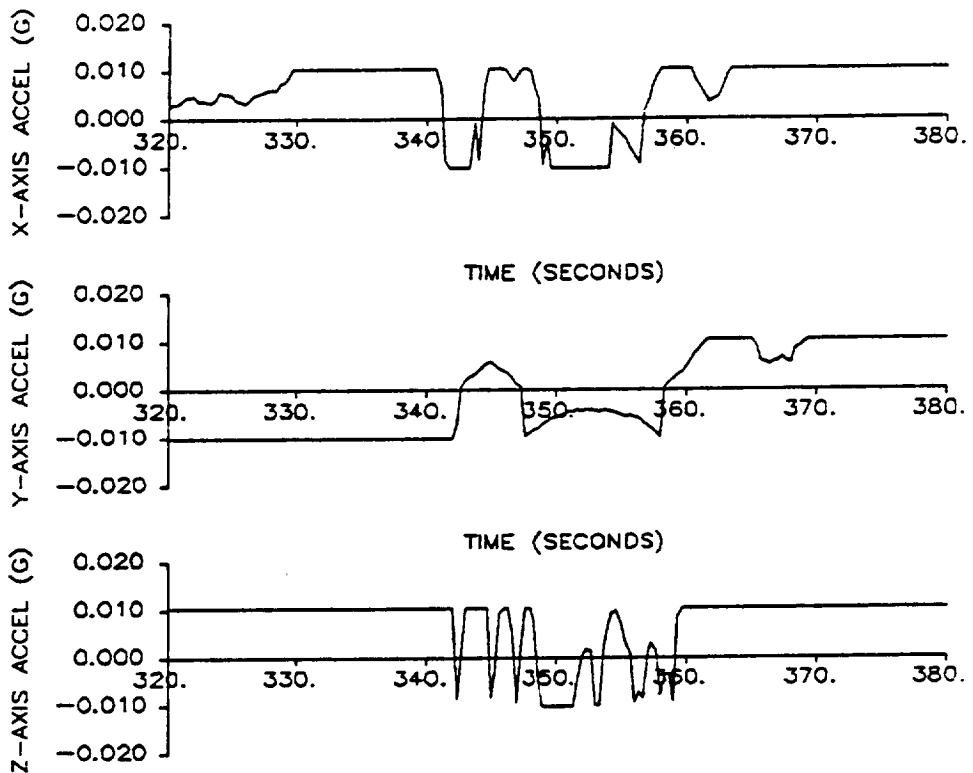


Figure 22: Aircraft Test Accelerometer Traces: One Typical Parabola

The other objectives were successfully met. It was confirmed that cavitation would be suppressed by the level of noncondensable gas planned to be added to the tank. Some cavitation—manifested as a reduction in flow rate during low-g—was seen at the lower value of NPSP, but the experiment was otherwise unaffected. Foaming of the liquid was also determined not to be a valid concern. Even in this worst-case test, with considerable sloshing of the fluid in combination with the high flow rate mixing, the bubbles were seen to rapidly coalesce and no tendency to form a persistent froth was found. The photographic quality proved to be good, providing visualization sufficient to meet the experiment requirements under all conditions.

The experiences resulted in several improvements to the payload design and operations that proved valuable on the STS flight. One camera was re-aimed to yield better coverage of boiling at heater B. The bumpers were redesigned, and a low-rate leakage problem with the tank assembly was identified and solved. Better procedures for erasing and downloading from the memory modules were developed to reduce the risk of data loss. No other problems relating to operation of the apparatus in low gravity were found.

IN-SPACE TEST

Payload Performance

General. The TPCE payload was flown in space on Shuttle mission STS-43 from August 2 to 11, 1991. Eight hours after launch, the Shuttle crew verified that the baroswitch had activated the payload. The "tail-first" (-X_{VV}) Orbiter attitude was initiated at approximately day zero, seven hours and fifty minutes (0/07:50:00) mission-elapsed time (MET), and continued through approximately 0/22:00:00 MET, for a total duration of about 14 hours. TPCE was deactivated on schedule two days after launch at 2/01:32:48 MET. Thus TPCE was powered up for approximately 49.5 hours.

After the flight the payload timeline was correlated with the mission timeline by comparison of mission events recorded on the accelerometer data channels. The deployment of the primary payload, a Tracking and Data Relay Satellite and its Inertial Upper Stage (TDRS/IUS), is visible as a 3-second sawtooth-wave centered at 0:07:09 on TPCE's clock. The actual time of deployment of the TDRS/IUS payload is known to be 6:12:39 MET, so that TPCE's time-zero is at 06:05:30 MET.

After recovery of the payload it was inspected and tested. No damage was observed to any components and no failures occurred. The systems testing performed at Kennedy Space Center showed no anomalies. The liquid level was inspected visually relative to references on the tank and no change was observed. After the ullage gas was sampled for analysis, the tank was drained and weighed. Allowing for evaporation during the sampling, the original fill quantity of 18.1 +/- 0.5 kg (40 +/- 1 lbm) was confirmed. This corresponds to a fill fraction (at room temperature) of 83%.

Ullage Gas Makeup. Measurements prior to shipment showed that pressure changes were occurring over time in the fluid system due to the permeability of the polymeric tank and seals. It was originally intended that the ullage consist only of refrigerant-113 vapor plus 14 kPa (2.0 psi) partial pressure of helium. However, the total partial pressure of noncondensable gases (P_{nc}) was observed to be dropping slowly during storage prior to the flight. P_{nc} is defined as the difference between the total pressure (with the tank well-mixed) and the vapor pressure of refrigerant 113 as calculated for its temperature at the time of the measurement. Based on the flight data (i.e., the pressures and temperatures recorded when the fluid was well mixed), the value of P_{nc} at the time of experiment operation was approximately 4.1 +/- 1.0 kPa (0.60 +/- 0.14 psi).

With the reduced P_{nc} to provide pump suction pressure (4.1 kPa versus the planned 14) there was concern that cavitation would limit the pumps' ability to provide the planned flow rates. In flight, however, for the two runs having the highest flow rate (runs 37 and 38) the measured flow rates averaged nearly 90% of the planned values. The other two effects of cavitation that had been observed in ground testing, besides flow rate limiting, were bubbles in the outflow line and erratic flow meter data due to bubbles in the line. Tiny, barely-visible bubbles are seen in most high flow rate runs, beginning some time after flow initiation, but these are not large or numerous enough to compromise the experiment results. No erratic flow meter data were seen at any time.

Samples of gas drawn from the ullage were analyzed with a mass spectrometer after the flight to determine the constituents of the noncondensable gas fraction. Figure 23 shows

the results of the measurement, in percent by partial pressure. The measurement shows that the majority of the helium gas diffused out of the system during the ten months between the tank fill operation and the flight. During that time water vapor, nitrogen, and other components of air permeated into the tank, partially replacing the volume of lost helium.

<u>Species:</u>	<u>% of Noncondensibles</u>	<u>Pressure, kPa</u>	<u>Pressure, psi</u>
helium	0.158	0.65	0.095
water	0.223	0.92	0.134
nitrogen	0.437	1.80	0.262
oxygen	0.155	0.64	0.093
argon	0.003	0.01	0.002
carbon dioxide	<u>0.025</u>	<u>0.11</u>	<u>0.015</u>
Total:	100	4.14	0.600

Figure 23: Approximate Noncondensibles Concentrations During Flight

Instrumentation. The lamps and cameras survived the flight environment and operated as planned, providing nearly four hours of real-time imagery. The quality of the photography is good and meets all the experiment requirements. Distortion and refraction limit visibility near the perimeter of the tank, though bubbles frequently provide a view of these regions by acting as a spherical "fish-eye" lens. The timing LEDs are visible at the extreme edge of the picture. Both heaters are easily observable.

The 3 megabytes of digital data were extracted and reduced in a multi-step process. Approximately 40 bytes were lost to transmission errors during this process. The data reduction software, which uses a mainframe computer to convert the binary data into formatted engineering-units data, has a bounds-checking feature that generates warnings whenever a value is above or below the range expected for a particular instrument. When this is encountered, the bad value is replaced by the previous value for that instrument and a warning is given. Approximately 500 warnings were generated from the STS-43 data, somewhat more than from ground test data sets. These warnings, which are randomly distributed through the flight data and are not peculiar to a particular instrument, could be due to noise, transmission errors, or possibly cosmic radiation upset of the memories (a known effect in the GAS radiation environment). In any case these represent a very small percentage of the data recorded (less than 600 bytes out of 3,145,000 bytes).

The pressure transducer signal was free of noise. Pressure oscillations observed in some phases of the experiment are believed to be real, consistent with heater temperature swings, thruster firings, and flow-induced oscillations. As discussed previously, a 2 kPa (0.3 psi) level shift was discovered in post-flight comparisons with three different calibrated gages; this shift is believed to have existed prior to the flight, so all flight data have been adjusted by subtracting this constant value from them.

Evaluation of the flight data indicates that all seven thermistors in the fluid were operating normally. The X-axis accelerometer's thermistor was consistent with the fluid thermistors to within 0.5°C at payload startup. The thermistor built into the computer reads consistently about 6-7°C higher than the accelerometer thermistor. This is acceptable since the computer temperature is for diagnostic information only.

All three accelerometers performed within specifications, as nearly as can be determined. The rated accuracy is +/-0.12% in scale-factor and +/-0.008g bias (zero-offset), with one-year repeatability in the bias of +/-0.0012g. The accelerometers were supplied with

factory-measured calibrations, which were confirmed by bench tests at Boeing prior to installation; however both of these measurements were made a year or more prior to the flight. The factory-supplied bias values for each unit (which is given as a function of temperature in the case of the X-axis unit) were subtracted from the data post-flight.

The average acceleration values, calculated over each entire run after applying the factory-supplied corrections, are plotted in figure 24. It may be noted that these time-averaged readings are not exactly zero in any of the three axes. This is almost entirely due to drifting of the bias values, or zero-offset, since the last calibration. All three units show a residual average reading of less than 0.0005g (absolute value). The amount of the drift is well within the one-year repeatability specification for the instrument. Therefore the absolute levels, or average values, of the accelerometer readings presented in this report do not indicate the true background g-level but represent residual instrument bias error. (However, as discussed in the next section, the change in these levels during the flight may be used to provide an indication of the background g level.)

Note also that the average indicated values for the Y and Z axis units vary over the mission, as the payload warms up. The X axis unit exhibits the same trend before the temperature correction is applied. Therefore this trend is not real, but is a temperature effect since the Y and Z units are not thermally compensated. Note also a slight transient—within specifications—at the beginning of operation shortly after being turned on, due to instrument "warmup".

Heater power and voltage measurements are consistent with ground tests and expected behavior. Heater A dissipates slightly more power than heater B (by approximately 0.5 watts). The flow meter output is good and is consistent with ground tests and other data. Battery voltage at the end of the mission is consistent with predictions and previous behavior, thus indicating that the batteries performed as designed.

The thermal environment was benign during flight operation. Payload temperatures recorded at the computer and at the accelerometers (near the tank at the lower end of the GAS canister) are plotted in figure 25. At turn-on all indicated temperatures were approximately 19.5°C (67°F), with the exception of the computer temperature which was 6°C higher. At the end of run 38, the accelerometers had warmed to less than 28°C (82°F), the computer indicated nearly 34°C (93°F), and the T7 trace indicates that the environment outside of the tank was less than 26°C (79°F). The fluid mixed temperature in run 38 was 26.5°C (79.7°F), and the maximum fluid temperature recorded at any time was 34°C (93°F). These are significantly lower than the worst-case high temperature of 46°C (115°F) that was used to predict the maximum design pressure in the tank.

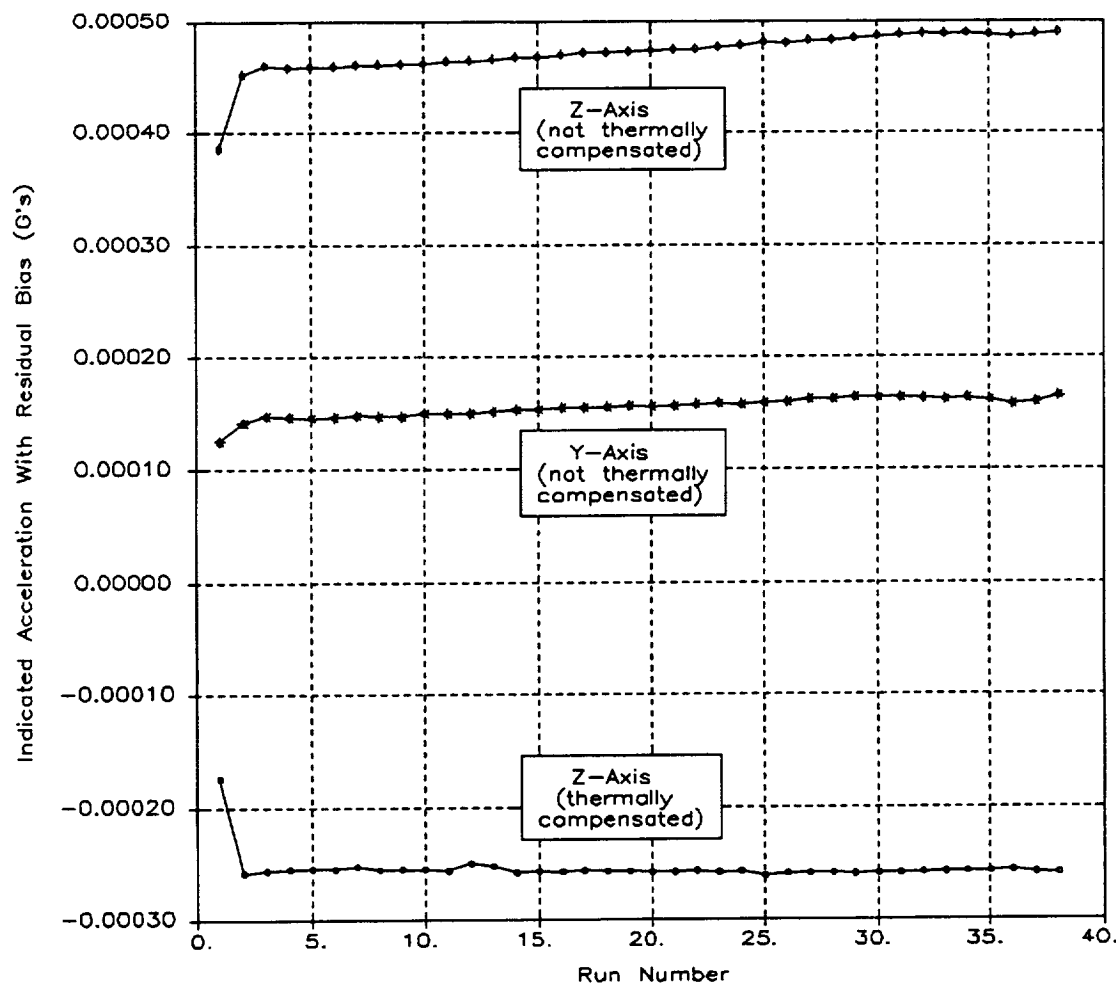


Figure 24: Average Indicated Acceleration Values In Flight (With Residual Bias)

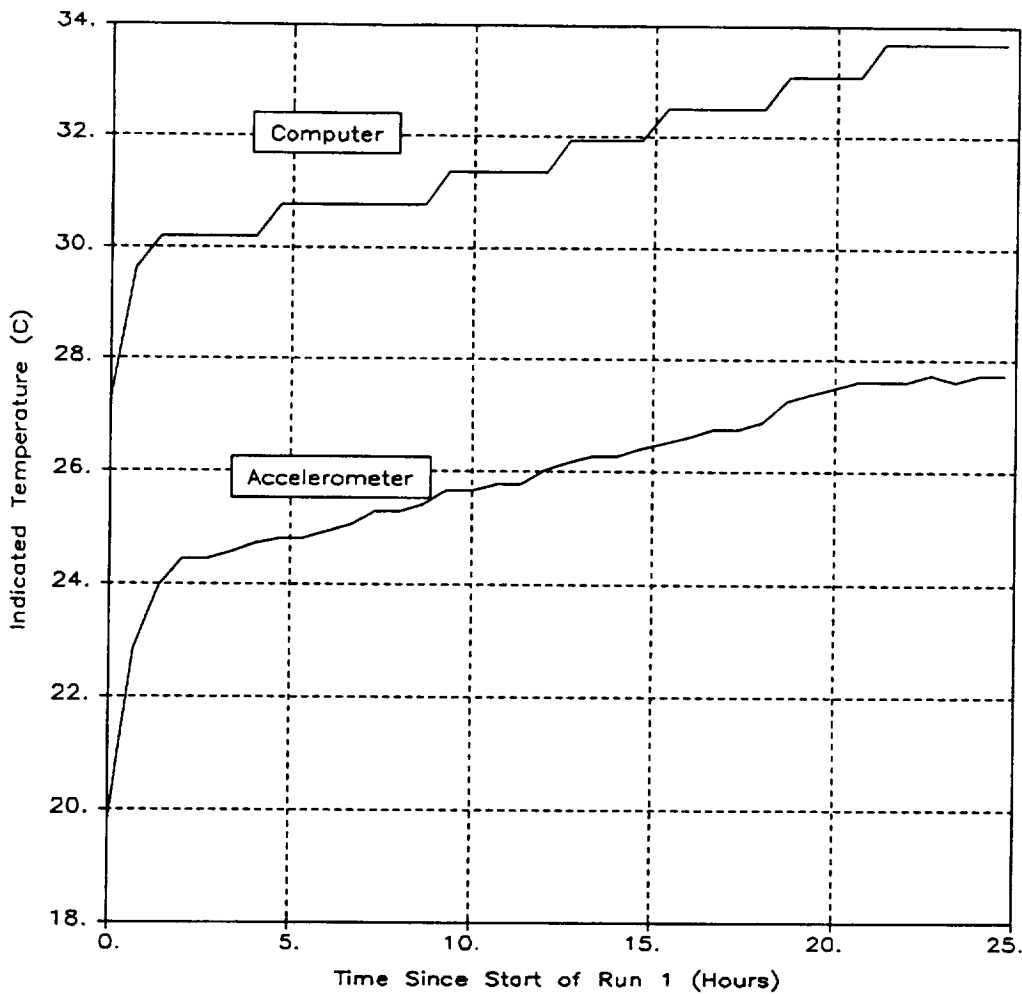


Figure 25: Payload Temperatures During Operation

Data Summary

Acceleration. The appendix contains plots of the complete set of digital data recorded during the STS-43 flight. Figures A-1 through A-38 display the accelerometer outputs for runs 1 through 38, respectively. Because the absolute value of the data ranges over four orders of magnitude, each figure consists of two plots. The upper graph displays the data at a scale that includes the maximum range of the instruments. The lower graph plots the same data with an expanded scale so that smaller events and noise are visible. The same scales are used for each run so that they may be easily compared. The X-axis of all plots is the experiment time scale (the time elapsed since the beginning of run 1).

Although the full-scale range of the accelerometers as read and recorded by the computer (uncorrected) is from -0.010g to +0.010g, the reduced data ranges from -0.014g to +0.008g. This is because the raw output has been corrected in the post-flight data reduction by applying the factory calibrations for each instrument. Again, note that none of the three channels' outputs are centered exactly on 0 g, due to the inherent bias drift of the accelerometers.

The measured amplitude of the acceleration jitter is on the order of 10^{-4} g peak-to-peak. Orbiter reaction control system (RCS) firings are visible in the data as nearly full-scale

spikes for the primary RCS thruster, and as 2 to 5×10^{-4} g spikes for the vernier thrusters. A firing of the orbit maneuvering system (OMS) thruster reaches full scale in both the X and Z axes during run 1.

Figure 26 shows the environment in run 3, a perhaps typical level of activity. The environment is quietest during the crew sleep period (approximately 240 minutes to 780 minutes, TPCE-time). Figure 27 illustrates this, showing a significantly lower peak-to-peak noise level although vernier RCS firings are still seen. At other times of high activity, particularly during the TDRS/IUS deployment from 0 to 40 minutes, the environment is extremely noisy, as can be seen in figure 28.

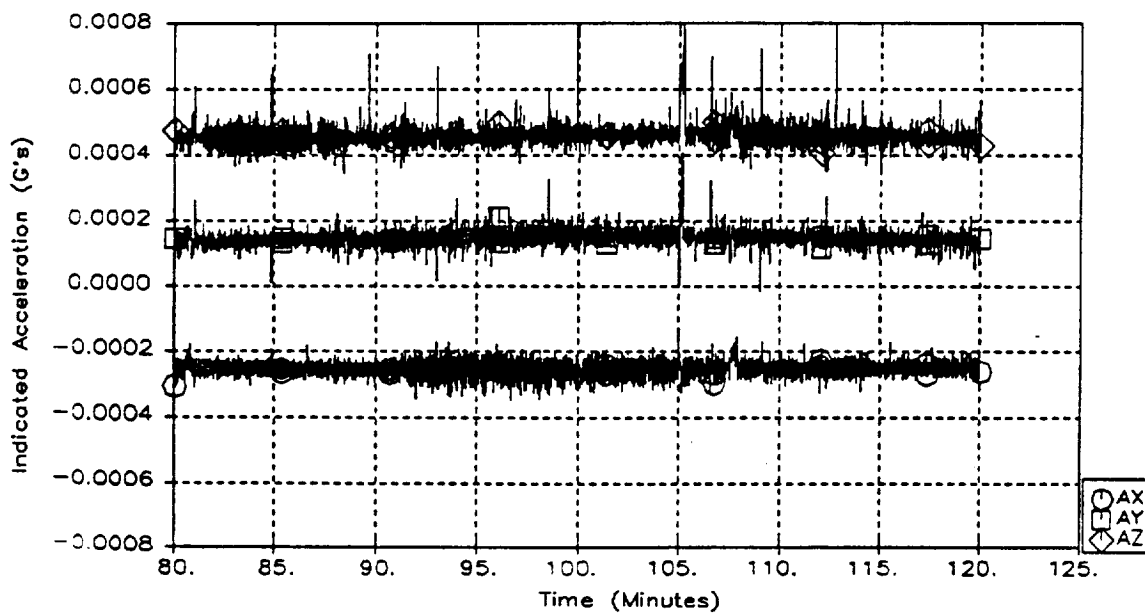


Figure 26: Typical Acceleration Environment (Run 3)

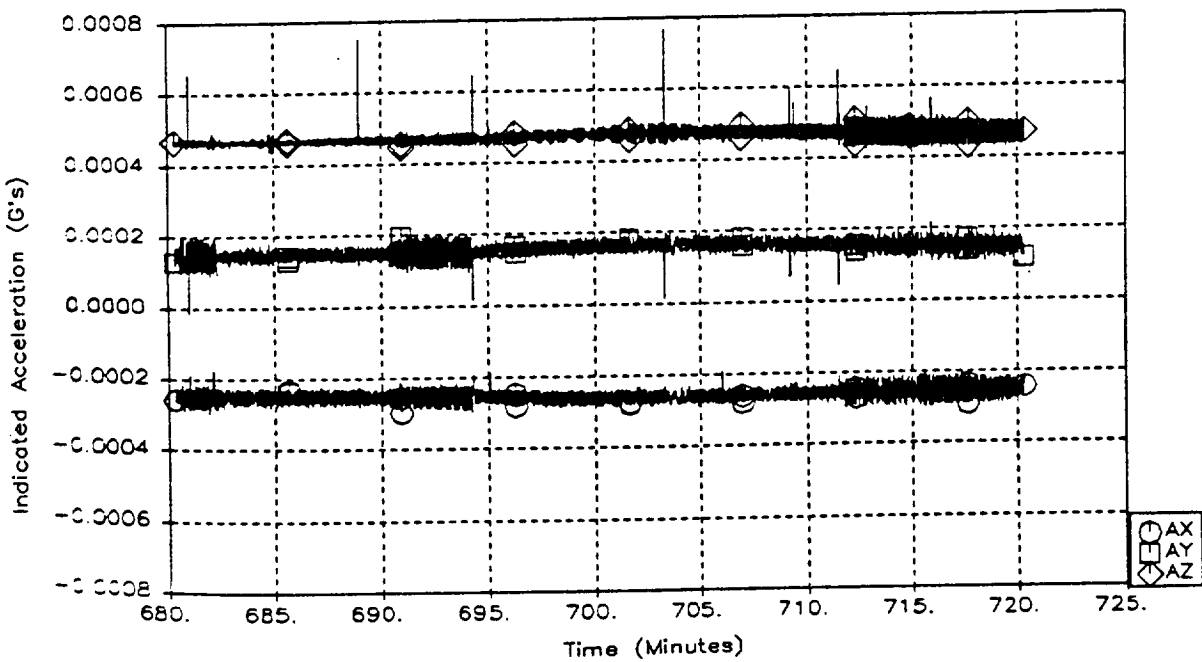


Figure 27: Sleep Period Acceleration Environment (Run 18)

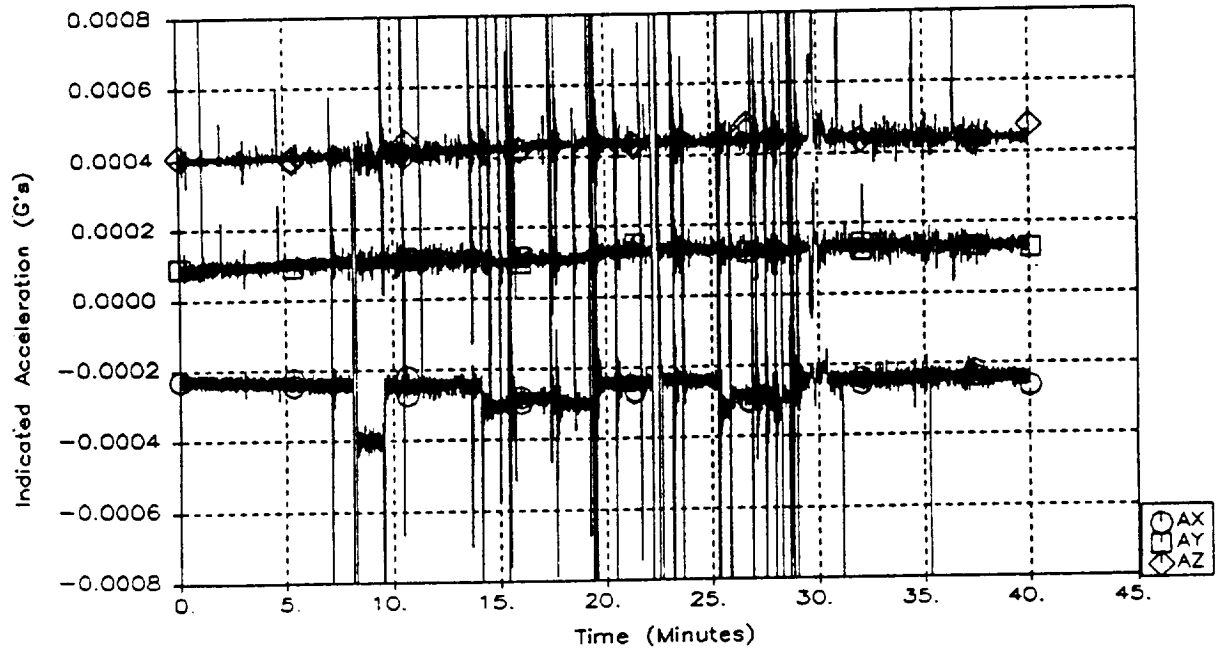


Figure 28: Noisy Acceleration Environment (Run 1)

Because the average acceleration level is very small in relation to the noise and to the range and accuracy of the accelerometers, it is not possible to directly determine the steady-state acceleration caused by drag and other background effects. It may however be estimated in the X axis, or at least given an upper bound, by averaging the values for each run and observing the trend in relation to Orbiter orientation, as plotted in figure 29 (these values are the same as plotted in figure 24 for the X axis). If one assumes that the average acceleration due to atmospheric drag when the Orbiter is oriented nose-first ($+X_{vv}$ attitude) is approximately equal and opposite to that experienced when it flies tail-first ($-X_{vv}$), then that value is one-half the difference between the average indicated levels for those two orientations. (Note however that time-averaging of the accelerations will tend to cancel out the random vibrations and crew motions, since they add no net impulse to the vehicle, while a thruster firing which adds velocity to the vehicle will change the average value for the run in which the firing occurs.) The approximate times during which the Orbiter was flown in the $+X_{vv}$ and $-X_{vv}$ attitudes, based on the nominal mission timeline, is displayed on the graph for comparison. A horizontal line is drawn on the graph, somewhat arbitrarily, through runs 14 - 24, which occurred during the sleep period while in the $-X_{vv}$ attitude, and another is drawn through runs 25 - 31, which occurred after the Orbiter was maneuvered to the $+X_{vv}$ attitude. The difference between these horizontal lines, $1.4 \times 10^{-6}g$, may be considered to be an upper bound of the step change in acceleration. Therefore the average acceleration due to drag is probably no more than one-half that value, or $7 \times 10^{-7}g$.

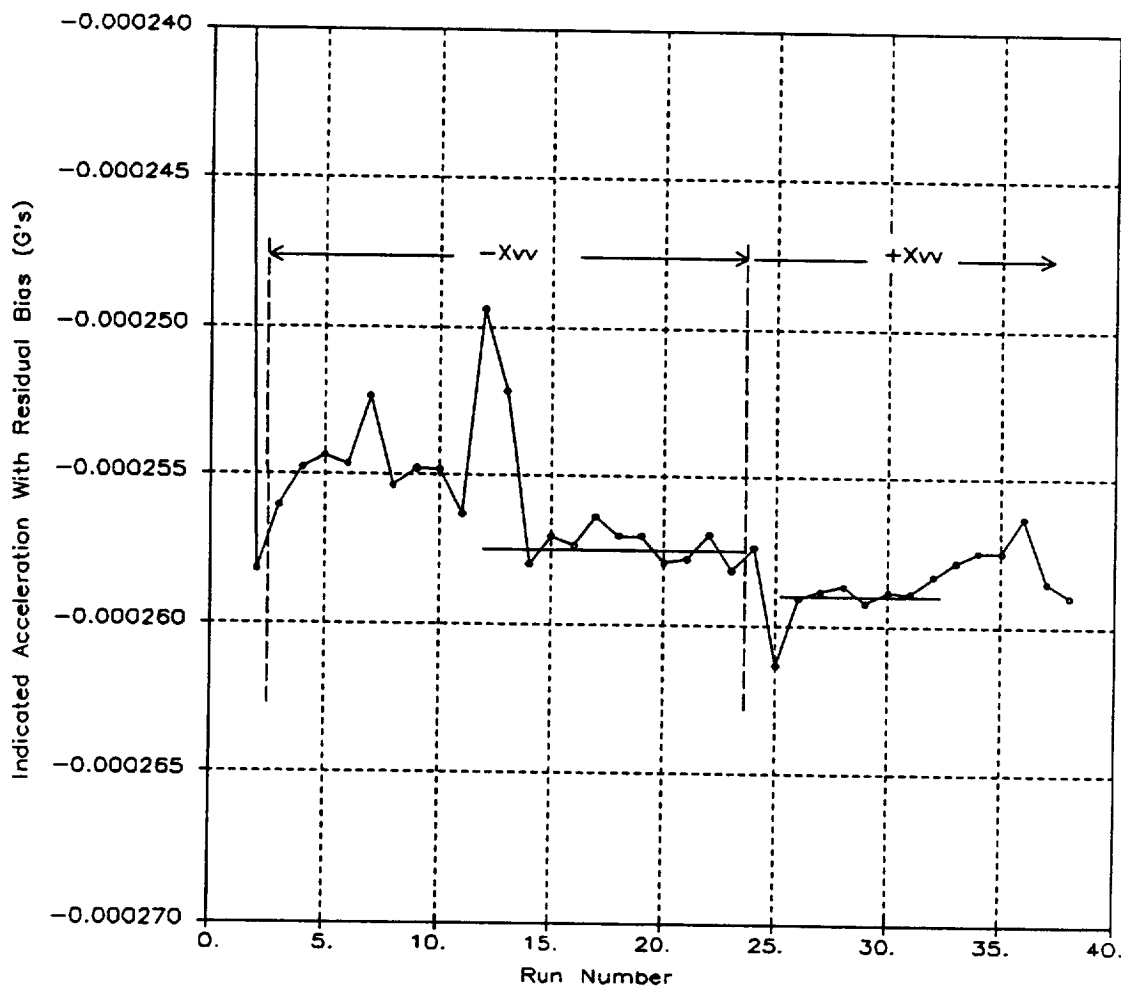


Figure 29: Average X-Axis Indicated Accelerations For Each Run (With Residual Bias)

Pressure. Figures A-39 through A-76 in the appendix display the pressure, heat input, and mixer flow rate for runs 1 through 38, respectively. A typical example of the pressure history from run 11 is shown in figure 30.

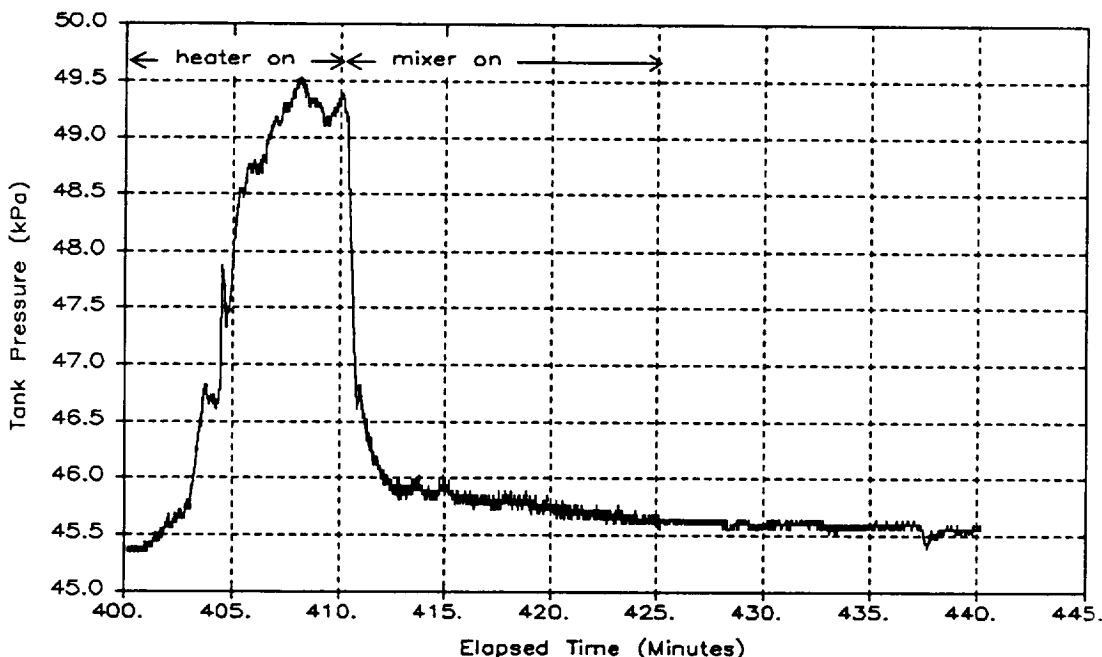


Figure 30: Typical Pressure History (Run 11, Mixer Flow 0.6 l/min)

The pressure rise limit of 20.7 kPa (3 psi) is never reached during any heating stage, so each run's heating stage lasts the full ten minutes. Pressures are often seen to rise higher than they did in one-g testing, but the pressure rise is not smooth or monotonic as it was in one g. The pressure often exhibits little or no change for several minutes, and then sharply rises to an unsteady plateau. In eight of the runs a spike is observed, where an increase of as much as 13.6 kPa (1.97 psi) occurs within two seconds. One of these spikes, recorded during run 13, is shown in figure 31. When they occur there is a simultaneous increase in the temperature recorded in the fluid nearest the active heater (T4 when heater A is active, and T5 when heater B is in use). In general, the longer the period in which the pressure does not increase, the larger the subsequent spike. These spikes occurred when the video cameras were not operating, although smaller spikes are observed in several runs before the cameras are turned off. In run 5, for example, a small acceleration event approximately one minute into the heating stage causes the ullage to drift from the center of the tank to heater B, which is the active heater. A small pressure spike occurs at sixty seconds, approximately the same time that the ullage contacts the heater.

When the mixer is turned on, ten minutes after the beginning of the run, the pressure drops rapidly as indicated in both figures 30 and 31. At low flow rates (such as figure 30) the rate of pressure reduction is faster than observed with the same apparatus in normal gravity tests. At all non-zero flow rates the pressure consistently collapses to near equilibrium, sometimes reaching a minimum value before beginning a slow increase as the pumps continue to run. In those runs having zero mixer flow, the pressure drops slowly (although faster than in one g), requiring five to fifteen minutes to approach

equilibrium. An exception is run 1, in which the accelerations caused by the deployment of the TDRS/IUS payload (which is pushed out of the payload bay by springs) cause a sudden pressure reduction. This self-mixing is shown in figure 32. The payload deployment produces a partial pressure reduction, and the OMS separation burn one minute later results in a more rapid pressure reduction.

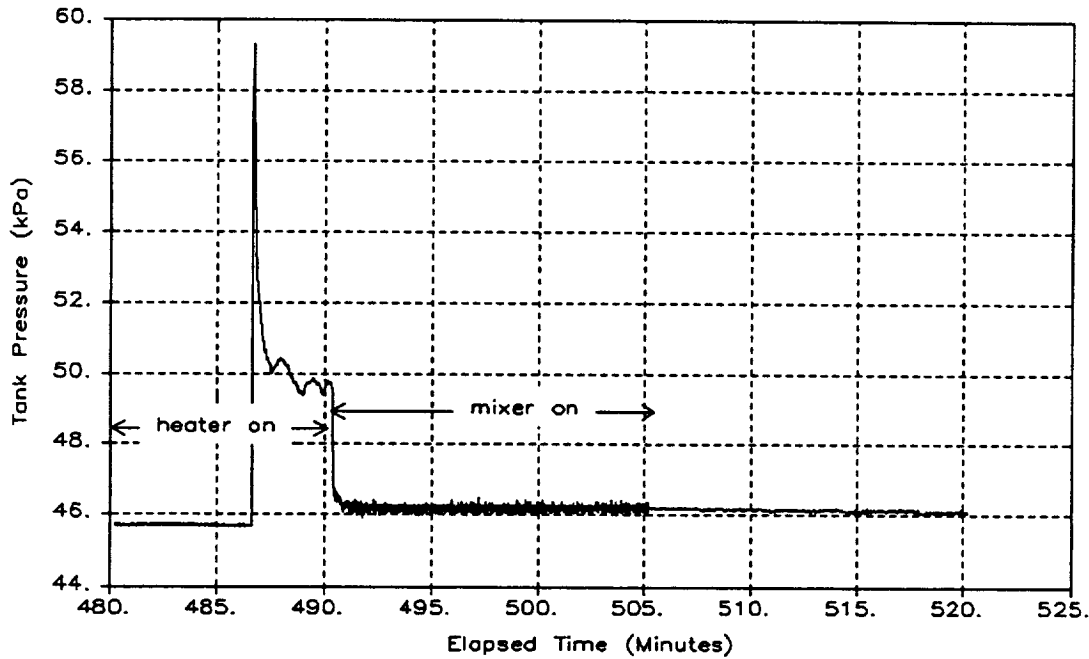


Figure 31: Pressure Spike During Heating Stage (Run 13, Mixer Flow 2.8 l/min)

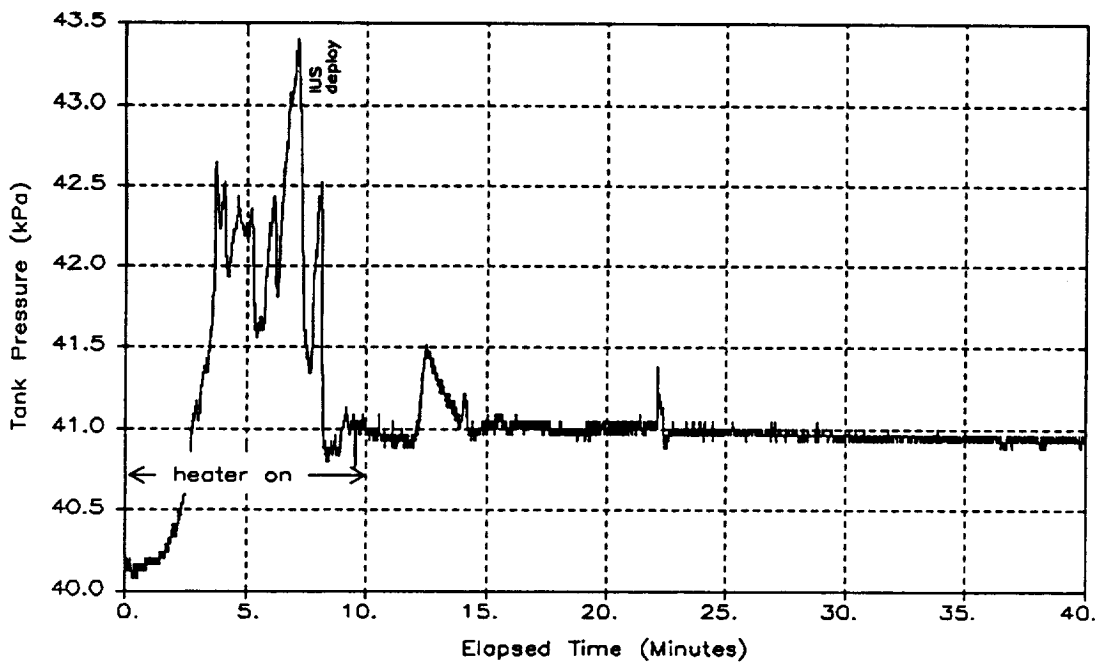


Figure 32: Self-Mixing Due To Accelerations (Run 1, Mixer Flow = 0)

Temperatures. Figures A-77 through A-114 in the Appendix show the seven recorded fluid temperatures during runs 1 through 38, respectively. In each figure the upper graph plots the response of the four thermistors immersed in the fluid (T1, T2, T4, and T5) plus that of the thermistor in the mixer loop (T7). The lower graph plots the two heater temperatures (T3 and T6). The heater temperatures are plotted separately because their responses are slower than the fluid temperatures due to their thermal mass and therefore they do not provide an indication of the fluid mixing time.

At the end of the heating stage the peak fluid temperatures are typically 3-4°C (5-7°F) above equilibrium. When the mixer is turned on they converge within the 0.1°C accuracy of the thermistors. The rate of convergence is a strong function of flow rate. Figure 33 is an example of the fluid temperature response to low-flow rate mixing (run 11). The temperature response at a higher flow rate is shown in figure 34 (run 10).

At the beginning of mixing in each run, the temperature of the fluid in the mixing jet (T7) is approximately 1.0°C to 2.5°C (1.8°F to 4.5°F) below the equilibrium temperature of the tank contents. This is because when fluid is not circulating through the loop during the 25 minutes between mixing stages, it dissipates heat to the cooler environment. Although the amount of fluid contained in the loop is small compared with the tank, this initially-cooler flow may have some effect on the pressure reduction times.

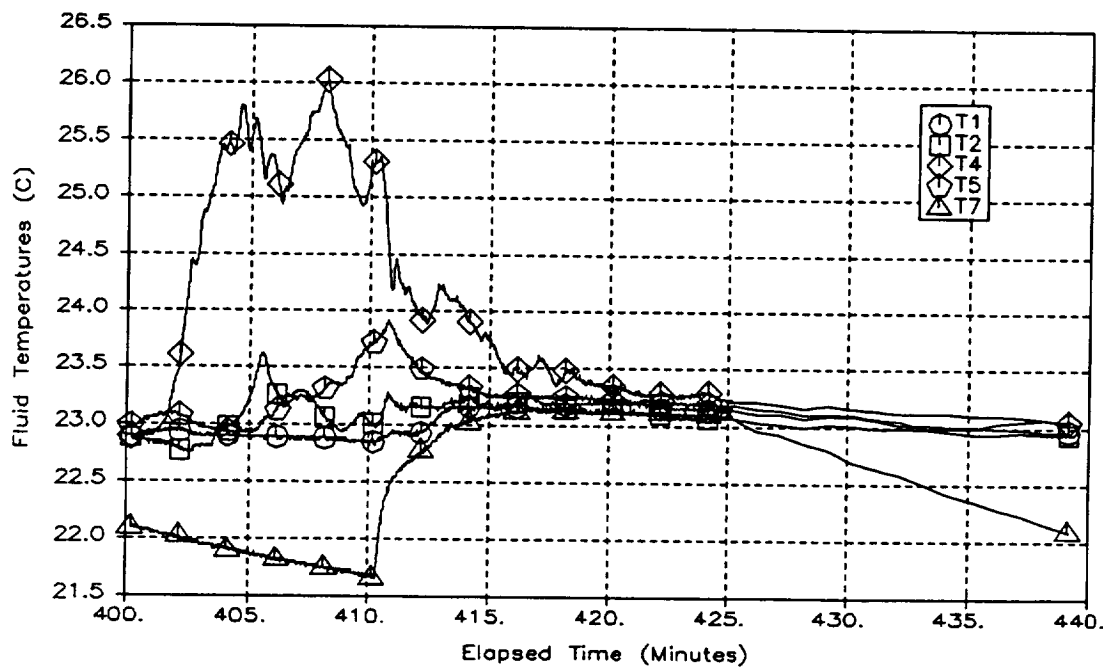


Figure 33: Fluid Temperature Response (Run 11, Mixer Flow = 0.6 l/min)

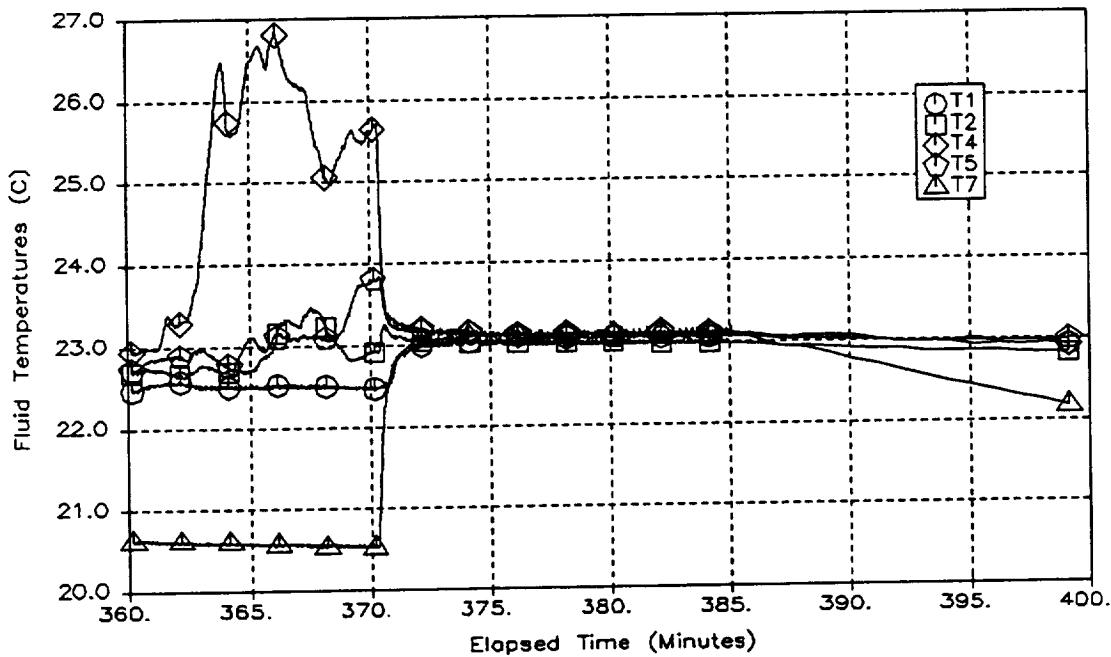


Figure 34: Fluid Temperature Response (Run 10, Mixer Flow = 2.7 l/min)

Video. The liquid/vapor initial conditions for each run were clearly capillary-force-dominated. The Bond number corresponding to the estimated 7×10^{-7} g-level is 0.01, for refrigerant 113 using the bubble radius of 13 cm (5 in). The ullage is generally a single spherical bubble that does not attach to the walls. One exception to this is that the accelerations during RCS firings occasionally force the bubble against a tank wall. Another exception is at the end of the heating phases, where the main ullage bubble is often attached to the heater, as will be discussed later. At other times the bubble drifts slowly, depending on the acceleration environment, but appearing to be repelled by protrusions such as the thermistor probes and the mixer nozzle.

Figure 35 is a still photograph taken from the videotape. It shows the initial conditions prior to heater turn-on at the beginning of run 9, typical of conditions during the crew sleep period for which the acceleration environment was most quiescent. This was also during the -X_{VV} ("tail-first") Orbiter orientation. The image (and all subsequent video still photos) is oriented such that the mixer nozzle is to the right, heater A is at the left side, and heater B is at the top of the photo (although these components are not always visible in the photos). The ullage is visible toward the left of the photo as a smooth sphere. (Objects inside the tank are magnified by the lens effect of the liquid, and objects inside the cylindrical portion of the tank are also distorted and appear "wider" in this orientation; this is why the ullage does not appear as a perfect sphere.)

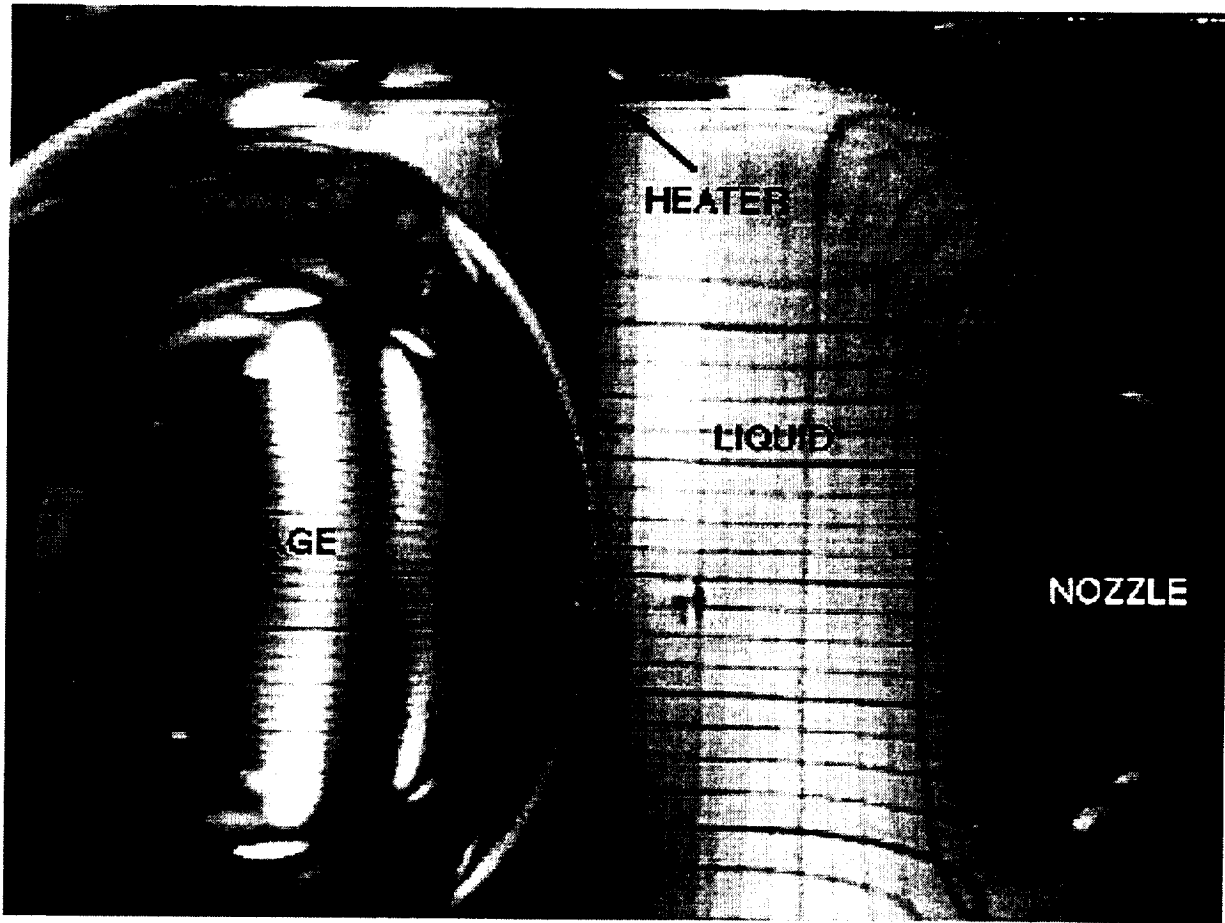


Figure 35: Initial Conditions: Quiescent Environment (Run 9)

The $-X_{vv}$ attitude exists from runs 4 through 25, approximately. In all but two of these runs the ullage bubble is initially located toward the nose of the Orbiter, as shown in figure 35, and is nearly motionless. In the remaining runs the initial orientation is variable. Thus it appears that the drag acceleration, $\sim 7 \times 10^{-7} g$, may be sufficient to give the fluid a preferred orientation. Although disturbances can cause the ullage to be displaced and to start drifting, it has a definite tendency to return to the end of the tank that is opposite the direction of flight.

Figure 36 shows the initial conditions during run 1, a time of greater acceleration noise. The effect of the disturbances on the surface can be seen as a significant amount of waviness and movement of the liquid/vapor interface. RCS thruster firings are sometimes seen to cause the ullage to begin drifting and, in a few cases, to flatten against a wall or heater plate.

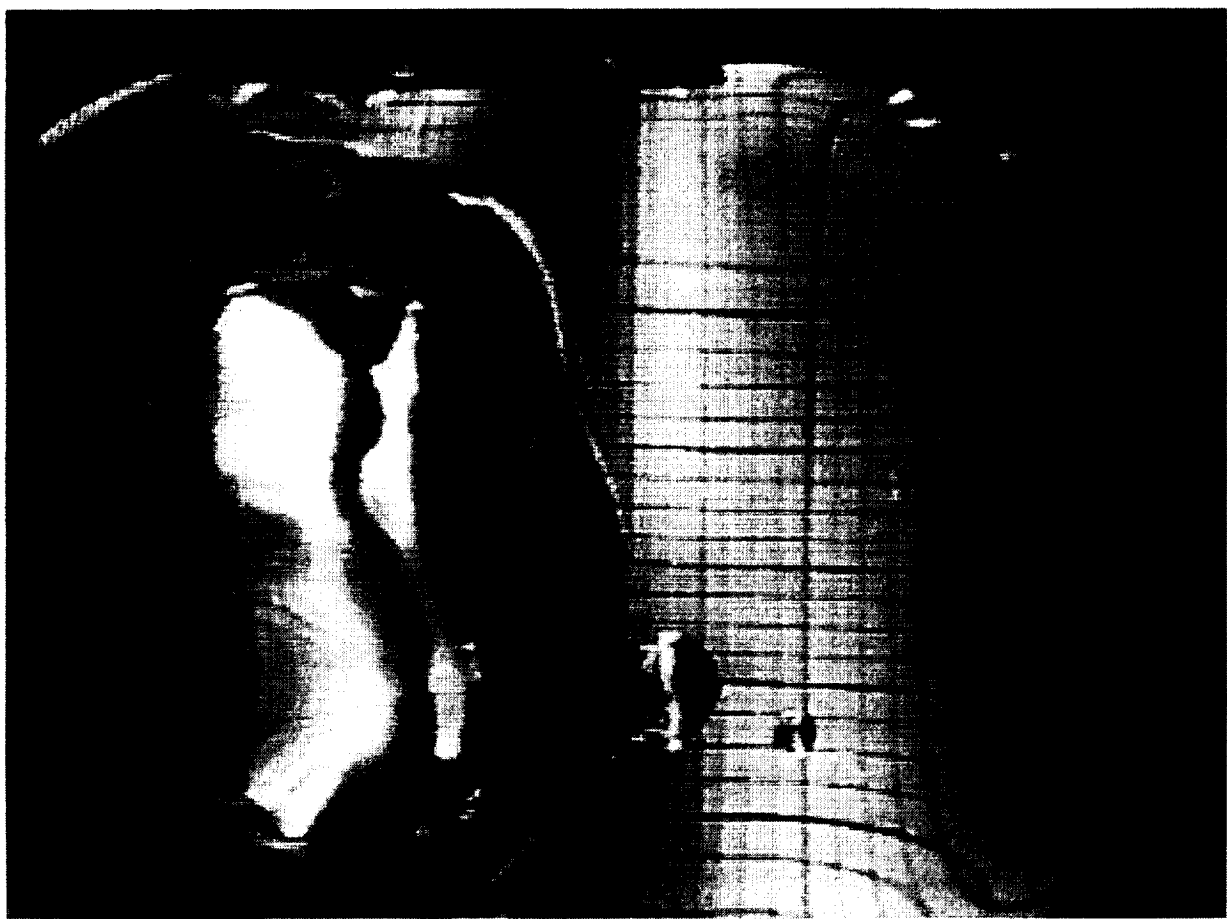


Figure 36: Initial Conditions: Active Environment (Run 1)

In most runs boiling is observed on the heaters during the heating phase. Boiling is not seen in runs 33 through 36, for which both heaters are operated with a total heat flux that is one-quarter that used in the other runs. Typically bubbles begin to be visible on the active heater approximately sixty seconds after the heater is turned on. The bubbles grow on both sides of the heater plate, remaining attached until they merge with other bubbles and detach or are otherwise dislodged. Figure 37 shows the conditions at the end of the heating phase in run 17, which used heater B. Several bubbles can be seen forming on the heater plate, and the main ullage bubble is also tangent to the heater.

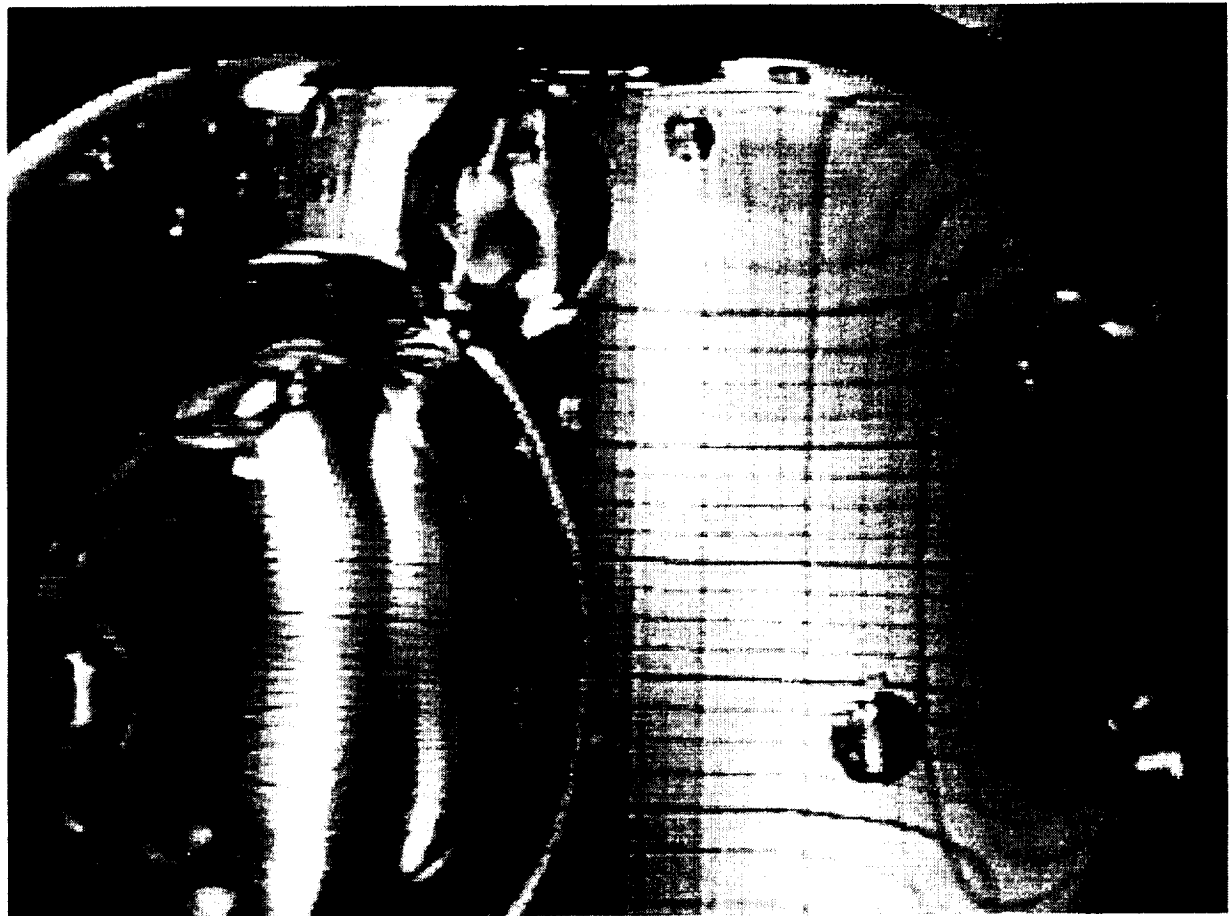


Figure 37: Boiling at End of Heating Stage (Run 17)

Although only the first two minutes of each ten-minute heating stage are videotaped, the conditions at the end of the heating stage can be seen in the video recorded immediately prior to the initiation of mixing (as in figure 37). By this time, in the majority of runs exhibiting boiling, the main ullage bubble is attached or adjacent to the heater that is active for that run. The movement of the ullage from its initial location to the heater takes place during the non-videotaped portion of each run.

In seven of the test runs a flow rate of zero is used to test the rate of pressure decay and re-equilibration in the absence of active mixing. The multiple bubbles present at the time the heater is turned off slowly re-combine into a single sphere by the time the following run is begun (thirty minutes later). The coalescence of bubbles creates large visible ripples and occasional rapid movements in the ullage. This appears to produce a significant amount of self-mixing in the fluid, even during a quiescent acceleration environment. In the active acceleration environment of run 1, the interface distortion is more severe.

The motion induced by the mixing jet is clearly visible in every run in which the jet is activated. Two main flow patterns are observed: ullage-penetrating and non-

penetrating. Both of these patterns are axisymmetric and are observed to form even when the initial location of the ullage is off-axis.

At low flow rates the jet impinges on the bubble, creating a dimple or short geyser, but does not penetrate the surface. The bubble tends to be positioned and held at the opposite end of the tank, on its centerline, and the flow pattern is symmetrical and stable. Figure 38 is representative of this nonpenetrating flow pattern. This photo is from run 11, which has an average flow rate of 0.59 l/min (0.16 gpm). At the lowest flow rate, 0.38 l/min (0.10 gpm), the jet forms a barely-visible depression in the ullage. This is shown in figure 39, which is from run 25.

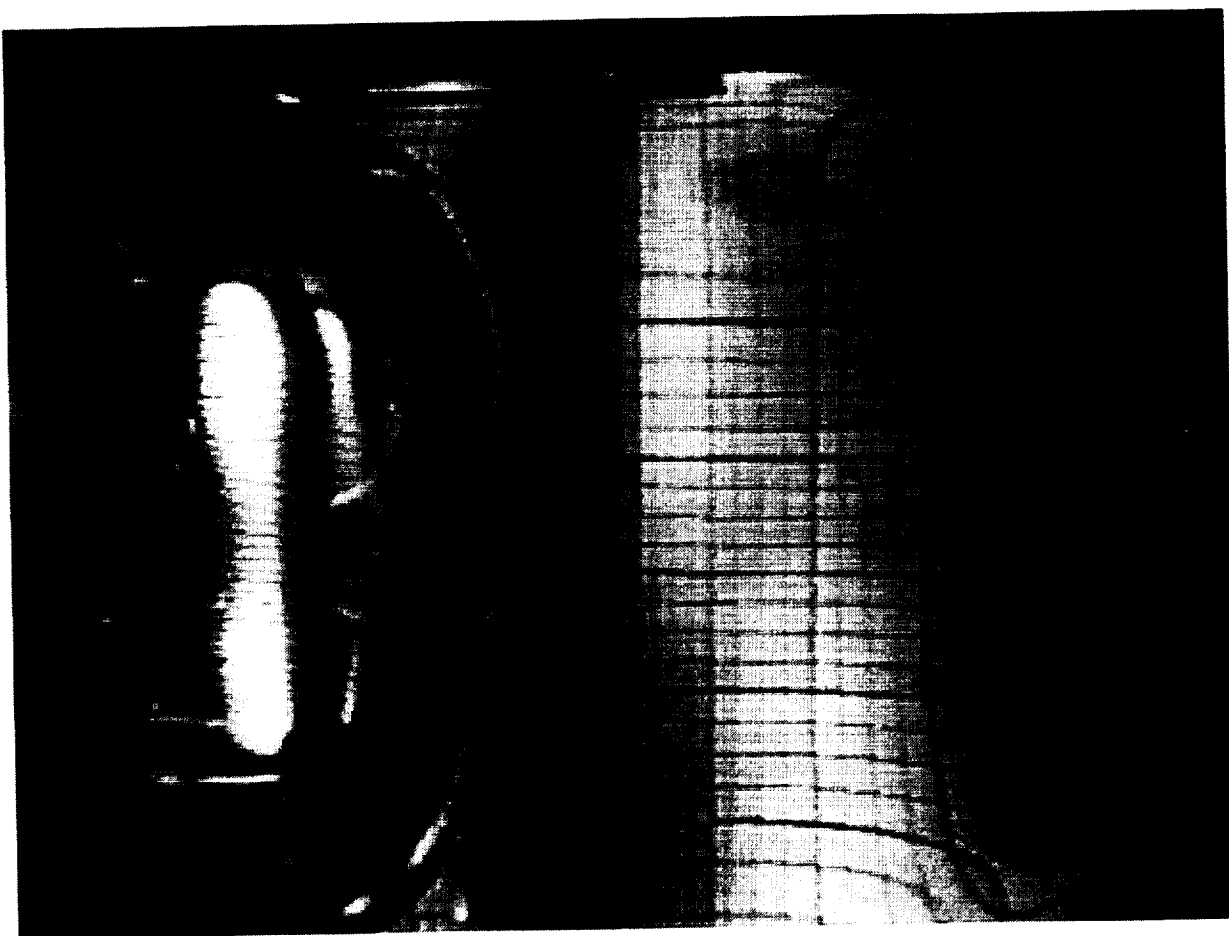


Figure 38: Nonpenetrating Flow Pattern (Run 11, Mixer Flow = 0.6 l/min)

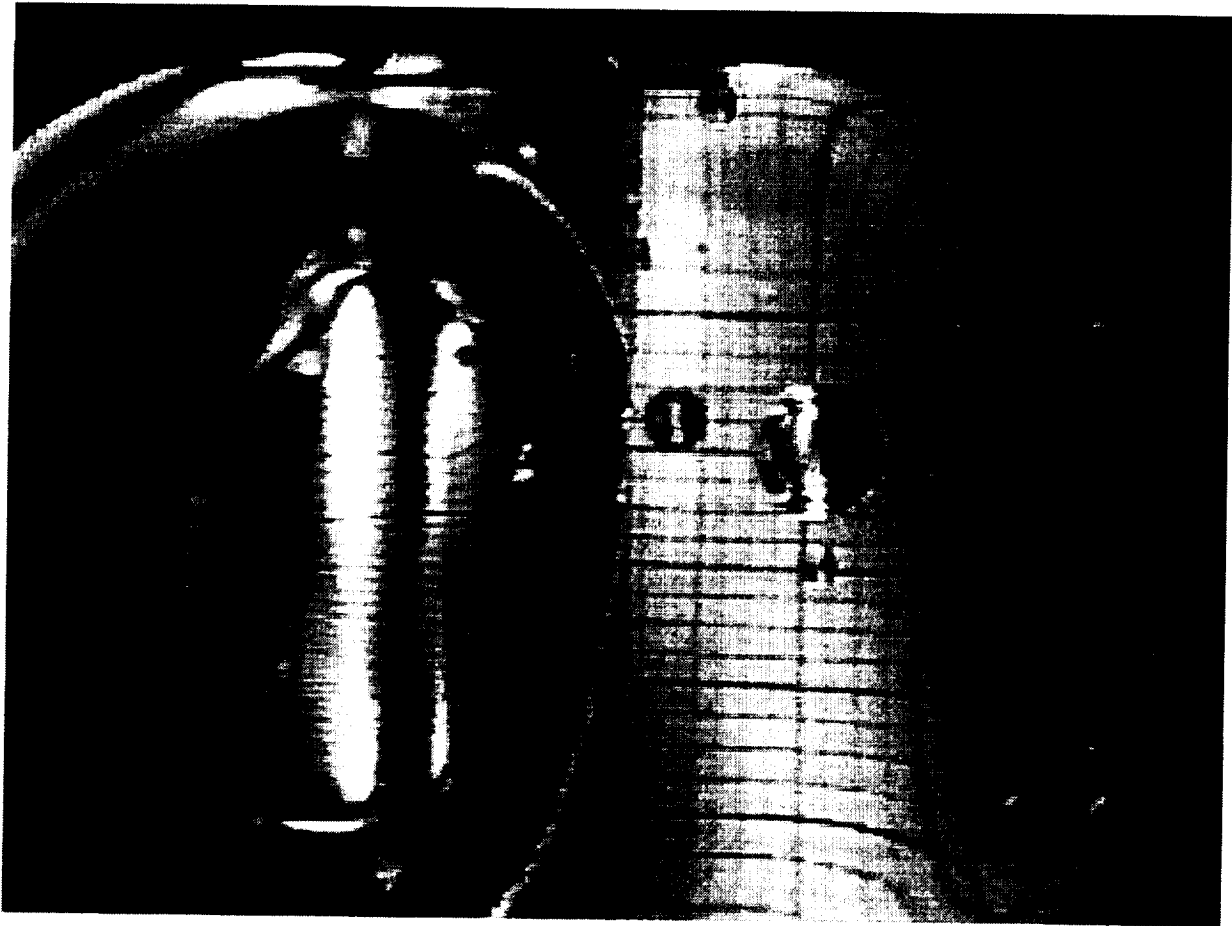


Figure 39: Lowest Flow Rate (Run 25, Mixer Flow = 0.4 l/min)

At higher flow rates the jet penetrates the liquid/vapor interface, impinges on the opposite end of the tank, and recirculates along the tank walls. This results in a symmetrical annular bubble. An example of this is shown in figure 40. This photo is from run 12, which has an average flow rate of 1.54 l/min (0.41 gpm). This flow rate is at the low end of the ullage-penetrating range. At the high end the jet forms approximately the same pattern, but the liquid/vapor interface appears highly energetic compared with the glassy appearance in run 12. Figure 41 shows run 38, which has the highest flow rate reached, 3.35 l/min (0.89 gpm). During both of the runs with this flow rate the jet breaks the ullage up into a large number of small bubbles.



Figure 40: Penetrating Flow Pattern (Run 12, Mixer Flow = 1.5 l/min)



Figure 41: Highest Flow Rate (Run 38, Mixer Flow = 3.3 l/min)

In every run having this symmetric penetrating flow, asymmetric flow is observed during some portion of the four minutes of video coverage. Often the flow begins as a symmetric pattern, degenerates into an asymmetric condition, and frequently returns to the symmetric pattern. A run is classified herein as "penetrating" if at any time during the four minutes a symmetric, recirculating geyser is visible. One kind of asymmetric flow frequently seen at the higher flow rates is shown in figure 42 from run 36, which has an average flow rate of 2.82 l/min (0.75 gpm). Here the jet appears to remain on the axis but the ullage shape deviates from the near-toroidal shape to a two-lobed or saddle shape. The lobes move and in some cases stretch as far as the nozzle end of the tank. In another asymmetric flow pattern frequently seen at moderate flow rates, the ullage is pushed to one side of the tank but otherwise is shaped like the symmetric penetrating pattern.



Figure 42: Asymmetric Flow Pattern (Run 36, Mixer Flow = 2.8 l/min)

At flow rates between those producing nonpenetrating and penetrating patterns, only asymmetric flow is observed. In this intermediate range the jet is generally deflected toward one side of the tank and the ullage is deflected toward the opposite side.

ANALYSIS AND DISCUSSION

Flow Patterns

The patterns observed in the videotape data may be compared with the four flow patterns identified by Aydelott (refs. 13, 14, 15) that were discussed in the introduction. The low-velocity nonpenetrating regime is comparable to Pattern I, in which no geyser is formed. The bulge or dimple seen in the ullage at these flow rates does not qualify as a geyser—its width is greater than its height, and it does not significantly penetrate into the ullage. Flow Pattern II, in which the jet forms a long stable geyser that extends into the ullage, is not seen, nor is Pattern III, in which the geyser reaches the end of the tank and pools there without recirculating. At the startup of some higher-flow rate runs, however, the jet penetrates the ullage at the initiation of mixing and forms a geyser, but the geyser quickly becomes either asymmetric (with the jet deflected to one side of the bubble) or reaches the end of the tank and forms the recirculating penetrating symmetric pattern. Thus it appears that Patterns II and III may not be steady-state flow patterns. Aydelott's drop tower tests were limited to 3.1 seconds duration, which may have prevented a stable flow pattern from developing fully. Moreover, the fluid initial conditions were symmetrical and undisturbed, which may have allowed an unstable symmetrical pattern to last the full three seconds of the test.

Flow Pattern IV is identical to the symmetric penetrating recirculating flow observed in TPCE. However, as discussed previously, in all runs that exhibit Pattern IV flow there are periods of asymmetry. The flow frequently flip-flops between symmetric and asymmetric behavior, with no obvious acceleration events to cause the change. At these flow rates ($>1.7 \text{ l/min}$) there does appear to be thorough mixing during both the symmetric and asymmetric periods—the jet sweeps all parts of the tank wall and is not blocked by the ullage from reaching any potential hot spots.

As discussed in the introduction, the jet Weber number, We_j , is a useful parameter for correlating low-g mixing performance. It is essentially the thrust of the jet divided by the resistance to penetration at the interface caused by surface tension. Since the jet thrust apparently determines mixing effectiveness, and since We_j can be reduced to Aydelott's flow characterization parameter and to several ullage-penetration criteria, this parameter can correlate both the flow patterns and the pressure control effectiveness.

Use of We_j requires estimation of the jet diameter at the liquid/vapor interface, D_j , accounting for spreading of the jet as it travels from the nozzle outlet to the interface. The Weber number calculations herein assume the following:

1. The jet spreads at 7° for the first 12.4 outlet diameters, and at 11° thereafter.
2. The distance from the nozzle outlet to the interface, h_b , is 12.7 cm (5 in).

The first assumption is based on typical values of spread angle for submerged turbulent jets as given in reference 15. The second assumption is an approximation based on the following: for an 83% fill level, a spherical ullage has a diameter of 16.5 cm (6.5 in). If the ullage is located at the opposite end of the tank at the critical moment when the jet either penetrates it or is turned back, then the distance to the closest point of the sphere is 12.7 cm (5.0 in). Using the nozzle outlet diameter of 1.0 cm (0.4 in) and the above spread angles, this results in a constant D_j of 4.94 cm (1.94 in). It is recognized that

this is a generalization and that D_j may vary somewhat from this approximation as the location and shape of the ullage changes, and that the spread angles are not necessarily correct when the jet impinges on an obstacle (the bubble). Rough scaling of the jet diameter from the video images does, however, confirm that this diameter is correct to within approximately 20% in both the symmetrical nonpenetrating and penetrating flow patterns.

Figure 43 lists the resulting Weber numbers for each run having a non-zero flow rate, in ascending order, along with the observed flow pattern. In this and subsequent figures, the nonpenetrating symmetrical pattern is identified by "Nonpen.", the penetrating symmetrical recirculating pattern is denoted by "Penetr.", and the asymmetric cases are identified by "Asym.". Nonpenetration is seen at $We_j \leq 1.4$, although at $We_j = 1.4$ the flow pattern is only marginally in this category. There is a gap in Weber number coverage between 1.4 and 3.1, which prevents an objective determination of the upper bound of the penetrating regime. However, since run 31 ($We_j = 1.4$) falls marginally in the nonpenetrating category, never appearing completely symmetric, while run 27 ($We_j = 1.3$) is symmetric and stable, it is believed that the upper bound of the symmetric non-penetrating flow pattern is at or near $We_j = 1.4$.

Penetration (Aydelott's Pattern IV) is found for $We_j \geq 4.8$, although there is an asymmetric run at a higher Weber number. Run 28 ($We_j = 5.9$) is difficult to categorize but the flow pattern is never observed to be symmetric. At mixer startup, the ullage is attached to heater B where vigorous boiling is occurring. This asymmetric initial condition, caused by the geometry of the heat input, may have prevented the jet from forming the symmetric penetrating flow pattern during the four minutes of video coverage. Therefore, notwithstanding run 28, the lower bound of the symmetric penetrating pattern is at or near $We_j = 4.8$.

These Weber number boundaries may be compared with Aydelott's boundaries. If the low- g data from reference 15 are presented in terms of Weber number rather than the flow characterization parameter F (and assuming that the jet Bond number Bo_j is negligible), then Aydelott's reported flow patterns have the following ranges: Pattern I is from $We_j = 0.31$ to 0.78, borderline Pattern I/II is seen from 0.39 to 1.11, Pattern II and II/III exists from 1.16 to 1.59, Pattern III is from 1.63 to 2.04, and Pattern IV is reported from $We_j = 1.33$ up to 283. The upper bound of TPCE's nonpenetrating pattern (1.4) is only slightly higher than the upper bound of Aydelott's Pattern I/II (1.11). Both are somewhat higher, however, than Poth's criterion (ref. 2) which gives $We_{j,critical} = 0.69$. The boundary between TPCE's asymmetric and penetrating flow patterns, $We_j = 4.8$, is higher than Aydelott's boundary between Patterns III and IV ($We_j = 1.33$ to 2.04).

The asymmetric range ($1.4 < We_j < 4.8$) produces irregular flow which, as will be seen, delivers inconsistent and sometimes less-effective mixing performance than either the penetrating or nonpenetrating regimes. At $3.1 \leq We_j < 4.8$, the jet is deflected to one side of the bubble and the return flow attaches to one side of the tank. This appears to be stable, since in this flow range the pattern is never seen to revert to a symmetric case. For $4.8 \leq We_j < 6.3$, the flow alternates between the symmetric Pattern IV and an asymmetric geometry, often taking the form of a saddle-shaped bubble. At higher Weber numbers (≥ 14.5) the ullage "saddle" becomes more pronounced, forming two peaks or arms, often with the flow also becoming symmetric. Figure 44 is a sketch of the characteristics typical of some of the asymmetric flows encountered, as a function of Weber number.

Run Number	Flow Rate (l/min)	Weber Number	Flow Pattern
25	0.38	0.29	Nonpen.
32	0.38	0.30	Nonpen.
3	0.54	0.59	Nonpen.
11	0.59	0.71	Nonpen.
16	0.60	0.72	Nonpen.
8	0.60	0.73	Nonpen.
20	0.60	0.73	Nonpen.
23	0.62	0.77	Nonpen.
33	0.64	0.82	Nonpen.
27	0.80	1.29	Nonpen.
31	0.84	1.44	Nonpen.
29	1.24	3.10	Asym.
26	1.24	3.11	Asym.
4	1.53	4.73	Asym.
7	1.53	4.74	Asym.
15	1.53	4.74	Asym.
12	1.54	4.78	Penetr.
34	1.54	4.79	Asym.
24	1.57	4.96	Penetr.
19	1.58	5.06	Penetr.
28	1.71	5.90	Asym.
30	1.77	6.30	Penetr.
2	2.68	14.51	Penetr.
5	2.72	14.91	Penetr.
10	2.74	15.16	Penetr.
13	2.78	15.55	Penetr.
17	2.78	15.62	Penetr.
36	2.82	16.08	Penetr.
22	2.84	16.22	Penetr.
37	3.34	22.48	Penetr.
38	3.35	22.64	Penetr.

Figure 43: Flow Pattern versus Flow Rate and We_j

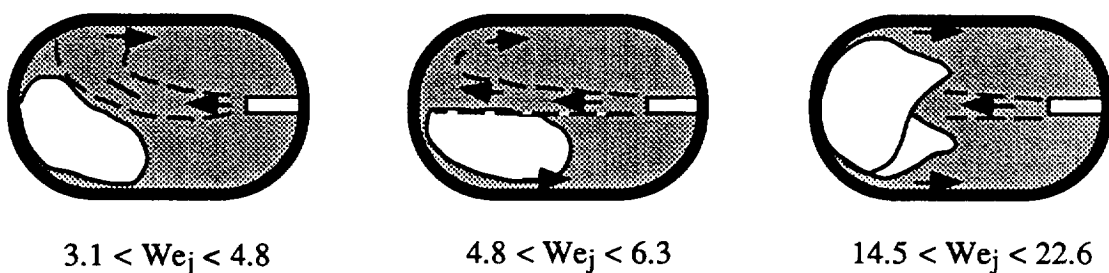


Figure 44: Observed Behavior of Asymmetric Flows

Mixing Times

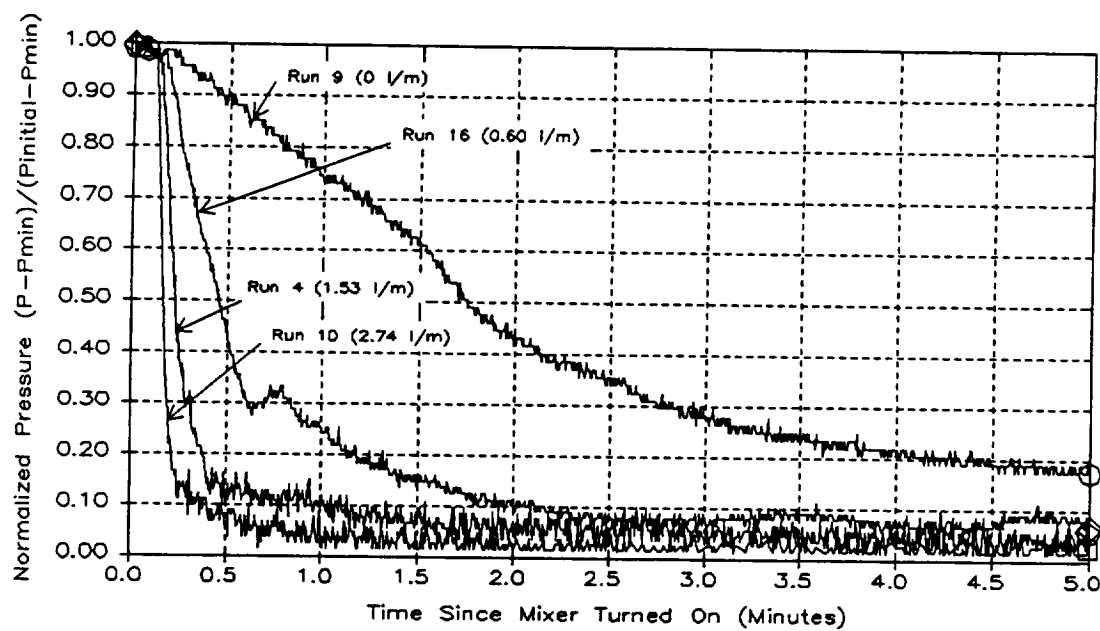
When the mixer is turned on, the pressure drops at a rate that is dependent on the mixer flow. In some high-flow rate cases, the pressure reaches a minimum value and then slowly increases. The minimum pressure value reached at any time during the fifteen-minute mixing stage (after smoothing of the data to remove high-frequency fluctuations) is defined as P_{\min} . Figure 45 displays the pressure decay traces for four typical runs, normalized as $(P - P_{\min}) / (P_{\text{initial}} - P_{\min})$. This dimensionless pressure is plotted on both linear (45a) and logarithmic (45b) scales. The effect of flow rate on pressure collapse rate is evident in this comparison. The initial portion of the pressure curve approximates an exponential decay in most of the runs, as indicated by the nearly straight lines on the logarithmic curves.

The time required to reach the minimum pressure is difficult to extract from the data because the flatness of the curve near the minimum and the amount of fluctuation in the data make the time value highly susceptible to small variations. However, this mixing time is not of significant practical interest. In application, a pressure control system in a propellant tank that operates on demand would probably not be designed to operate until the minimum pressure is reached. Because of diminishing returns as the pressure decay rate flattens out, it would probably be more efficient to operate a mixer until the excess pressure has been reduced by some fraction, or until it reaches the lower bound of a "dead-band" control pressure.

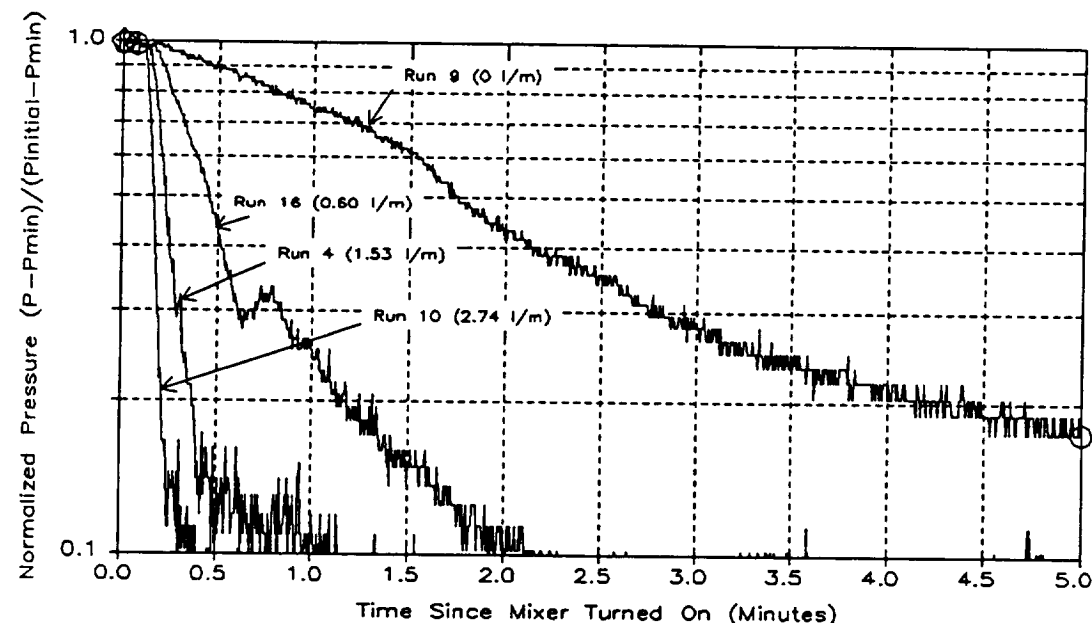
Pressure collapse times and thermal equilibration times have often been defined as the time required to bring the pressure or temperatures some percentage of the way to their equilibrium values. This procedure is used to derive pressure collapse times from TPCE's data. (Some data smoothing was also used here to reduce the effects of random fluctuations and of resolution limits.) For instance, the 75% pressure collapse time, $t_{P75\%}$, is defined as the time elapsed from mixer turn-on until

$$\frac{P(t) - P_{\min}}{P_{\text{initial}} - P_{\min}} = 0.25 \quad (13)$$

This mixing time, along with the 50% collapse time and the 95% collapse time, was calculated (by a computer code) for all 38 runs. The 95% collapse time proved to be an inconsistent measure of pressure control effectiveness due to numerical problems caused by fluctuations in the curves. If one approximates the pressure response as having the form of an exponential decay, then the time constant of the pressure decay can also be calculated as another measure of the pressure collapse rate which is potentially less sensitive to fluctuations in the data. This time constant, which is inversely proportional to the slope of the decay on a logarithmic plot (figure 45b), was also calculated for each run, by curve-fitting an exponential function to each decay. However this also proved to be prone to numerical problems and did not always represent the collapse rate well. The 75% pressure collapse time proved to be the least susceptible to numerical problems and is therefore presented herein as the most useful basis of comparison.



(a) *Linear Scale*



(b) *Logarithmic Scale (Same Data)*

Figure 45: Normalized Pressure Reduction Traces: Four Typical Runs

Figure 46 displays the 75% pressure collapse time, $t_{p75\%}$, versus We_j and flow pattern. In this and subsequent plots We_j is based on the average flow rate during the mixing stage, as calculated by a computer program. (Note however that in some runs the flow rate at the beginning of the mixing stage—where much of the pressure collapse occurs—varies by up to 5% from the average value over the entire stage.) Figure 47 plots the same information as figure 46 but on a logarithmic scale to better separate the high-flow rate mixing times.

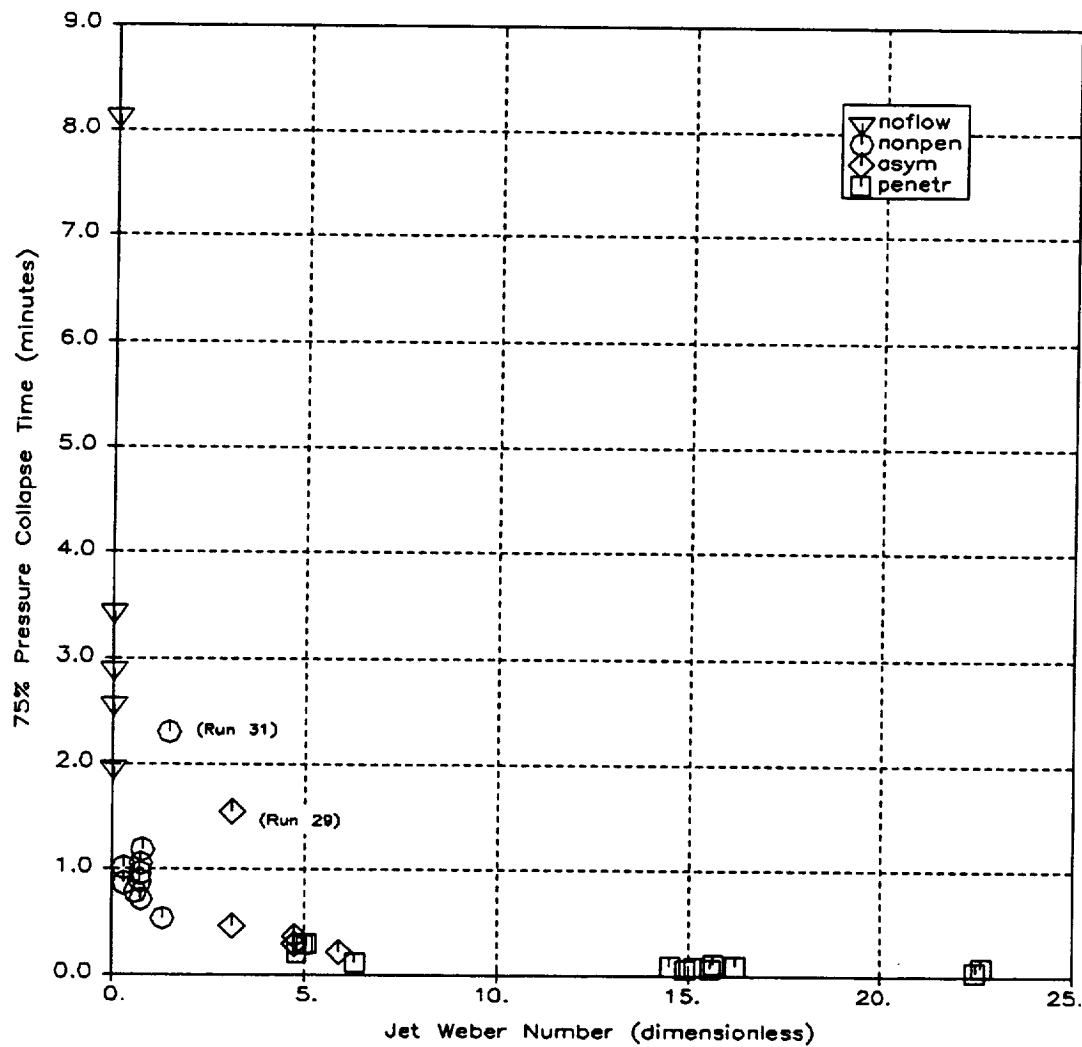


Figure 46: 75% Pressure Collapse Time Versus Weber Numer and Flow Pattern

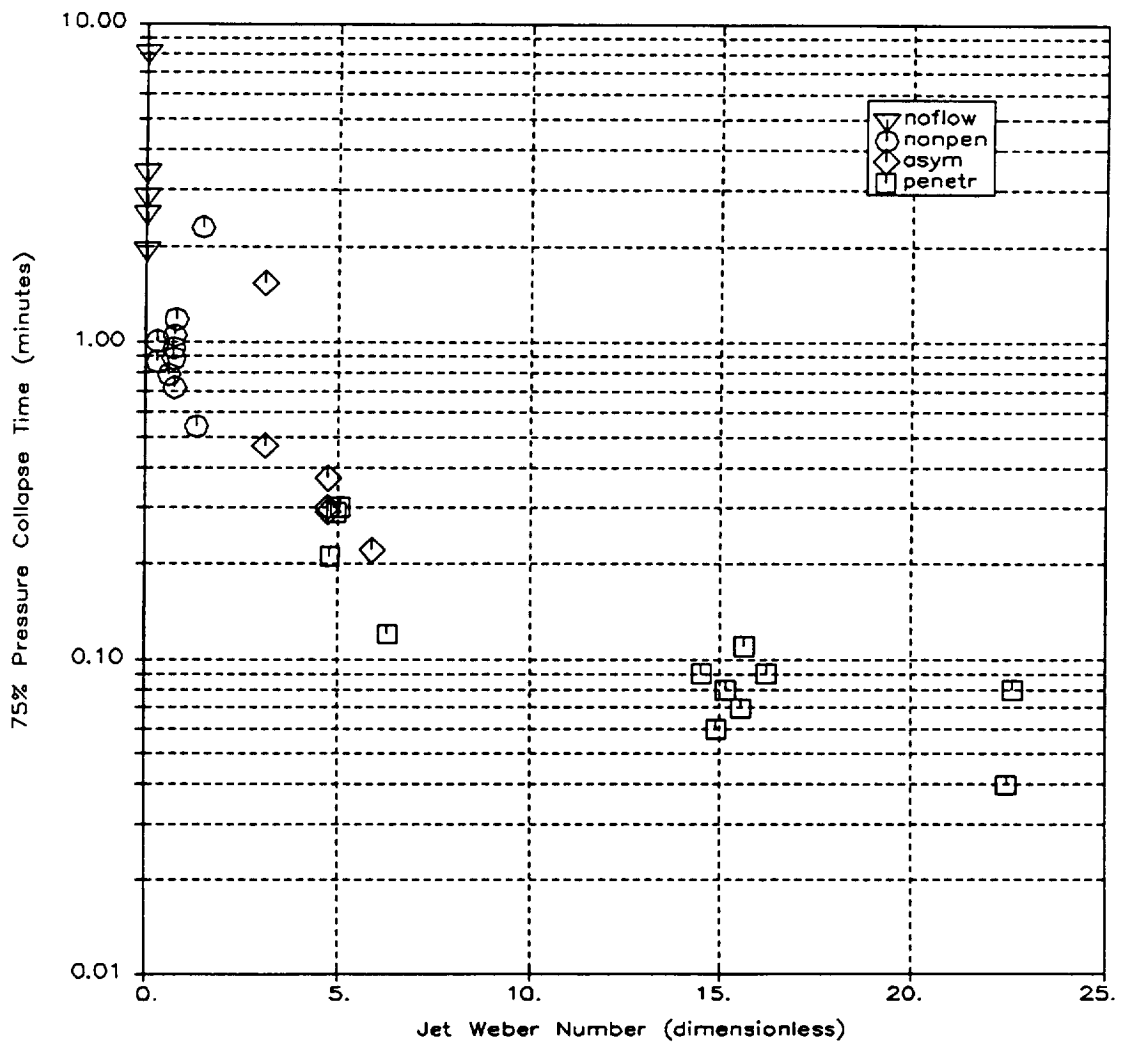


Figure 47: 75% Pressure Collapse Time: Logarithmic Scale

The higher flow rates—those that produce the penetrating symmetric flow pattern denoted on the plots by the square symbols—provide rapid pressure reduction, as expected. However, the low flow rates that do not result in ullage penetration (shown as circles) still cause the pressure to be reduced positively and consistently. Pressure collapse times are consistent for Weber numbers between 0.29 and 1.3. Although the nonpenetrating jet does not directly impinge on areas of the tank blocked by the ullage, it appears to impart significant motion to all surfaces of the bubble, which enhances heat and mass transfer well above that expected with conduction alone. The lone nonpenetrating data point that is well above the curve is run 31, which is at a borderline Weber number and displays asymmetric flow shortly after startup. Another data point that displays asymmetric flow (run 29) also falls significantly above the rest of the points. A possible reason for this lack of repeatability in the asymmetric range is that

when the ullage deflects the jet to one side, the hot region may or may not be effectively cooled by the jet, depending on its location. Therefore asymmetric flow is potentially less consistent in its pressure control effectiveness.

Pressure control efficiency—defined as the total jet kinetic energy expended in reducing the pressure 75% of the way to its equilibrium level—is plotted in figure 48. This is calculated by multiplying the jet power (or the kinetic energy added by the jet per unit time, $(\pi/8)\rho V_o^3 D_o^2$) by the 75% pressure collapse time, $t_{P75\%}$. Here an advantage of low-velocity mixing can be seen: the energy required at the low flow rates differs from that at the highest ones by approximately a factor of five. The longer time required to reduce the pressure at a low flow rate is more than compensated for by the lower energy of the jet, because the kinetic energy addition rate scales with velocity to the third power. Again, runs 29 and 31 lie well above the trend of the other points. (Although the total amounts of energy added by TPCE's mixer are small, the mixer energy input could be significant for a large-scale cryogen tank operating for long durations in space.)

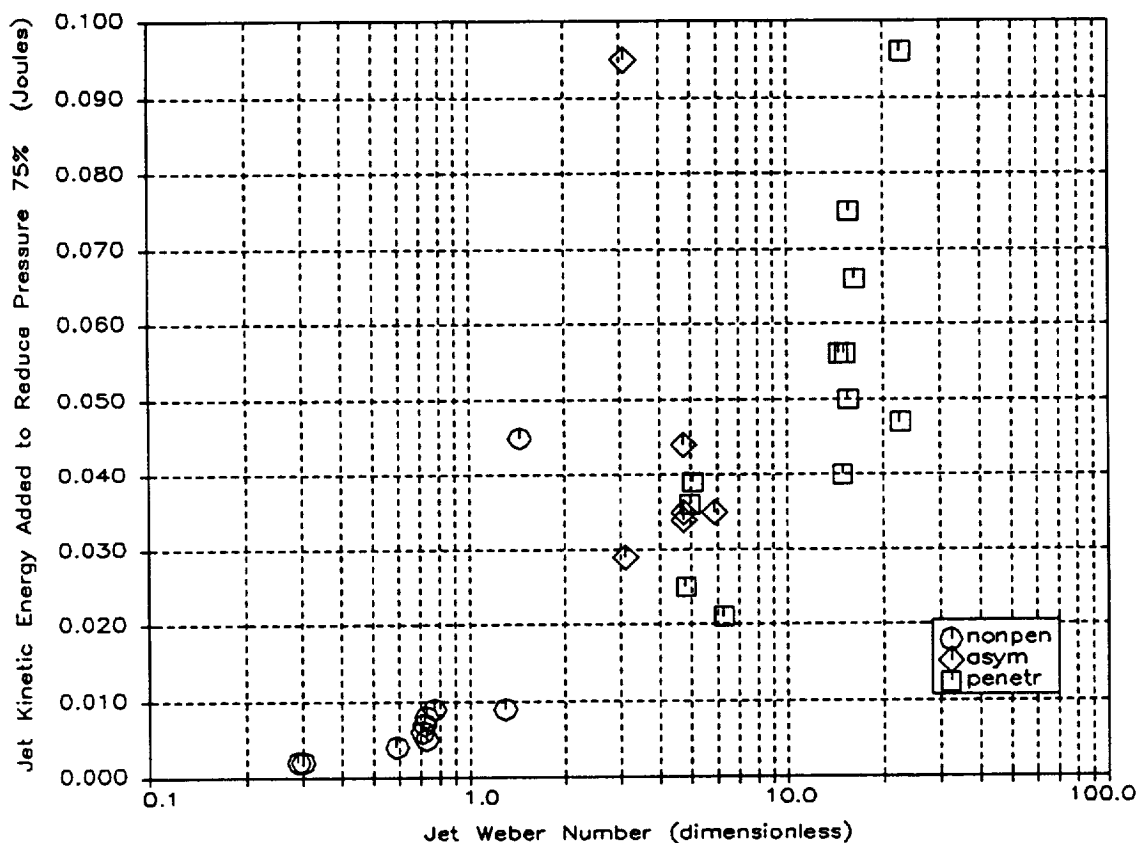


Figure 48: Pressure Control Efficiency: Jet Kinetic Energy Added to Fluid to Reduce Pressure by 75%

Thermal equilibration times are calculated for each run in a manner similar to the calculation of the pressure collapse times. At any given time the maximum fluid temperature spread, ΔT , is defined as the highest measured temperature minus the lowest measured temperature (after again smoothing the data by time-averaging each data point with its adjacent points). This calculation is limited to the four fluid temperatures in the tank: T1, T2, T4, and T5. The thermal equilibration times are defined as the time required for this temperature spread to be reduced by a given percentage. The minimum value of ΔT measured in each run, or ΔT_{\min} , is not zero because the 0.1°C accuracy of each thermistor results in an approximately 0.2°C spread between the temperatures when the fluid is well-mixed.

For example, the 75% thermal equilibration time, $t_{T75\%}$, is defined as the elapsed time at which

$$\frac{\Delta T(t) - \Delta T_{\min}}{\Delta T_{\text{initial}} - \Delta T_{\min}} = 0.25 \quad (14)$$

The thermal equilibration time constant was also calculated by fitting an exponential function to each run, as with the pressure, but again this method proved to be unreliable due to numerical problems. Therefore the 75% thermal equilibration time is presented as the best measure of bulk liquid mixing effectiveness. This is plotted as a function of Weber number and flow pattern in Figure 49.

Since temperature is only measured at a few discrete locations, there is less repeatability in the thermal mixing times than in the pressure collapse times. Temperature, unlike pressure, is an intensive property and there is no assurance, or even likelihood, that the four temperatures measured represent the maximum and minimum temperatures in the fluid. However the upper bound of the $t_{T75\%}$ data envelope may be considered to represent the thermal equilibration effectiveness. This curve is similar in shape to the pressure curve. The pressure reduction times average approximately 30 percent less than the upper bound of the temperature reduction envelope, except at the highest flow rates where they are up to 90% less.

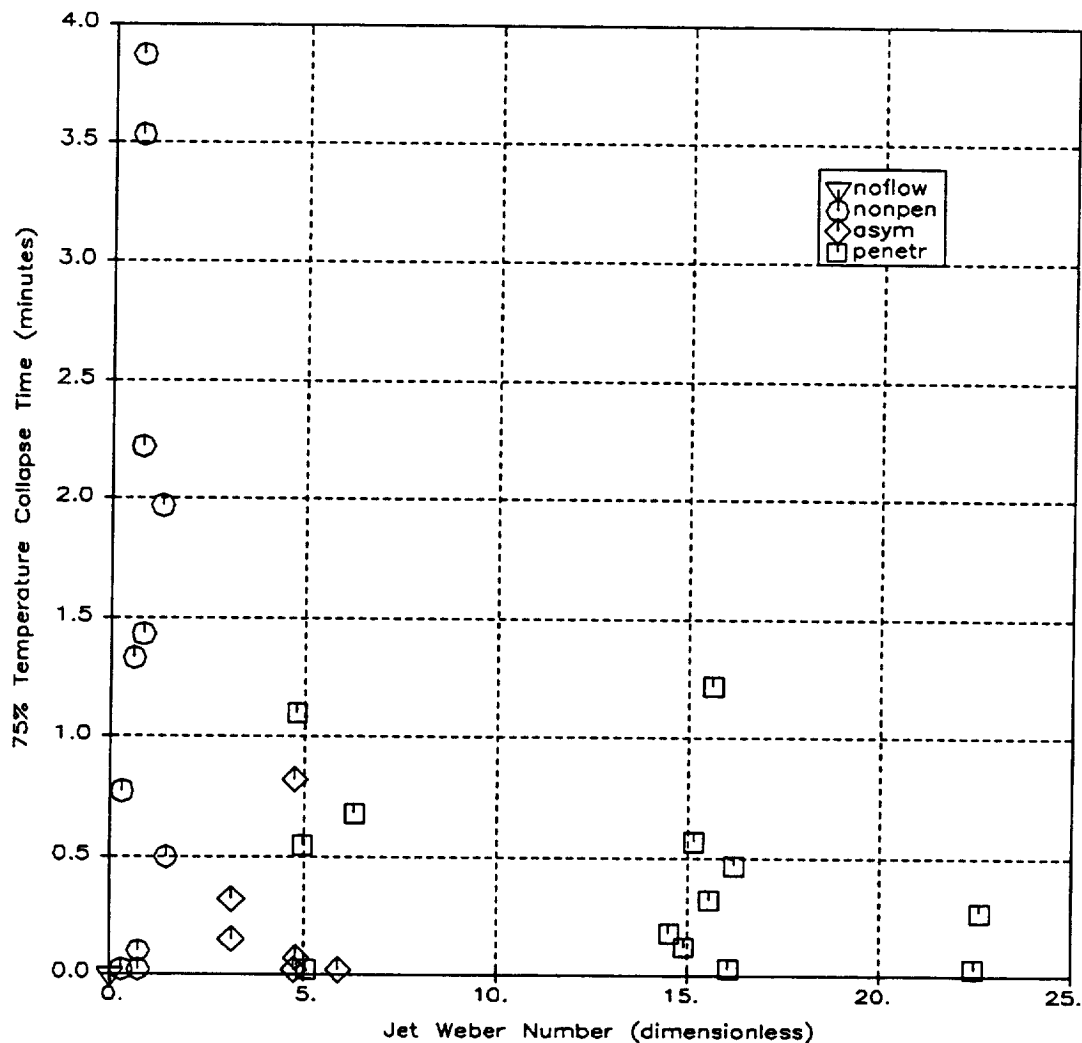


Figure 49: 75% Thermal Equilibration Time versus Weber Number and Flow Pattern

Figure 50 lists the calculated mixing times for each of the 38 runs. These include the 75% thermal equilibration time and the thermal equilibration time constant, plus the 50%, 75%, and 95% pressure collapse times and the pressure decay time constant. Also given is the time constant fitted to the temperature decay for the active heater in each run (i.e., if a particular run uses heater A, then the heater time constant given is based on fitting an exponential function to the T3 [heater A temperature] data). The flow rates and Weber numbers given are average values for the entire mixing period. Figure 51 lists the same data but sorted in ascending order of flow rate for ease in reviewing the trends and repeatability of the data.

Run Number	Heater	Avg. Flowrate (liters/min)	Weber Number	Flow Pattern	Thermal Mixing Times (Minutes):			Pressure Reduction Times (Minutes):			
					75%	Time Const.	Heater Const.	50%	75%	95%	Time Const.
1	B	0.00	0.00	-	4.18	16.98	4.30	0.62*	0.95*	1.09*	13.9*
2	B	2.68	14.51	Penetr.	0.18	***	0.62	0.06	0.09	0.58	0.09
3	B	0.54	0.59	Nonpen.	1.33	9.23	1.80	0.54	0.79	2.32	0.76
4	B	1.53	4.73	Asym.	0.02	***	1.08	0.17	0.30	0.47	0.32
5	B	2.72	14.91	Penetr.	0.12	0.35	0.71	0.04	0.06	0.09	0.06
6	B	0.00	0.00	-	0.02	***	2.74	1.36	2.89	7.82	2.03
7	B	1.53	4.74	Asym.	0.02	***	1.13	0.16	0.29	0.52	0.21
8	B	0.60	0.73	Nonpen.	0.02	***	1.61	0.54	0.72	7.82	1.20
9	A	0.00	0.00	-	7.28	6.78	3.23	1.66	3.44	12.27	2.66
10	A	2.74	15.16	Penetr.	0.57	0.65	0.56	0.04	0.08	0.89	0.07
11	A	0.59	0.71	Nonpen.	3.87	4.86	4.08	0.33	0.89	6.22	0.60
12	A	1.54	4.78	Penetr.	1.10	1.22	***	0.09	0.21	3.57	0.15
13	A	2.78	15.55	Penetr.	0.32	0.56	0.55	0.04	0.07	0.46	0.06
14	A	0.00	0.00	-	11.12	22.57	4.37	1.10	2.56	6.71	1.89
15	A	1.53	4.74	Asym.	0.82	0.69	0.74	0.13	0.37	5.14	0.27
16	A	0.60	0.72	Nonpen.	3.53	3.64	3.99	0.43	0.96	7.19	0.85
17	B	2.78	15.62	Penetr.	1.22	0.27	0.84	0.07	0.11	0.30	0.12
18	B	0.00	0.00	-	0.92	0.80	4.59	1.06	1.96	4.56	1.73
19	B	1.58	5.06	Penetr.	0.02	***	0.80	0.17	0.30	7.22	0.25
20	B	0.60	0.73	Nonpen.	0.10	***	1.59	0.36	1.05	11.56	0.71
21	A	0.00	0.00	-	7.08	12.59	5.46	7.02	8.13	12.80	42.7*
22	A	2.84	16.22	Penetr.	0.47	0.57	0.56	0.04	0.09	3.47	0.08
23	A	0.62	0.77	Nonpen.	2.22	1.71	5.77	0.36	1.18	6.36	0.81
24	A	1.57	4.96	Penetr.	0.55	0.89	0.81	0.12	0.29	4.25	0.22
25	B	0.38	0.29	Nonpen.	0.02	***	2.67	0.79	1.01	9.47	1.74
26	B	1.24	3.11	Asym.	0.15	0.20	1.39	0.28	0.47	9.81	0.54
27	B	0.80	1.29	Nonpen.	1.97	16.25	1.50	0.29	0.54	8.58	0.46
28	B	1.71	5.90	Asym.	0.02	***	0.96	0.09	0.22	0.53	0.17
29	A	1.24	3.10	Asym.	0.32	0.26	1.15	0.49	1.54	11.00	1.23
30	A	1.77	6.30	Penetr.	0.68	1.77	0.83	0.07	0.12	0.92	0.09
31	A	0.84	1.44	Nonpen.	0.50	0.49	3.18	0.50	2.30	11.44	1.68
32	A	0.38	0.30	Nonpen.	0.77	0.73	3.38	0.51	0.87	2.54	0.83
33	AB	0.64	0.82	Nonpen.	1.43	3.21	1.47	0.26*	3.46*	12.63*	4.16*
34	AB	1.54	4.79	Asym.	0.07	0.06	1.19	0.69*	2.33*	13.07*	48.5*
35	AB	0.00	0.00	-	10.12	39.80	8.01	0.09*	0.09*	0.79*	0.29*
36	AB	2.82	16.08	Penetr.	0.03	***	0.95	0.18*	0.22*	0.77*	0.35*
37	B	3.34	22.48	Penetr.	0.03	***	0.65	0.02	0.04	0.06	0.04
38	A	3.35	22.64	Penetr.	0.27	0.26	0.41	0.03	0.08	0.34	0.06

* values not meaningful (see text)

*** value could not be fitted to data

Figure 50: Summary of Mixing Times

Note that certain pressure collapse values are flagged with asterisks in these tables. This indicates that the mixing time obtained by the data reduction program is not meaningful because of an insufficient initial pressure differential. In run 1 an acceleration disturbance causes complete self-mixing prior to the start of the mixing phase. In runs 33 to 36, which use both heaters and produce one-quarter the heat flux, the initial pressure differential is small compared with the resolution and noise level in the data (see for example the pressure trace for run 34, figure A-72). These five runs are not included in the 75% pressure collapse time plots. In other cases, denoted by "***", the code was unable to fit a time constant to the data.

Run Number	Heater	Avg. Flowrate (liters/min)	Weber Number	Flow Pattern	Thermal Mixing Times (Minutes):			Pressure Reduction Times (Minutes):			
					75%	Time Const.	Heater Const.	50%	75%	95%	Time Const.
1	B	0.00	0.00	-	4.18	16.98	4.30	0.62*	0.95*	1.09*	13.9*
6	B	0.00	0.00	-	0.02	***	2.74	1.36	2.89	7.82	2.03
9	A	0.00	0.00	-	7.28	6.78	3.23	1.66	3.44	12.27	2.66
14	A	0.00	0.00	-	11.12	22.57	4.37	1.10	2.56	6.71	1.89
18	B	0.00	0.00	-	0.92	0.80	4.59	1.06	1.96	4.56	1.73
21	A	0.00	0.00	-	7.08	12.59	5.46	7.02	8.13	12.80	42.7*
35	AB	0.00	0.00	-	10.12	39.80	8.01	0.09*	0.09*	0.79*	0.29*
25	B	0.38	0.29	Nonpen.	0.02	***	2.67	0.79	1.01	9.47	1.74
32	A	0.38	0.30	Nonpen.	0.77	0.73	3.38	0.51	0.87	2.54	0.83
3	B	0.54	0.59	Nonpen.	1.33	9.23	1.80	0.54	0.79	2.32	0.76
11	A	0.59	0.71	Nonpen.	3.87	4.86	4.08	0.33	0.89	6.22	0.60
16	A	0.60	0.72	Nonpen.	3.53	3.64	3.99	0.43	0.96	7.19	0.85
8	B	0.60	0.73	Nonpen.	0.02	***	1.61	0.54	0.72	7.82	1.20
20	B	0.60	0.73	Nonpen.	0.10	***	1.59	0.36	1.05	11.56	0.71
23	A	0.62	0.77	Nonpen.	2.22	1.71	5.77	0.36	1.18	6.36	0.81
33	AB	0.64	0.82	Nonpen.	1.43	3.21	1.47	0.26*	3.46*	12.63*	4.16*
27	B	0.80	1.29	Nonpen.	1.97	16.25	1.50	0.29	0.54	8.58	0.46
31	A	0.84	1.44	Nonpen.	0.50	0.49	3.18	0.50	2.30	11.44	1.68
29	A	1.24	3.10	Asym.	0.32	0.26	1.15	0.49	1.54	11.00	1.23
26	B	1.24	3.11	Asym.	0.15	0.20	1.39	0.28	0.47	9.81	0.54
4	B	1.53	4.73	Asym.	0.02	***	1.08	0.17	0.30	0.47	0.32
7	B	1.53	4.74	Asym.	0.02	***	1.13	0.16	0.29	0.52	0.21
15	A	1.53	4.74	Asym.	0.82	0.69	0.74	0.13	0.37	5.14	0.27
12	A	1.54	4.78	Penetr.	1.10	1.22	***	0.09	0.21	3.57	0.15
34	AB	1.54	4.79	Asym.	0.07	0.06	1.19	0.69*	2.33*	13.07*	48.5*
24	A	1.57	4.96	Penetr.	0.55	0.89	0.81	0.12	0.29	4.25	0.22
19	B	1.58	5.06	Penetr.	0.02	***	0.80	0.17	0.30	7.22	0.25
28	B	1.71	5.90	Asym.	0.02	***	0.96	0.09	0.22	0.53	0.17
30	A	1.77	6.30	Penetr.	0.68	1.77	0.83	0.07	0.12	0.92	0.09
2	B	2.68	14.51	Penetr.	0.18	***	0.62	0.06	0.09	0.58	0.09
5	B	2.72	14.91	Penetr.	0.12	0.35	0.71	0.04	0.06	0.09	0.06
10	A	2.74	15.16	Penetr.	0.57	0.65	0.56	0.04	0.08	0.89	0.07
13	A	2.78	15.55	Penetr.	0.32	0.56	0.55	0.04	0.07	0.46	0.06
17	B	2.78	15.62	Penetr.	1.22	0.27	0.84	0.07	0.11	0.30	0.12
36	AB	2.82	16.08	Penetr.	0.03	***	0.95	0.18*	0.22*	0.77*	0.35*
22	A	2.84	16.22	Penetr.	0.47	0.57	0.56	0.04	0.09	3.47	0.08
37	B	3.34	22.48	Penetr.	0.03	***	0.65	0.02	0.04	0.06	0.04
38	A	3.35	22.64	Penetr.	0.27	0.26	0.41	0.03	0.08	0.34	0.06

* values not meaningful (see text)

*** value could not be fitted to data

Figure 51: Summary of Mixing Times (Sorted by Flow Rate)

Comparison With Mixing Models

The dimensionless correlation of mixing times, $t_{mix}V_0D_o/D^2_{tank}$, used by Wollen (ref. 7) and others is applied to the 75% pressure collapse data and plotted in figure 52. Wollen's experimental value of this parameter, a constant 3.46 at Reynolds numbers greater than 5000, is plotted in the same figure as a horizontal line. Although Wollen's correlation is based on equilibration within the liquid, rather than pressure reduction, the pressure data agree approximately (to within a factor of three) except for two asymmetric flow cases (runs 29 and 31). Figure 53 shows Wollen's correlation versus the 75% thermal equilibration times. Here the dimensionless mixing parameter does not correlate the data well, and even increases the spread of the mixing times.

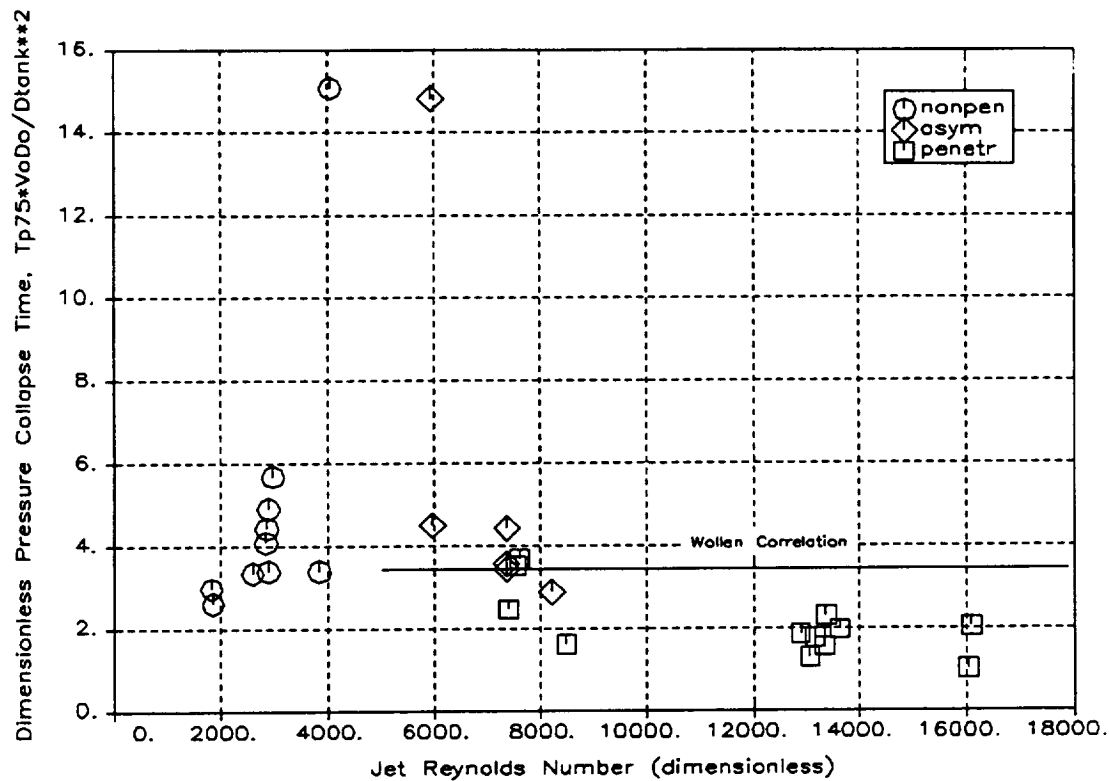


Figure 52: Pressure Collapse Times Compared with Wollen's Correlation

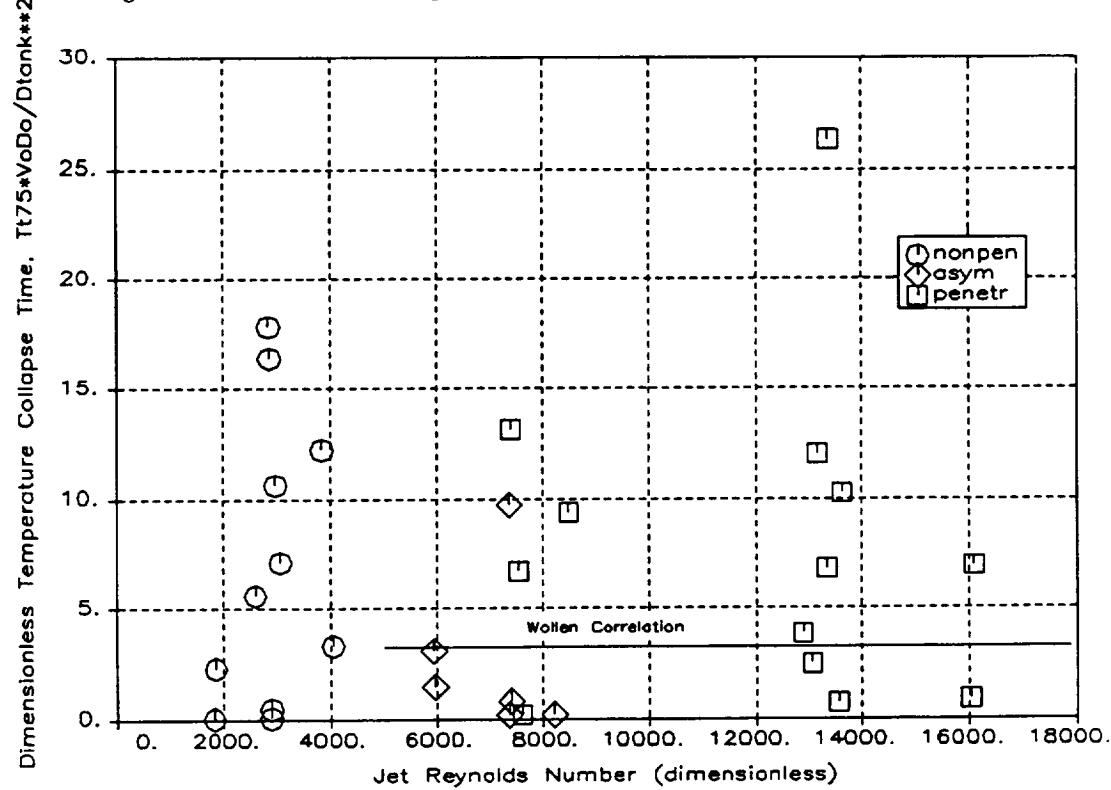


Figure 53: Thermal Equilibration Times Compared with Wollen's Correlation

Aydelott's (ref. 15) mixing time correlation (equations 5 and 6) is shown in figure 54 in comparison with the 75% pressure collapse data. It is compared with the 75% thermal equilibration time in figure 55. In both cases the data do not confirm the correlation, and the trends with increasing flow rate do not match the slope of the line. Note, however, that this correlation was based on the time required to distribute dye in the jet to the bulk liquid, and might not be expected to compare well with pressure collapse and thermal equilibration times.

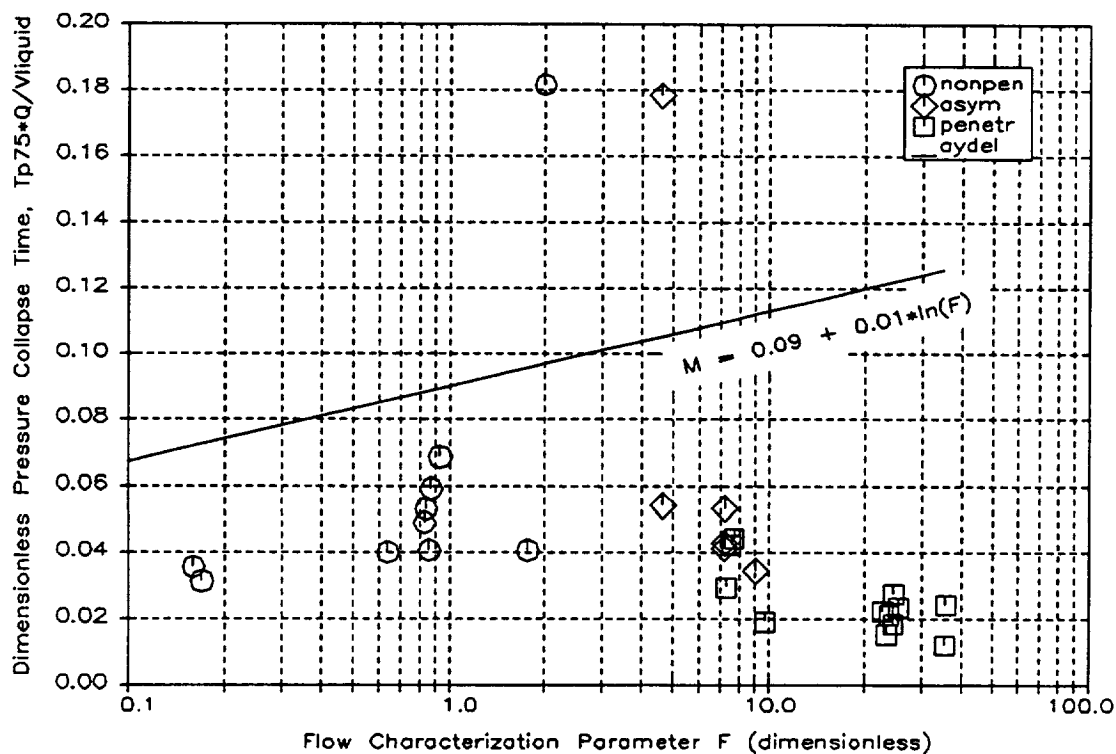


Figure 54: Pressure Collapse Times Compared with Aydelott's Correlation

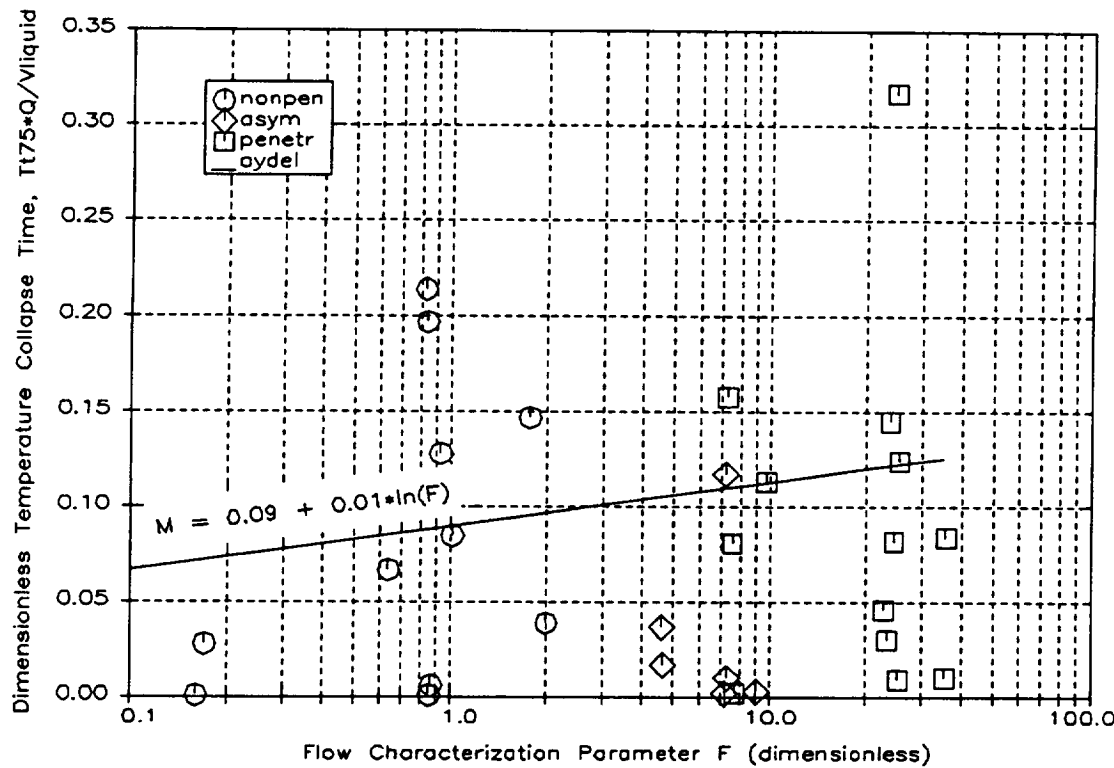


Figure 55: Thermal Equilibration Times Compared with Aydelotti's Correlation

A simplified closed-form solution for the pressure collapse time was developed and first presented (in a slightly different form) in reference 20. This model makes the following assumptions: (1) the ullage gas expands isothermally, (2) the ullage consists only of propellant vapor, (3) the vapor is an ideal gas with constant specific heats and constant compressibility, and (4) there is no heat transfer from the ullage to the liquid. With a constant-temperature ullage,

$$\frac{dP}{dt} = \frac{P}{m} \frac{dm}{dt} \quad (15)$$

where dm/dt is the mass change due to condensation. An energy balance on the liquid surface whose area is A yields an expression for the evaporation/condensation rate:

$$\frac{dm}{dt} = -\frac{h A}{\lambda} (T_{sat} - T_{liquid}) \quad (16)$$

where h is the heat transfer coefficient between the bulk liquid and the interface, λ is the latent heat of evaporation, T_{sat} is the saturation temperature corresponding to the instantaneous pressure, and T_{liquid} is the temperature of the bulk liquid away from the interface. Using the Clapeyron equation, and assuming that the liquid density is much greater than the vapor density, one can approximate the dependence of T_{sat} on pressure as

$$\frac{dT_{sat}}{dP} = \frac{T_i}{\rho_i} \lambda \quad (17)$$

where T_i and ρ_i are the initial temperature and density of the ullage gas. Since the final (or minimum) pressure is the saturation pressure corresponding to the bulk liquid temperature (which is assumed to be invariant), one can approximate that

$$T_{\text{sat}} - T_{\text{liquid}} = \frac{T_i}{\rho_i} \lambda (P - P_{\text{final}}) \quad (18)$$

which when substituted into equations (16) and (15) yields

$$\frac{dP}{dt} = -\frac{h A}{\lambda} \frac{T_i}{\rho_i \lambda} (P - P_{\text{final}}) \frac{P}{\rho V} \quad (19)$$

where P is the instantaneous pressure and V is the ullage volume. Since we are assuming that the ullage remains at a constant temperature during the pressure decay, $(P/\rho) = (P_i/\rho_i)$. The solution to equation (19), which is an exponential decay, is then

$$\frac{P(t) - P_{\text{final}}}{P_i - P_{\text{final}}} = e^{-t/\tau} \quad (20)$$

where the time constant τ is:

$$\tau = \frac{\rho_i^2 \lambda^2 V}{h A T_i P_i} \quad (21)$$

The time required for $(P - P_{\text{final}})/(P_i - P_{\text{final}})$ to drop to 0.25 (which is the definition of the pressure collapse time used elsewhere in this report) is equal to 1.39τ . Therefore

$$t_{P75\%} = \frac{1.39 \rho_i^2 \lambda^2 V}{h A T_i P_i} \quad (22)$$

Dominick (ref. 9) reported that the following expression from Jakob (ref. 21) adequately predicted the convection coefficient, h , between the bulk liquid and a flat liquid surface layer on which an axial submerged jet impinges:

$$\frac{h D_j}{k_l} = (0.205) Re^{0.731} Pr_l^{1/3}. \quad (23)$$

Inserting equation (23) into equation (22) yields

$$t_{P75\%} = \frac{6.78 \rho_i^2 \lambda^2 V D_j}{T_i P_i A k_l} Re^{-0.731} Pr_l^{-1/3}. \quad (24)$$

This equation suggests that mixing time is a strong function of the initial ullage mass times its heat of condensation, which determines the energy that must be dispersed into the liquid to accomplish the pressure reduction. The previous correlations do not account for these parameters. (If the ullage expansion is modelled as an isentropic process, rather than isothermal, then the mixing time equation also has the ratio of specific heats in the denominator. However, the isothermal assumption probably more closely approximates most situations, and is conservative.)

Pressure collapse times predicted by equation (24) are calculated for TPCE using typical values for ρ_i , T_i , and P_i . For A , the interface area acted on by the jet, the projected area

of a sphere having the same volume as the ullage is used, i.e., $A = \pi r_{ullage}^2$. This prediction is shown in figure 56 in comparison with the measured pressure collapse times. The closed-form prediction agrees well with the data, although it slightly underpredicts pressure collapse times in the nonpenetrating flow regime. Given the generalizations and assumptions made in the model, its agreement with the data points to the potential value of a closed-form prediction such as this in estimating mixing times.

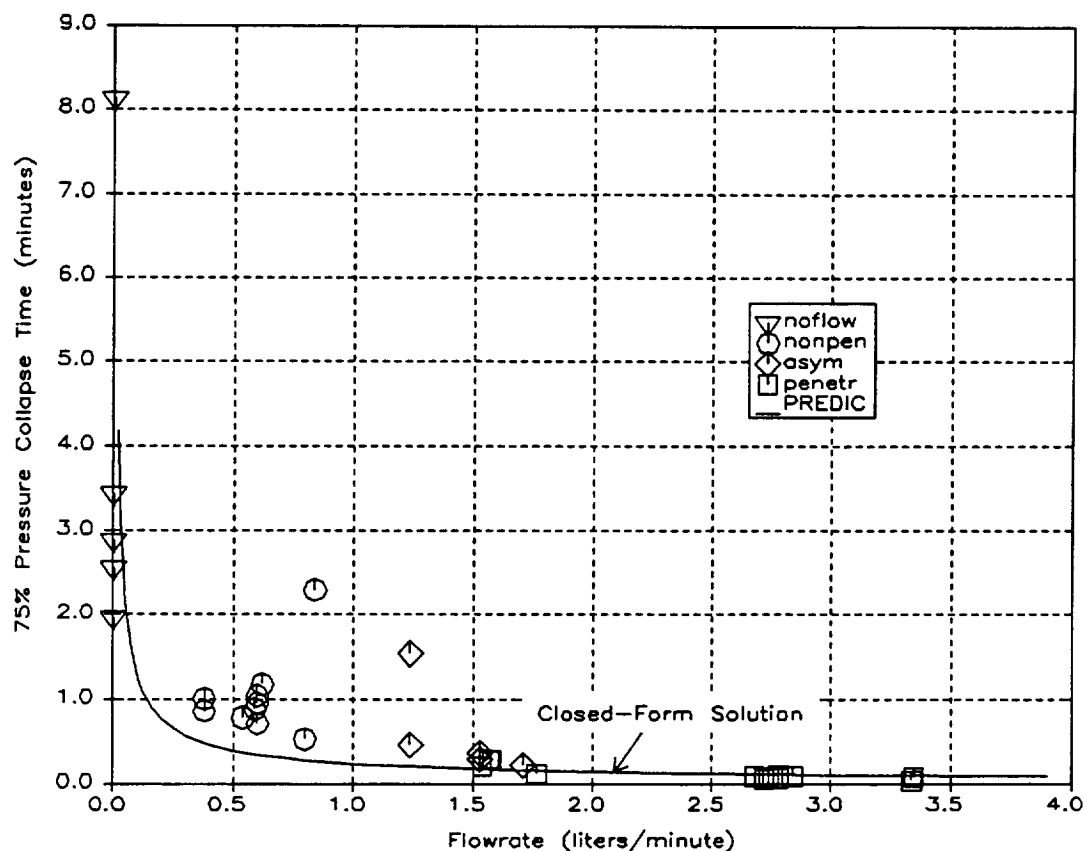


Figure 56: Pressure Collapse Time Versus Closed-Form Prediction (Eq. 24)

Heater Plate Convection

The heater plates are constructed with a significant amount of thermal mass to help meet STS flight safety requirements by limiting the maximum potential heater surface temperatures. Because of this thermal mass, the heater temperature decay does not occur at the same rate as the fluid temperature equilibration. The heater temperature decay does, however, offer an opportunity to estimate the convective heat transfer under the influence of jet flow in a low-g two-phase fluid environment. This heat transfer data could be useful in future design studies for estimating the effectiveness of axial jets at cooling tank walls and other objects, as a function of the jet Reynolds number, flow pattern, and location of the area being cooled.

A time constant τ is obtained for each run by fitting an exponential function to the temperature decay curve of the active heater. The convection coefficient h is obtained from this time constant by the relation $\tau = hA/mc_p$, where A is the total surface area of the heater plate (including both sides), m is its mass, and c_p is its specific heat. The coefficient is nondimensionalized by calculating the Nusselt number, hd/k_l , where d , the characteristic dimension, is the length of the heater plate and k_l is the liquid thermal conductivity. These Nusselt numbers are presented in figure 57 as a function of the jet Reynolds number at the outlet of the nozzle. The open symbols on the plot are heater A runs, and the filled symbols are heater B runs.

The results indicate that heater A receives better cooling than heater B at high flow rates. This is not surprising because at these flow rates the jet penetrates the ullage and impinges directly on heater A, and heater B sees only a portion of the recirculating flow along the tank sidewall. However, at lower flow rates that do not result in ullage penetration heater B experiences more cooling from the jet than does heater A, which is blocked by the ullage bubble from direct jet impingement.

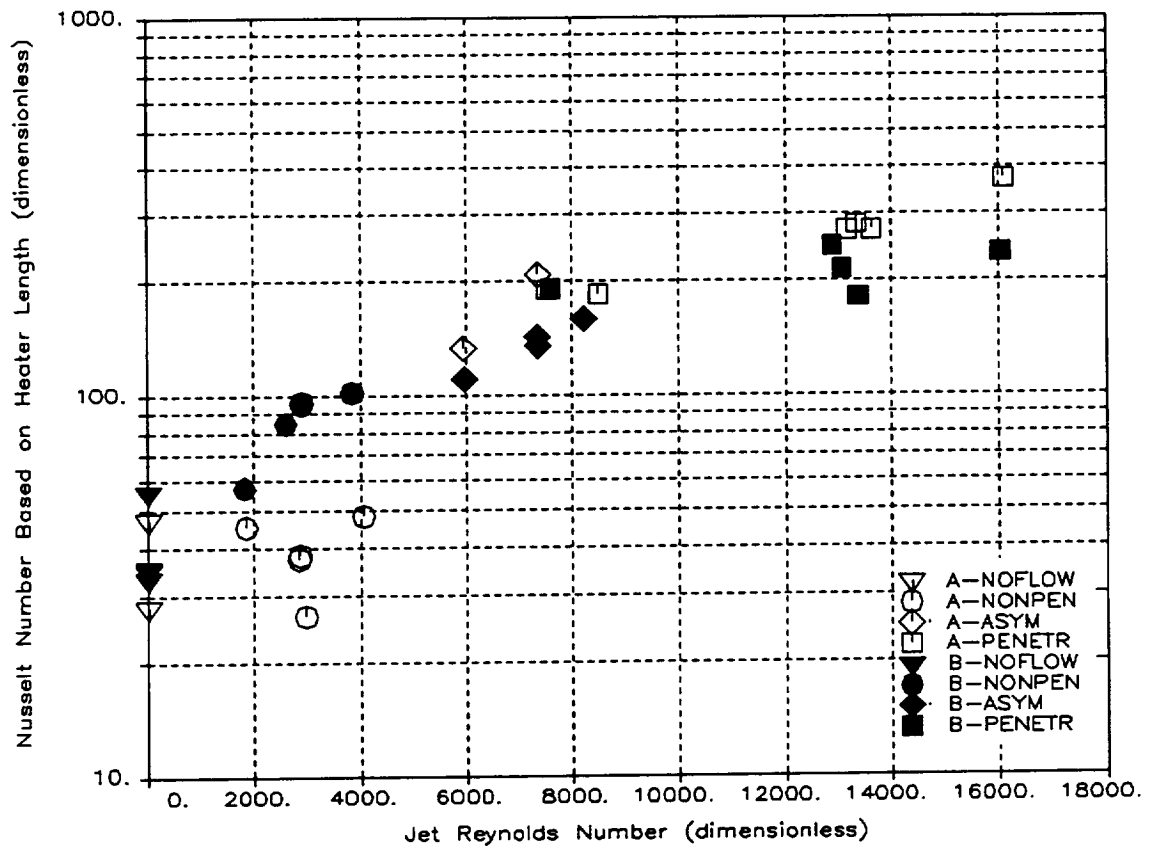


Figure 57: Flow-Induced Cooling of Heater Plates

Heating Phase Effects

As discussed earlier, the main ullage bubble was observed to migrate to the active heater during nearly every heating period. This effect, also observed by other low-g experimenters, is due to Marangoni convection. As illustrated in figure 58, when a thermal gradient exists along a liquid/vapor interface there is a gradient in surface tension force that causes liquid to be pulled in the direction of lower temperature (which has higher surface tension). This results in motion of the bubble toward the heat source. The dimensionless Marangoni number is estimated to be on the order of 300 for TPCE, which is sufficient to drive this convection mechanism. The mechanism does not exist, though, until the thermal gradient induced by the heater reaches the bubble. In most cases this probably takes several minutes, which is why the ullage migration is not observed in the two minutes of video at the beginning of each heating stage.

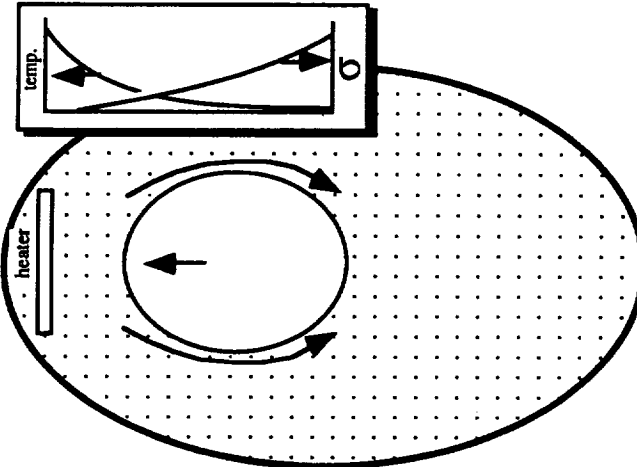


Figure 58: Marangoni Convection Mechanism

The pressure spikes seen in several of the heating phases, as discussed previously, are suspected of being related to this ullage migration. In at least two cases (runs 5 and 8) the ullage travels to the active heater early enough in the heating phase to be captured on the video because of an acceleration event. A small spike is seen in the pressure data at the same time that the ullage reaches the heater in these cases. It is not known if the larger spikes seen in other runs occur at the same time the ullage reaches the heater because there is no video coverage of those events. However this suggests a mechanism, as follows, to explain the spikes.

When the ullage is not adjacent to the heat source in low-g, the heat that is added to the fluid cannot affect the pressure unless and until evaporation occurs. Boiling at the heater is suppressed in TPCE by the presence of noncondensable gases in the ullage and by the lack of nucleation sites. These factors mean that the liquid must be superheated above the refrigerant partial pressure existing in the ullage before evaporation can occur. Thus a significant amount of heat is added to the liquid surrounding the heater, creating an unstable situation. When the temperature gradient eventually reaches the ullage, Marangoni convection attracts the bubble toward the warmer fluid. As the liquid/vapor interface reaches the region of superheated liquid the excess energy results in sudden evaporation, or flash boiling. The pressure quickly falls back to a new equilibrium, however, as vapor condenses on the cold side of the bubble.

This explanation is supported by the temperature and pressure data. The later in the heating phase that the pressure spike occurs, the greater the spike usually is, indicating that more energy had been stored in the liquid. An example is run 13, which uses heater A. Immediately before the pressure spike occurs the temperature of the liquid near heater A (T4) is 4.8°C above the bulk liquid temperature (the heater temperature is 14°C higher than the bulk liquid). A 4.8°C superheat corresponds to a 12.6 kPa (1.83 psi) vapor pressure differential. The pressure spike that occurs 7.5 minutes after heater turn-on has an amplitude of 13.6 kPa (1.97 psi).

This phenomenon is not seen in normal gravity because buoyancy continuously draws the warmest liquid to the liquid/vapor interface. In low gravity, however, the potential for pressure spikes may exist whenever localized heating occurs at a higher rate than the heat can be dissipated into the bulk liquid. Mixing would increase this heat dissipation beyond that expected with conduction alone and therefore should reduce the likelihood of these sudden pressure increases.

CONCLUSIONS

The Tank Pressure Control Experiment accomplished all of its objectives in flight on STS-43. The flow patterns produced by an axial jet mixer in a tank with an 83% fill fraction were characterized as a function of flow rate. The effectiveness of the mixing was determined in terms of (1) the jet's ability to penetrate the ullage and reach all portions of the tank, (2) the time required to reduce the pressure in the tank, and (3) the time required to mix the fluid and equilibrate its temperature.

Two symmetric flow patterns were found: a nonpenetrating jet at jet Weber numbers less than approximately 1.4, and a penetrating, recirculating jet at Weber numbers of 4.8 and above. Effective mixing was found with both flow patterns. At intermediate Weber numbers the flow was asymmetric and the mixing performance was sometimes less effective and was less repeatable. The highest flow rates, at Weber numbers near 23, resulted in breakup of the ullage into numerous small bubbles.

Mixing times—both pressure reduction times and thermal equilibration times—were shortest at the highest Weber numbers, but the low end of the ullage-penetrating regime (Weber numbers between 4.8 and 6.3) still produced rapid, positive pressure collapse. This range could be used in applications requiring a rapid reduction of tank pressure. Based on the observed behavior at high flow rates, Weber numbers in excess of approximately 16 could result in undesired ullage breakup and fluid motions in large cryogenic propellant tanks. The nonpenetrating flow range (Weber numbers between 0.3 and 1.4) produced a slower but still positive and repeatable pressure reduction. This range of Weber numbers might be used in applications requiring minimum energy dissipation. In this nonpenetrating range, the total kinetic energy dissipated to accomplish a 75% pressure reduction is approximately one-fifth of that dissipated when the Weber number is in the ullage-penetrating range.

Comparison of the results with prior work indicated that jet Weber number is a useful measure of both flow pattern and mixing effectiveness. This means that a target Weber number would be selected when designing a mixer to meet a given performance requirement. One implication of this is that a mixer can be designed to be more efficient by using a larger-diameter mixer nozzle which, at a given Weber number, would result in less kinetic energy addition.

Previous mixing correlations did not accurately predict either the pressure reduction times or thermal equilibration times. However, a closed-form equation predicting the pressure reduction time, based on a simple thermodynamic model, approximately matched the results. This model has greater potential for accurately predicting pressure collapse times than previous correlations because the effects of ullage volume and other important parameters are included.

The results indicate that an active cryogenic tank pressure control system could be designed using a low-velocity axial jet mixer that would have an insignificant boiloff penalty associated with its kinetic energy addition. Low-energy mixing—either continuous or periodic—can provide positive and consistent pressure control. Mixing also offers the advantage of making the fluid state more predictable and stable by reducing the thermal nonuniformities that can cause sudden changes in pressure.

REFERENCES

1. Sorensen, G. L., Niggemann, R. E., Bassett, C. E., and Sedillo, M., "A Zero-Gravity Thermodynamic Vent System for the Shuttle/Centaur Hydrogen Tank," SAE 840976, July 1984.
2. Poth, L. J., Van Hook, J. R., Wheeler, D. M., and Kee, C. R., Jr., "A Study of Cryogenic Propellant Mixing Techniques—Final Report," General Dynamics FZA-439-1, Contract No. NAS8-20330, November 1968.
3. Fosset, H., and Prosser, L. E., "The Application of Free Jets to the Mixing of Fluids in Bulk," *Proc. Mech. Engrs.*, Vol. 160, 1948.
4. Fox, E. A., and Gex, V. E., "Single-Phase Blending of Liquids," *A.I.Ch.E. Journal*, Vol. 2, No. 4, December 1956.
5. Van Hook, J. R., and Poth, L. J., "Study of Cryogenic Fluid Mixing Techniques—Final Report," General Dynamics FZA-450-1, Contract No. NAS8-24882, September 1970.
6. Poth, L. J., and Van Hook, J. R., "Control of the Thermodynamic State of Space-Stored Cryogens by Jet Mixing," *J. Spacecraft*, Vol. 9, No. 5, May 1972.
7. Wollen, M., "Evaluation of Jet Induced Mixing for Centaur LH₂ Tank," General Dynamics TM 696-83-333, Contract NAS3-22901, August 1983.
8. Meserole, J. S., Jones, O. S., Fortini, A., and Brennan, S. M., "Mixing-Induced Ullage Condensation and Fluid Destratification," AIAA-87-2018, July 1987.
9. Dominick, S. M., "Mixing Induced Condensation Inside Propellant Tanks," AIAA 84-0514, January 1984.
10. Bullard, B. R., "Liquid Propellant Thermal Conditioning System Test Program—Final Report," Lockheed D159262, NASA CR-72971, Contract No. NAS-12033, July 1972.
11. Sterbentz, W. H., "Final Report—Liquid Propellant Thermal Conditioning System," Lockheed No. LMSC-K-07-68-2, NASA CR-72365, Contract No. NAS3-7942, August 1968.
12. Berenyi, S. G., Nussle, R. C., and Abdalla, K. L., "An Experimental Investigation of the Effect of Gravity on a Forced Circulation Pattern for Spherical Tanks," NASA TN D 4409, February 1968.
13. Aydelott, J. C., "Axial Jet Mixing of Ethanol in Spherical Containers During Weightlessness," NASA TM X-3380, 1976.
14. Aydelott, J. C., "Axial Jet Mixing of Ethanol in Cylindrical Containers During Weightlessness," NASA TP-1487, 1979.

15. Aydelott, J. C., "Modeling of Space Vehicle Propellant Mixing," NASA TP-2107, January 1983.
16. Hochstein, J. I., Gerhart, P. M., and Aydelott, J. C., "Computational Modeling of Jet Induced Mixing of Cryogenic Propellants in Low-G," NASA TM 83703, AIAA-84-1344, June 1984.
17. Wendl, M. C., "Jet-Induced Mixing of Propellant in Partially Filled Tanks in a Reduced Gravity Environment," Master of Science Thesis, Washington University, St. Louis, Missouri, August 1990.
18. Wendl, M. C., Hochstein, J. I., and Sasnal, G. P., "Modeling of Jet-Induced Geyser Formation in a Reduced Gravity Environment," AIAA-91-0803, January 1991.
19. Zuber, N., "On the Stability of Boiling Heat Transfer," *Trans. ASME*, vol. 80, p. 711, 1958.
20. Jones, O. S., Meserole, J. S., and Bentz, M. D., "Correlation of Ullage Condensation Rate with Mixing Intensity in Propellant Tanks," AIAA-91-2543, June 1991.
21. Jakob, M., Heat Transfer, Vol. I, John Wiley and Sons, New York, 1959.

APPENDIX A:

BASIC DATA

CONTENTS

Accelerations	A-2
Pressure, Heater Power, and Flow Rate	A-40
Temperatures	A-78

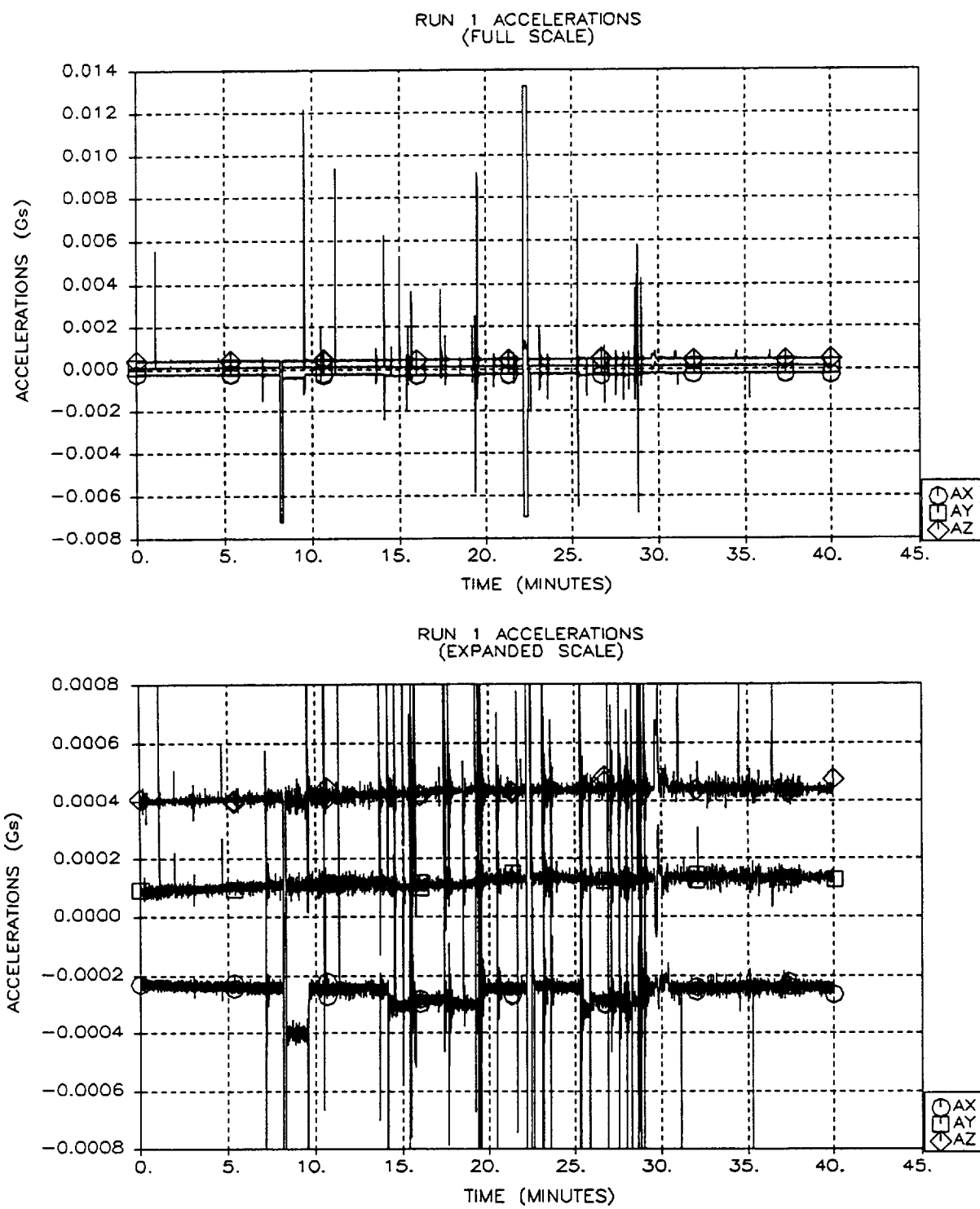


Figure A-1: Run 1 Accelerations
A-2

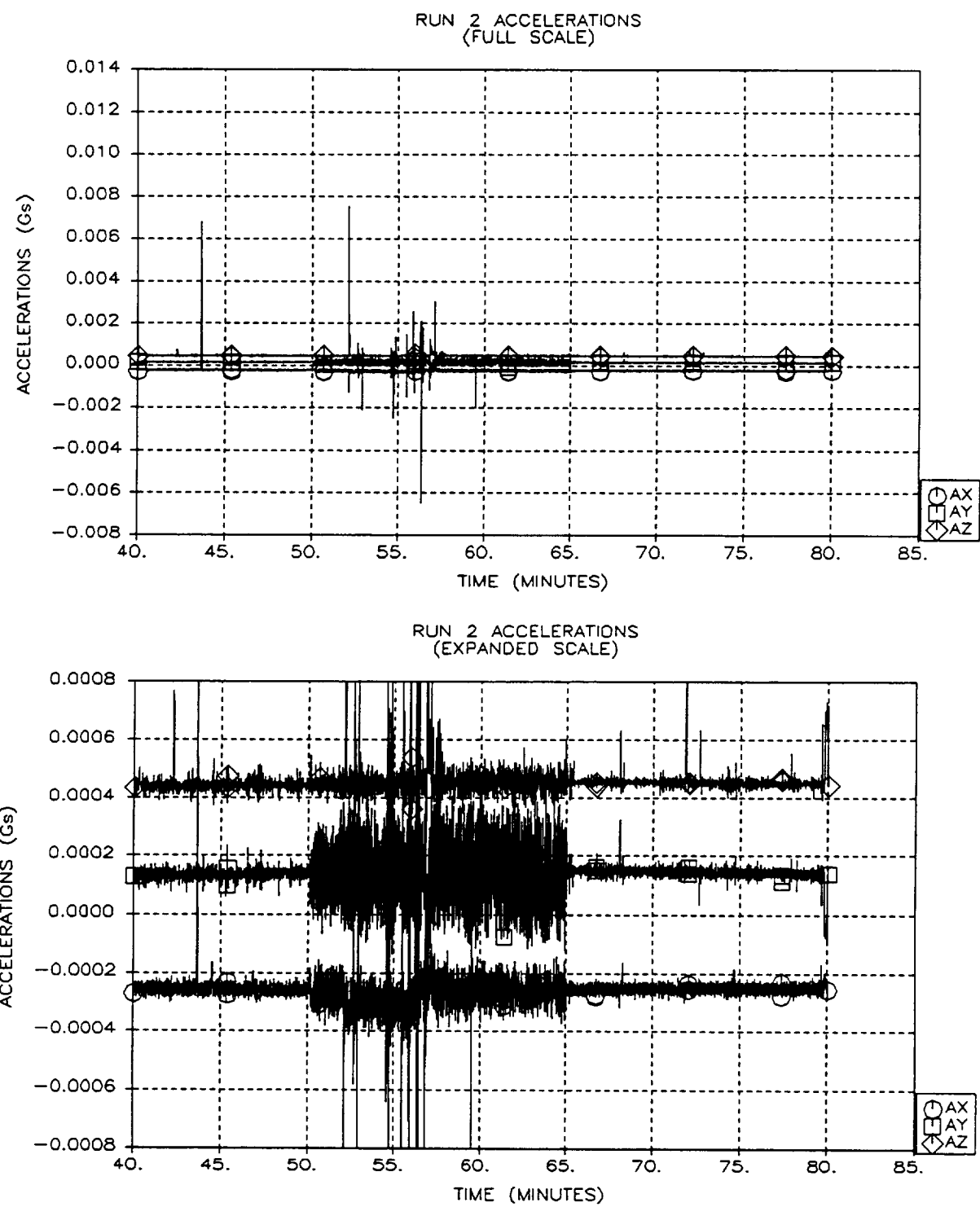


Figure A-2: Run 2 Accelerations
A-3

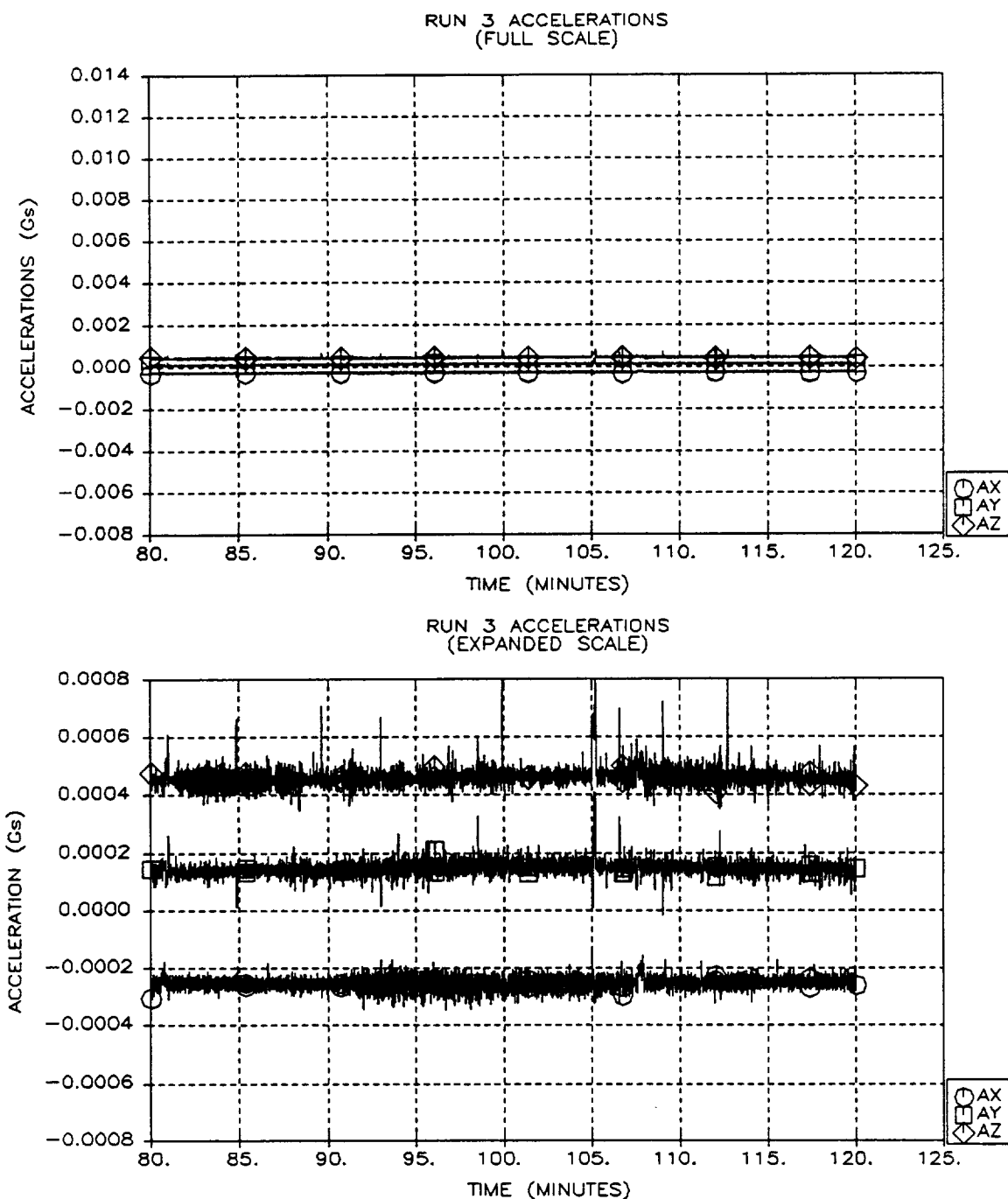


Figure A-3: Run 3 Accelerations
A-4

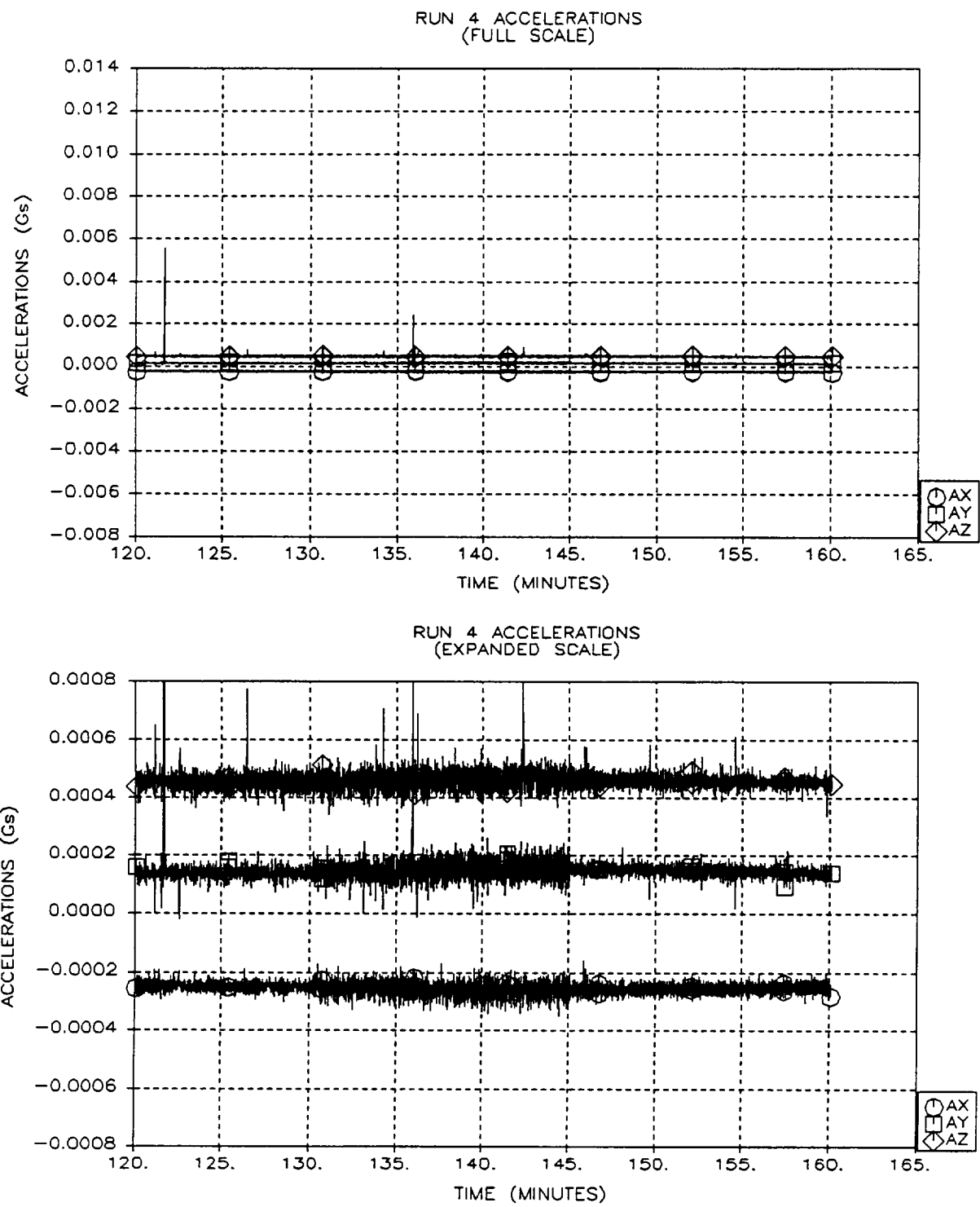


Figure A-4: Run 4 Accelerations
A-5

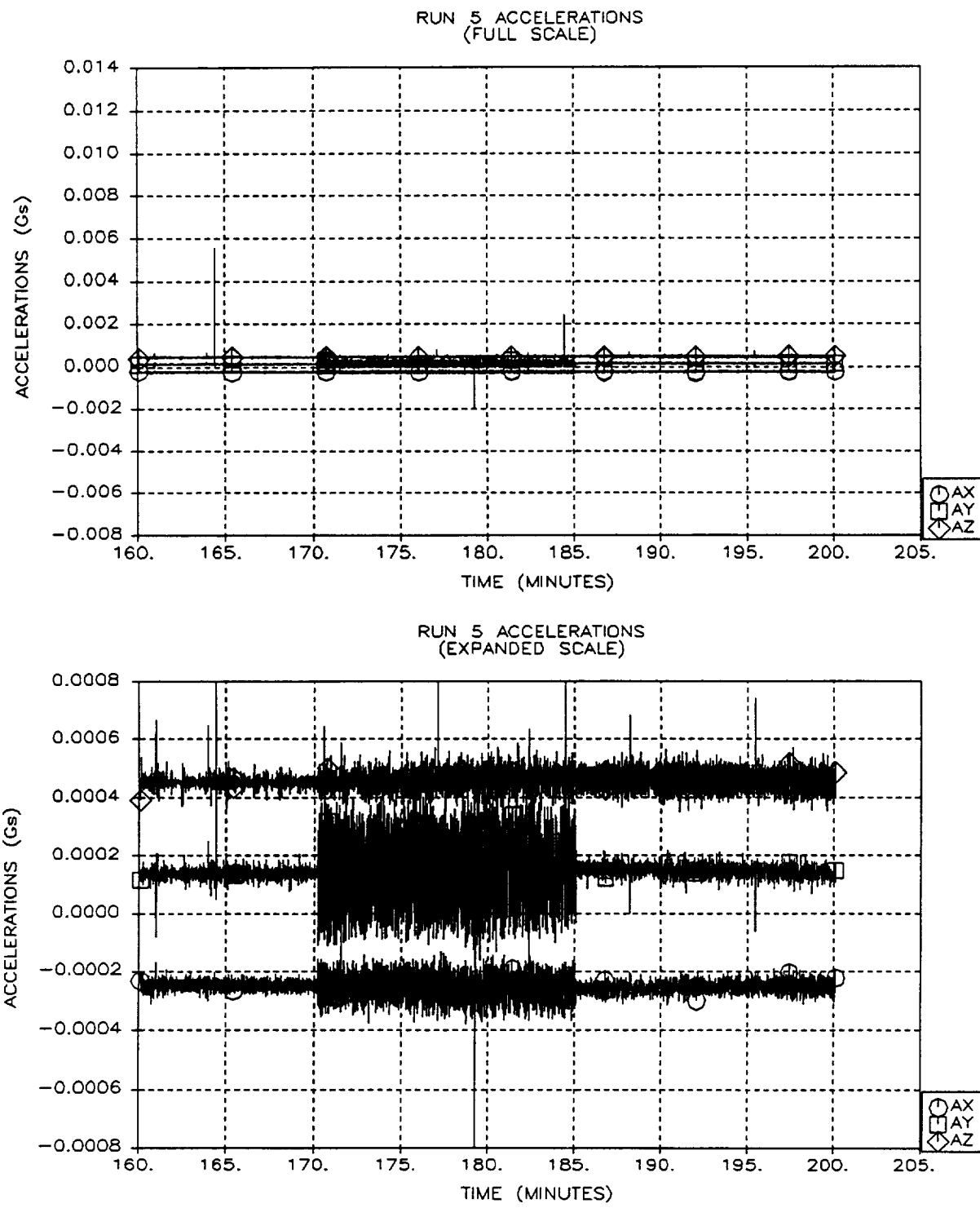


Figure A-5: Run 5 Accelerations
A-6

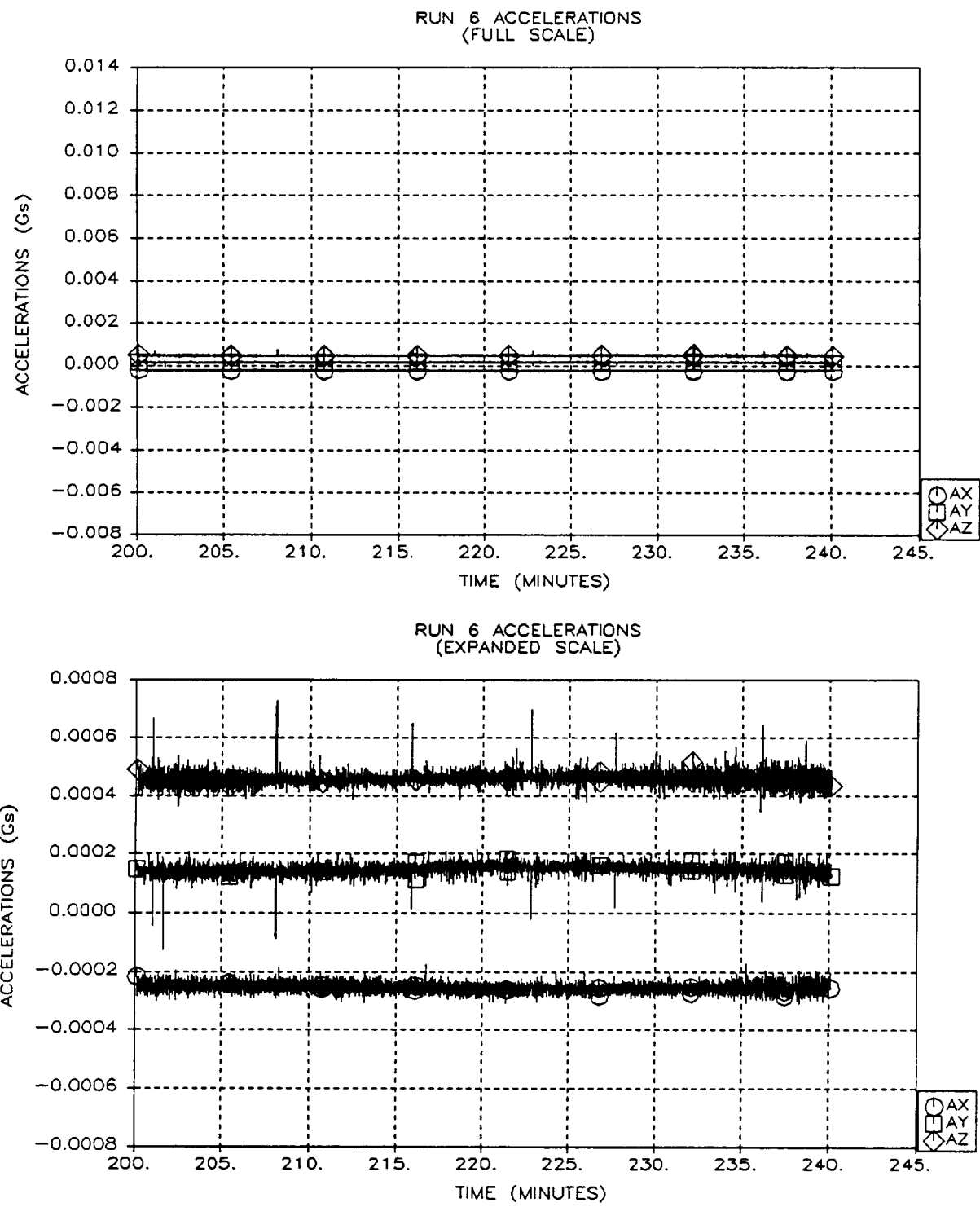


Figure A-6: Run 6 Accelerations
A-7

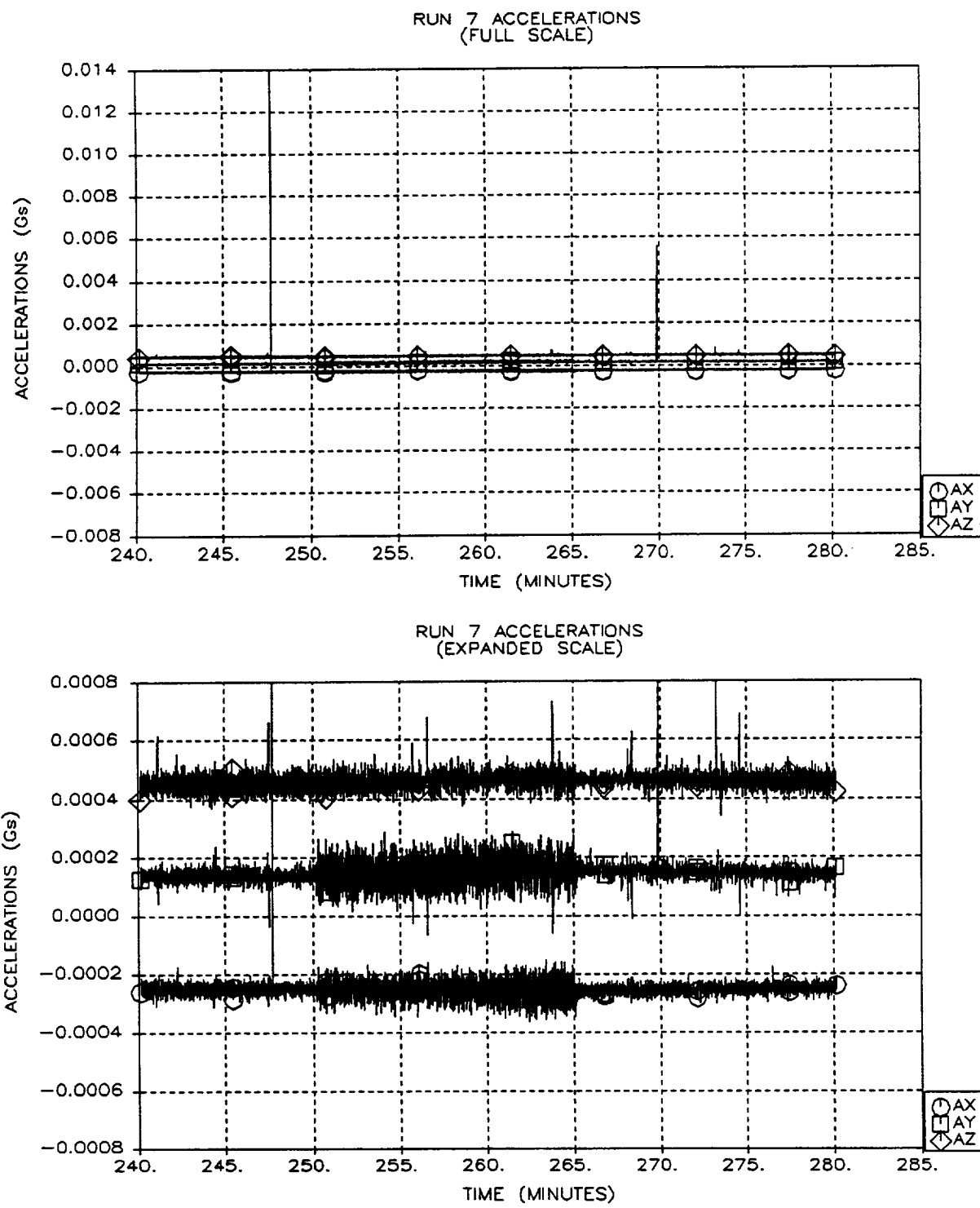


Figure A-7: Run 7 Accelerations
A-8

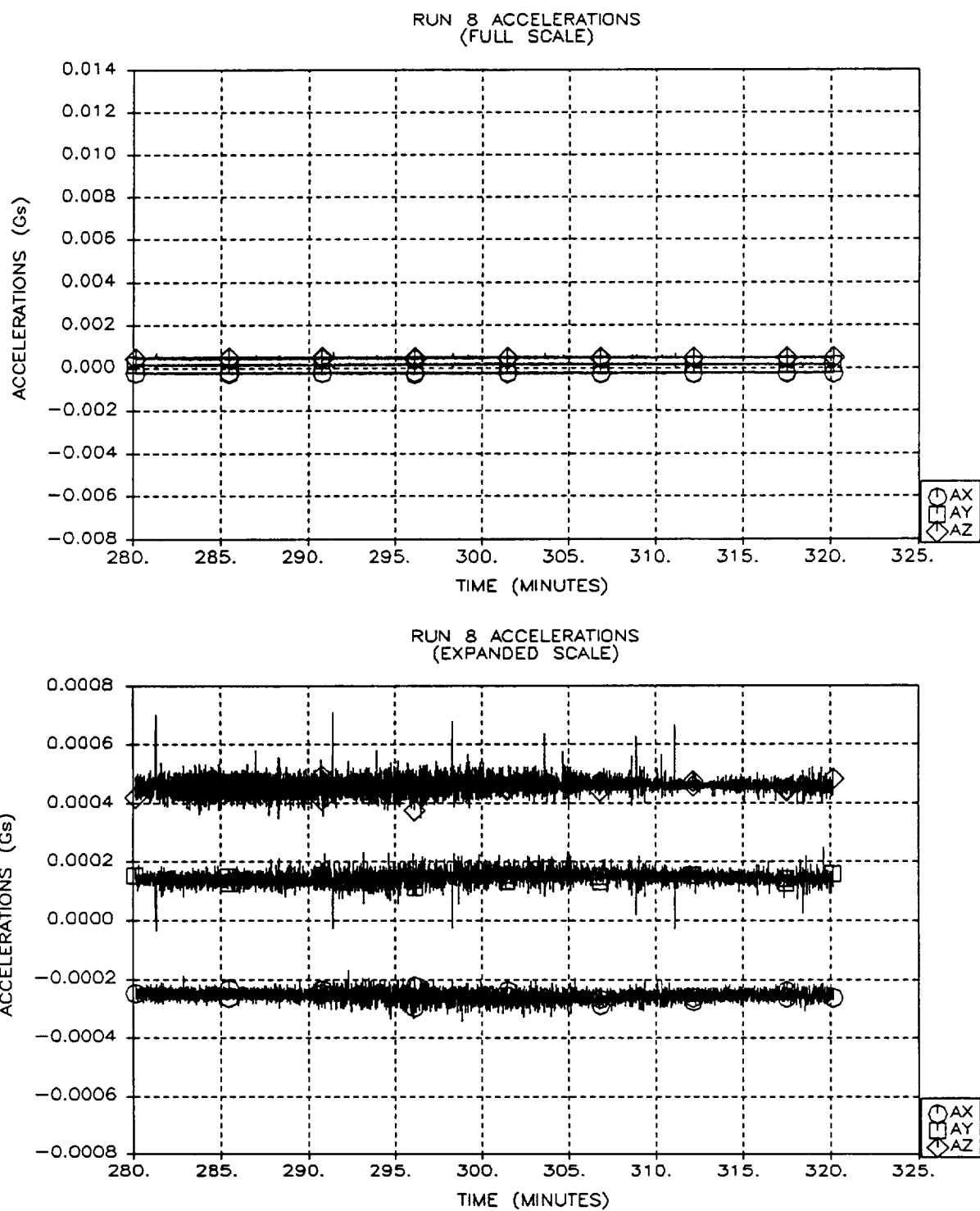


Figure A-8: Run 8 Accelerations
A - 9

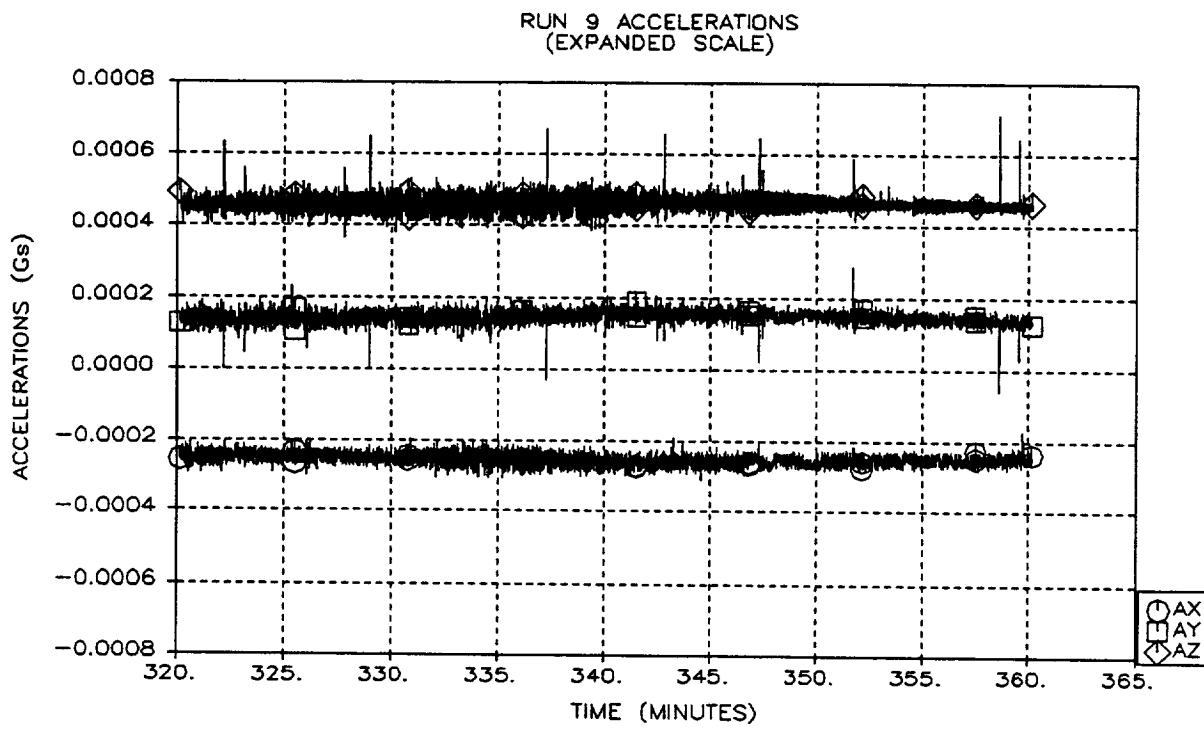
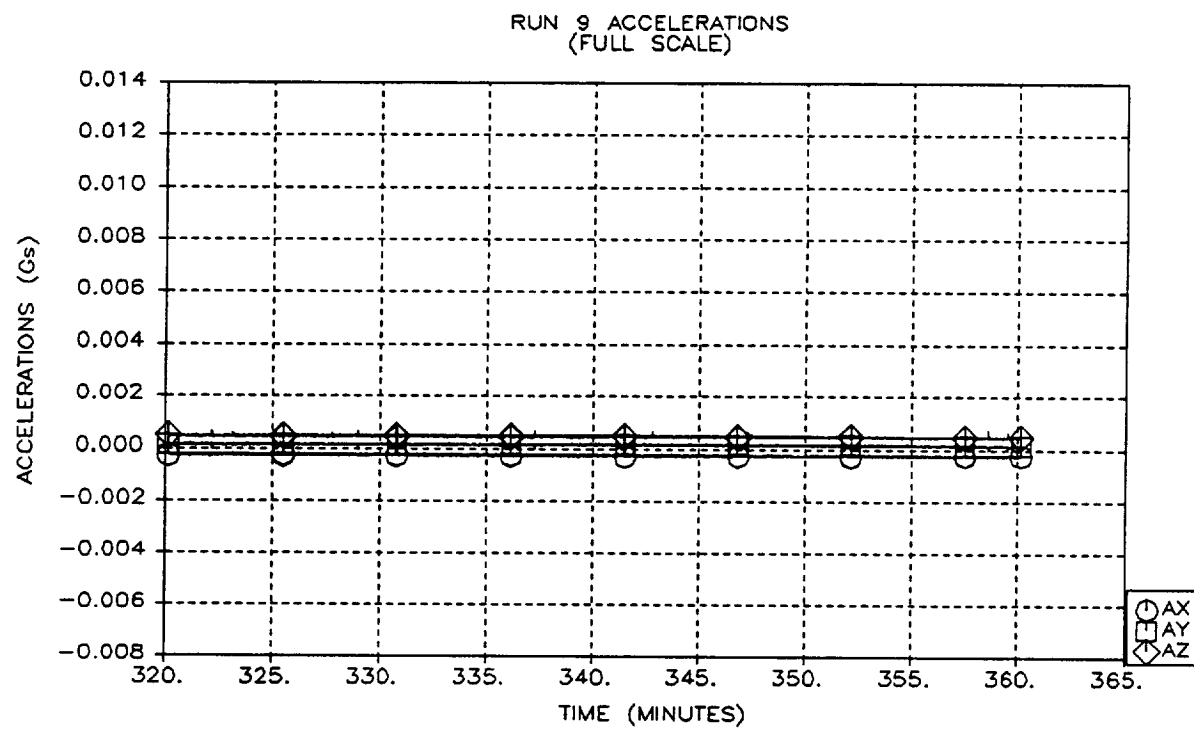


Figure A-9: Run 9 Accelerations
A-10

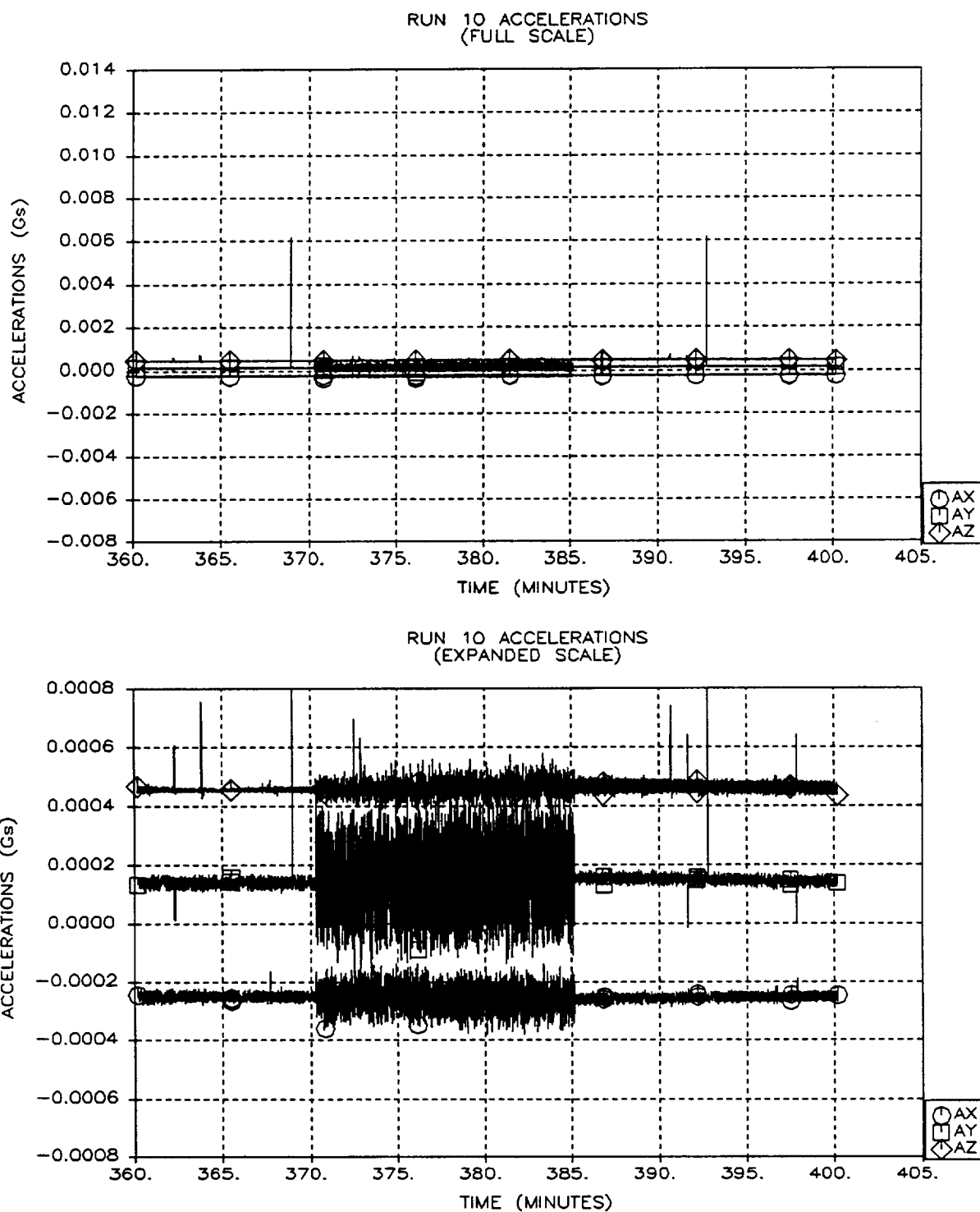


Figure A-10: Run 10 Accelerations
A-11

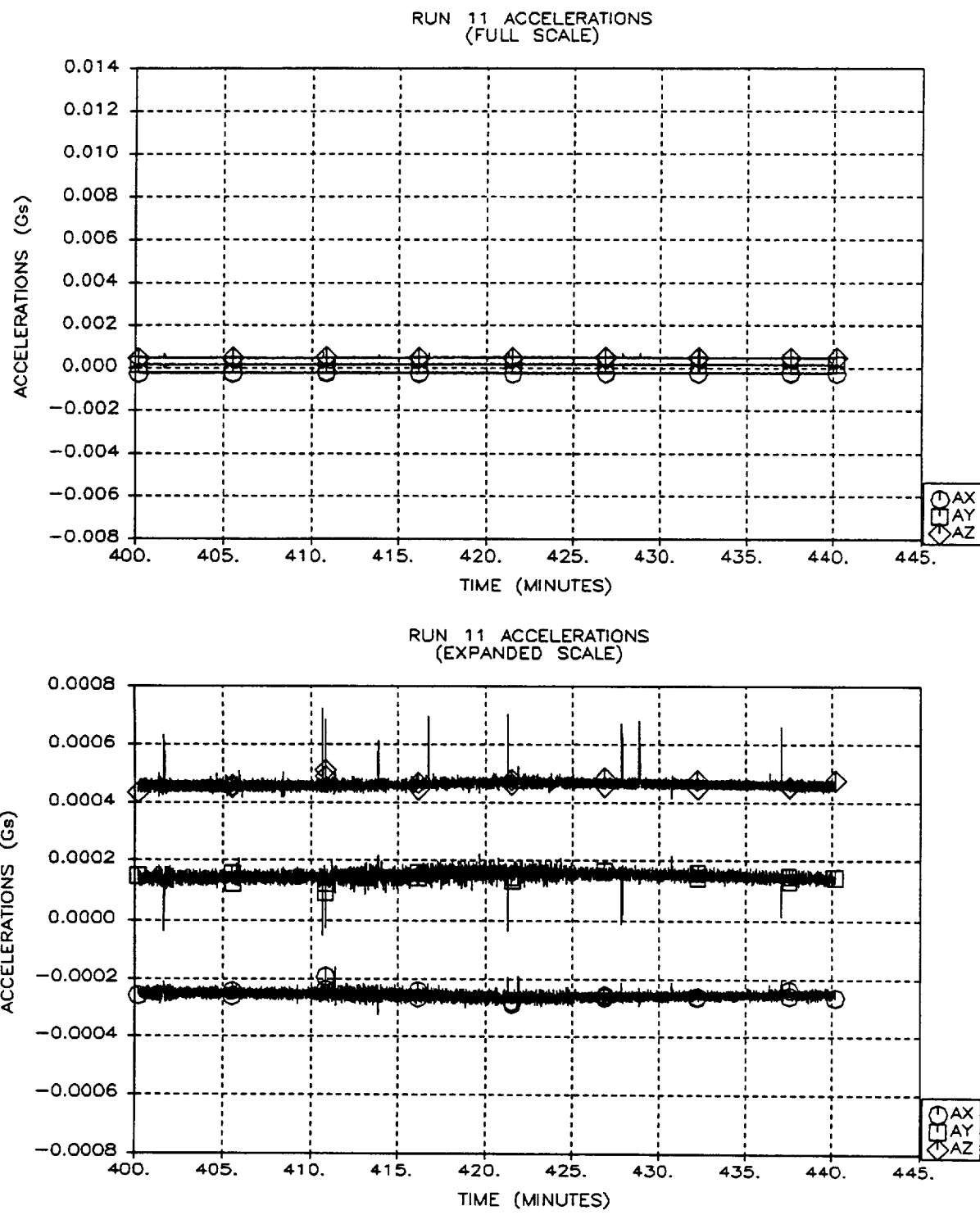


Figure A-11: Run 11 Accelerations
A-12

C-2

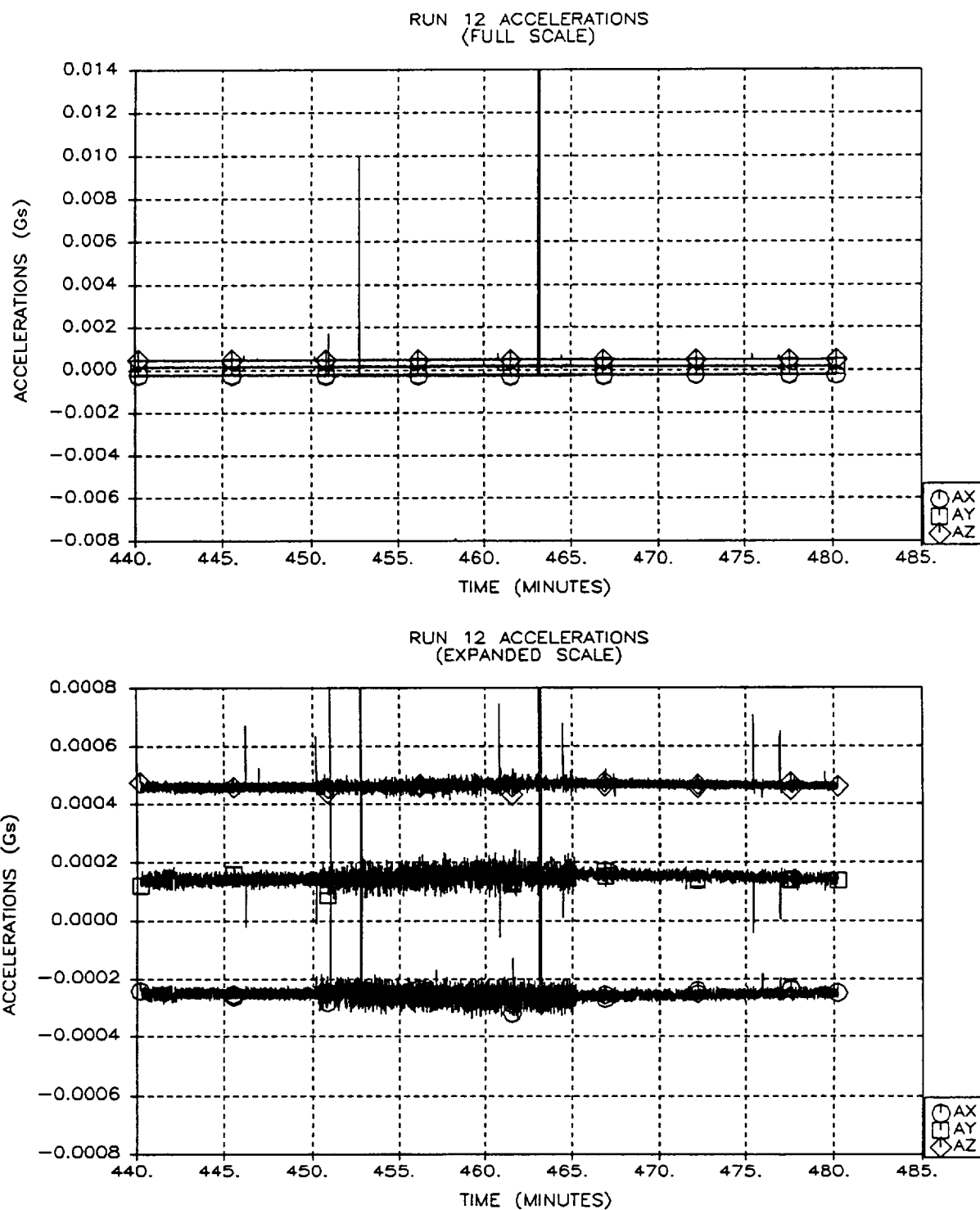


Figure A-12: Run 12 Accelerations
A-13

C-2

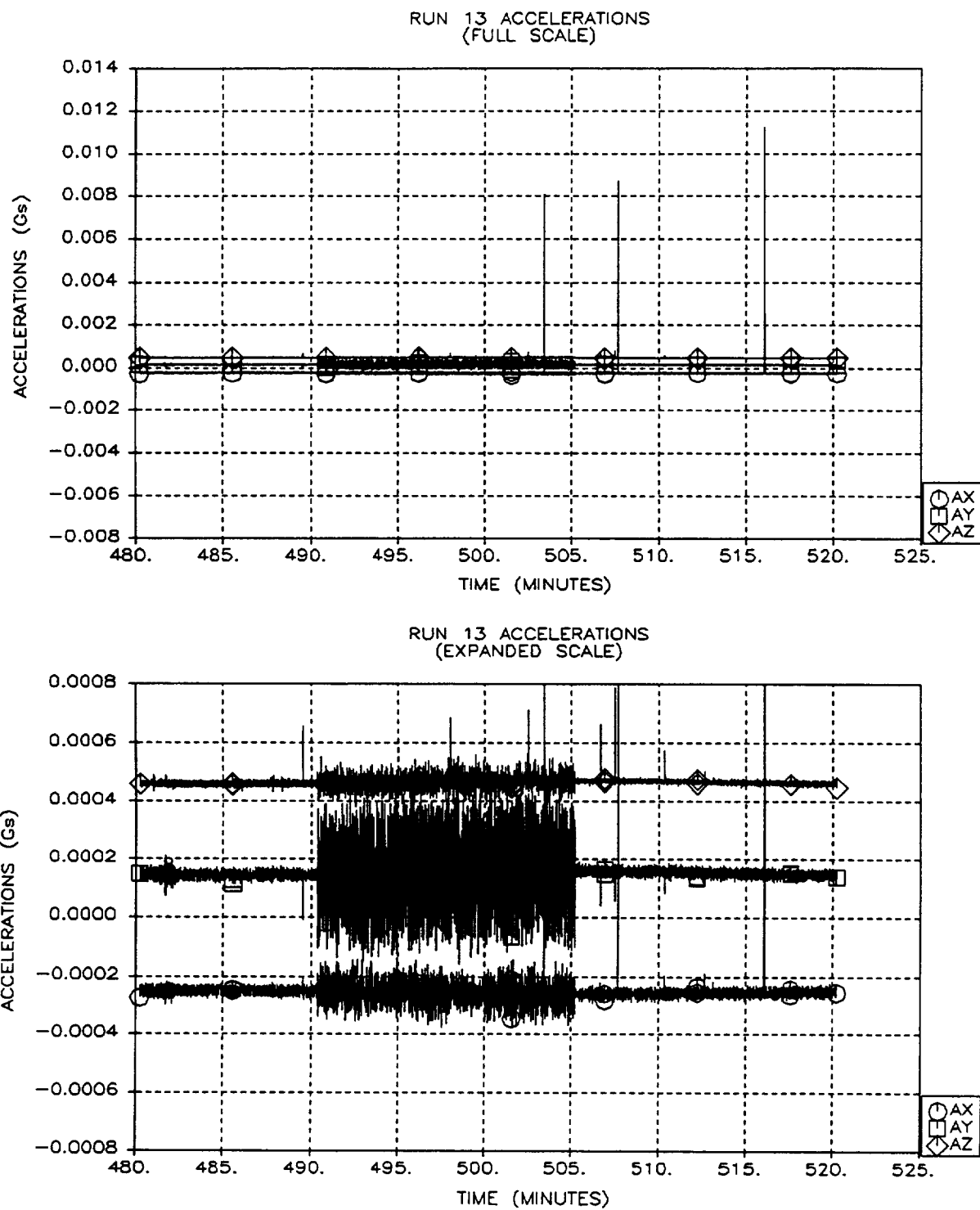


Figure A-13: Run 13 Accelerations
A-14

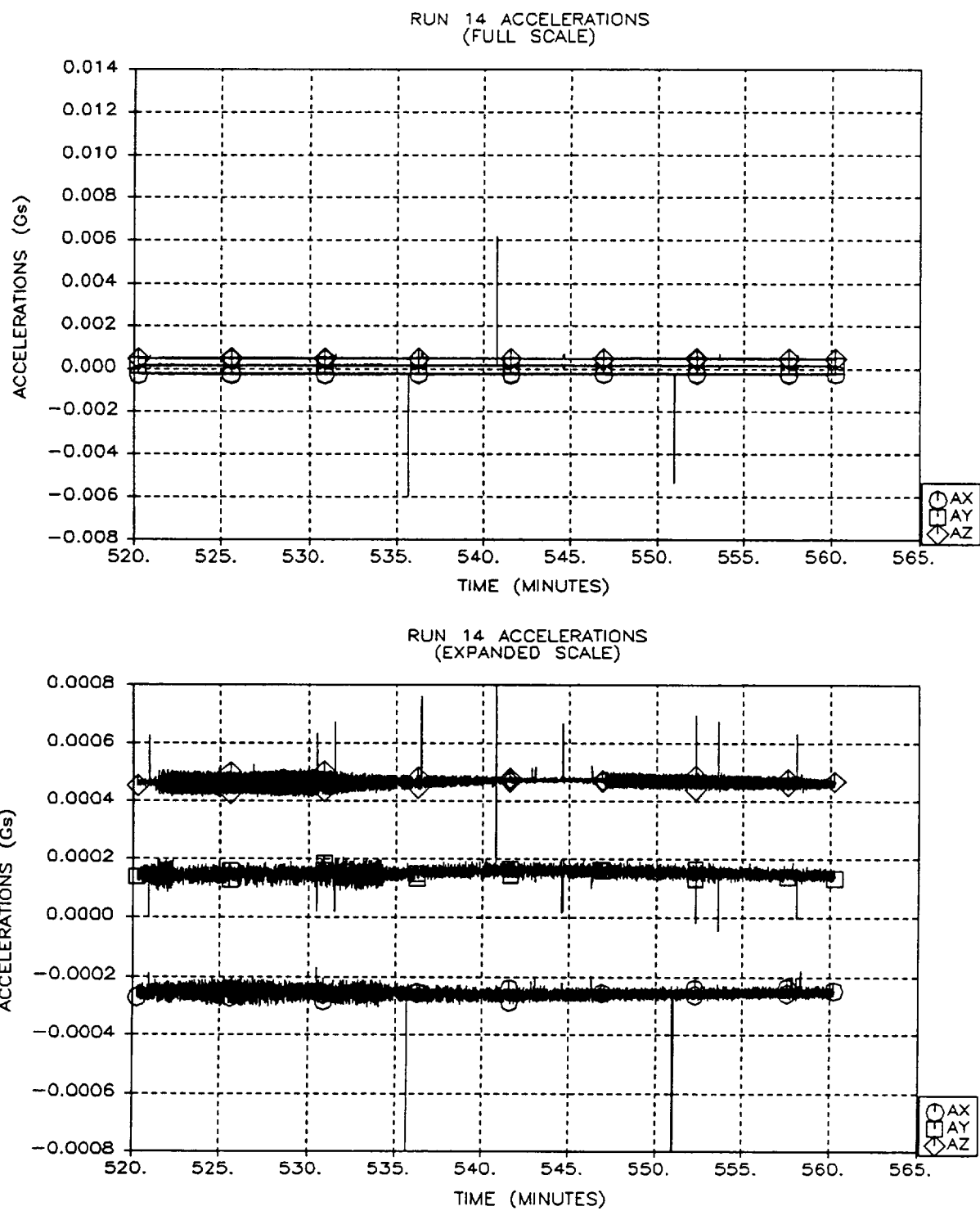


Figure A-14: Run 14 Accelerations
A-15

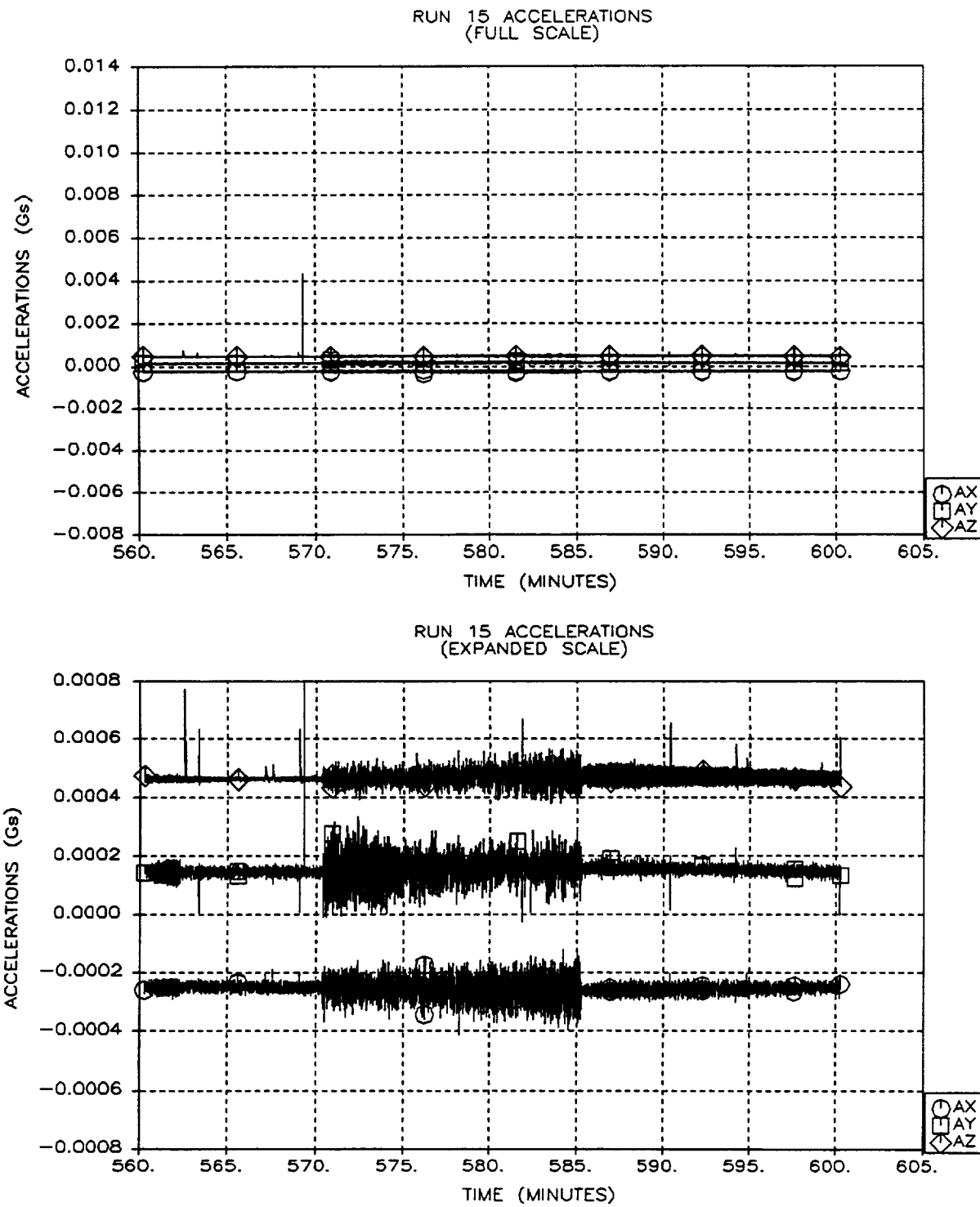


Figure A-15: Run 15 Accelerations
A-16

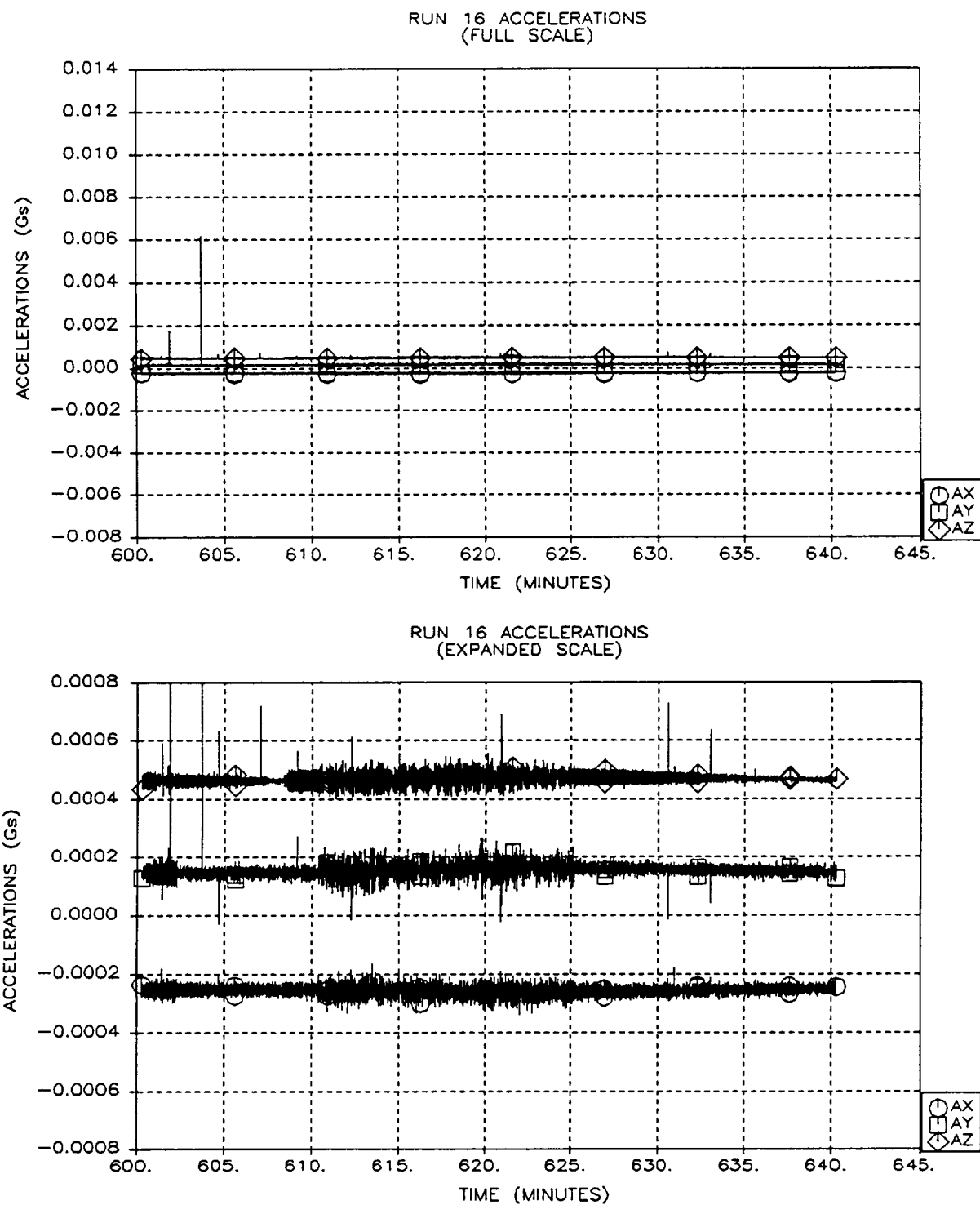


Figure A-16: Run 16 Accelerations
A-17

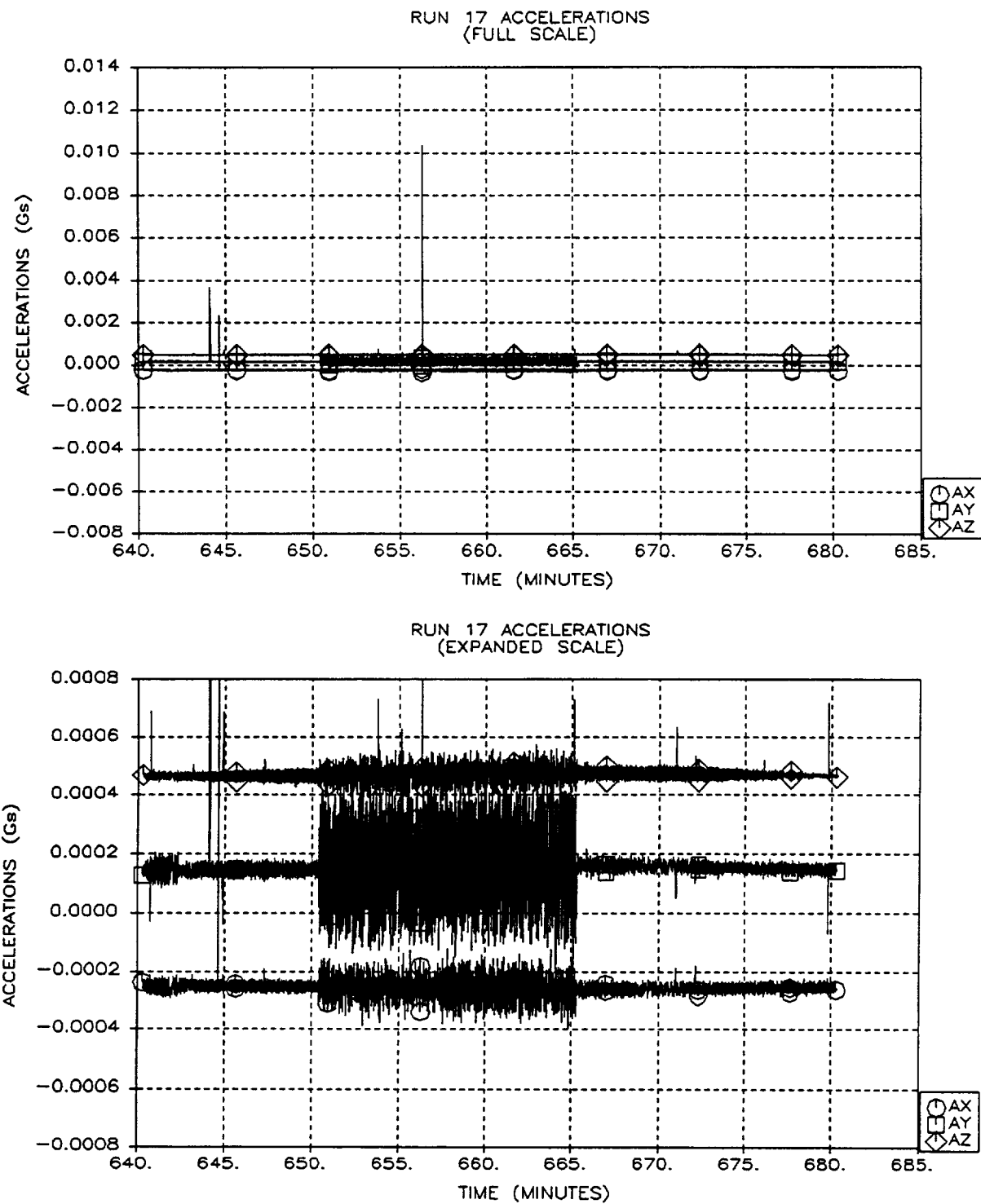


Figure A-17: Run 17 Accelerations
A-18

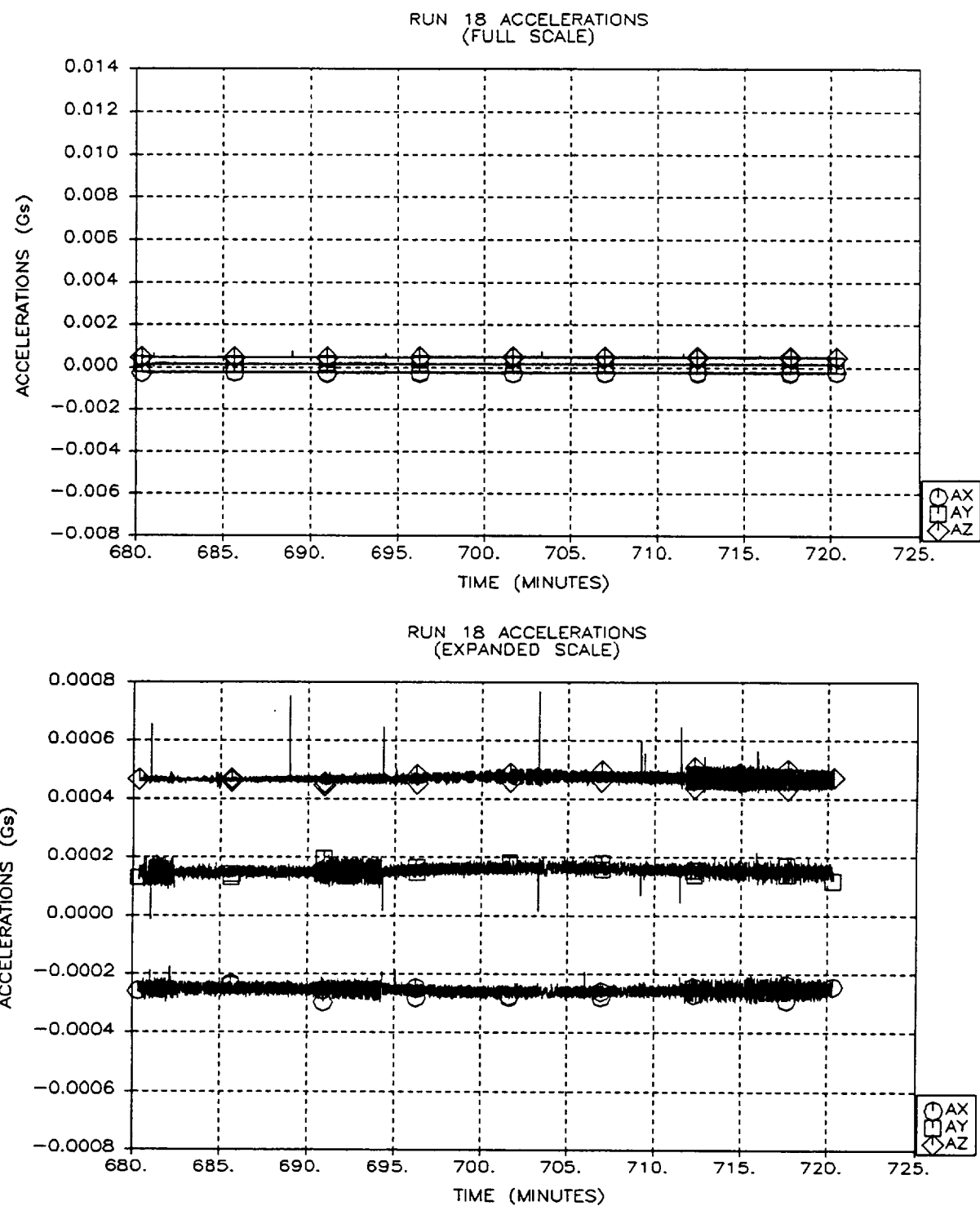


Figure A-18: Run 18 Accelerations
A-19

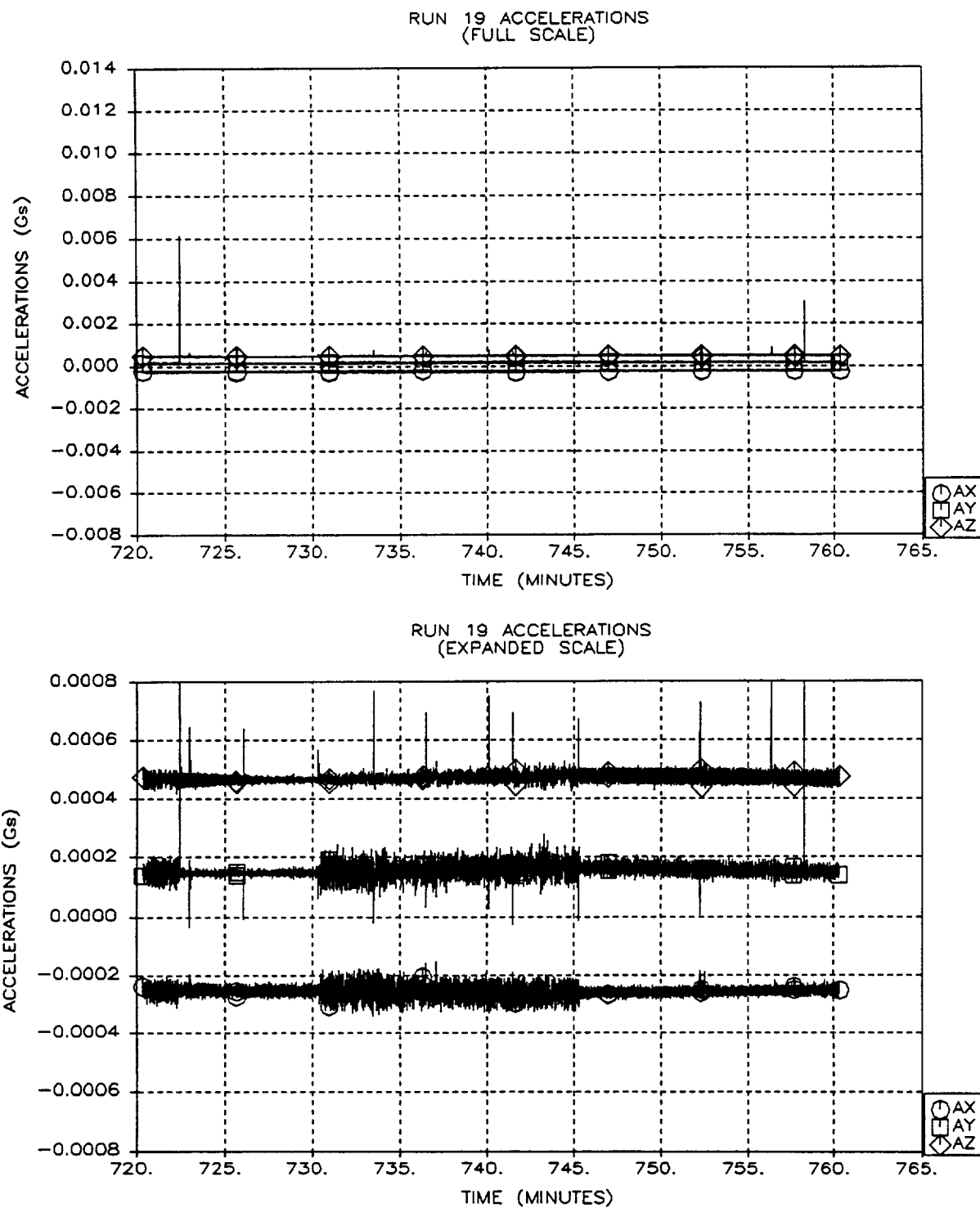


Figure A-19: Run 19 Accelerations
A-20

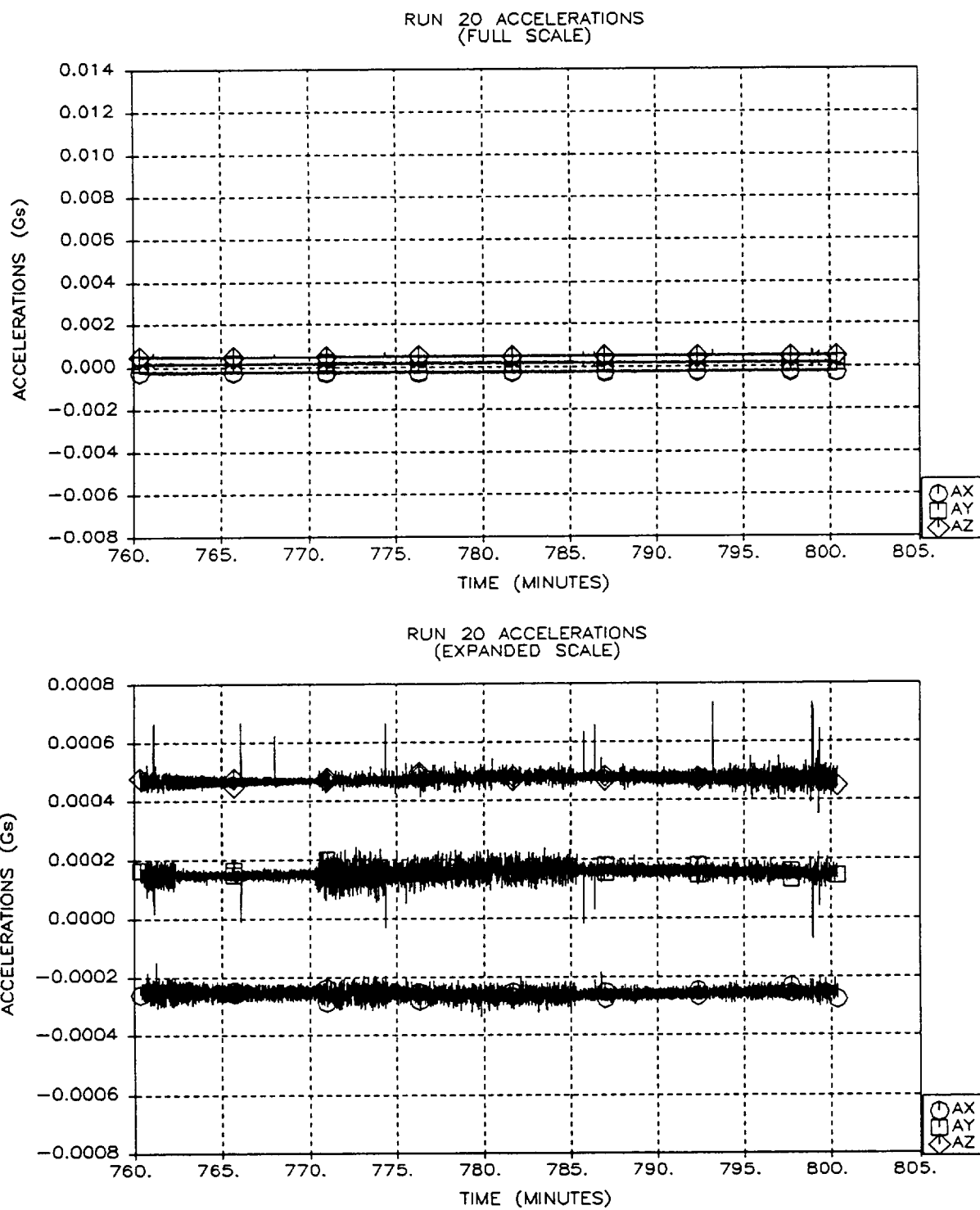


Figure A-20: Run 20 Accelerations
A-21

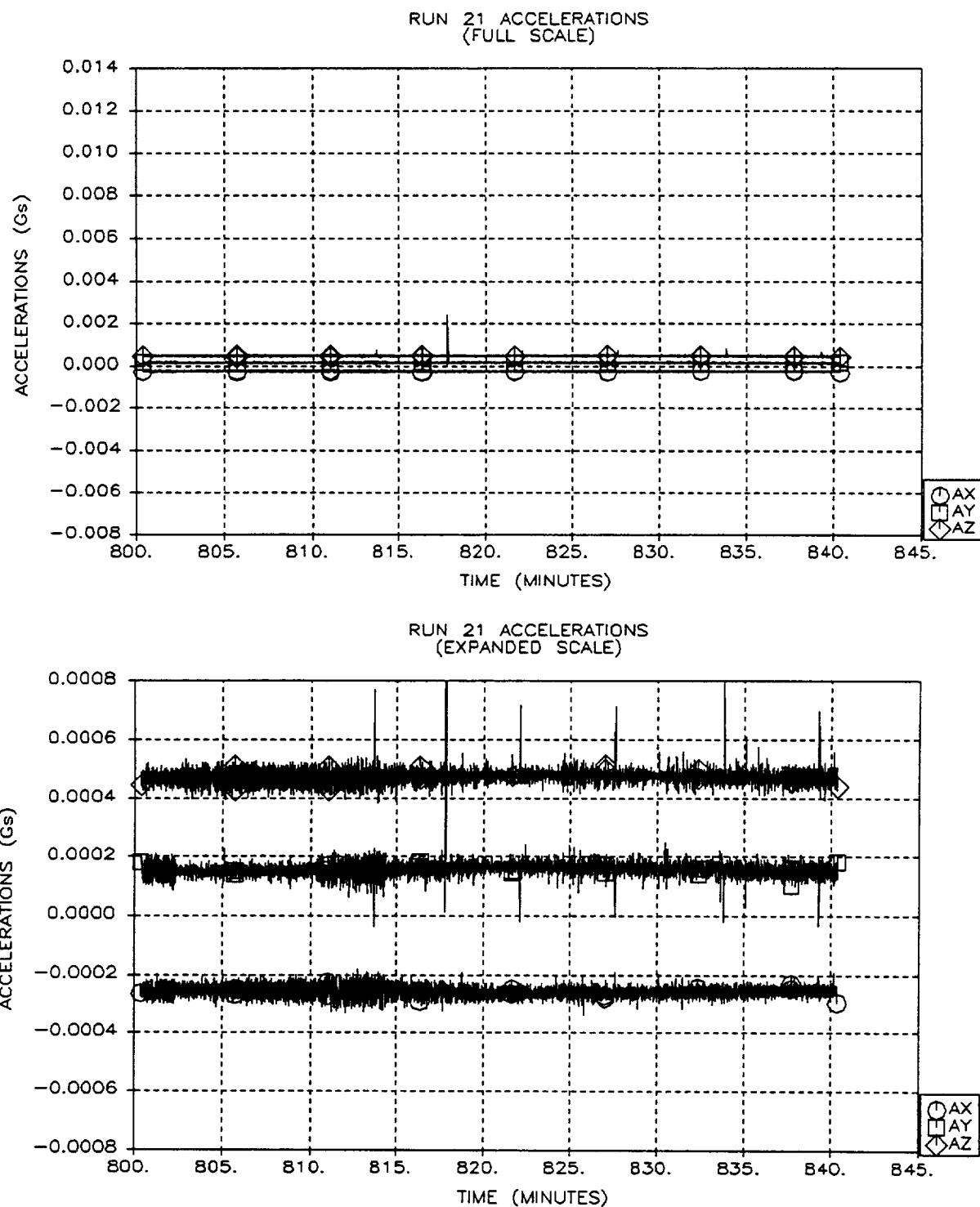


Figure A-21: Run 21 Accelerations
A-22

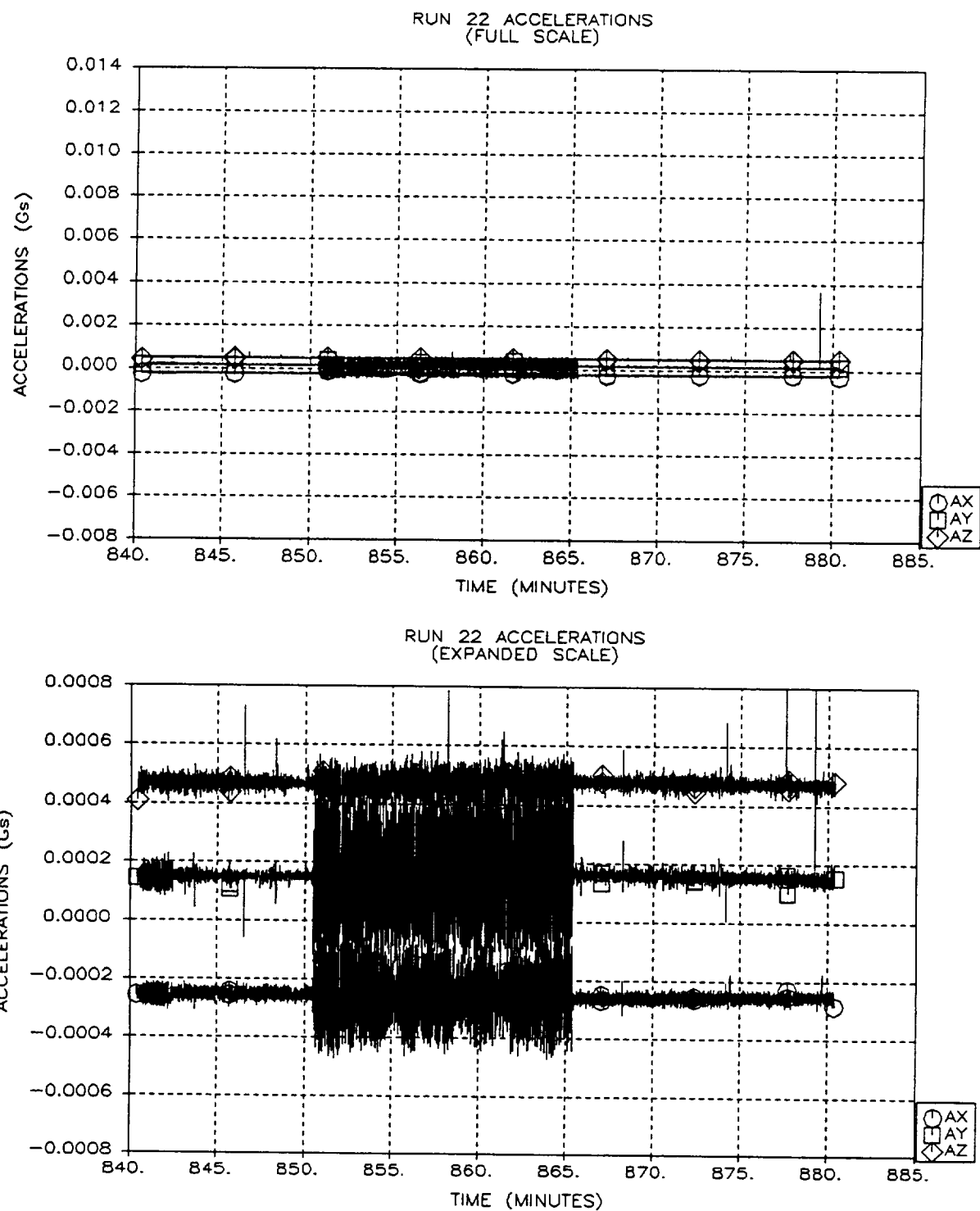


Figure A-22: Run 22 Accelerations
A-23

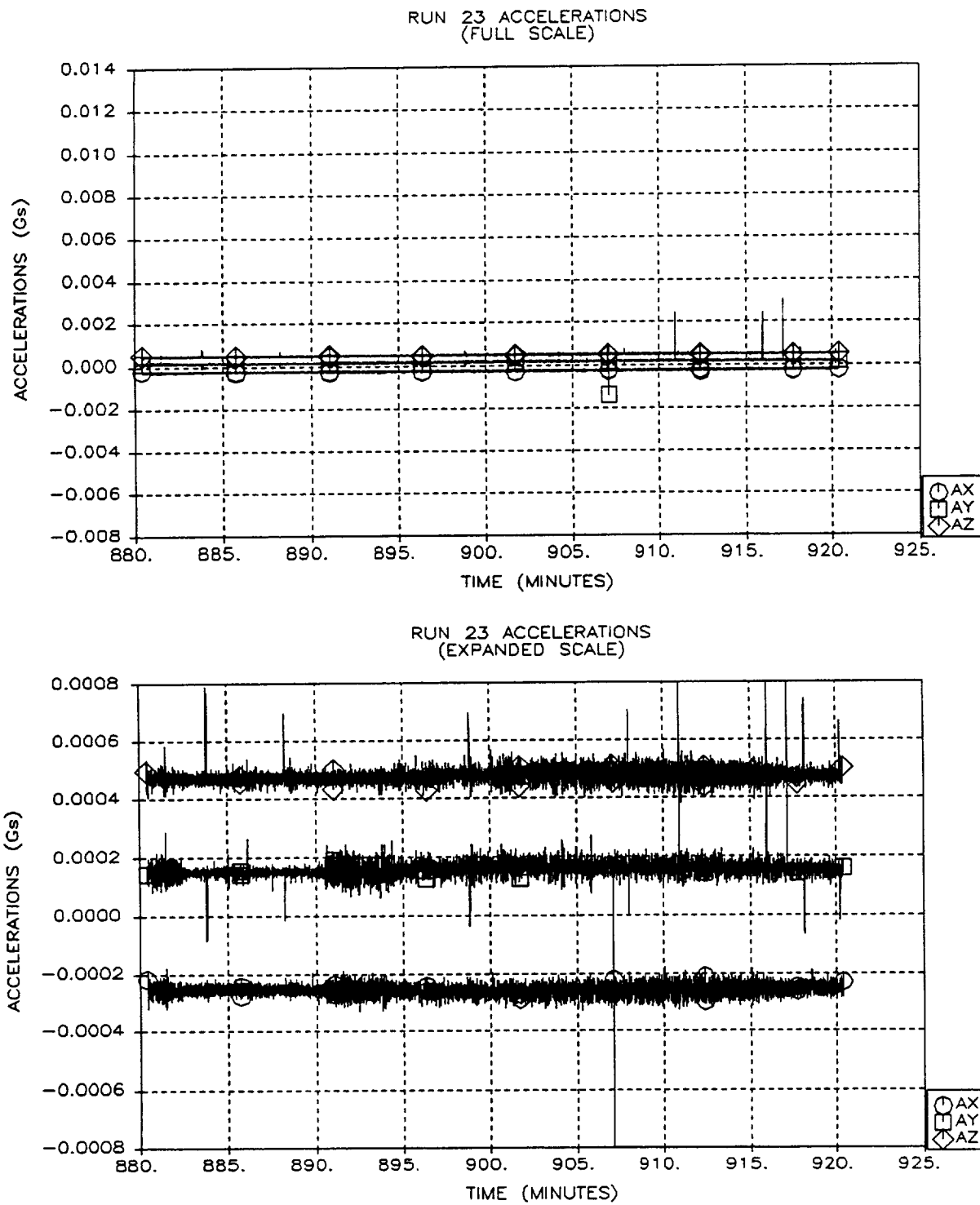


Figure A-23: Run 23 Accelerations
A-24

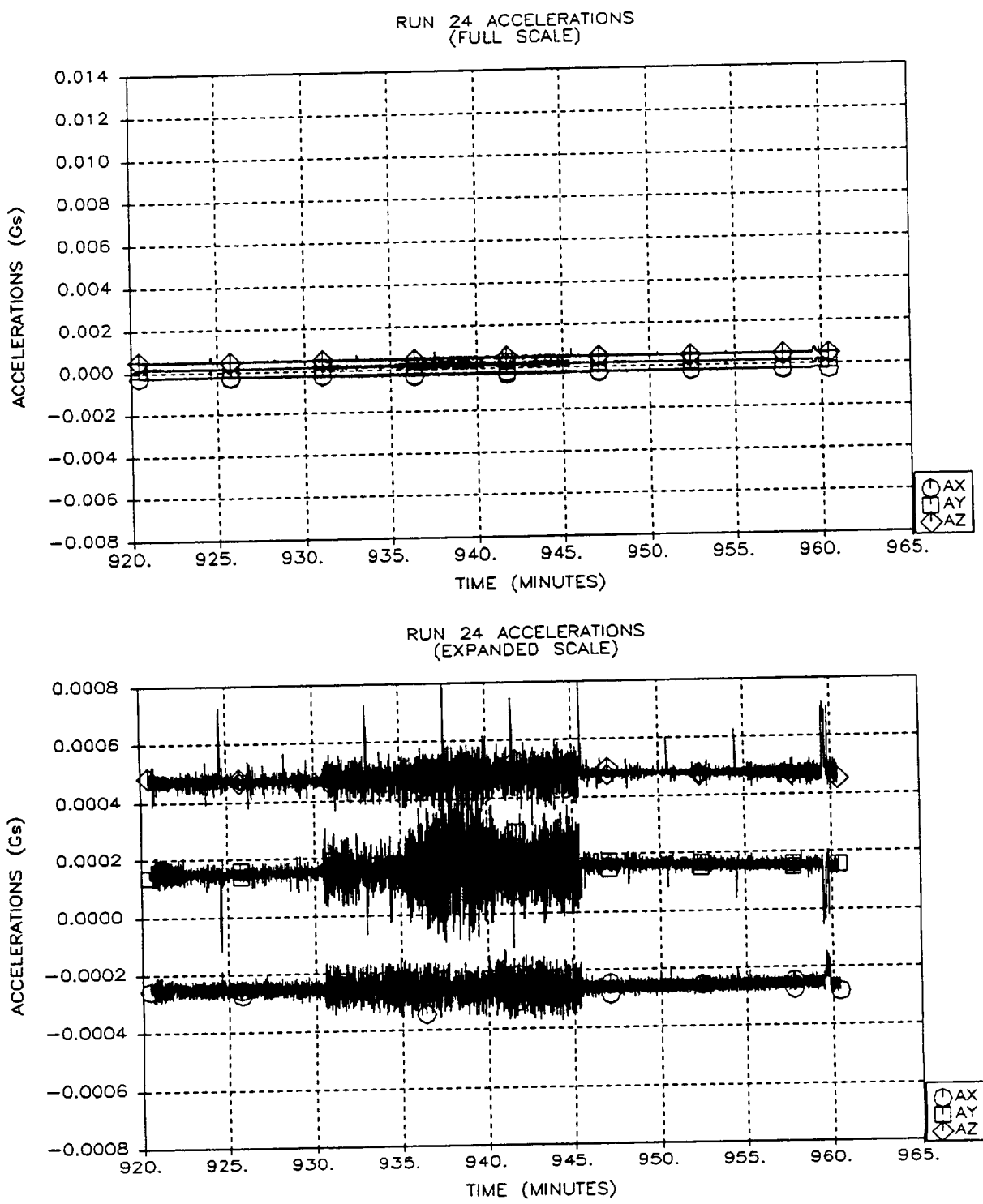


Figure A-24: Run 24 Accelerations
A-25

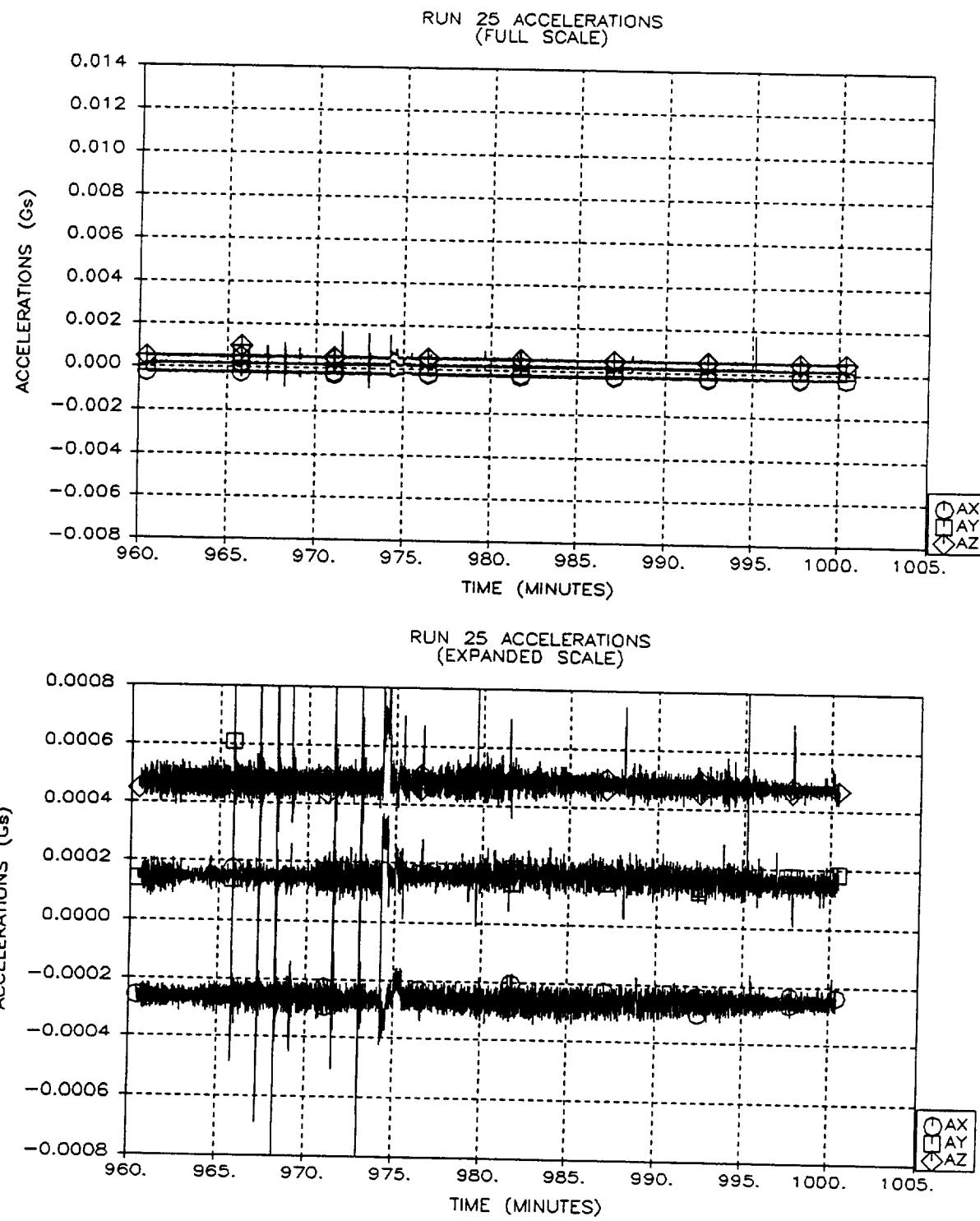


Figure A-25: Run 25 Accelerations
A-26

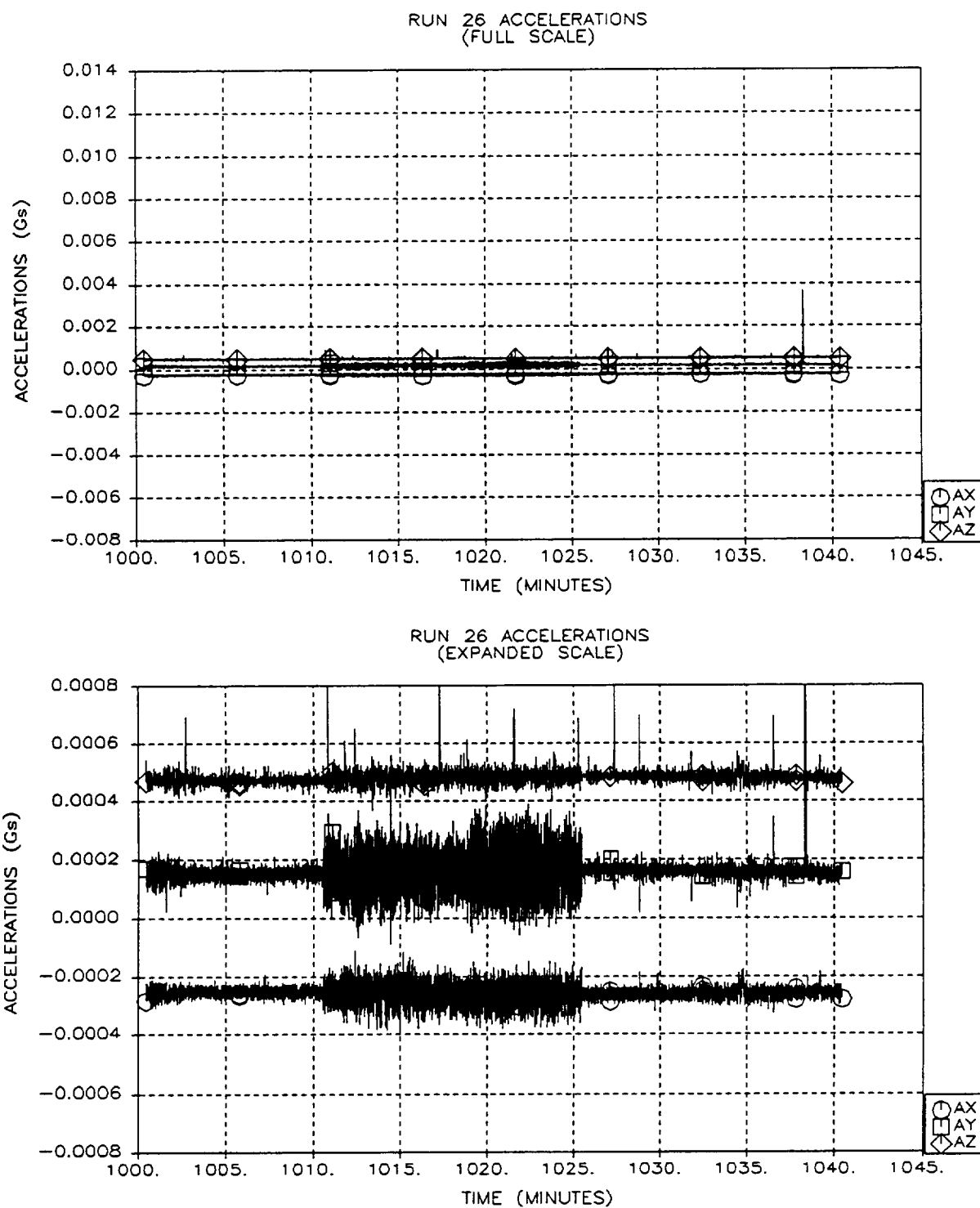


Figure A-26: Run 26 Accelerations
A-27

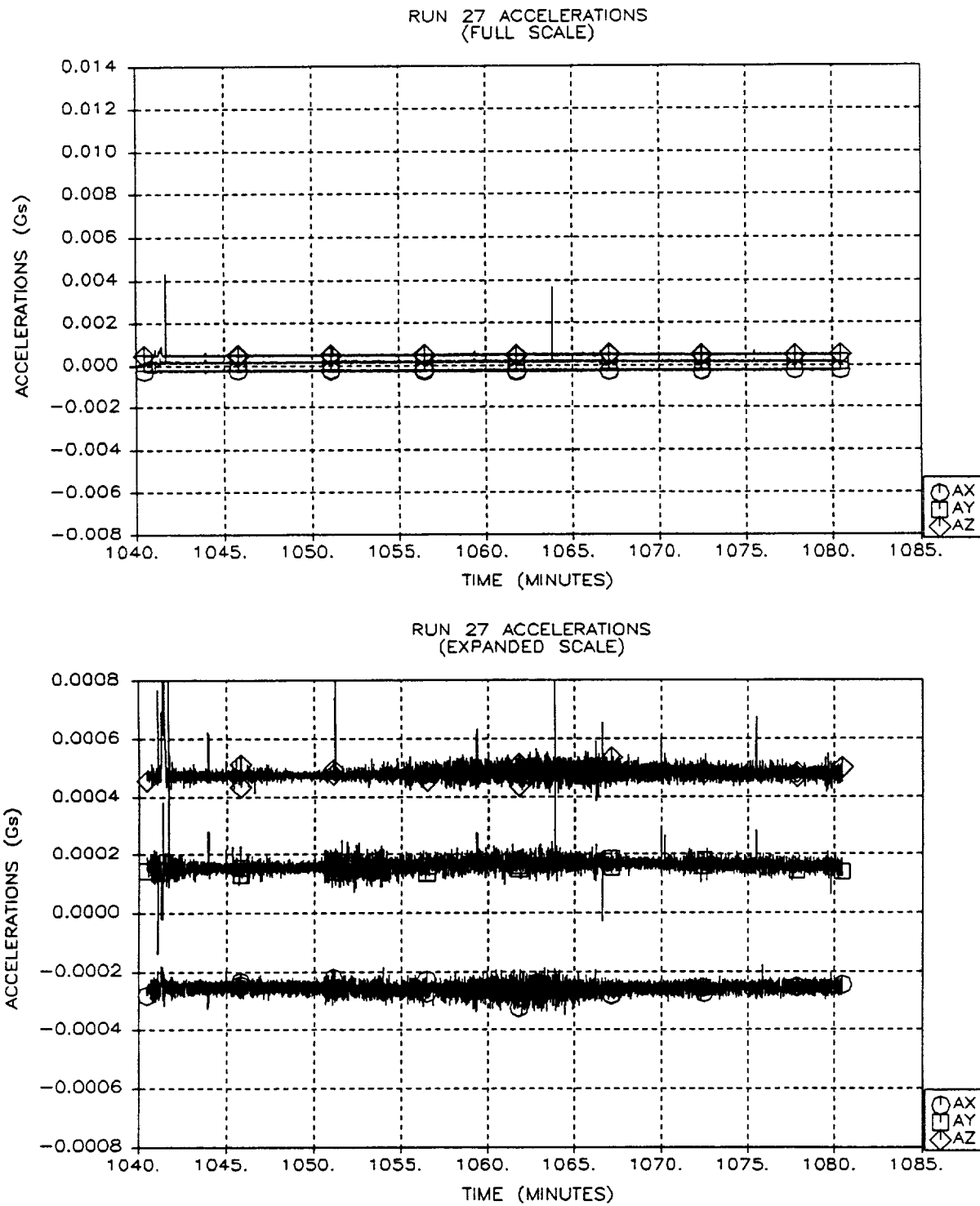


Figure A-27: Run 27 Accelerations
A-28

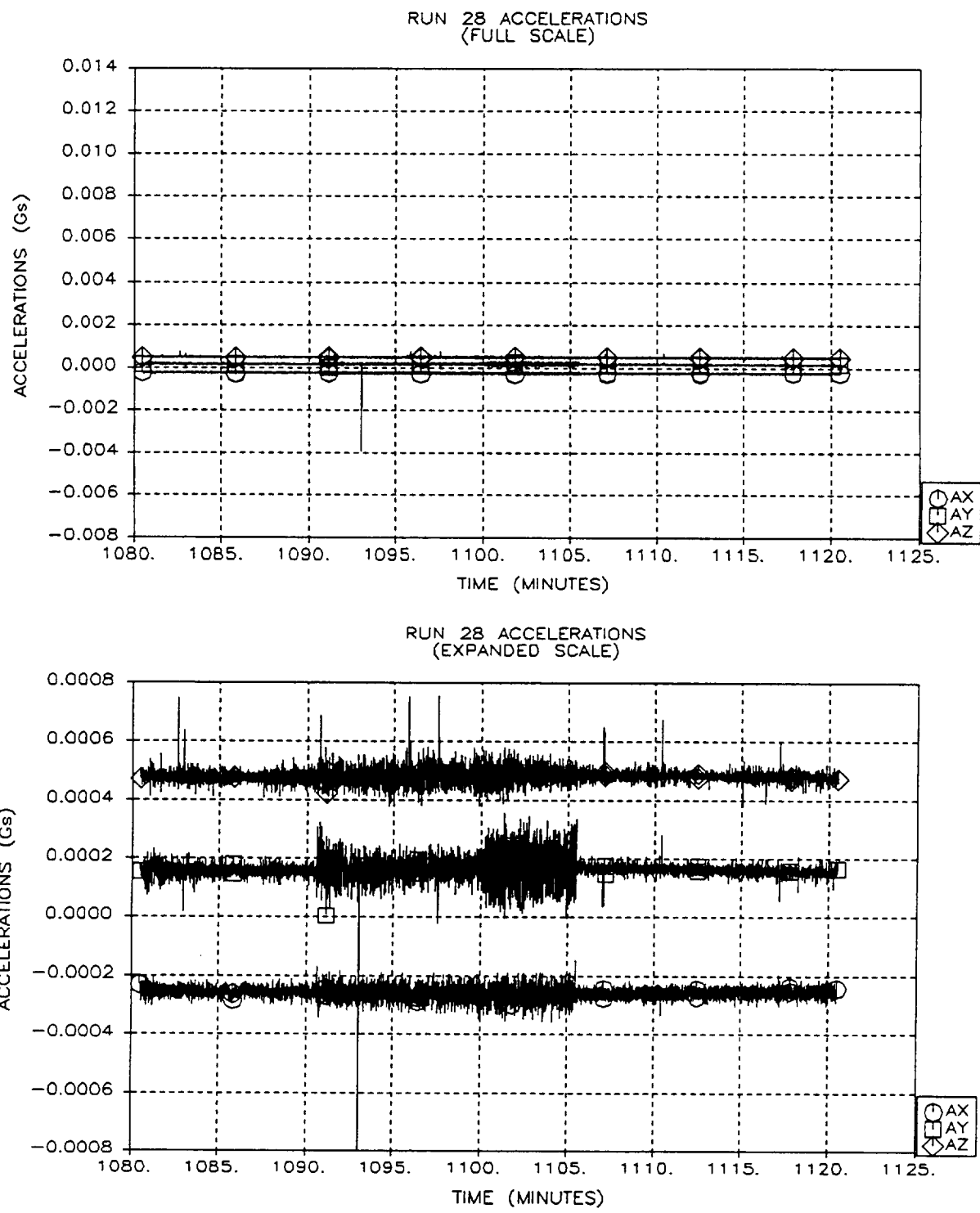


Figure A-28: Run 28 Accelerations
A-29

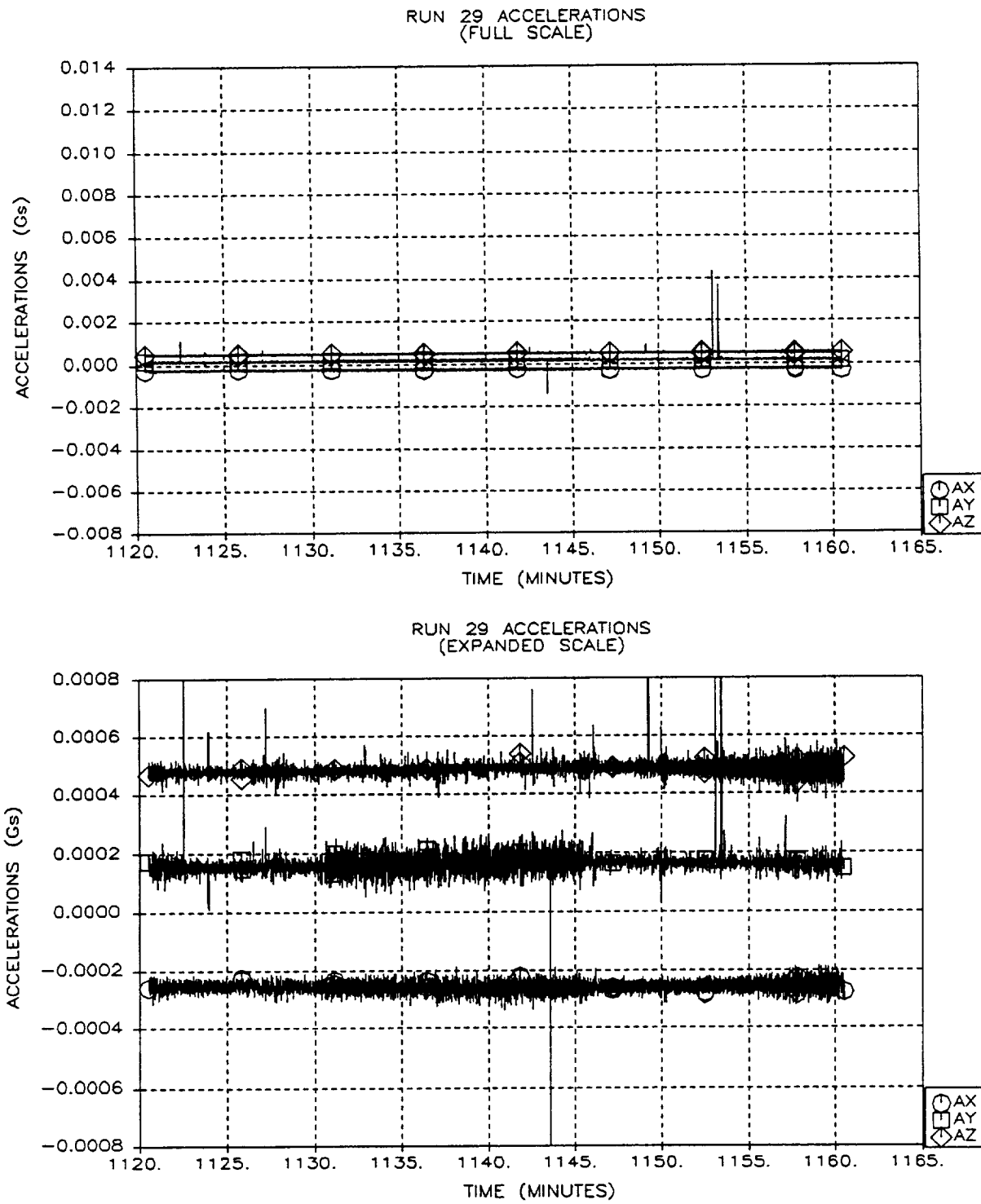


Figure A-29: Run 29 Accelerations
A-30

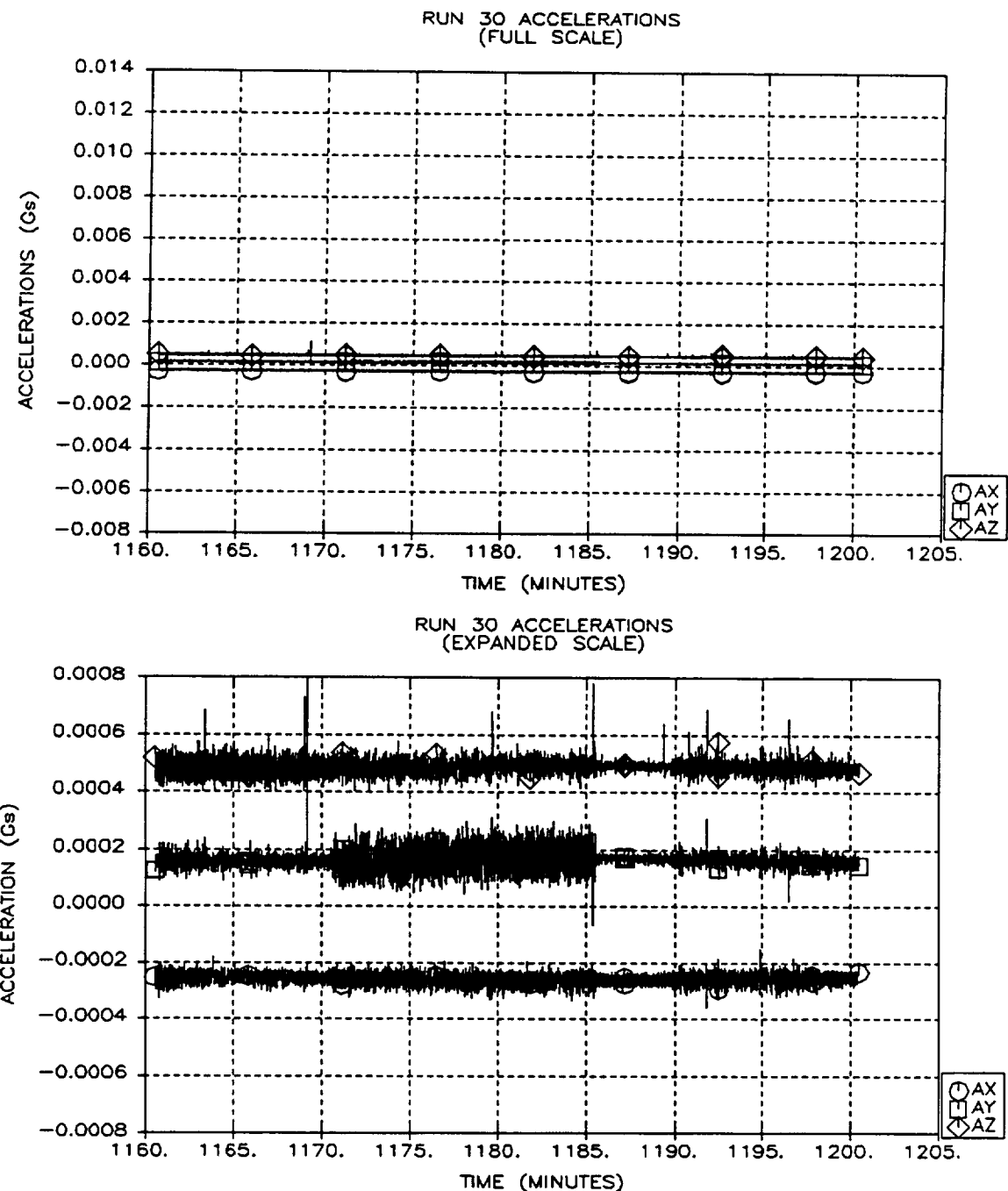


Figure A-30: Run 30 Accelerations
A-31

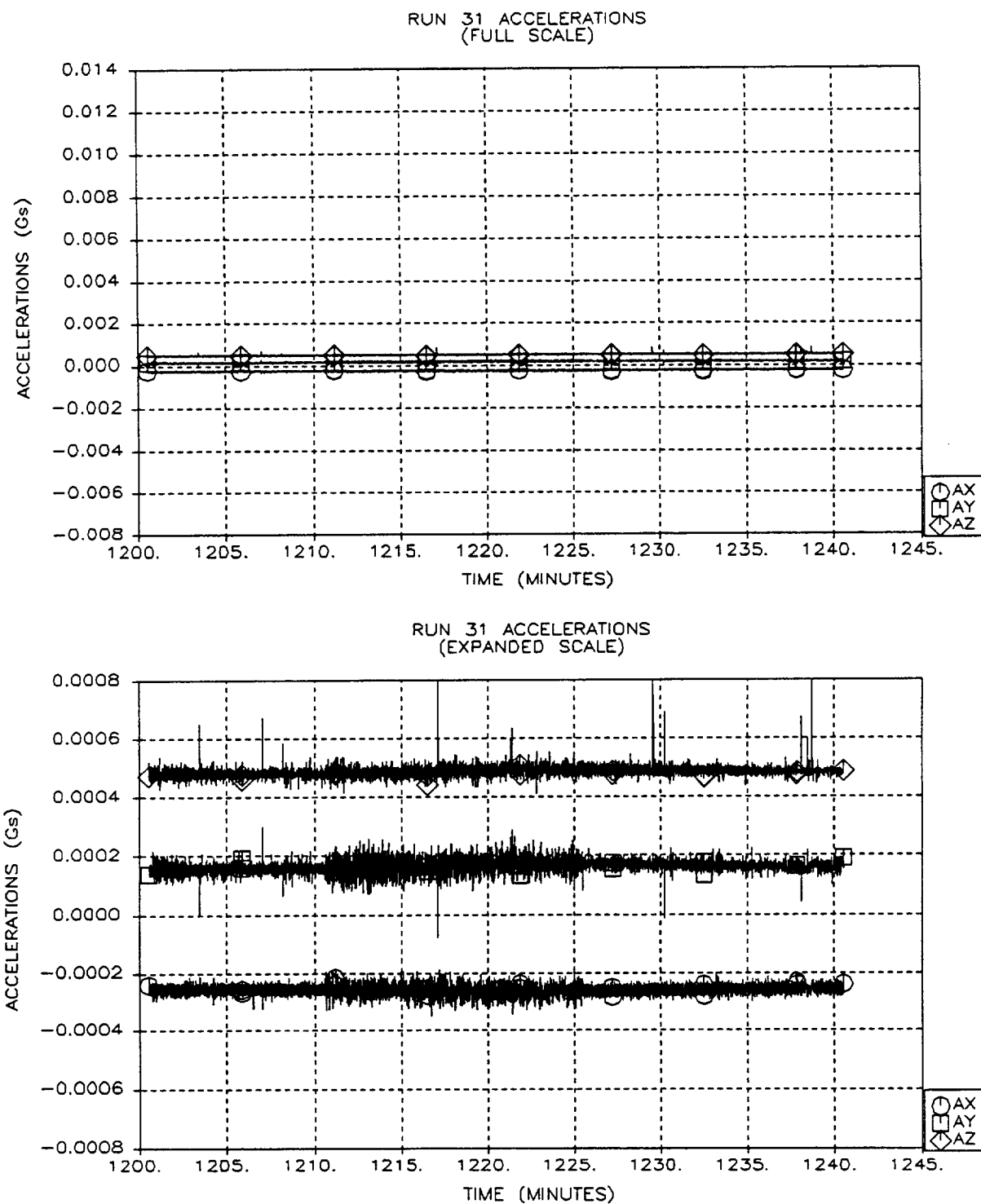


Figure A-31: Run 31 Accelerations
A-32

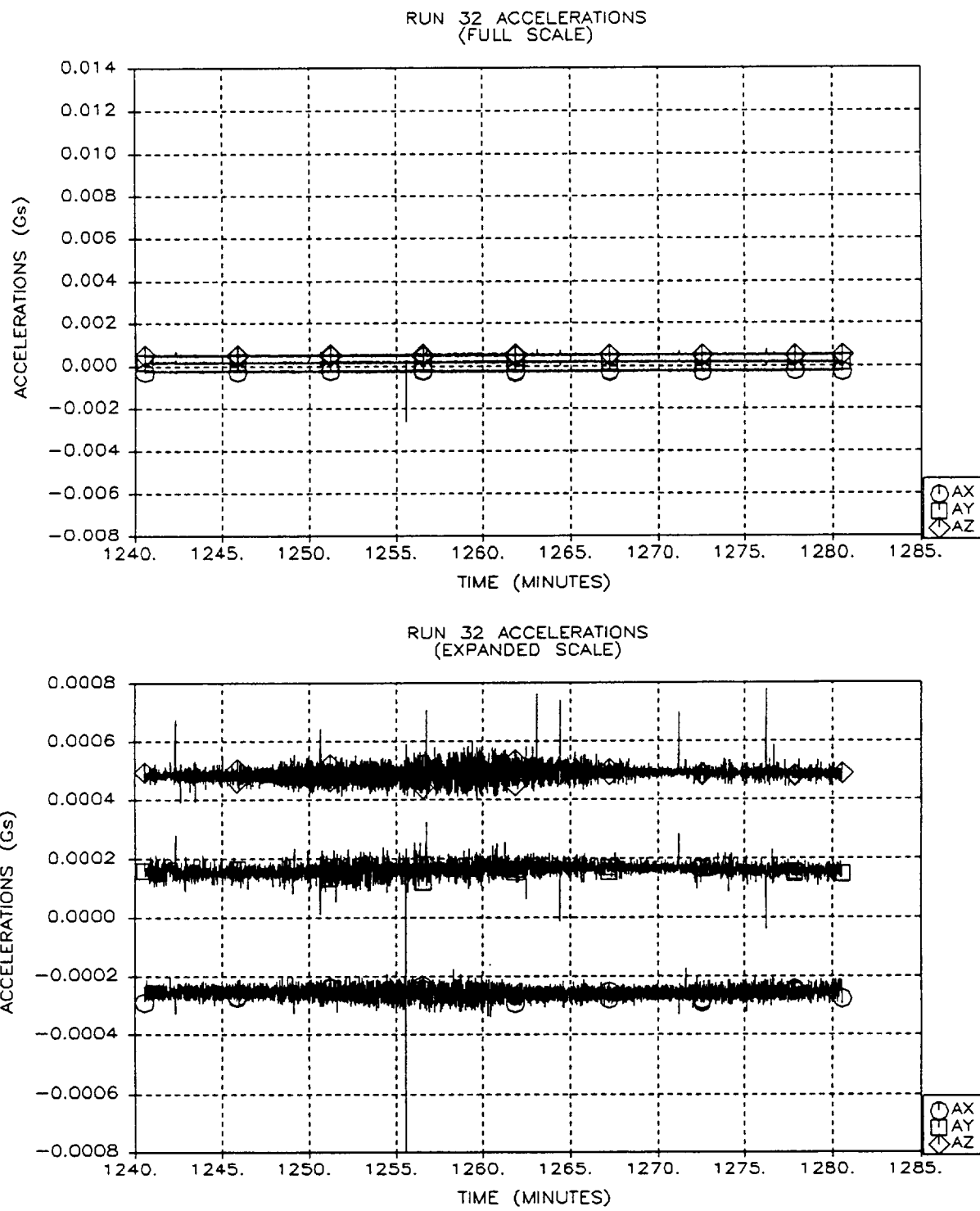


Figure A-32: Run 32 Accelerations
A-33

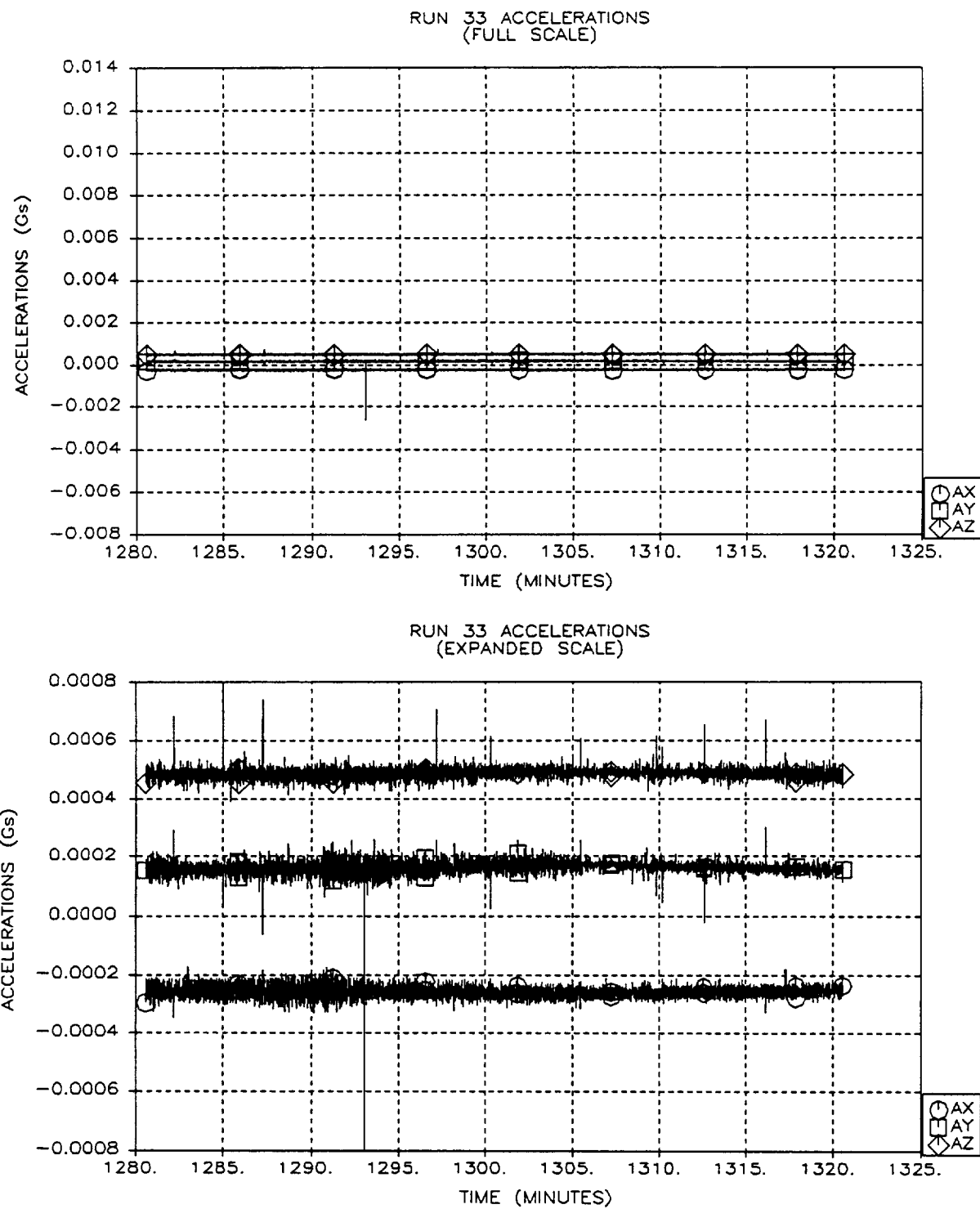


Figure A-33: Run 33 Accelerations
A-34

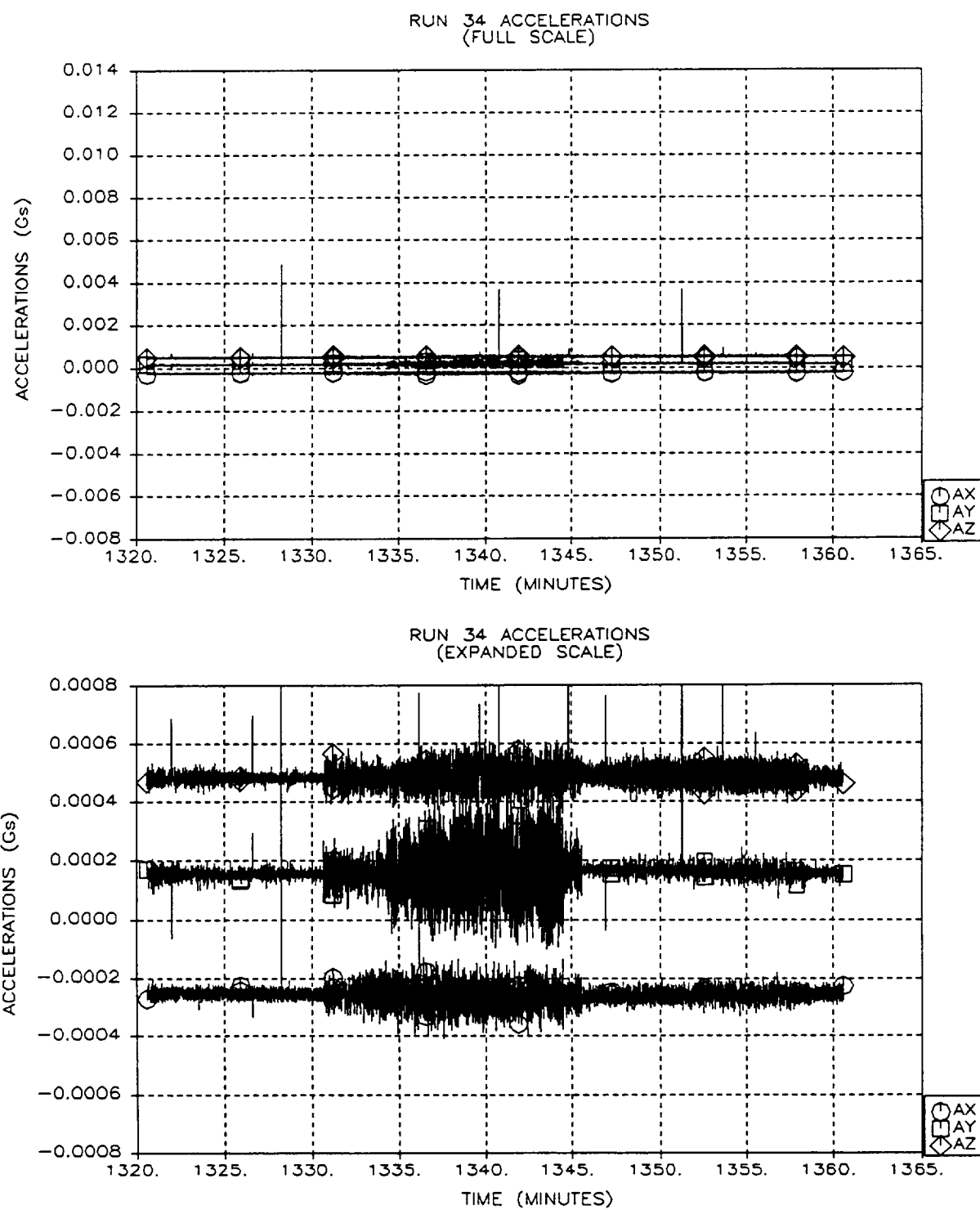


Figure A-34: Run 34 Accelerations
A-35

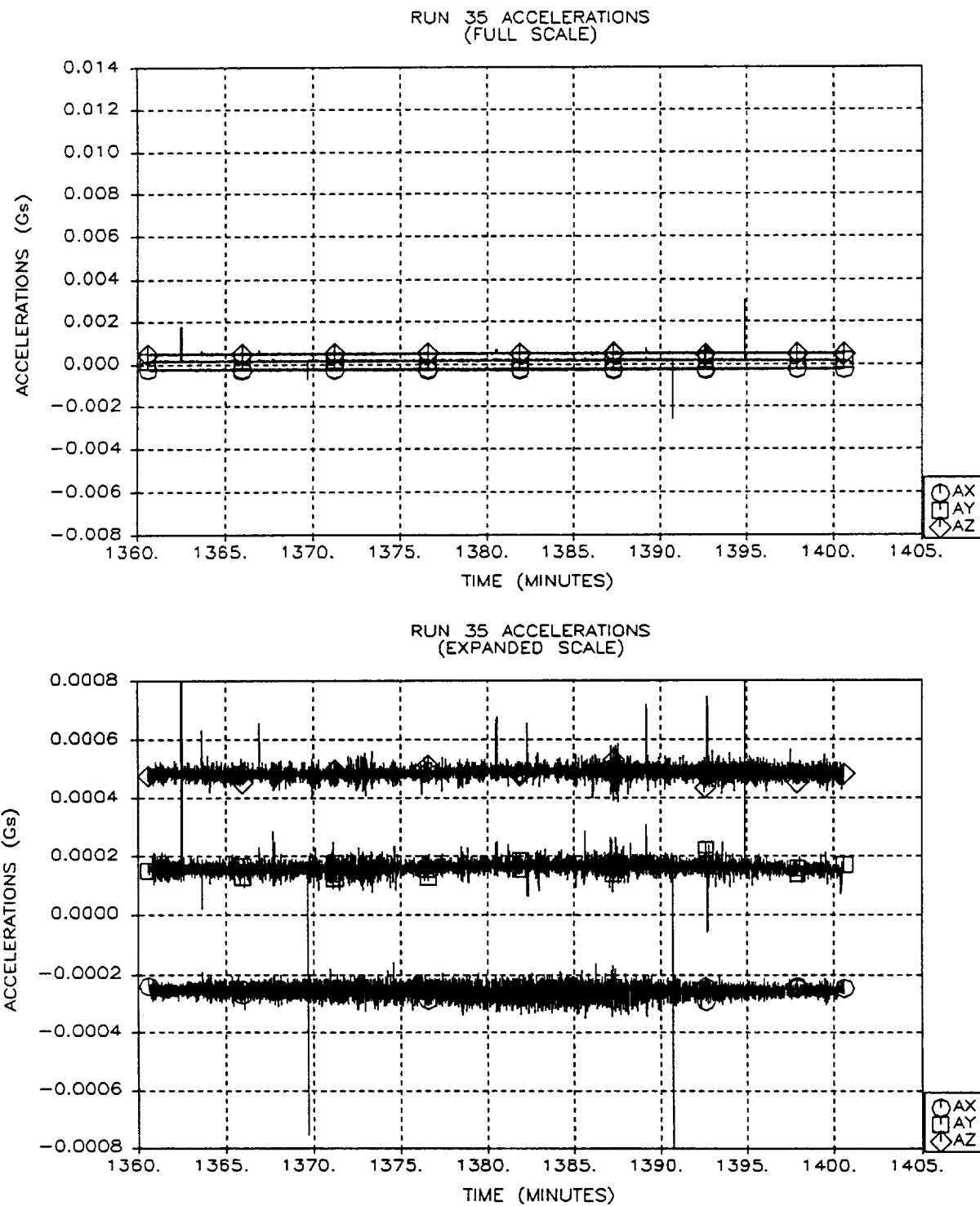


Figure A-35: Run 35 Accelerations
A-36

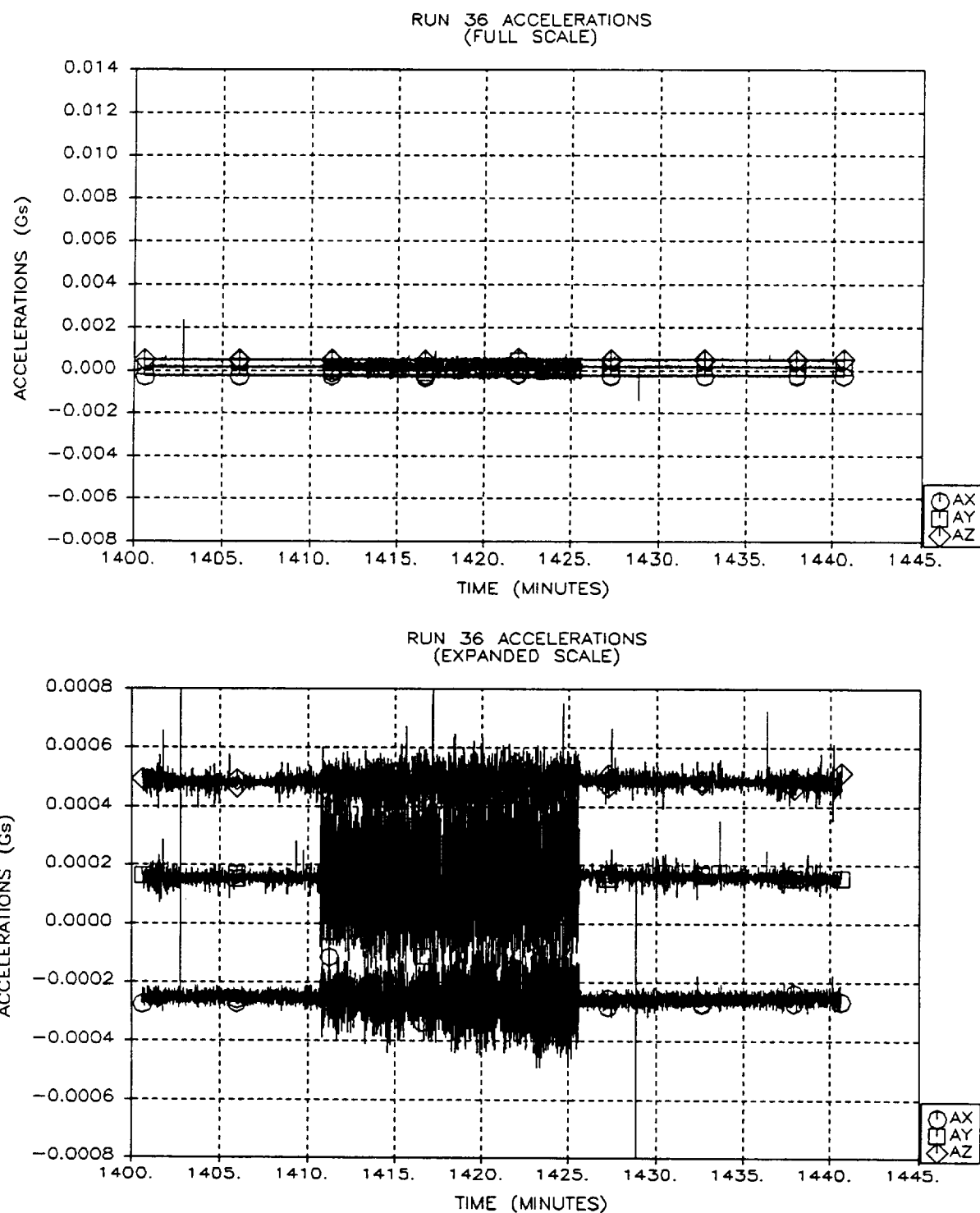


Figure A-36: Run 36 Accelerations
A-37

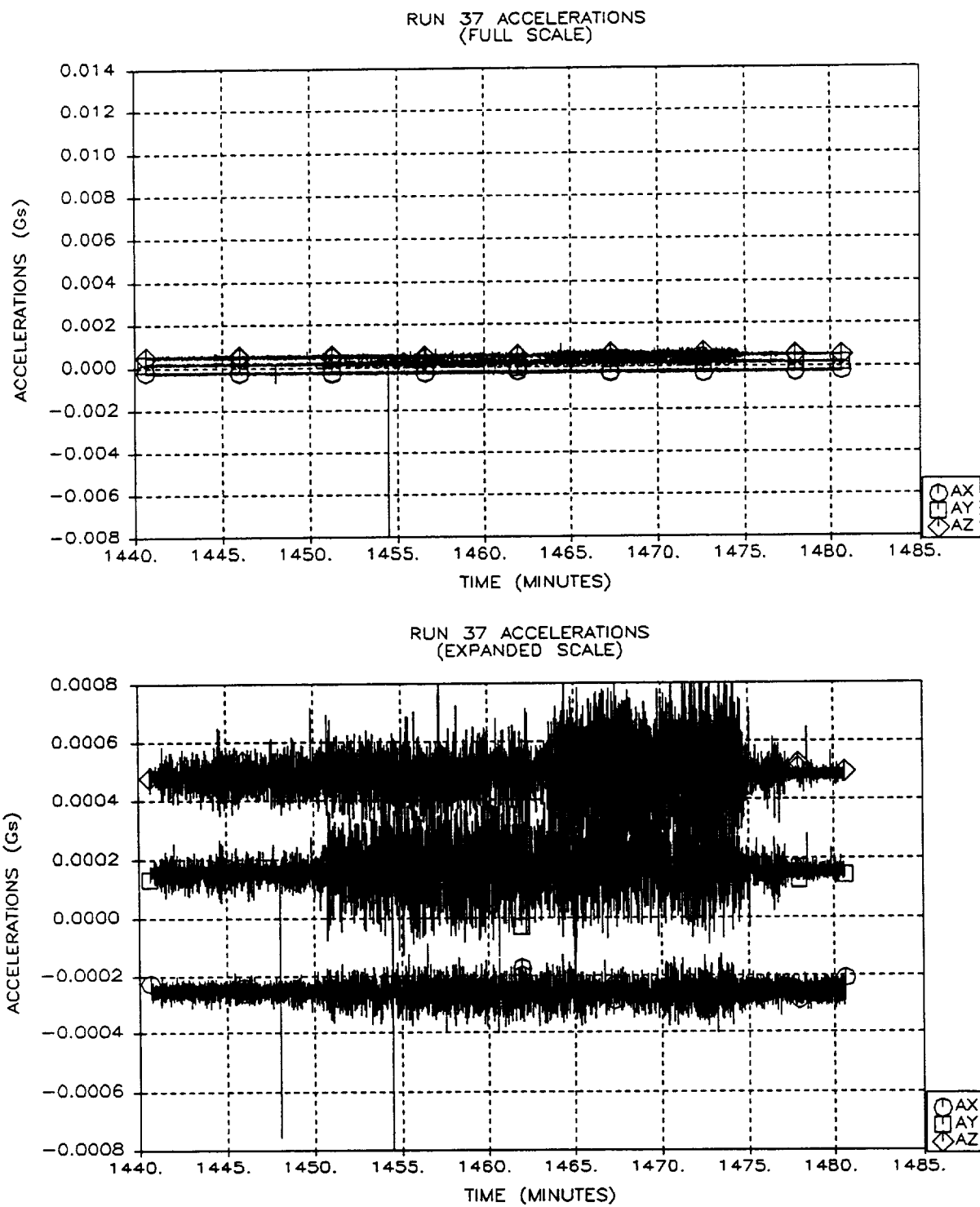


Figure A-37: Run 37 Accelerations
A-38

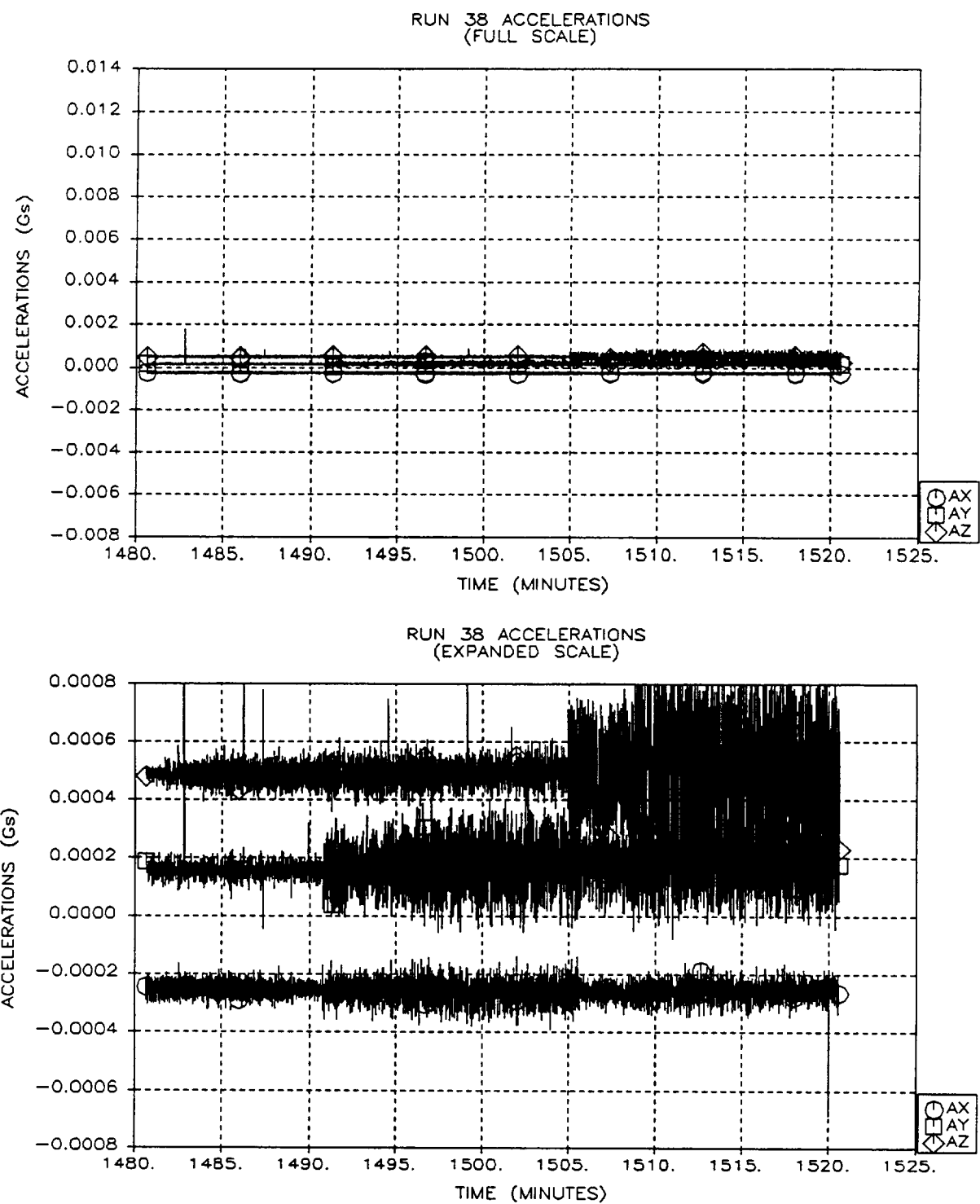


Figure A-38: Run 38 Accelerations
A-39

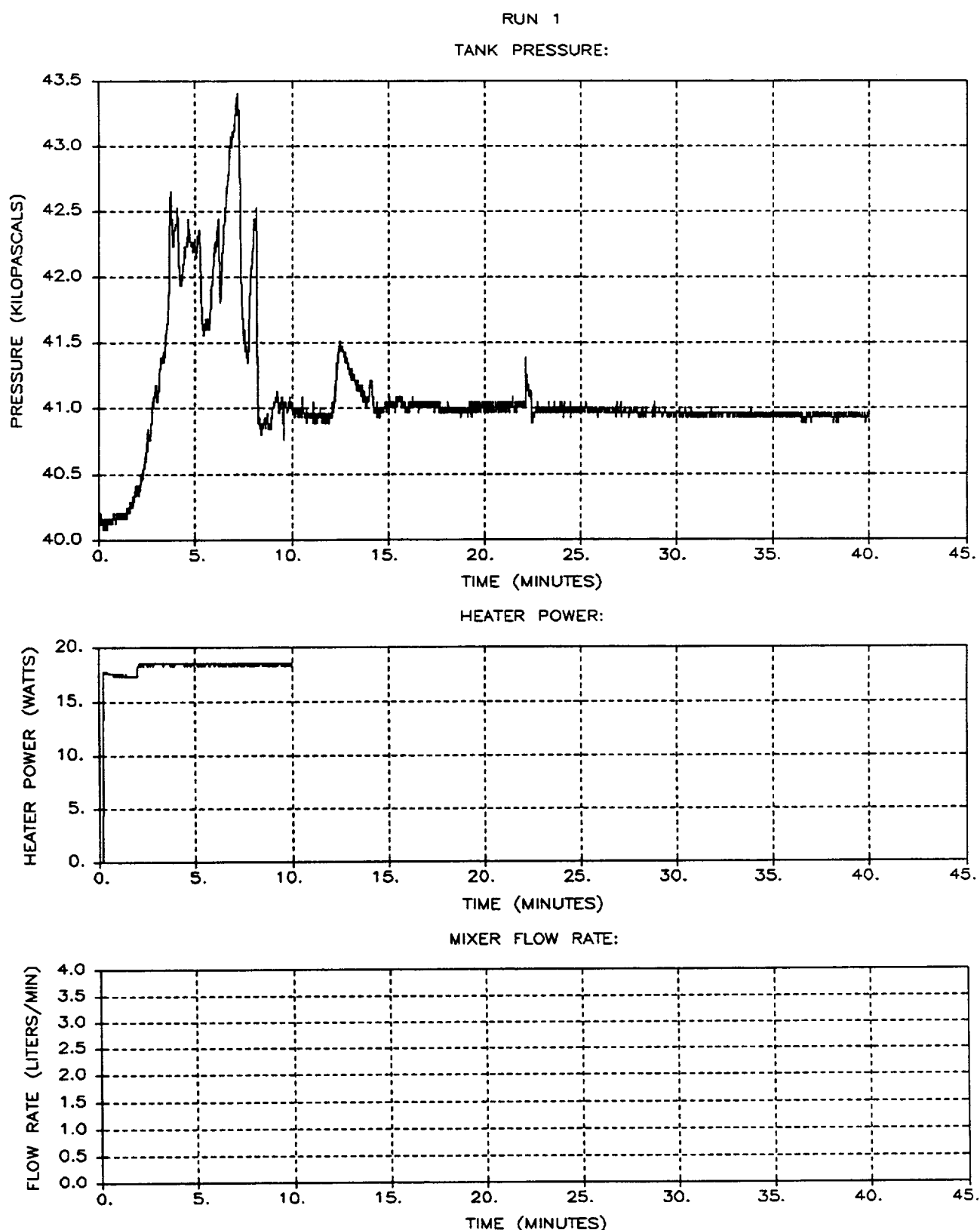


Figure A-39: Run 1 Pressure, Heater Power, and Flow Rate
A-40

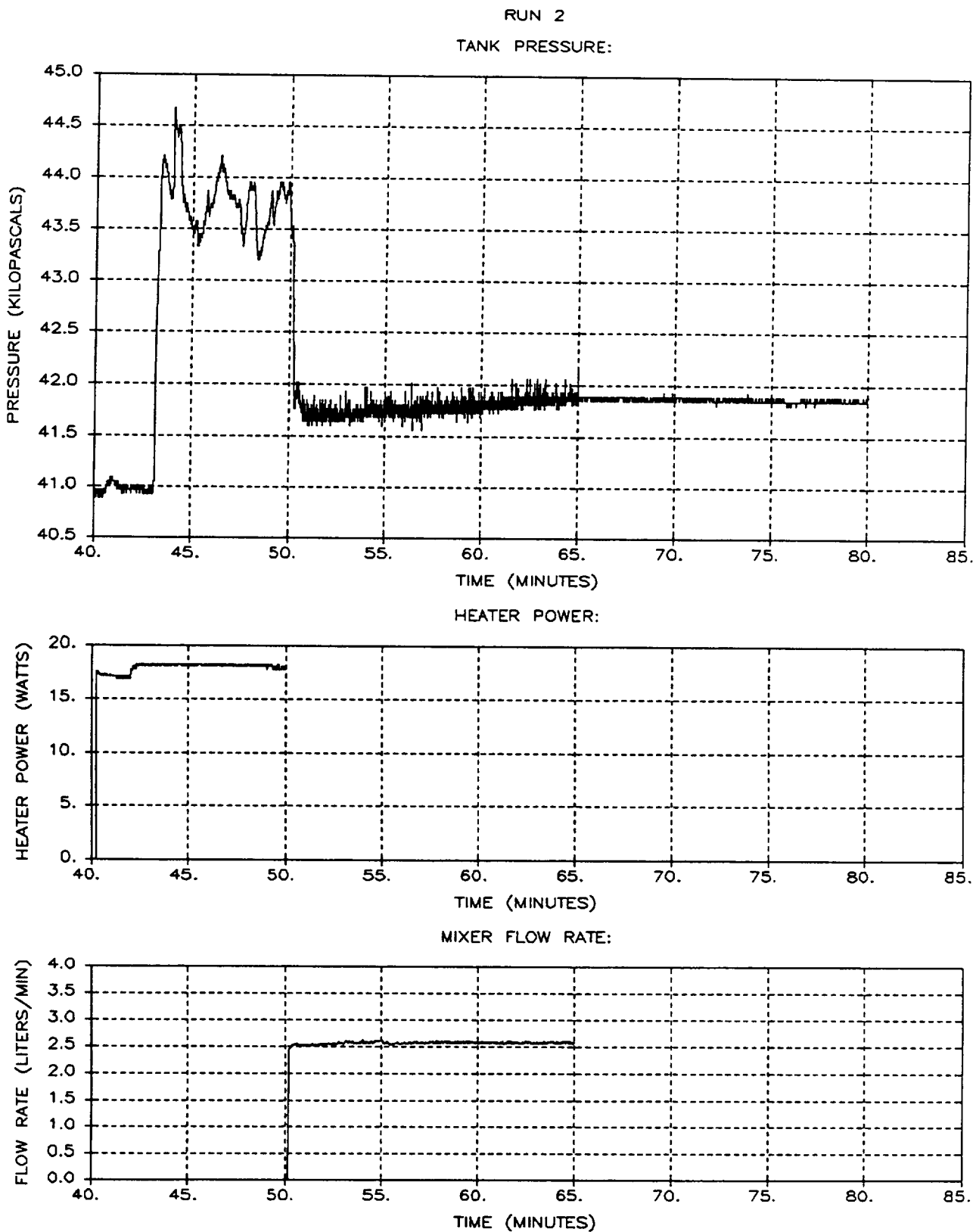
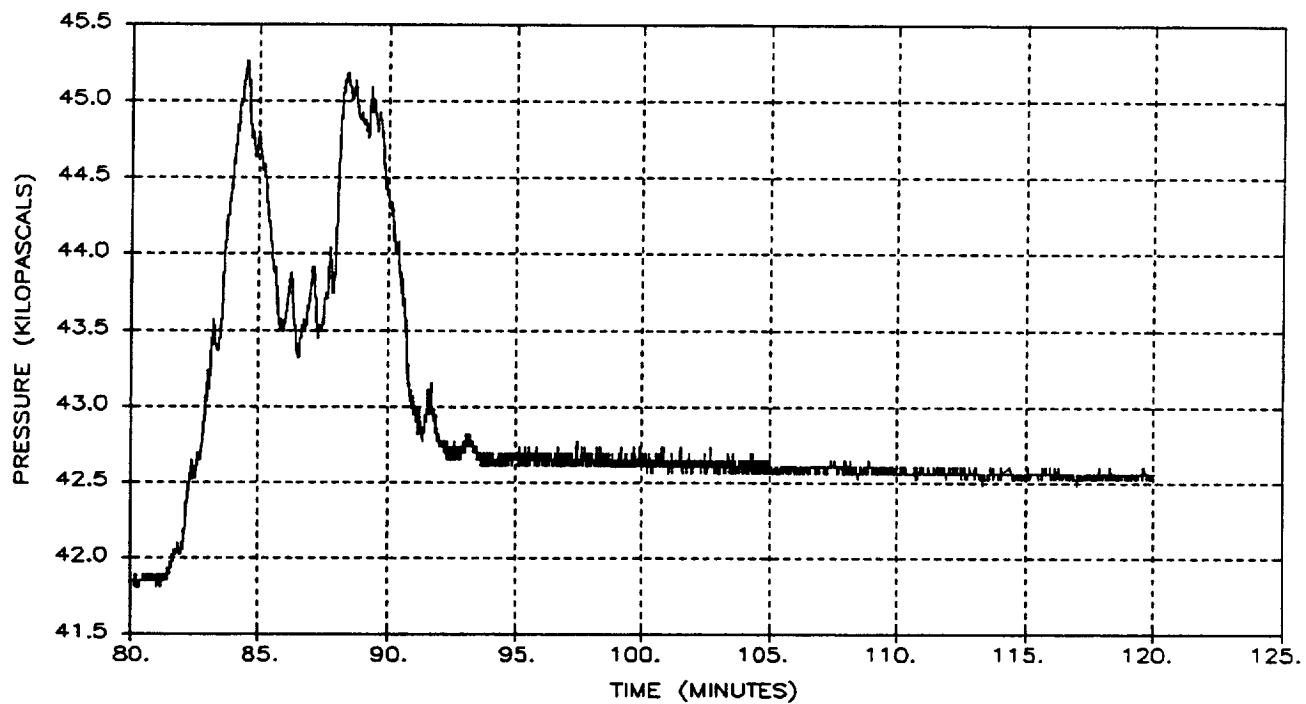


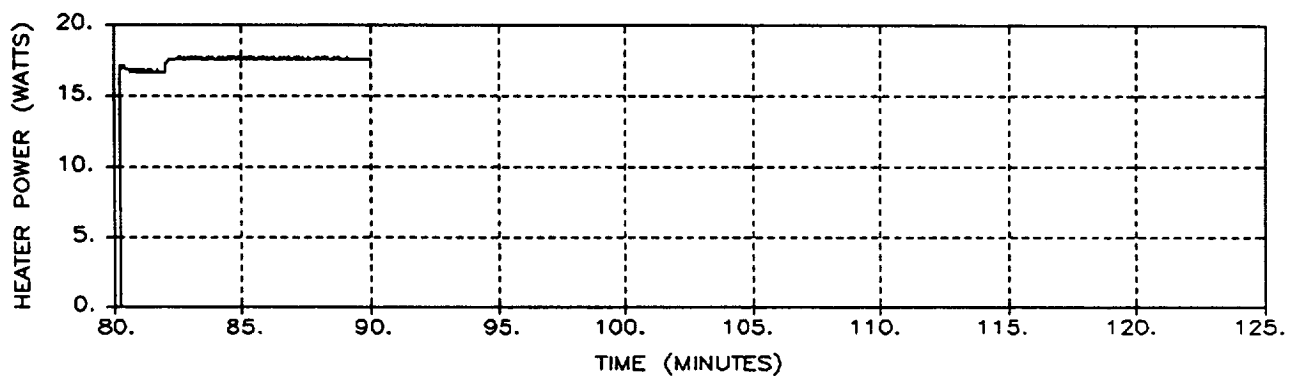
Figure A-40: Run 2 Pressure, Heater Power, and Flow Rate
A-41

RUN 3

TANK PRESSURE:



HEATER POWER:



MIXER FLOW RATE:

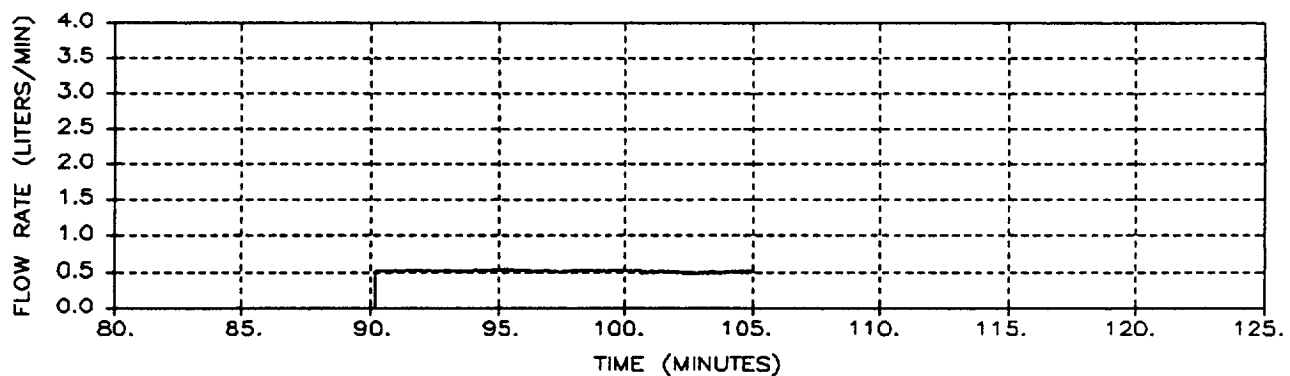


Figure A-41: Run 3 Pressure, Heater Power, and Flow Rate

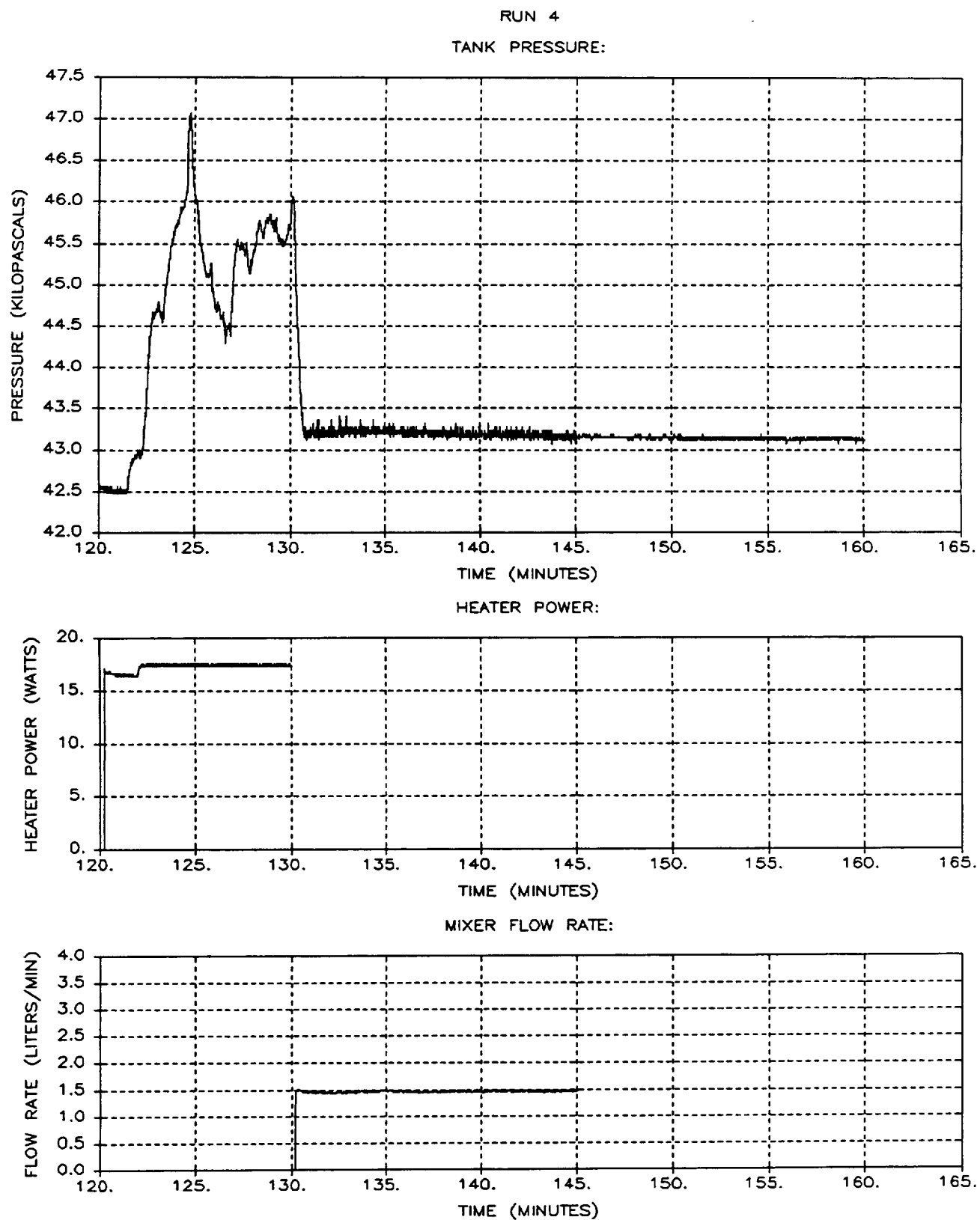
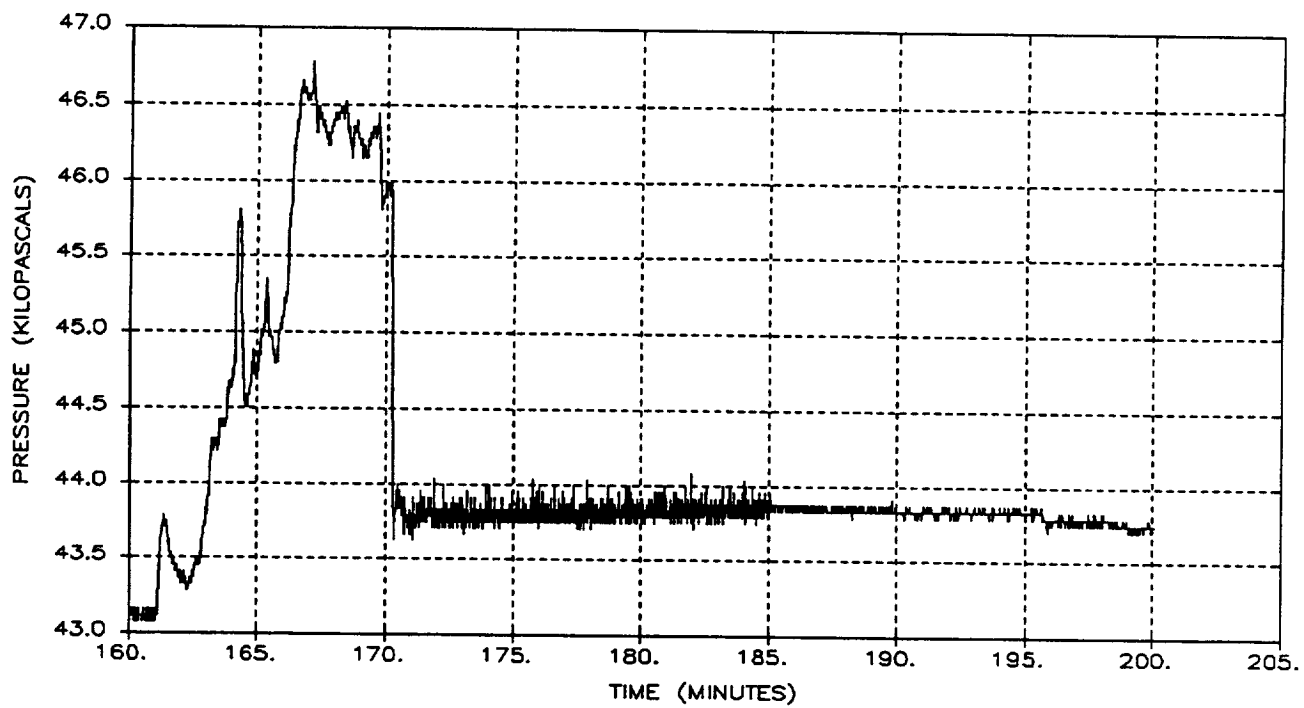


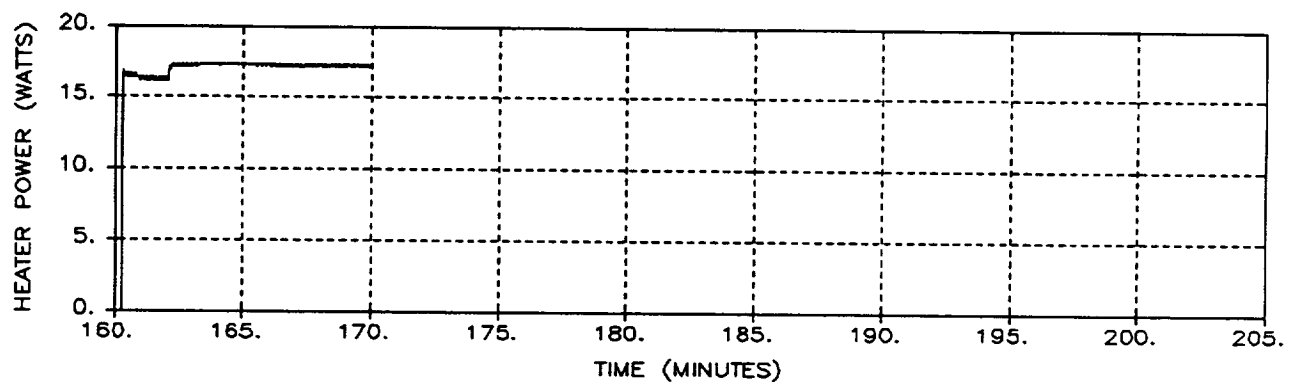
Figure A-42: Run 4 Pressure, Heater Power, and Flow Rate

RUN 5

TANK PRESSURE:



HEATER POWER:



MIXER FLOW RATE:

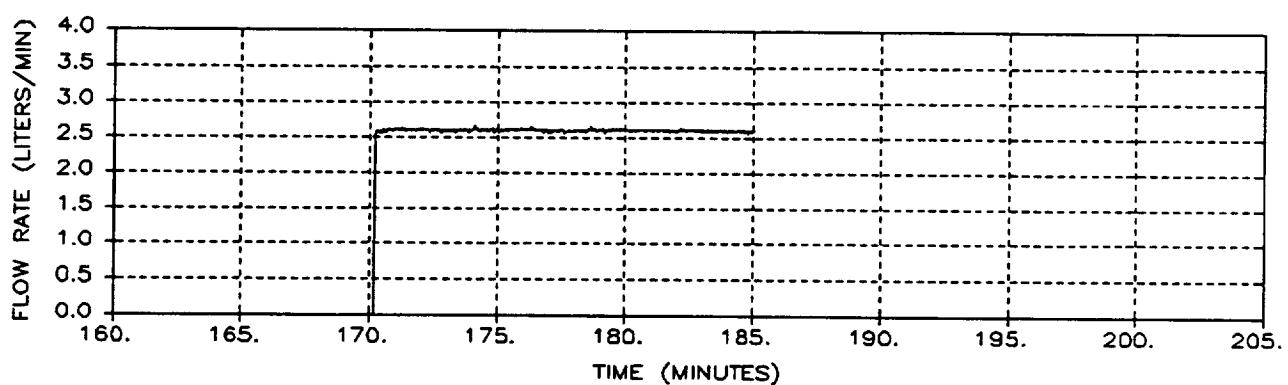


Figure A-43: Run 5 Pressure, Heater Power, and Flow Rate
A-44

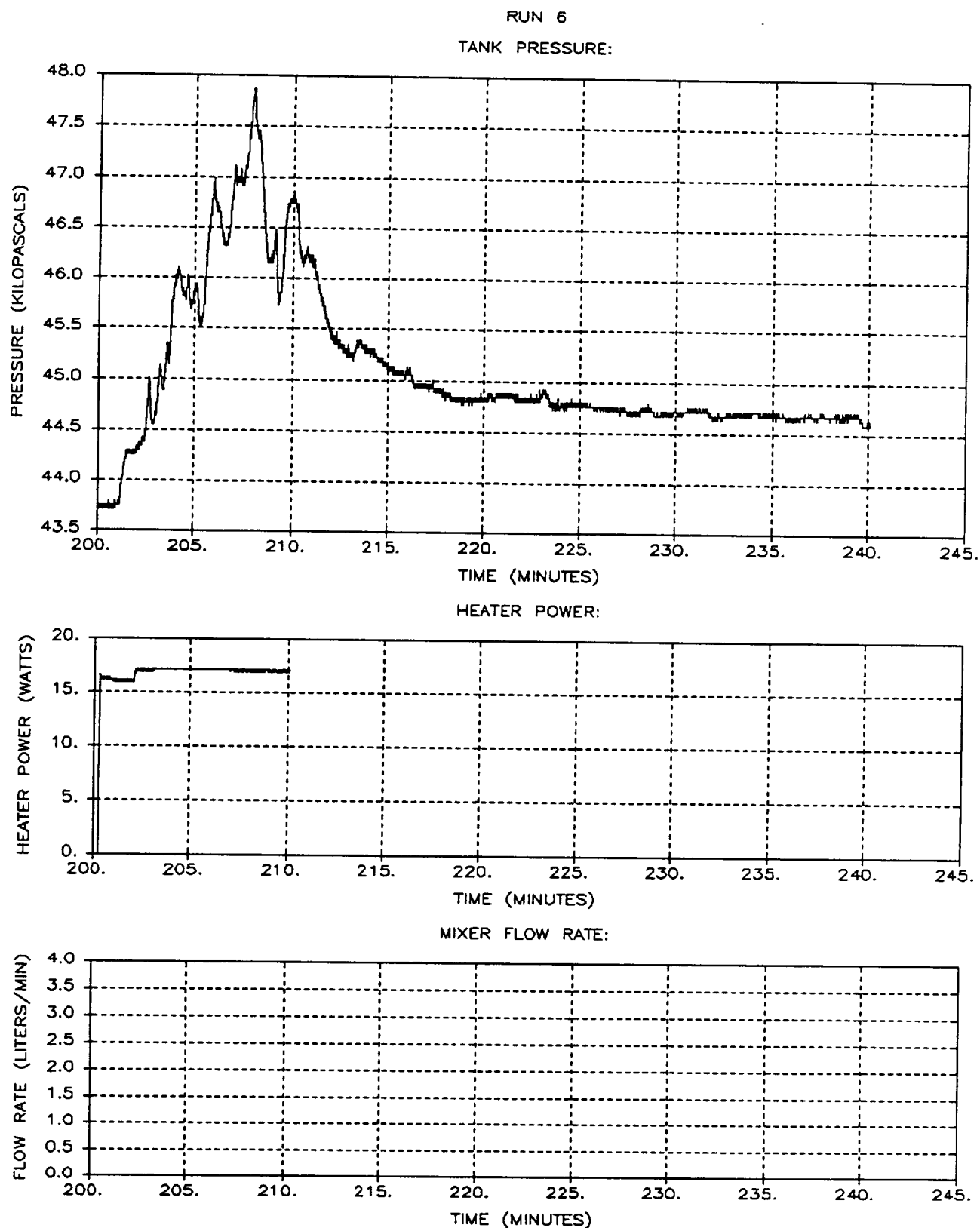


Figure A-44: Run 6 Pressure, Heater Power, and Flow Rate
A-45

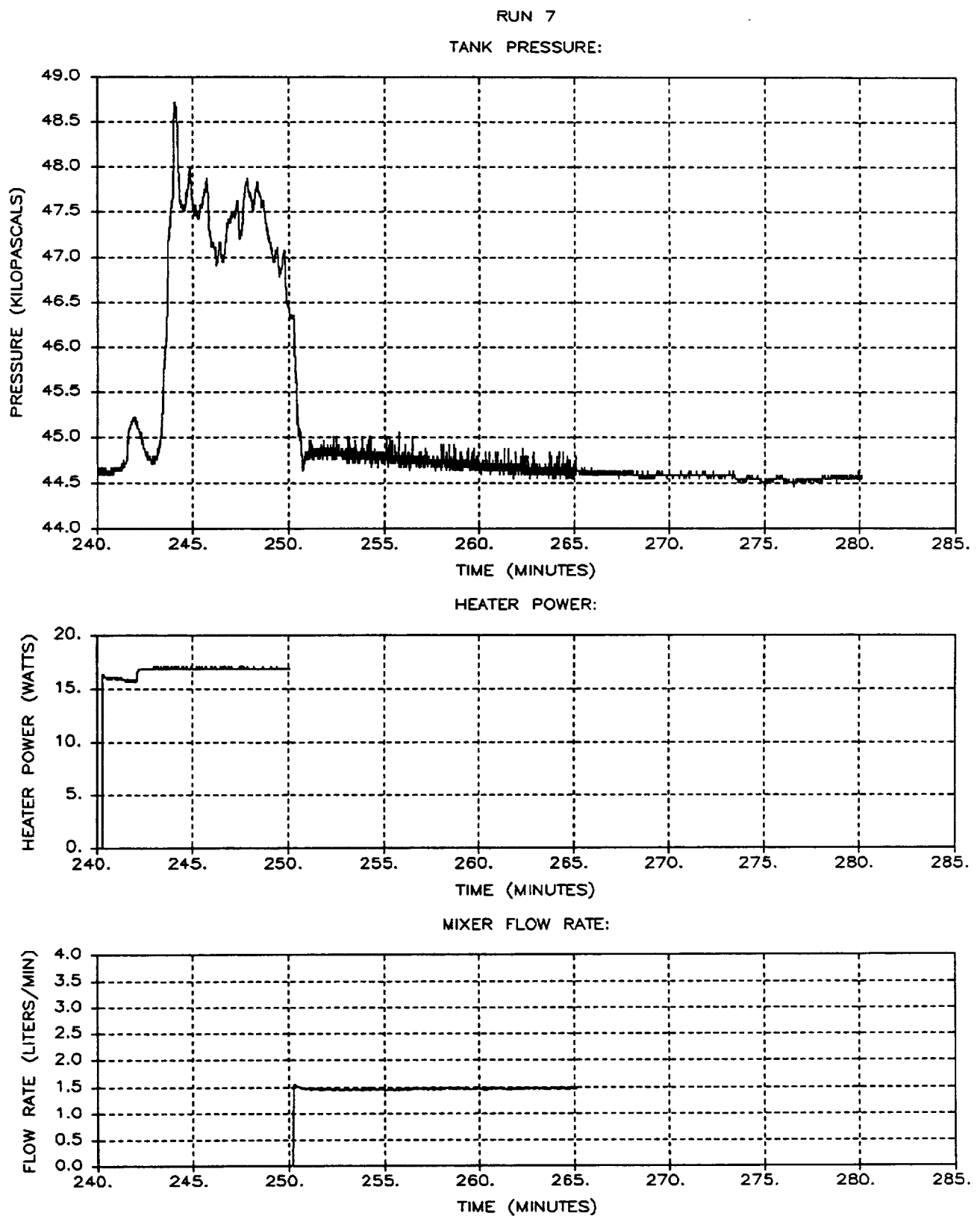


Figure A-45: Run 7 Pressure, Heater Power, and Flow Rate
A-46

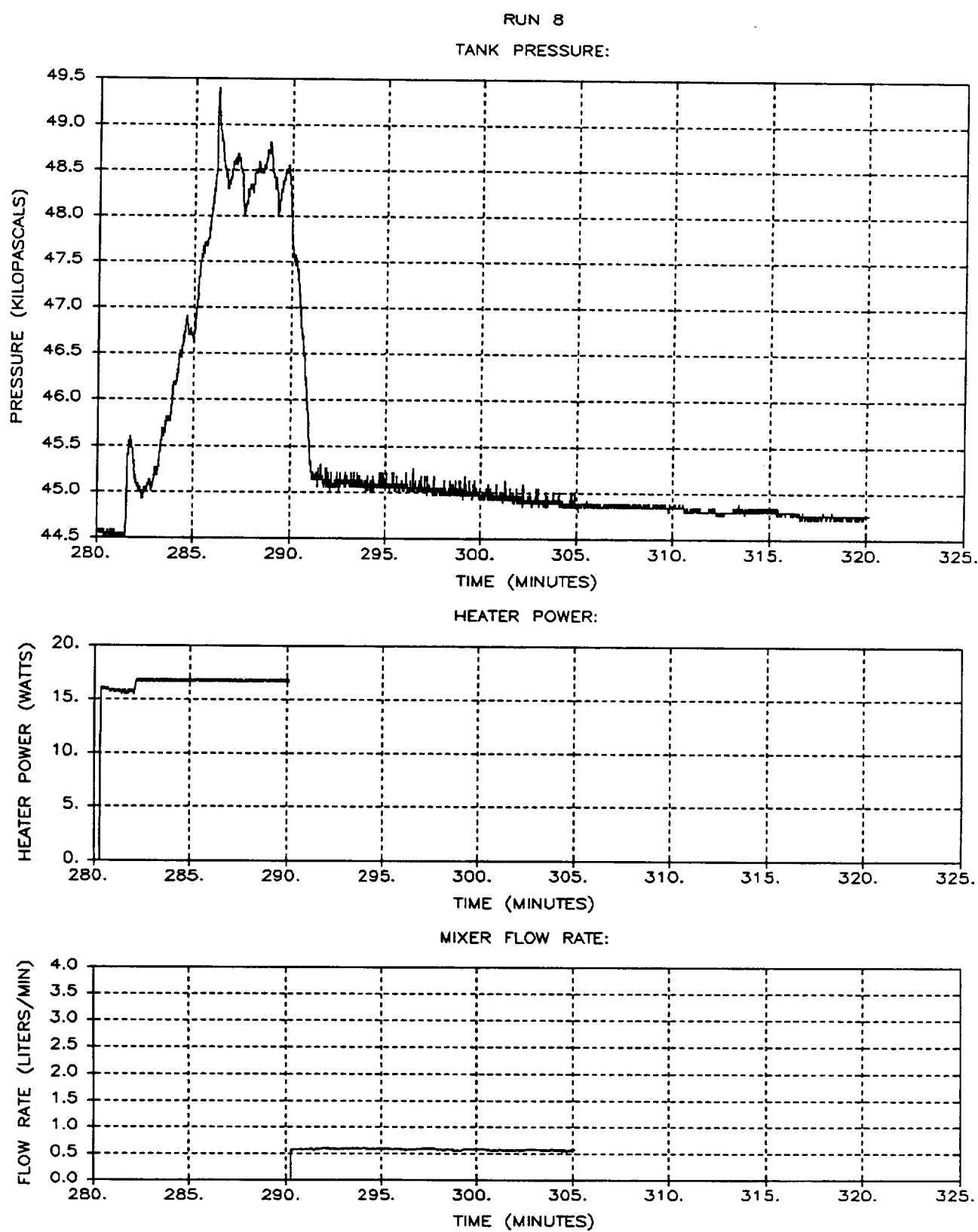
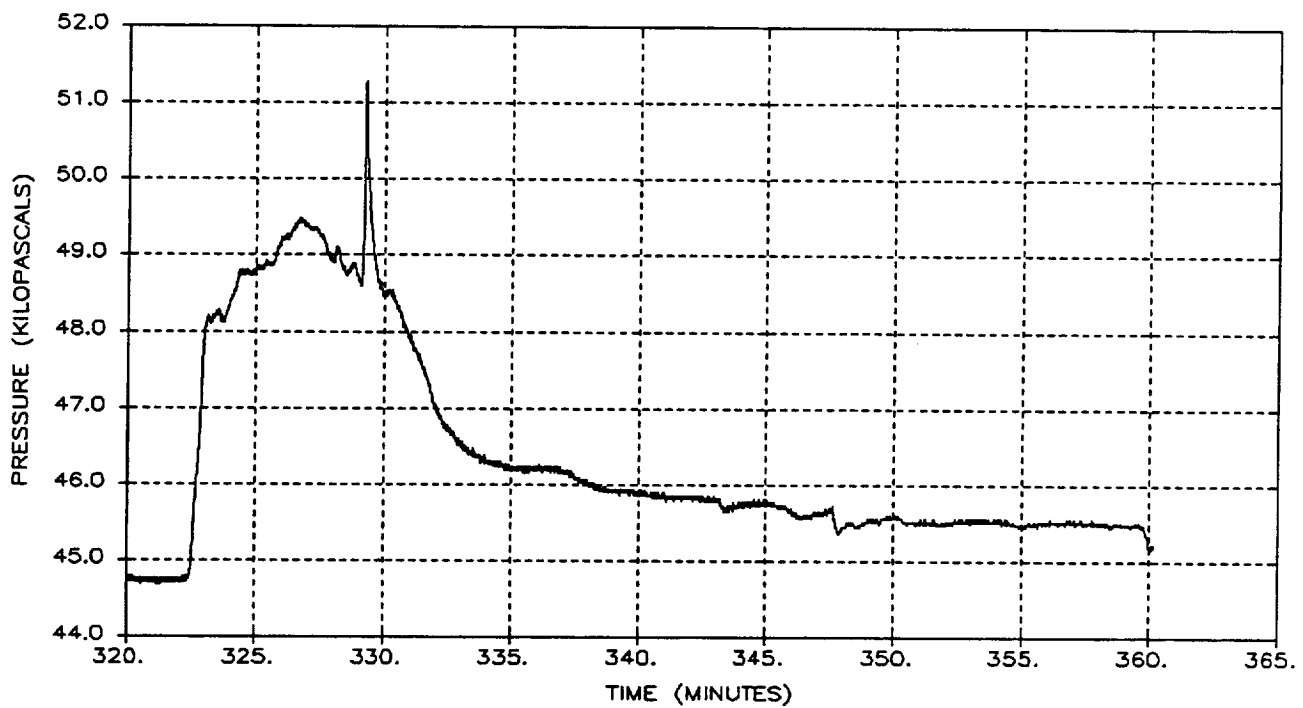


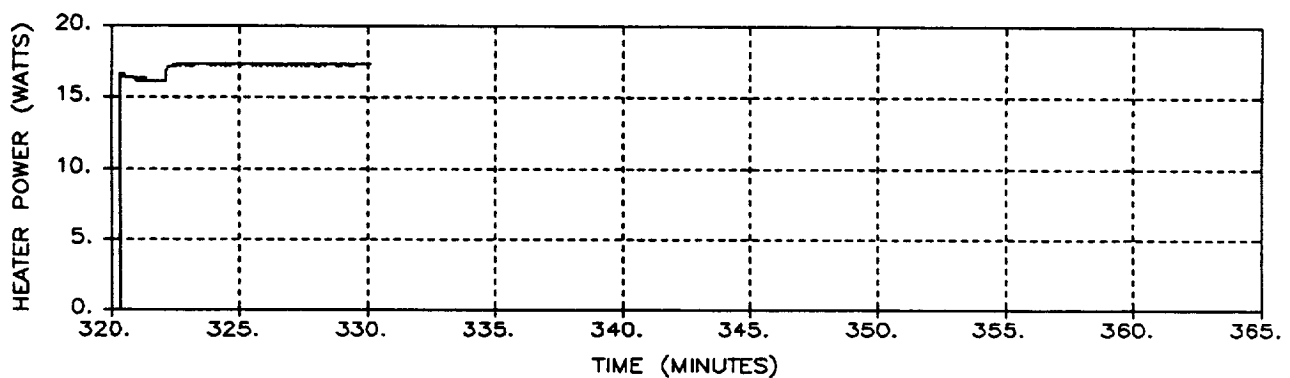
Figure A-46: Run 8 Pressure, Heater Power, and Flow Rate
A-47

RUN 9

TANK PRESSURE:



HEATER POWER:



MIXER FLOW RATE:

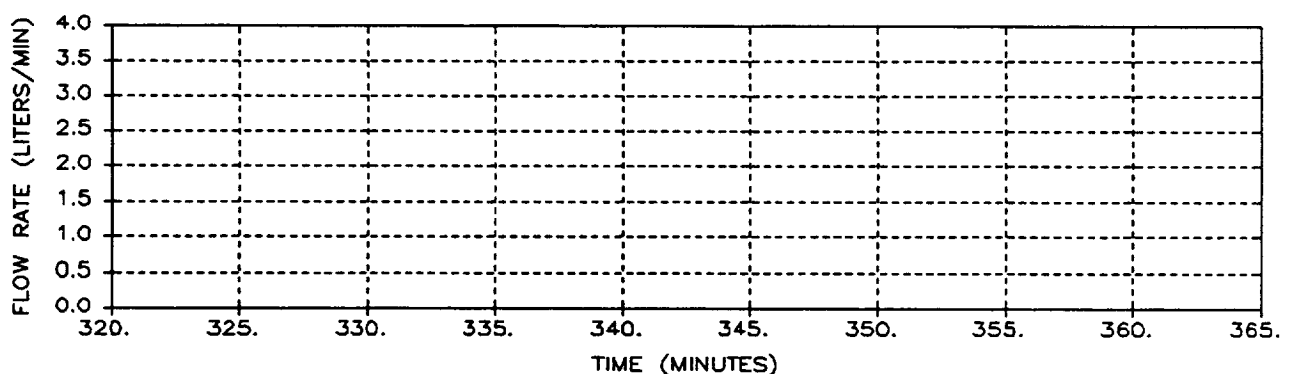


Figure A-47: Run 9 Pressure, Heater Power, and Flow Rate

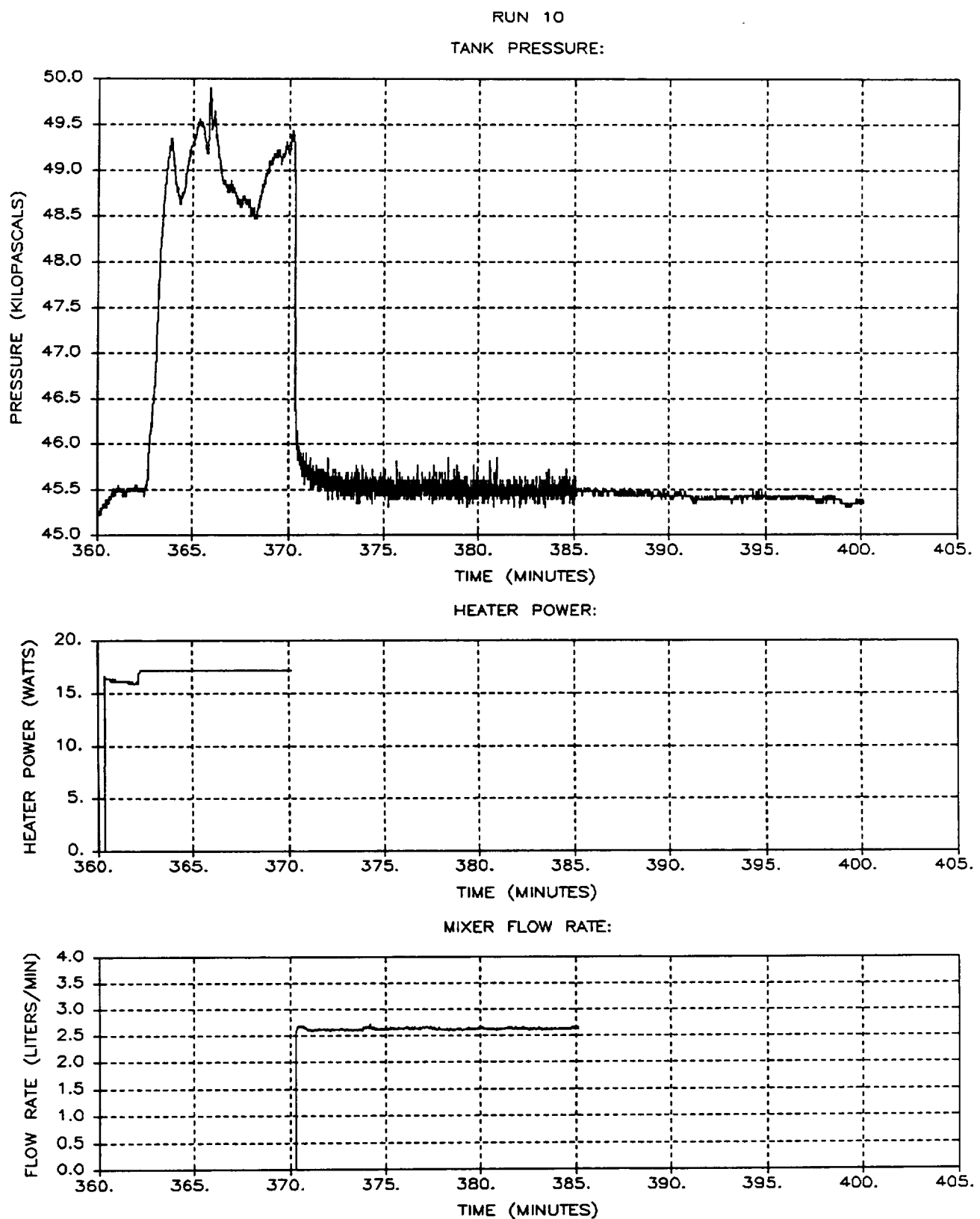


Figure A-48: Run 10 Pressure, Heater Power, and Flow Rate
A-49

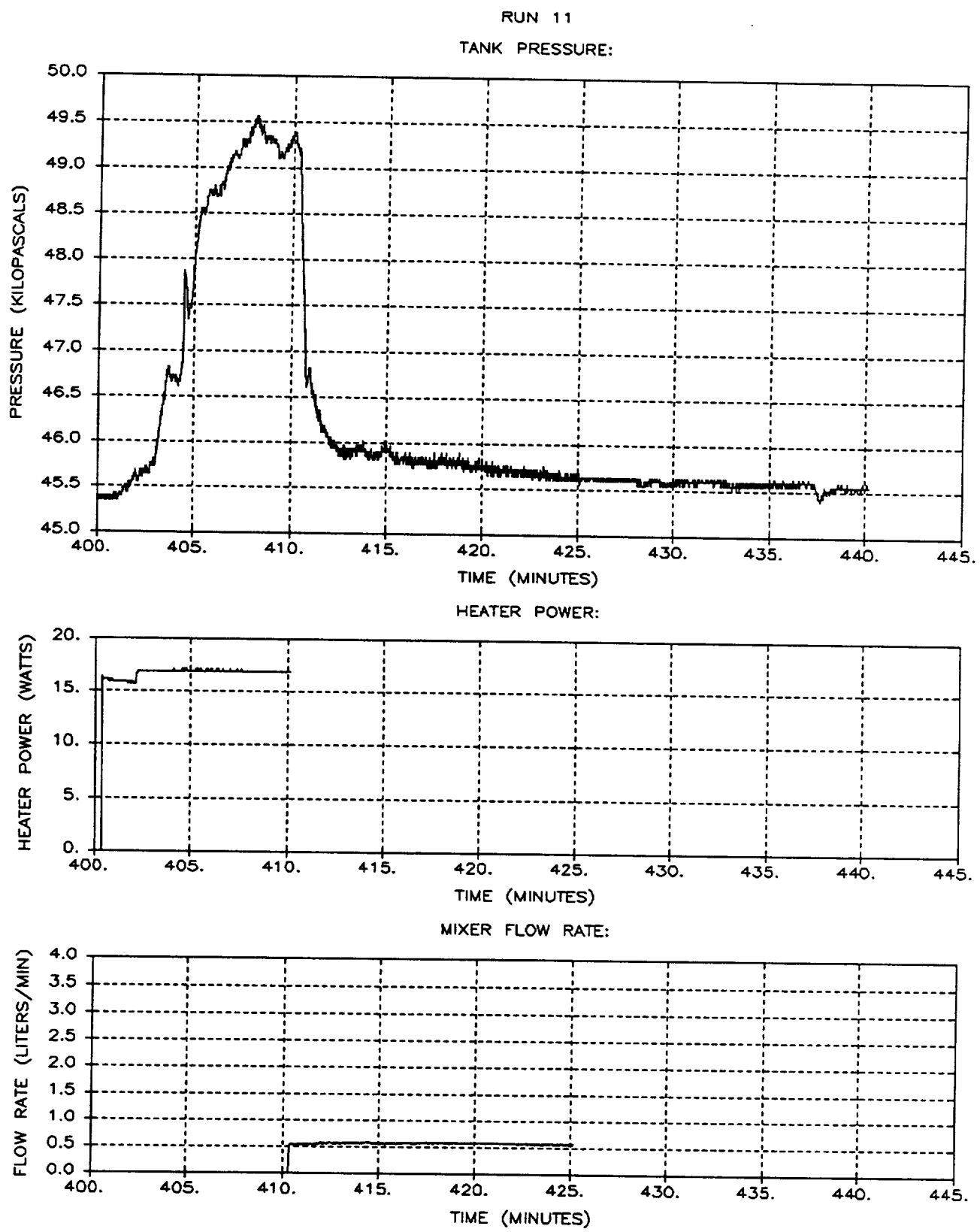


Figure A-49: Run 11 Pressure, Heater Power, and Flow Rate
A-50

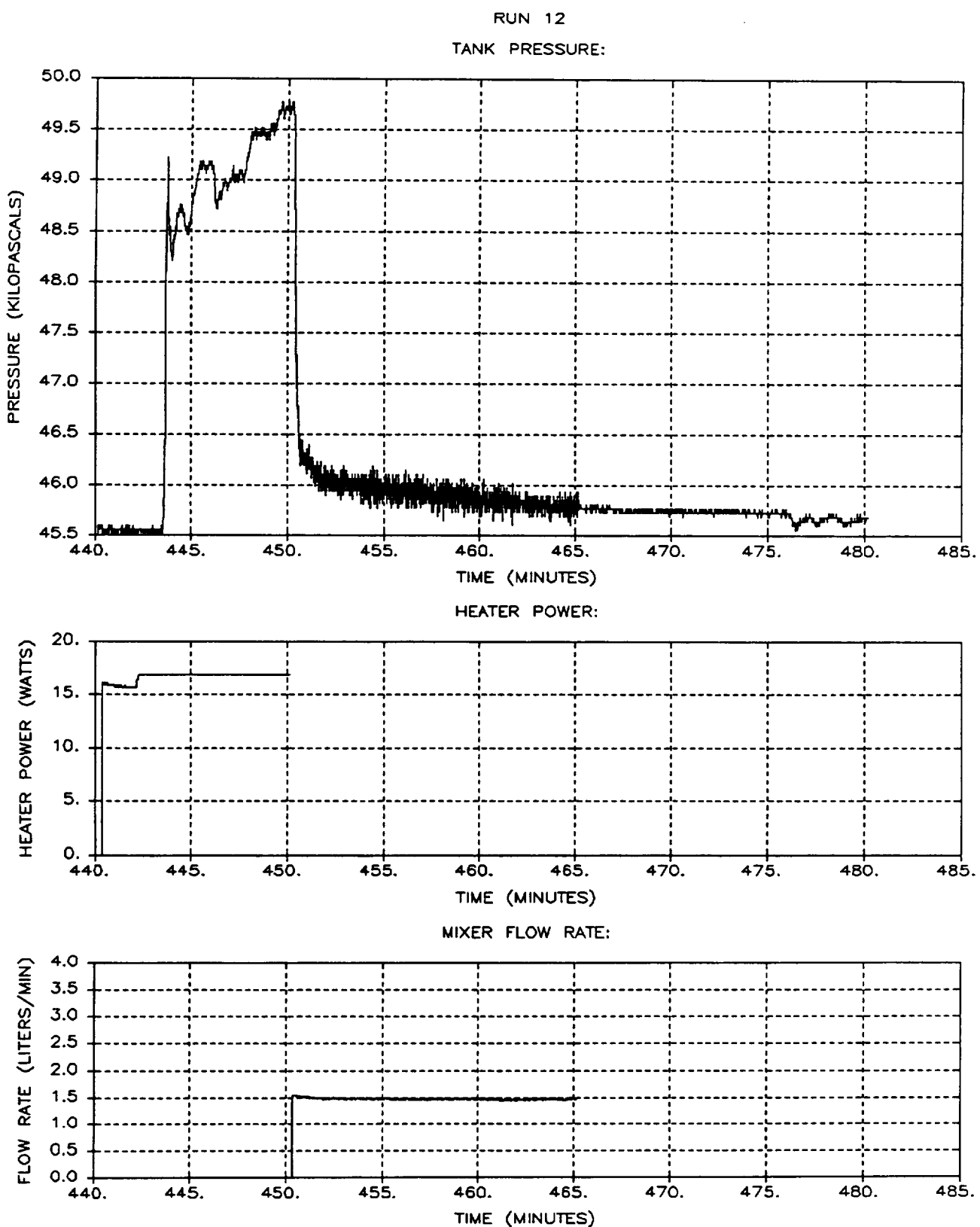


Figure A-50: Run 12 Pressure, Heater Power, and Flow Rate
A-51

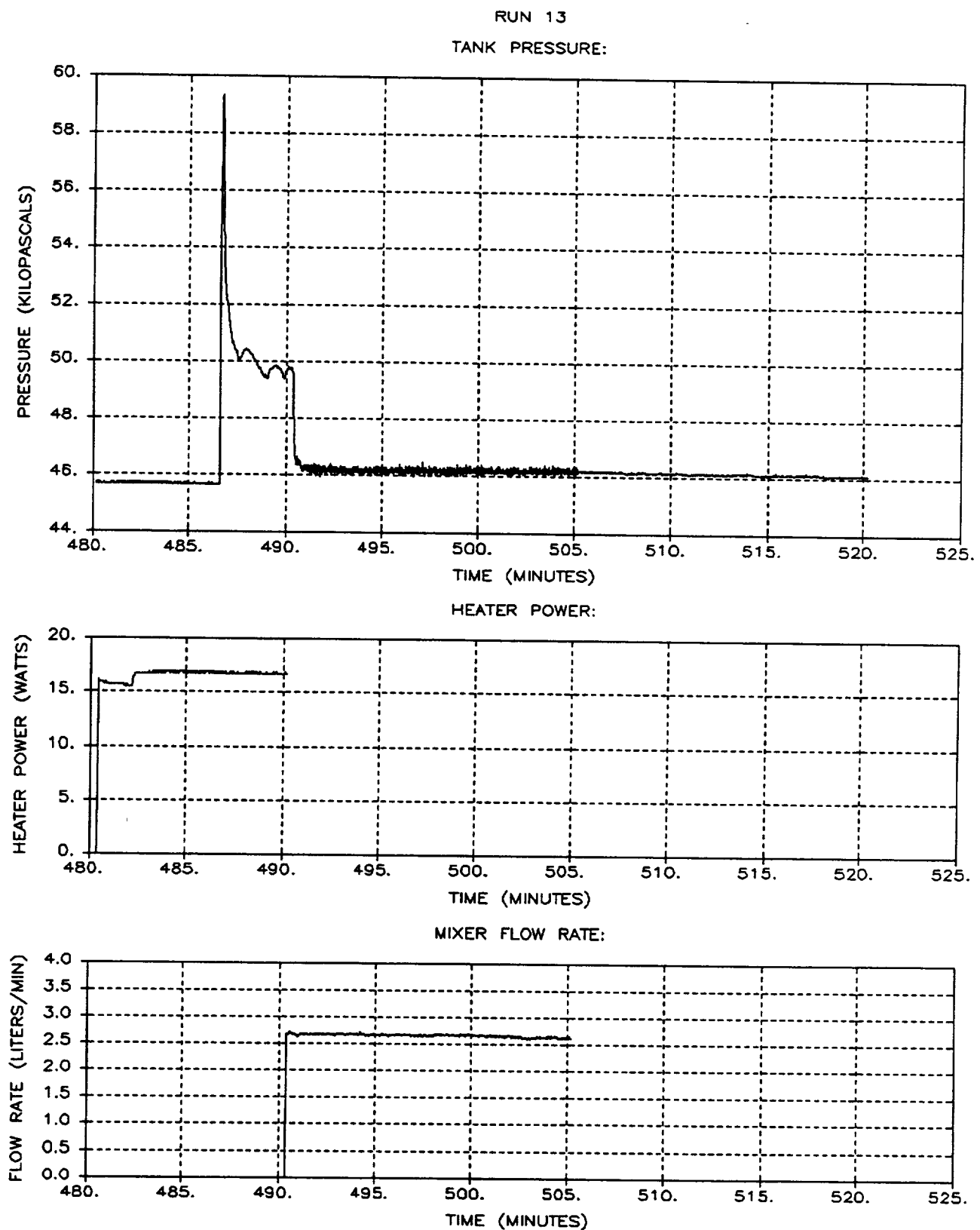


Figure A-51: Run 13 Pressure, Heater Power, and Flow Rate
A-52

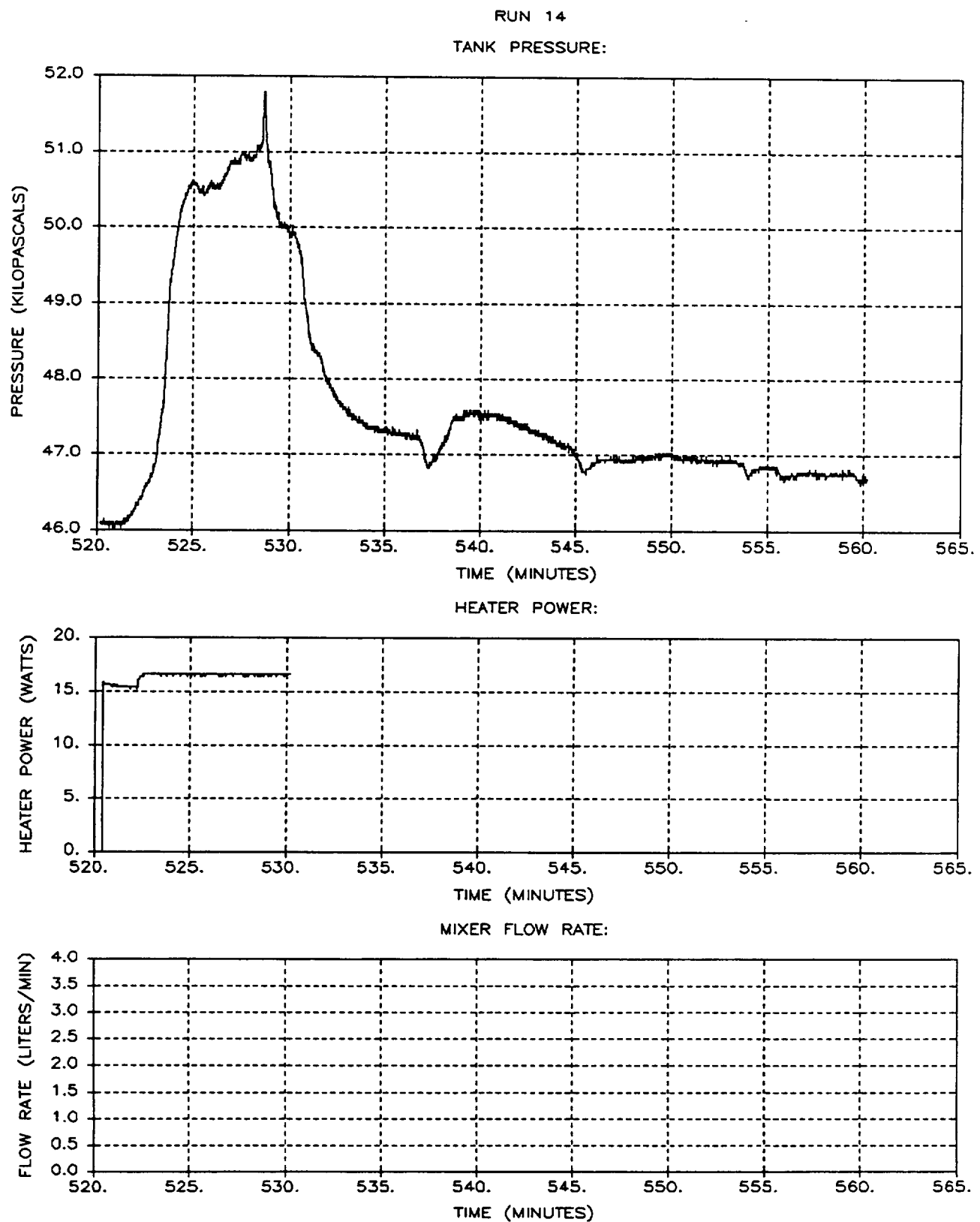


Figure A-52: Run 14 Pressure, Heater Power, and Flow Rate

A-53

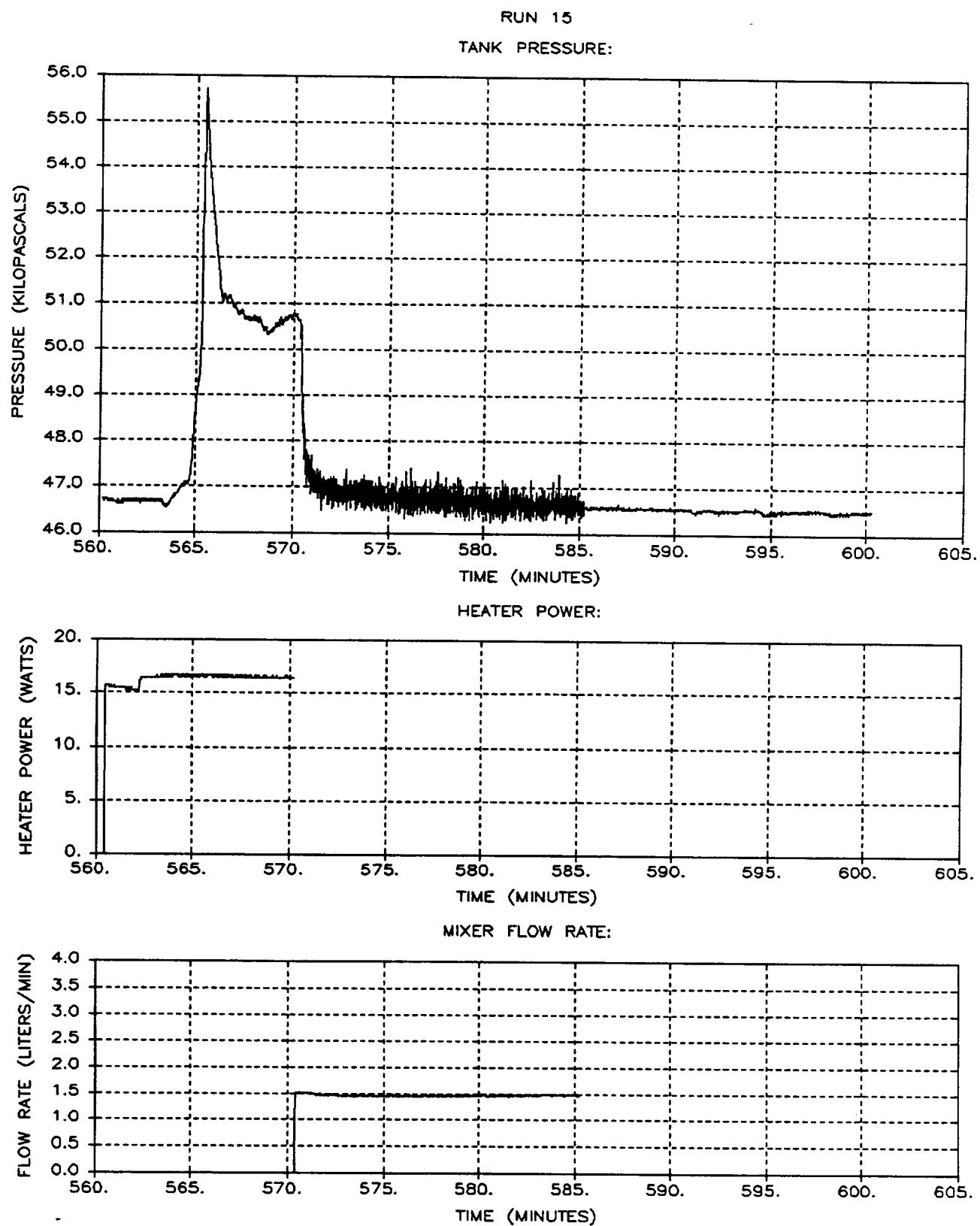


Figure A-53: Run 15 Pressure, Heater Power, and Flow Rate
A-54

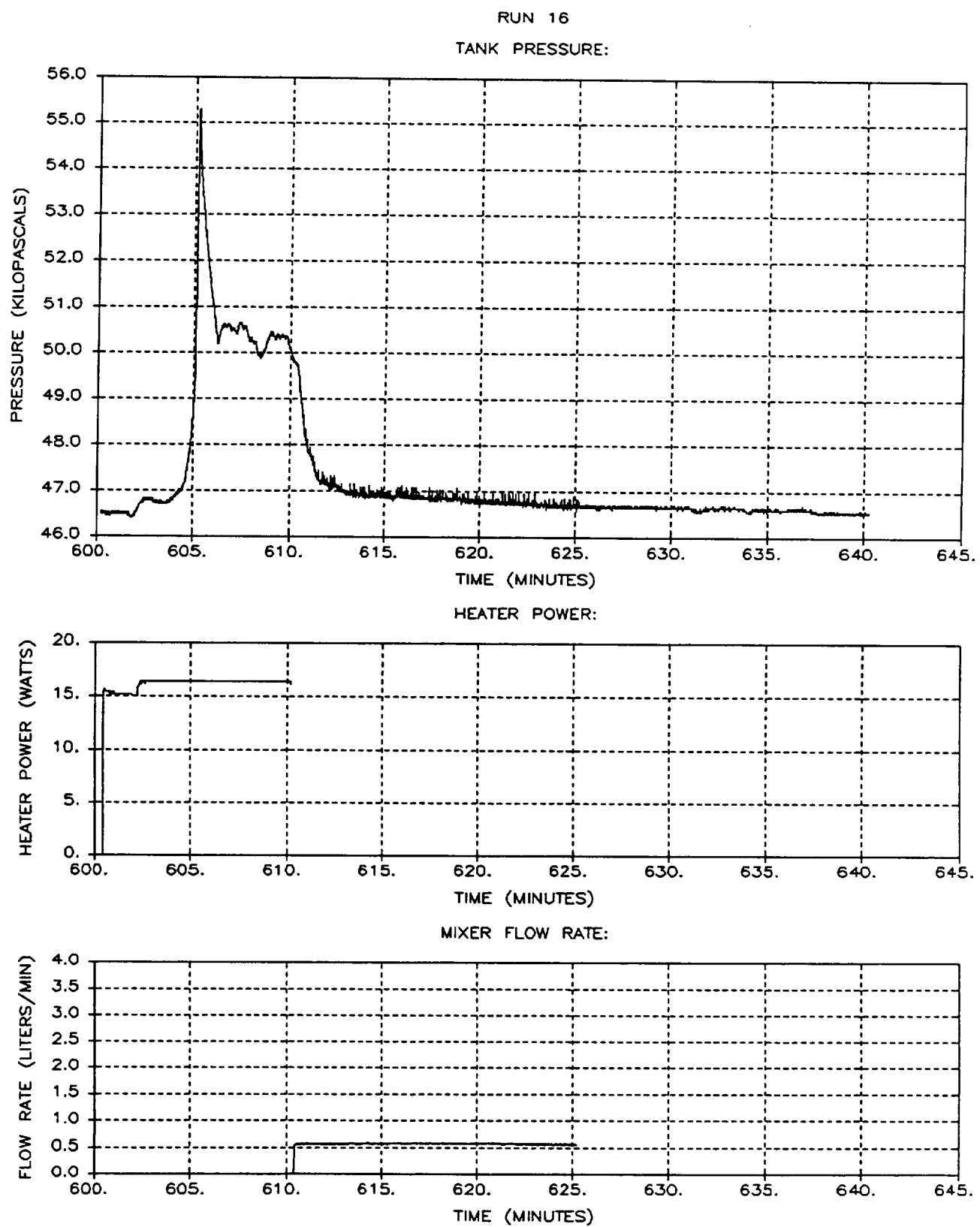


Figure A-54: Run 16 Pressure, Heater Power, and Flow Rate
A-55

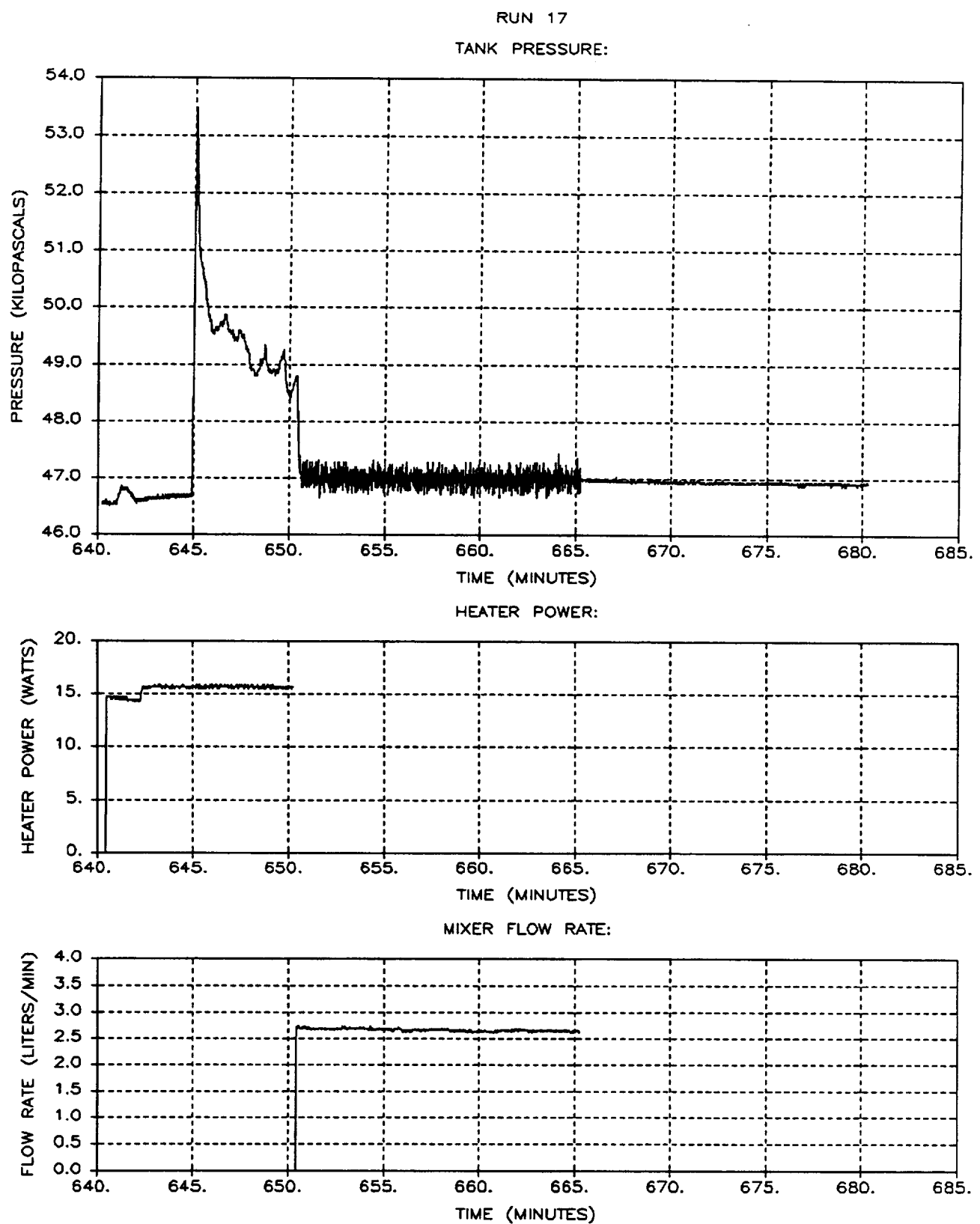


Figure A-55: Run 17 Pressure, Heater Power, and Flow Rate
A-56

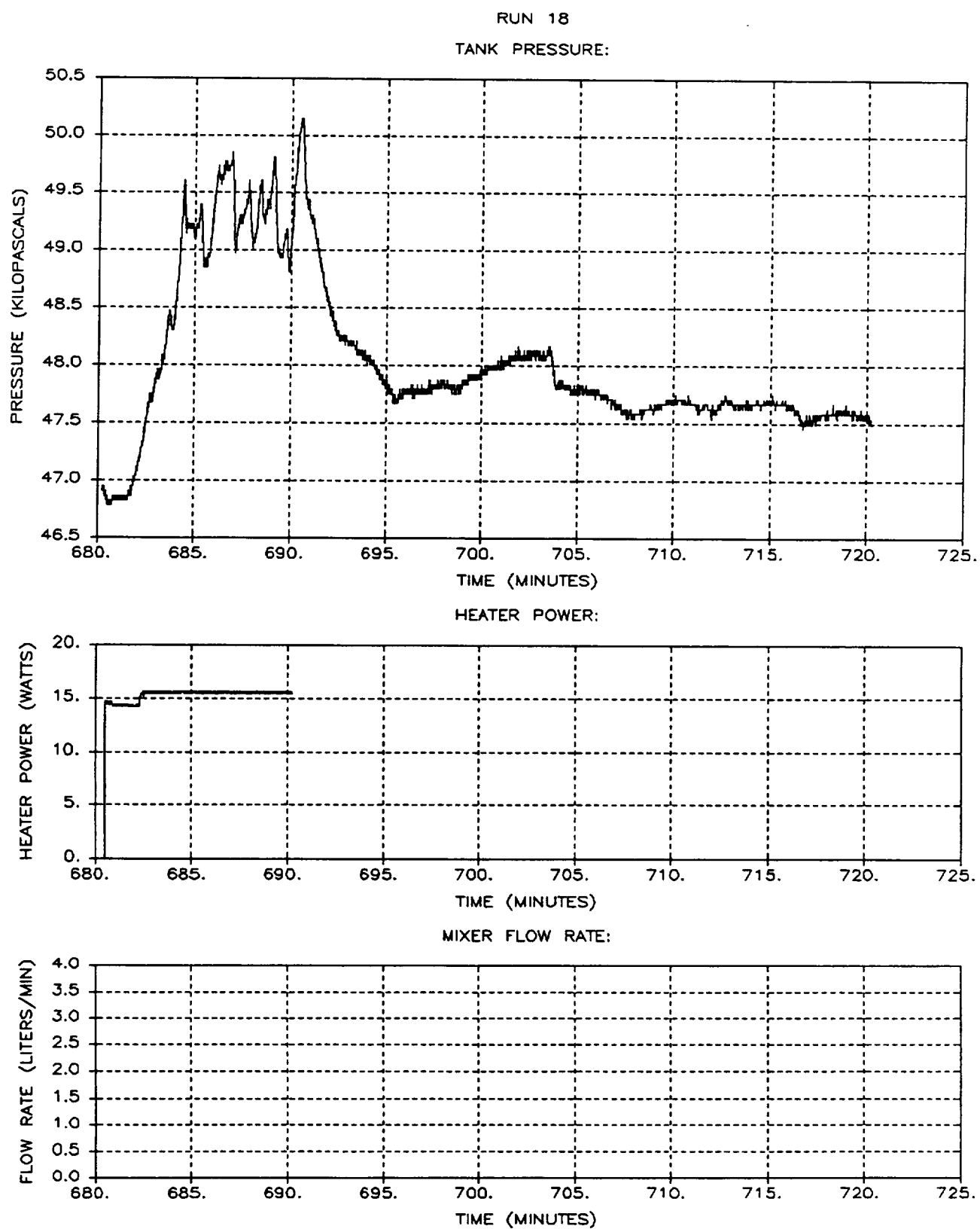


Figure A-56: Run 18 Pressure, Heater Power, and Flow Rate
A-57

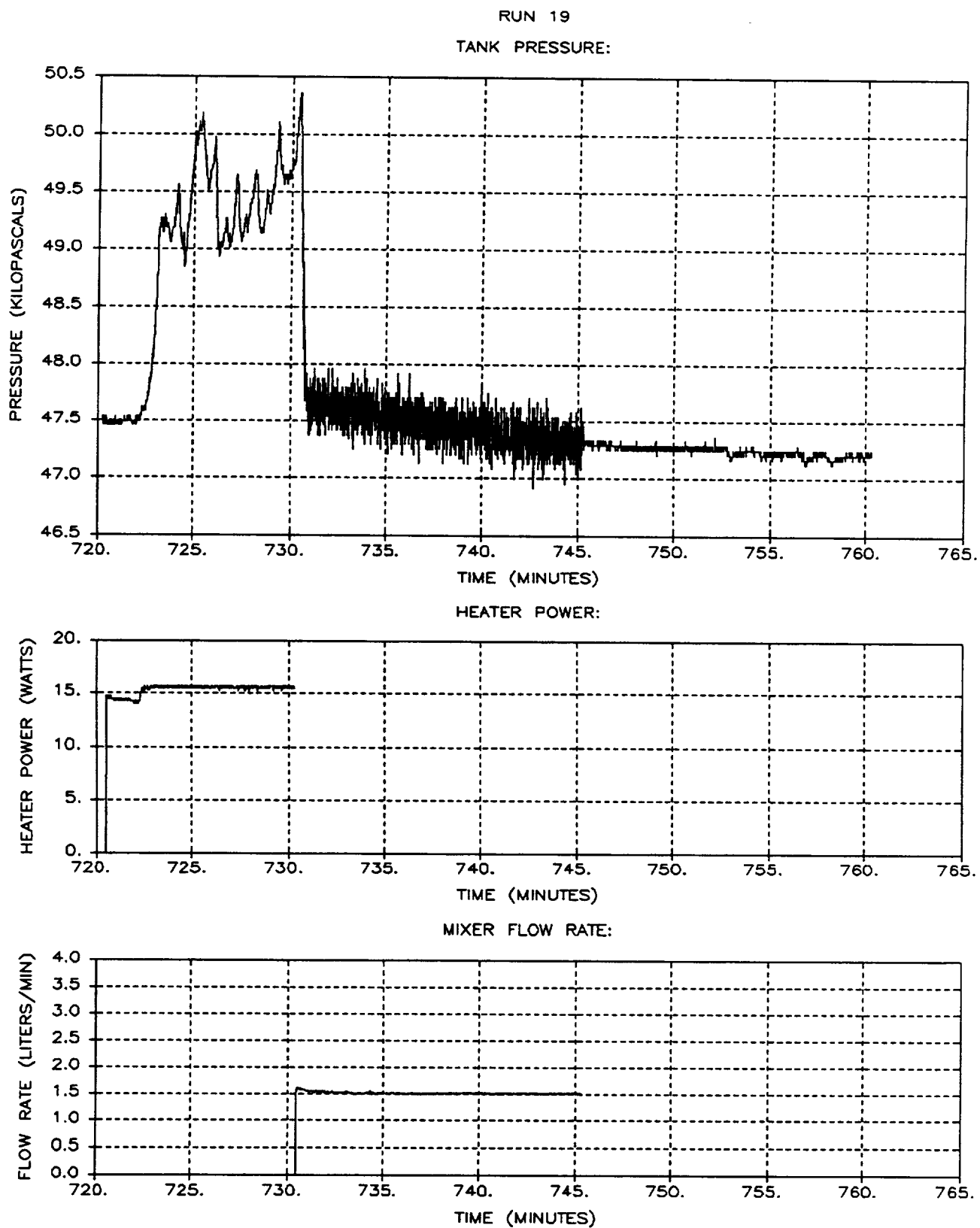


Figure A-57: Run 19 Pressure, Heater Power, and Flow Rate

A-58

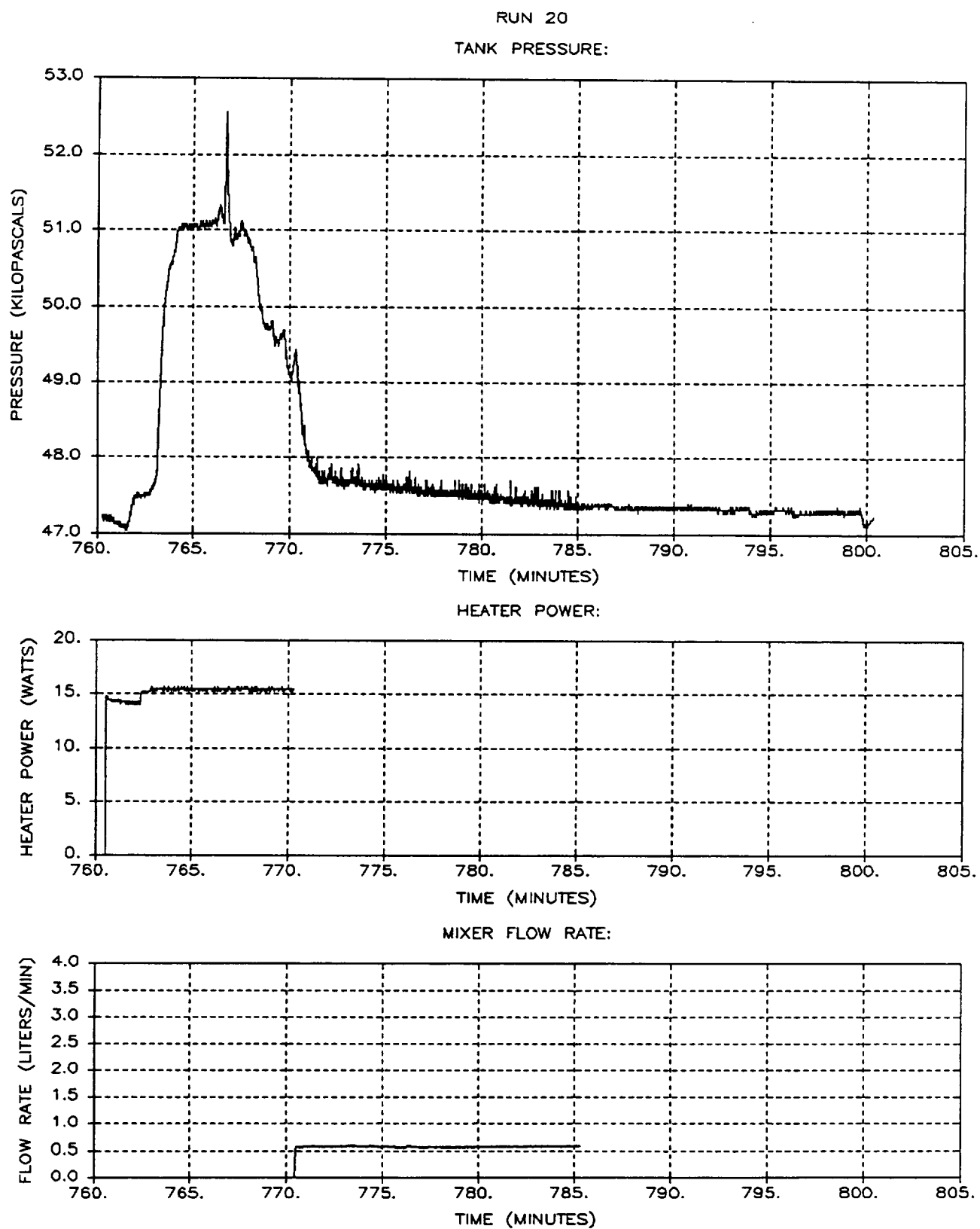
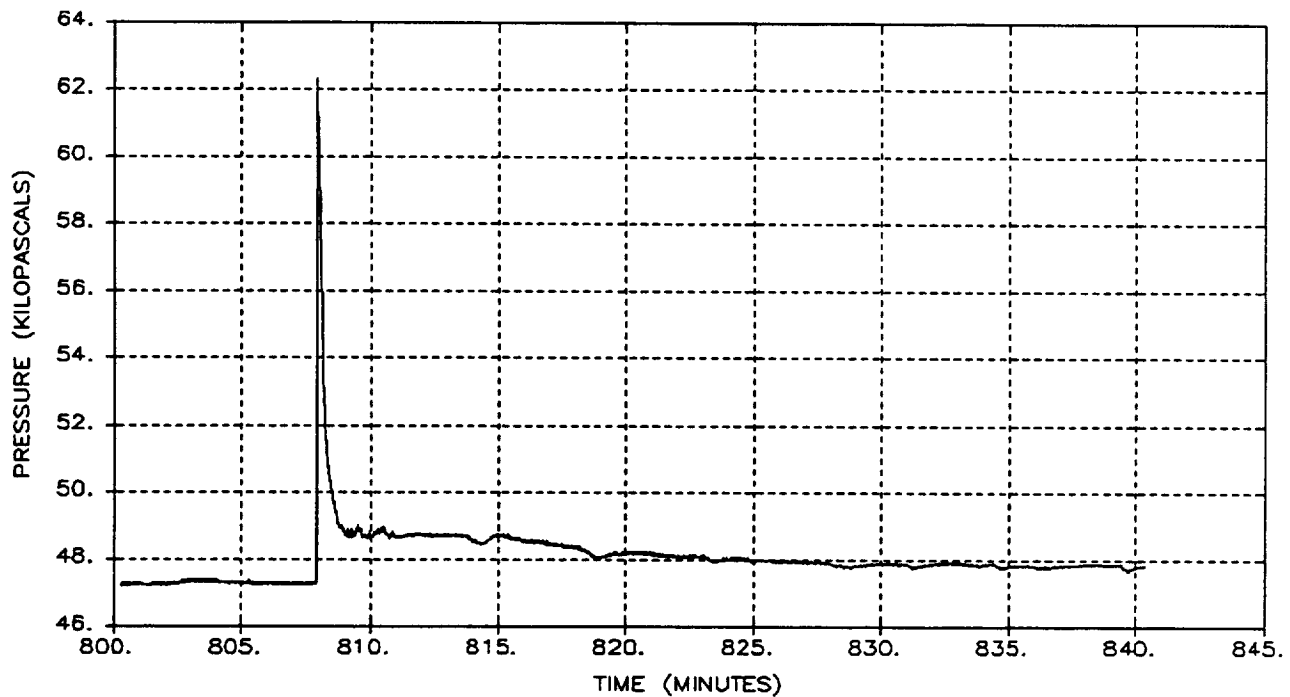


Figure A-58: Run 20 Pressure, Heater Power, and Flow Rate

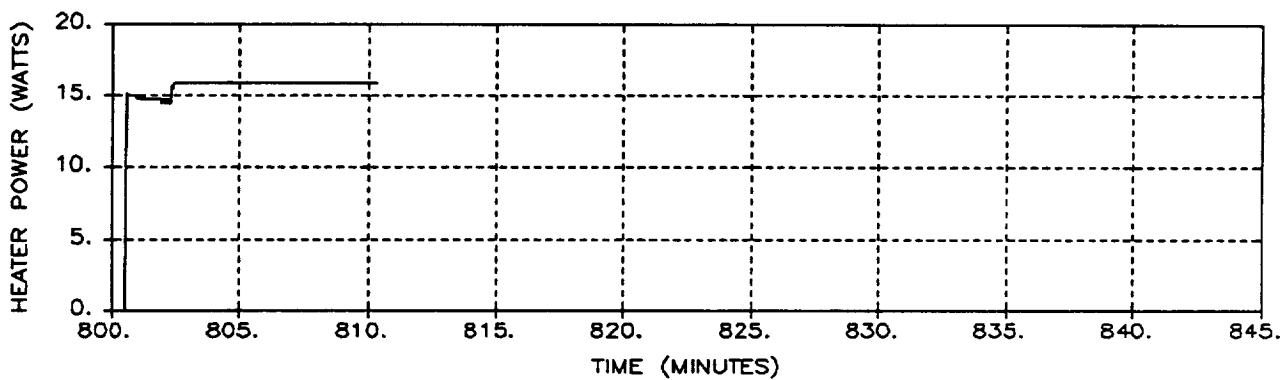
A-59

RUN 21

TANK PRESSURE:



HEATER POWER:



MIXER FLOW RATE:

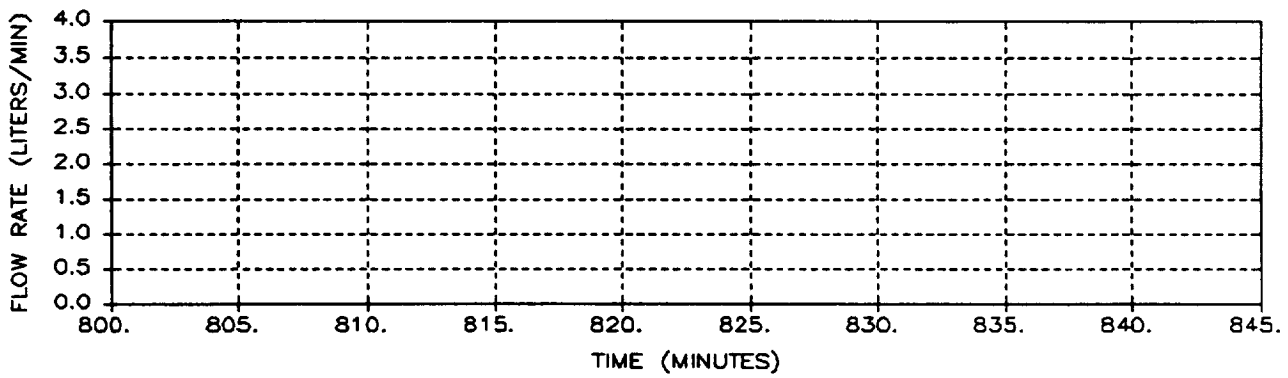


Figure A-59: Run 21 Pressure, Heater Power, and Flow Rate
A-60

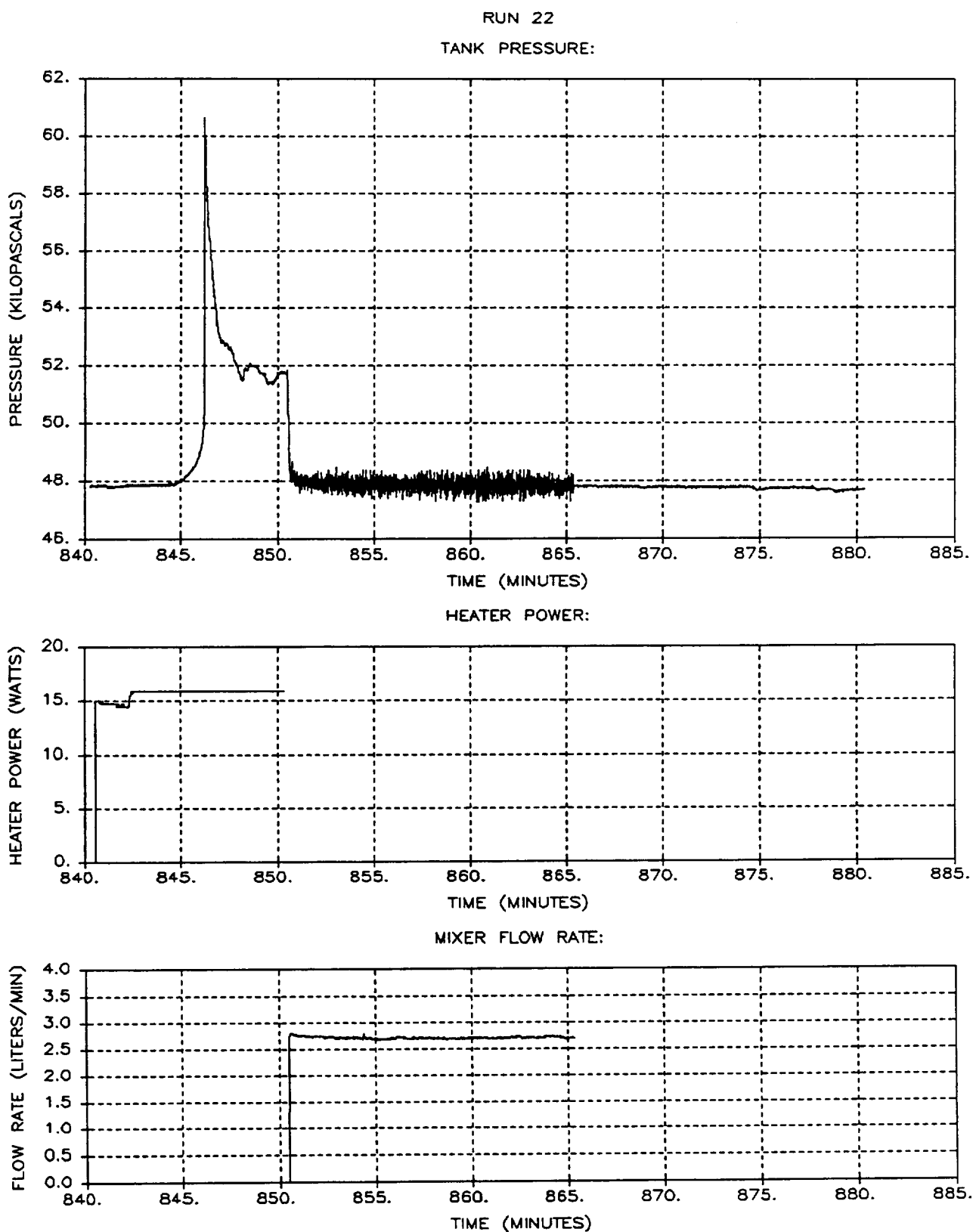


Figure A-60: Run 22 Pressure, Heater Power, and Flow Rate

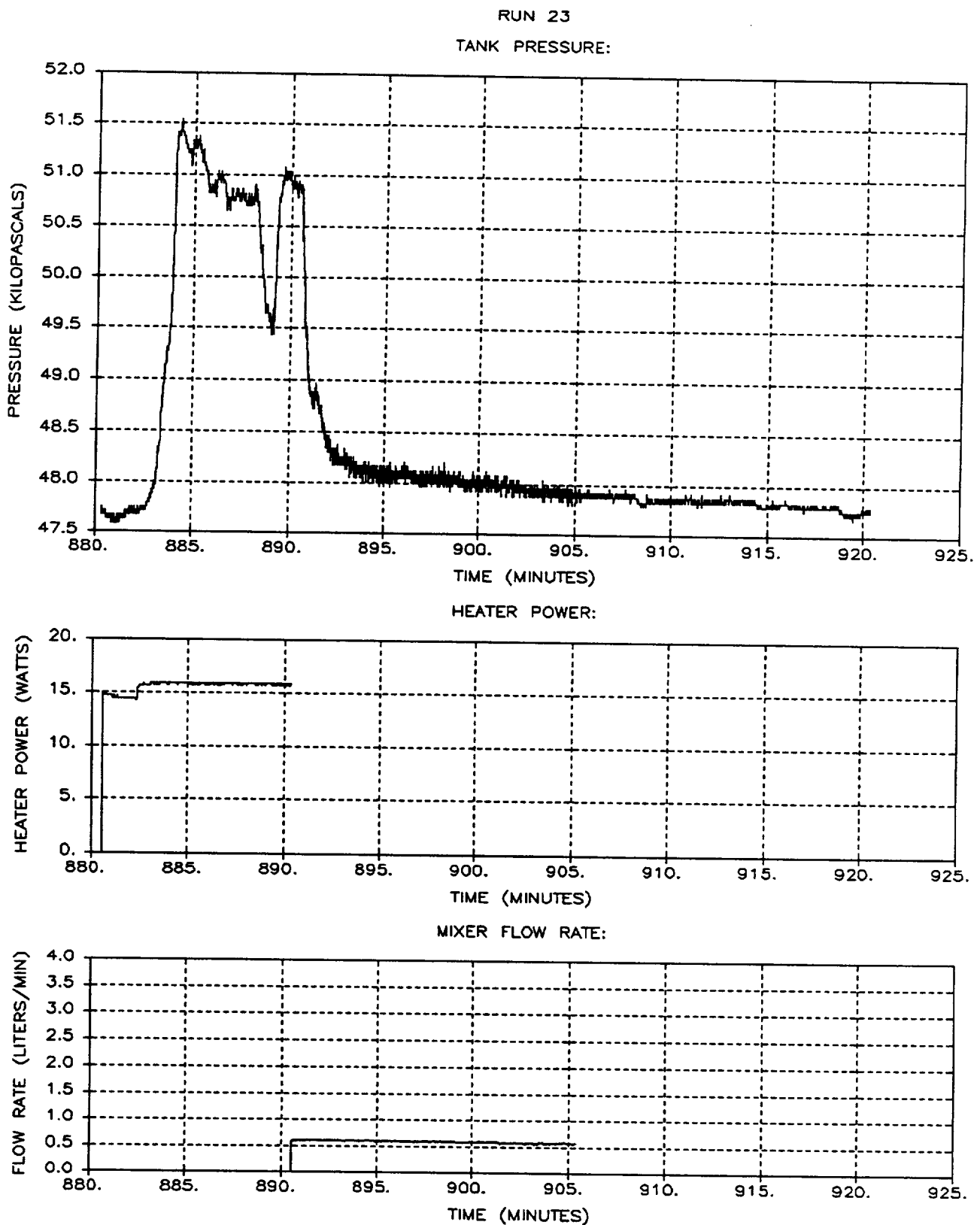


Figure A-61: Run 23 Pressure, Heater Power, and Flow Rate
A-62

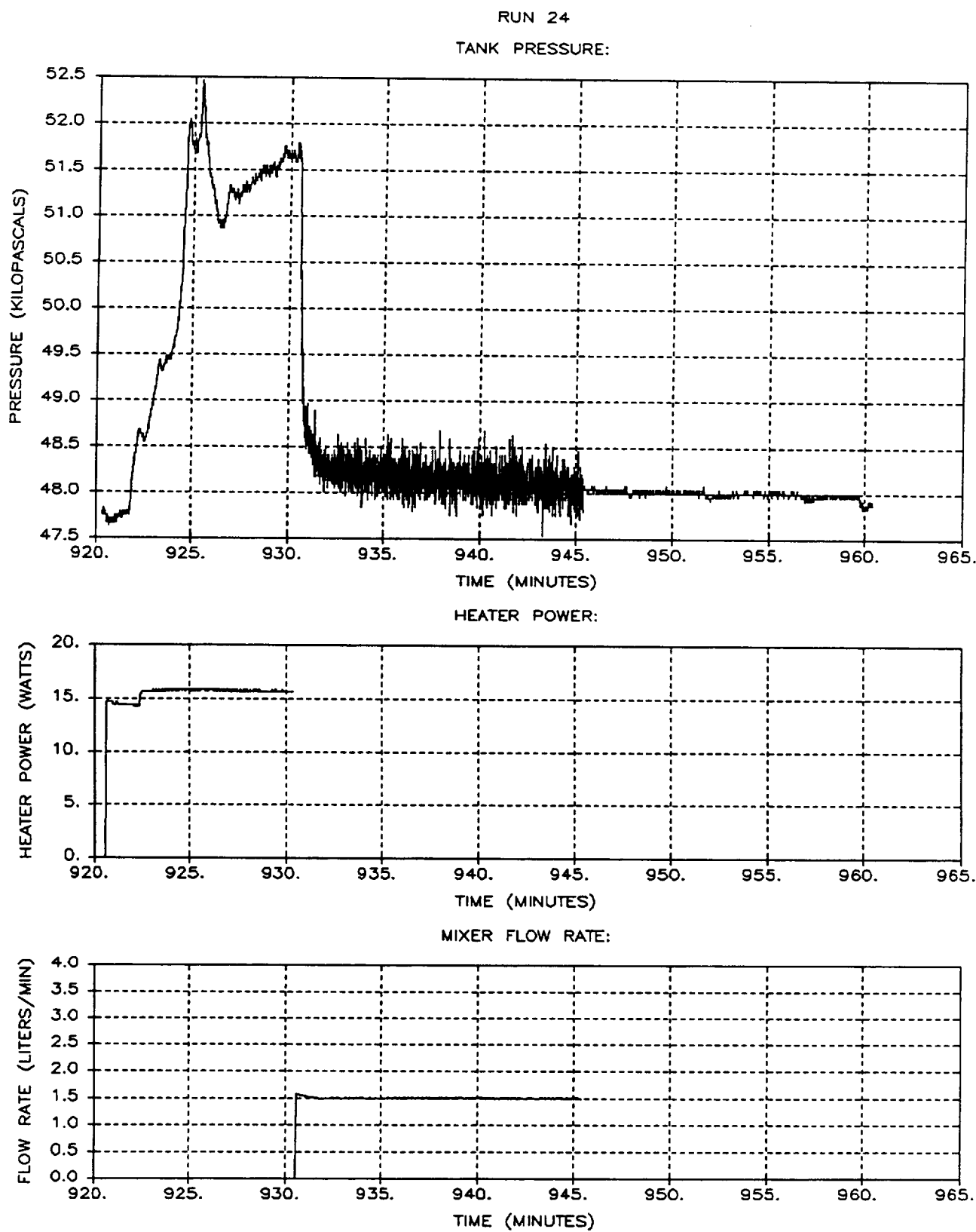
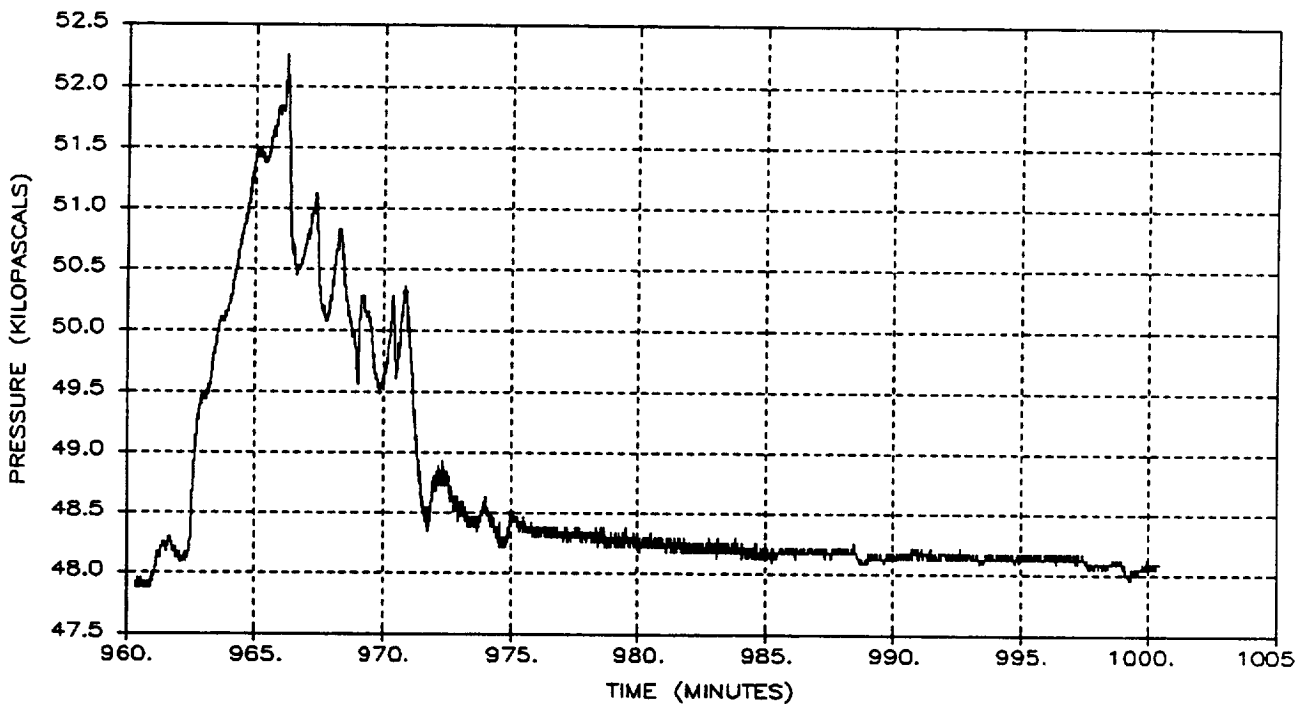


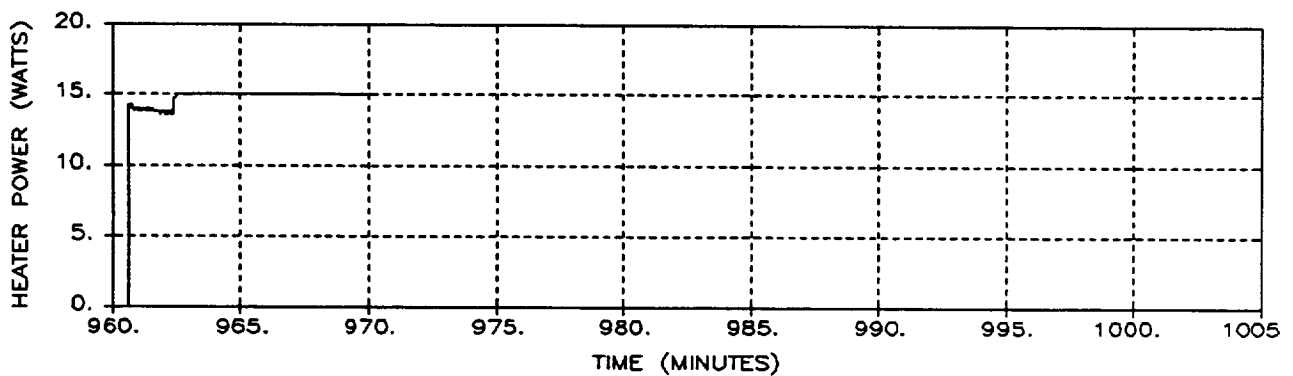
Figure A-62: Run 24 Pressure, Heater Power, and Flow Rate
A-63

RUN 25

TANK PRESSURE:



HEATER POWER:



MIXER FLOW RATE:

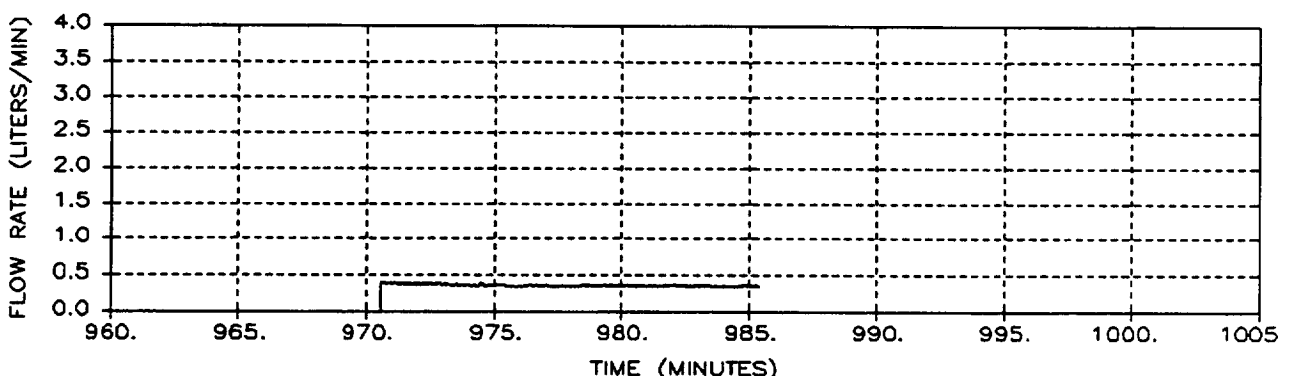


Figure A-63: Run 25 Pressure, Heater Power, and Flow Rate
A-64

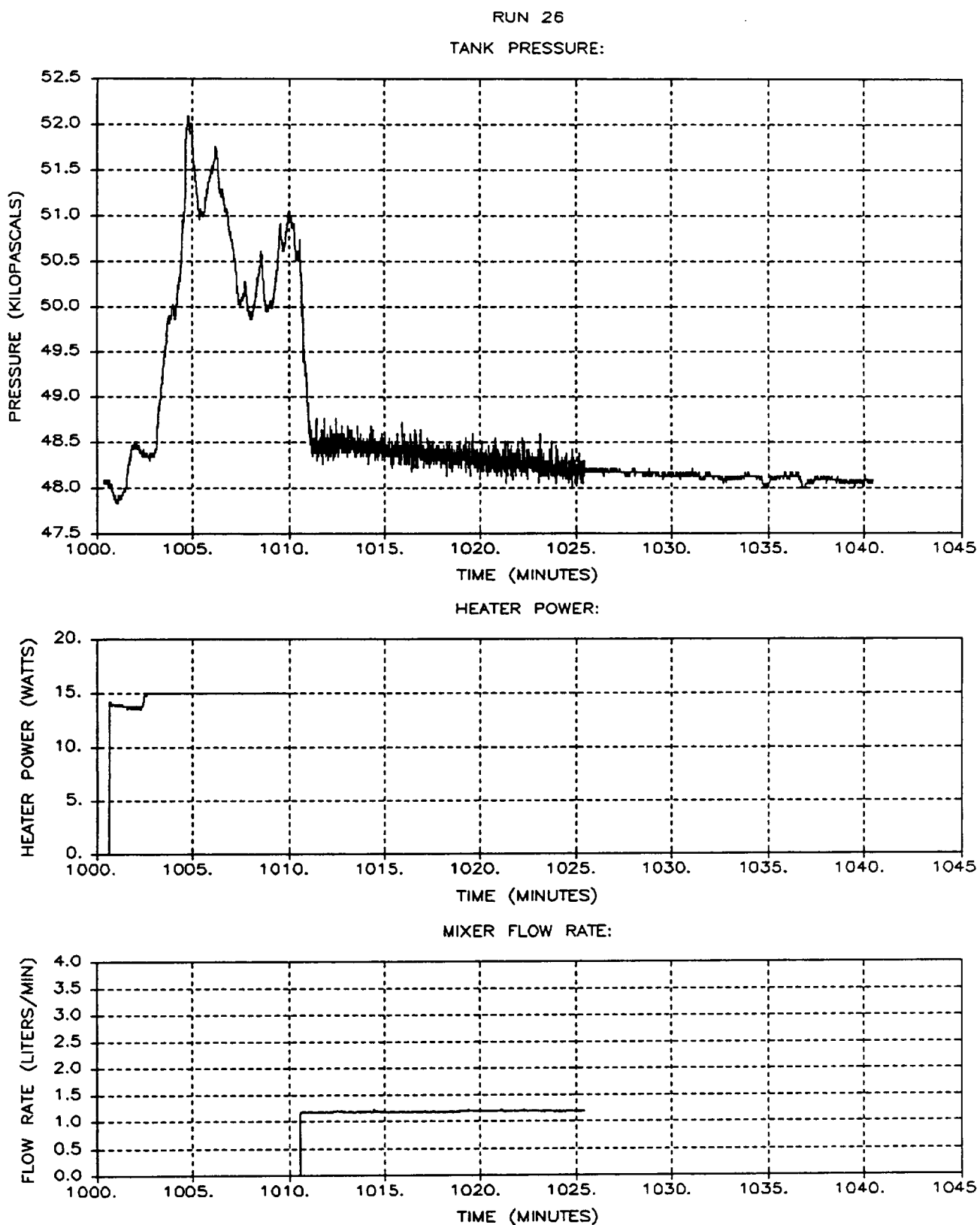
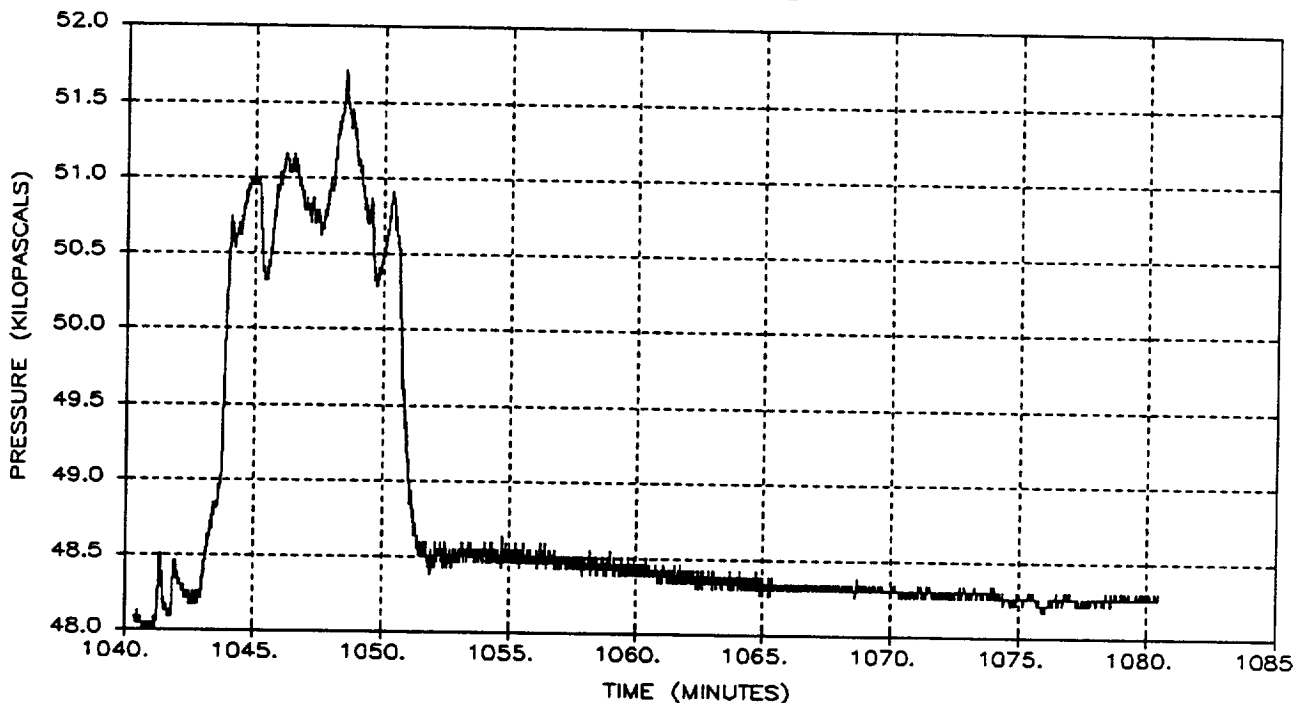


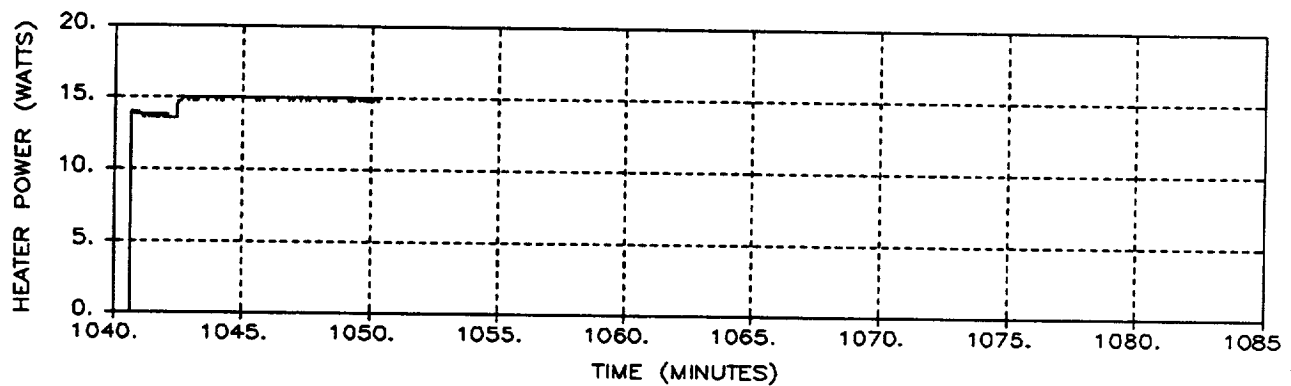
Figure A-64: Run 26 Pressure, Heater Power, and Flow Rate
A-65

RUN 27

TANK PRESSURE:



HEATER POWER:



MIXER FLOW RATE:

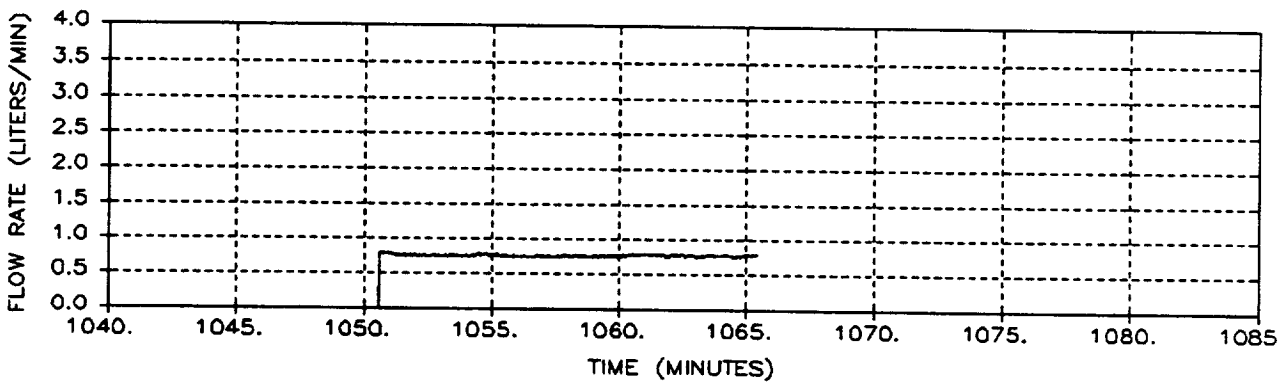


Figure A-65: Run 27 Pressure, Heater Power, and Flow Rate
A-66

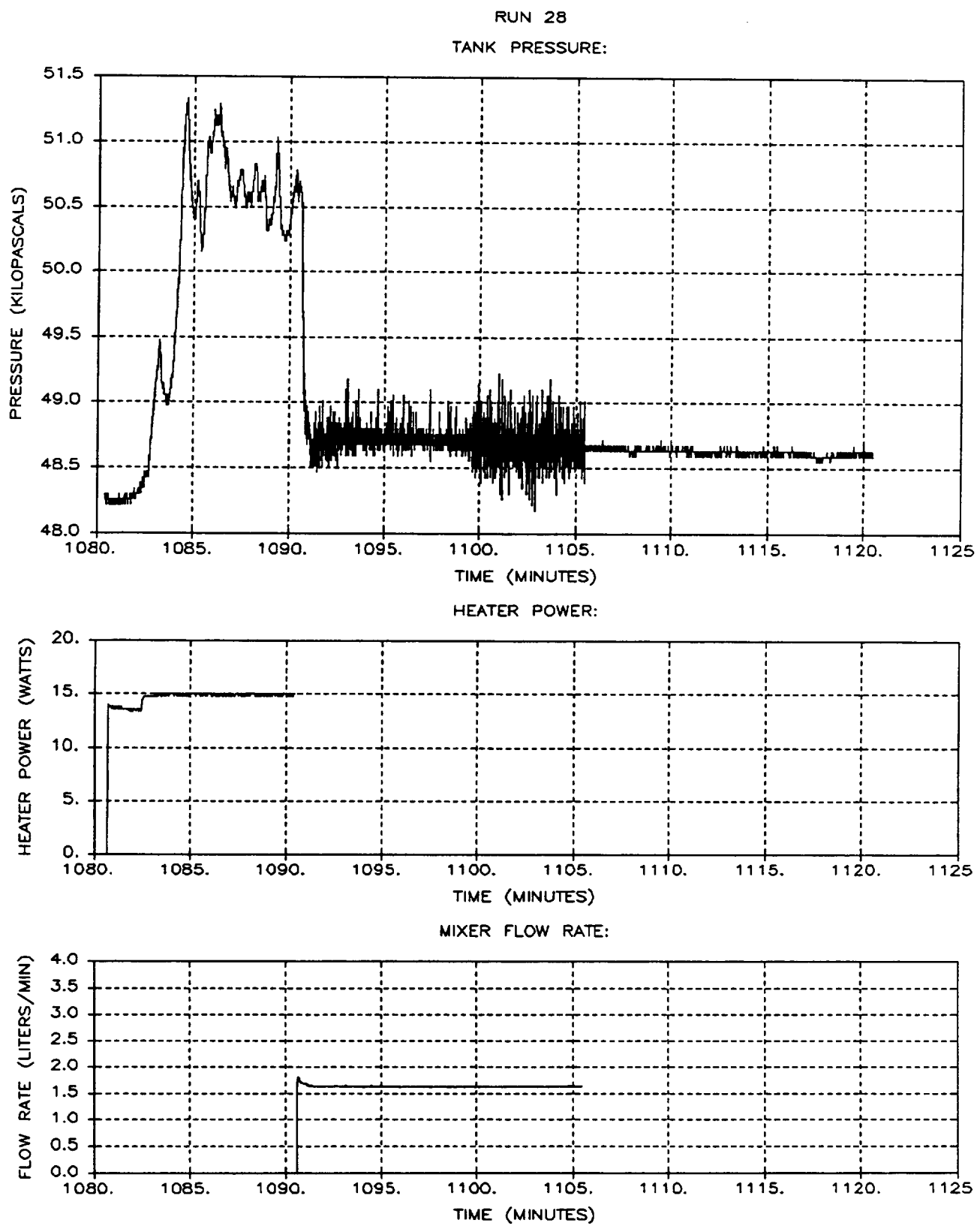
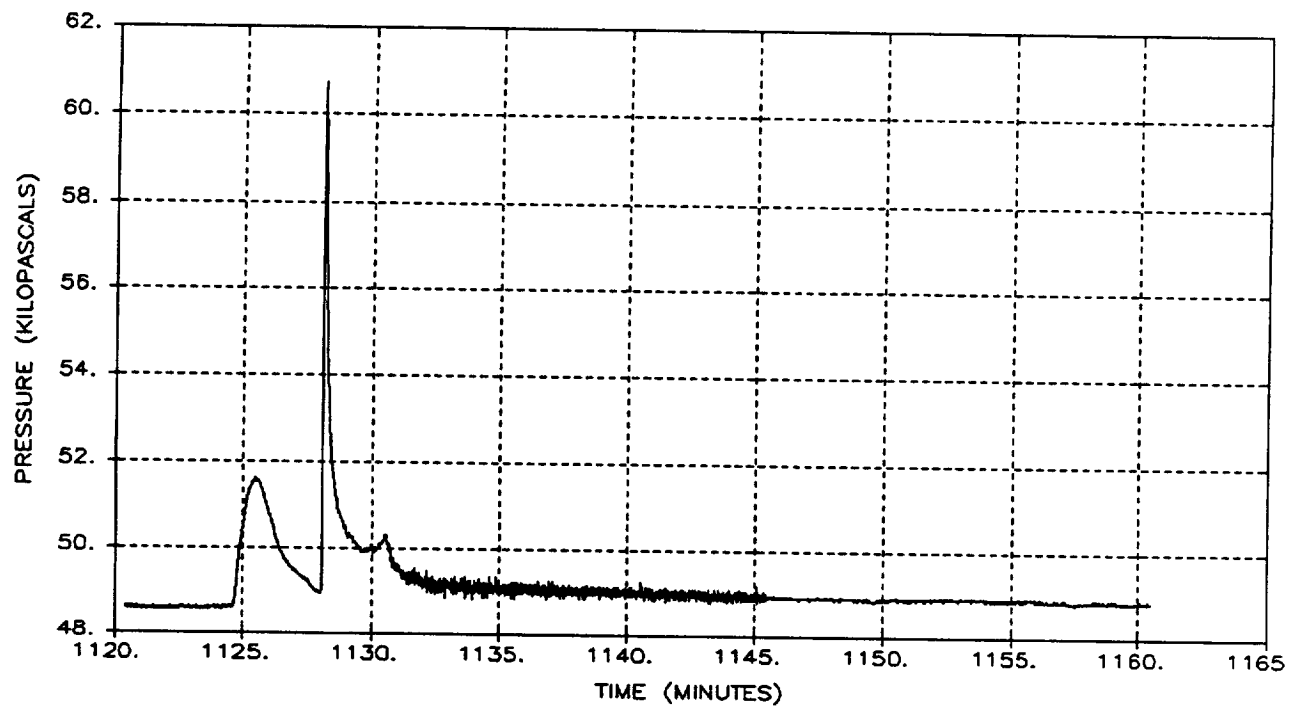


Figure A-66: Run 28 Pressure, Heater Power, and Flow Rate

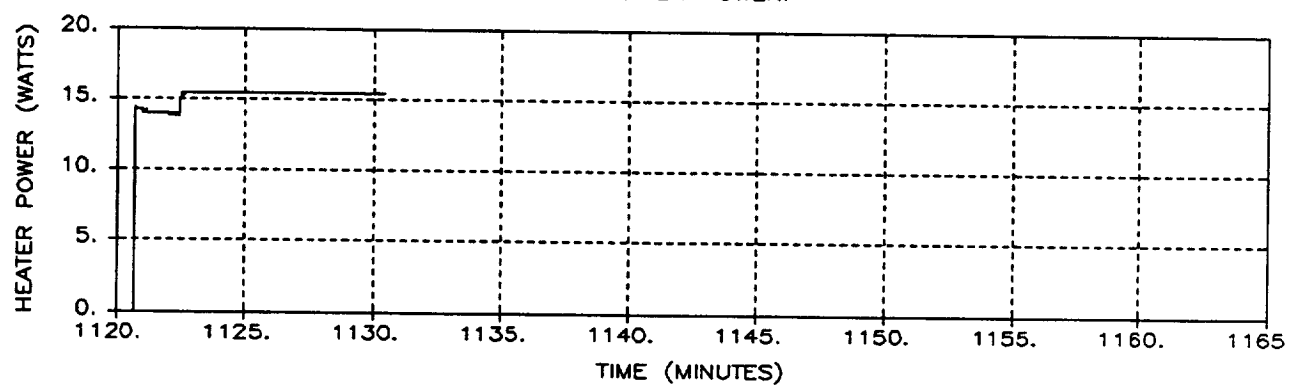
A-67

RUN 29

TANK PRESSURE:



HEATER POWER:



MIXER FLOW RATE:

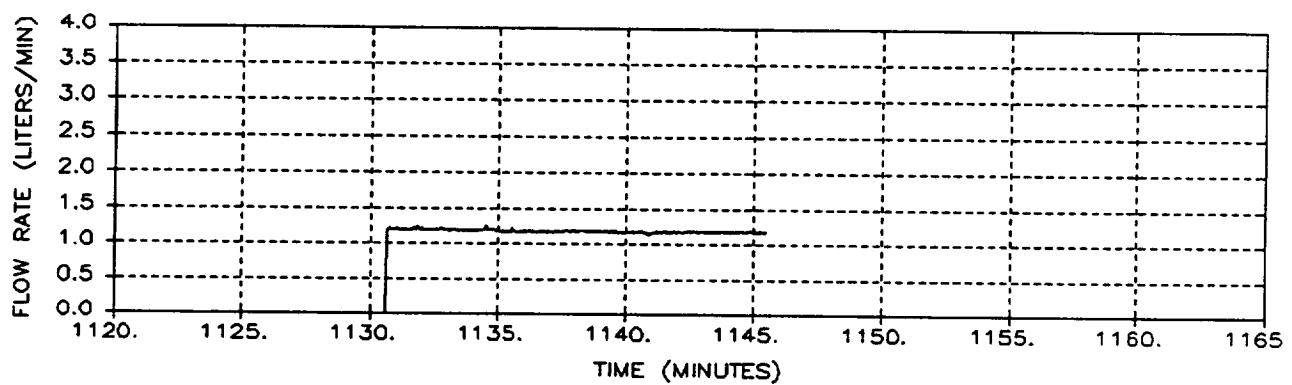


Figure A-67: Run 29 Pressure, Heater Power, and Flow Rate

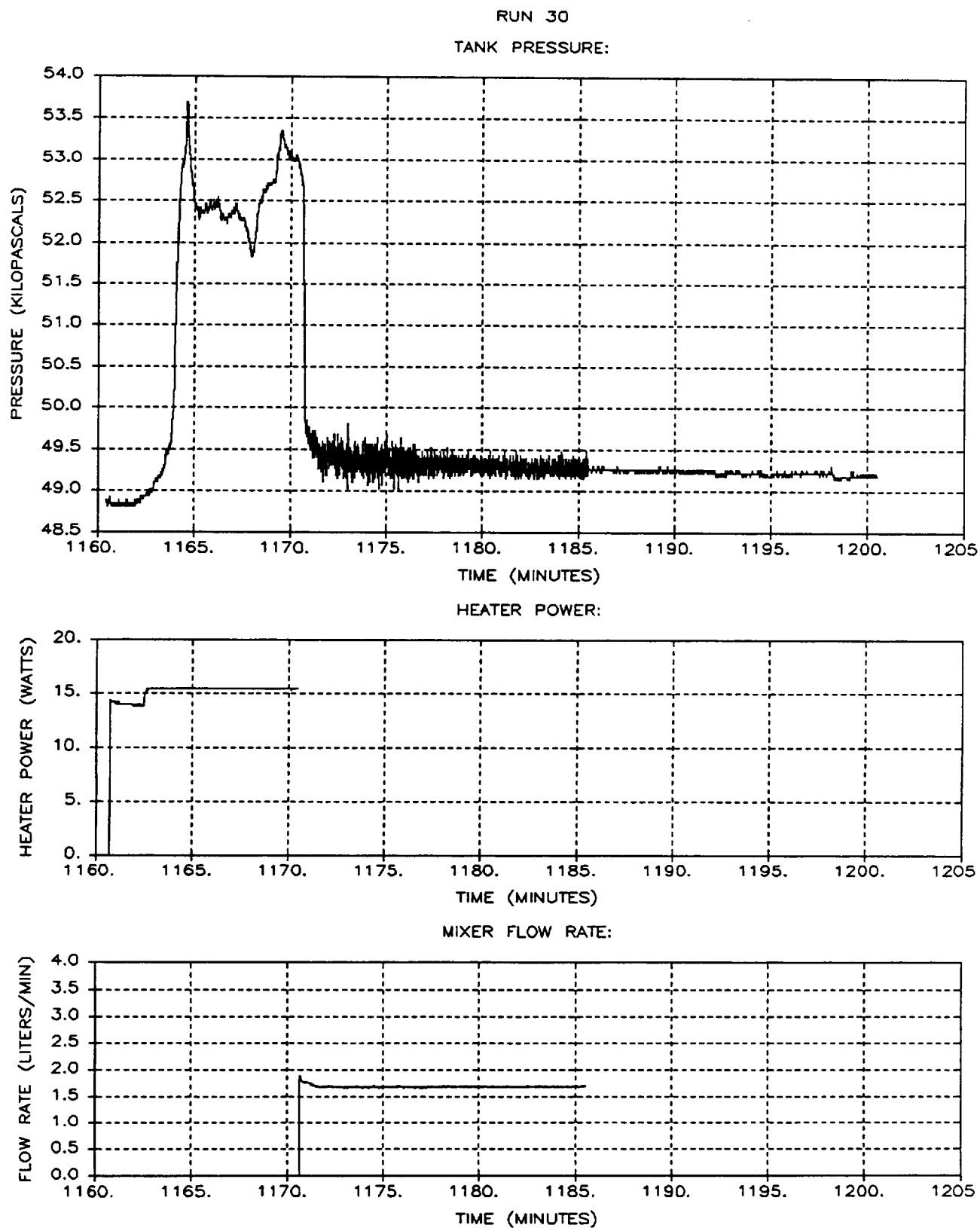
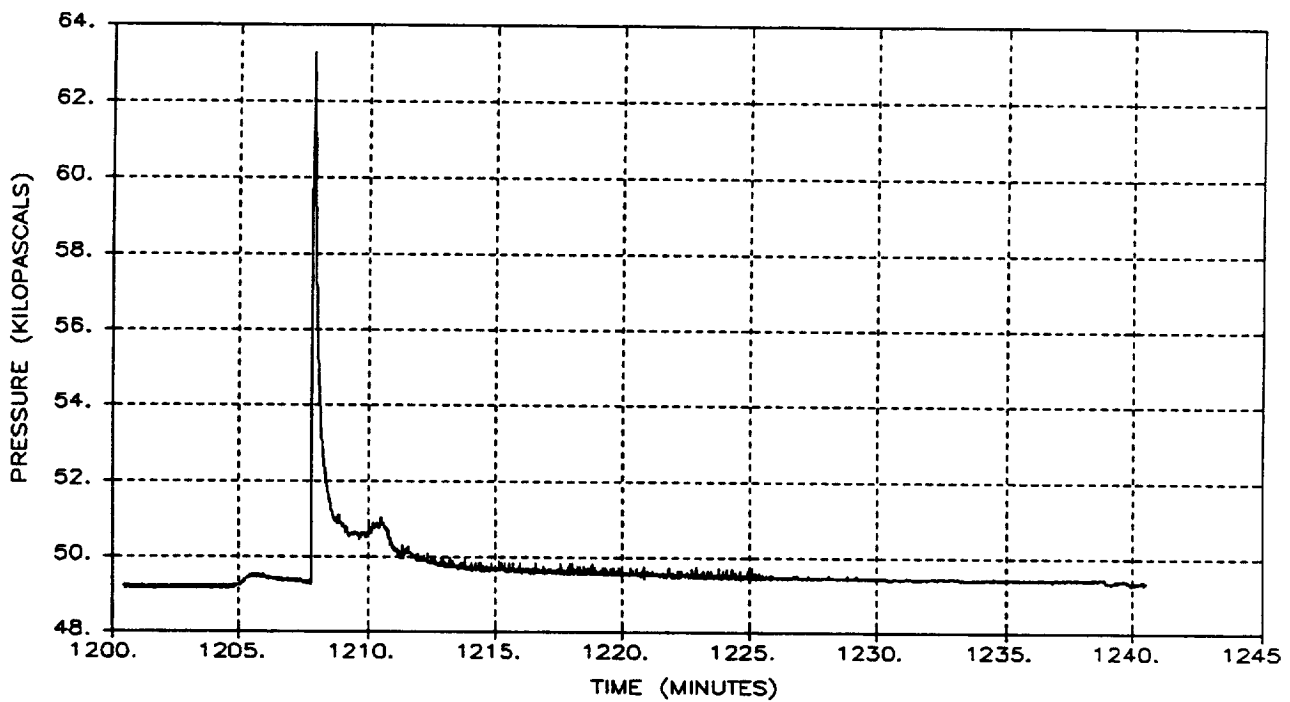


Figure A-68: Run 30 Pressure, Heater Power, and Flow Rate

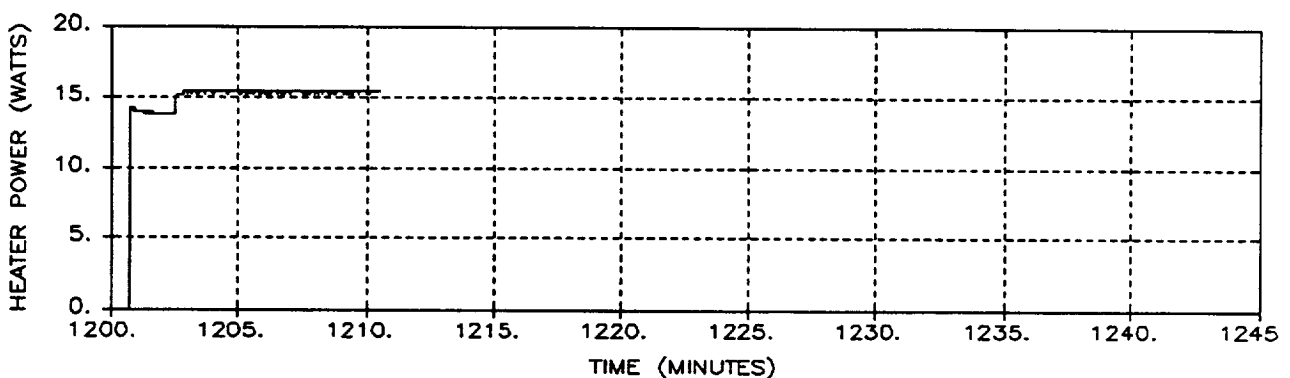
A-69

RUN 31

TANK PRESSURE:



HEATER POWER:



MIXER FLOW RATE:

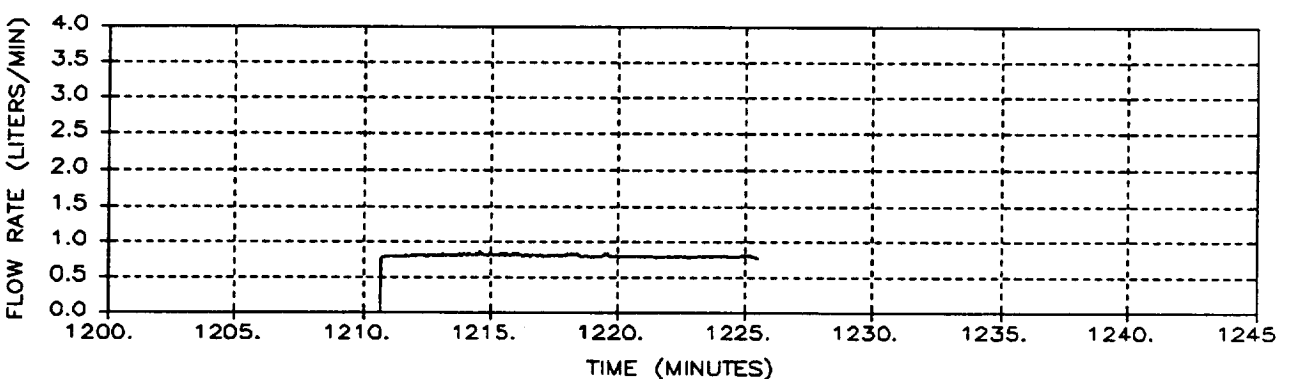
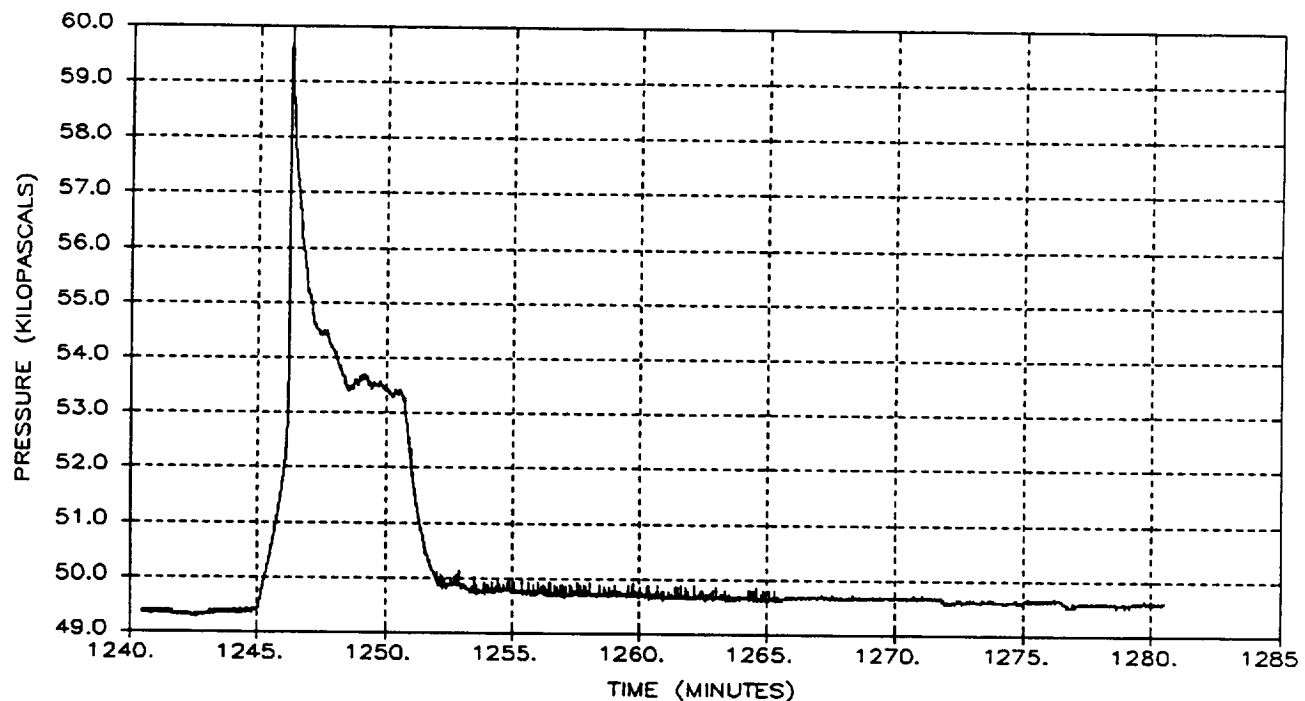


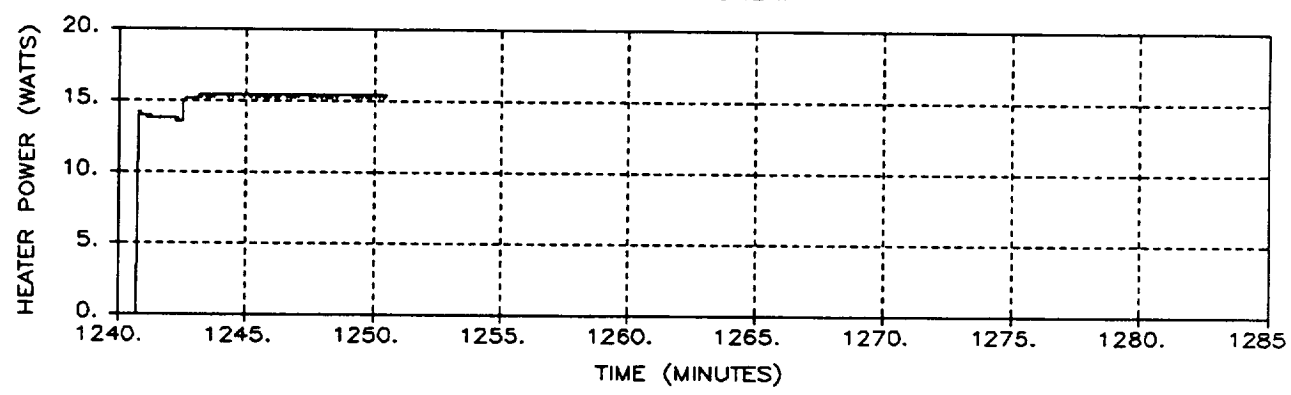
Figure A-69: Run 31 Pressure, Heater Power, and Flow Rate

RUN 32

TANK PRESSURE:



HEATER POWER:



MIXER FLOW RATE:

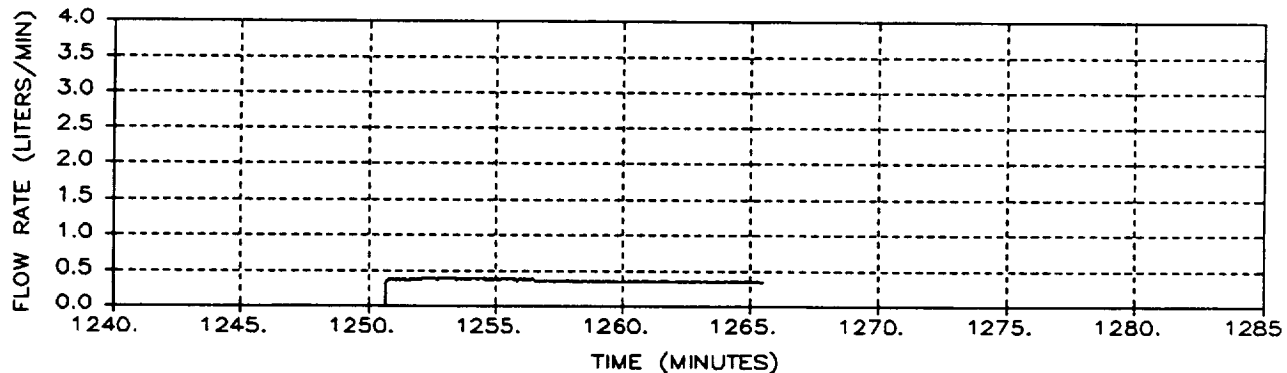


Figure A-70: Run 32 Pressure, Heater Power, and Flow Rate

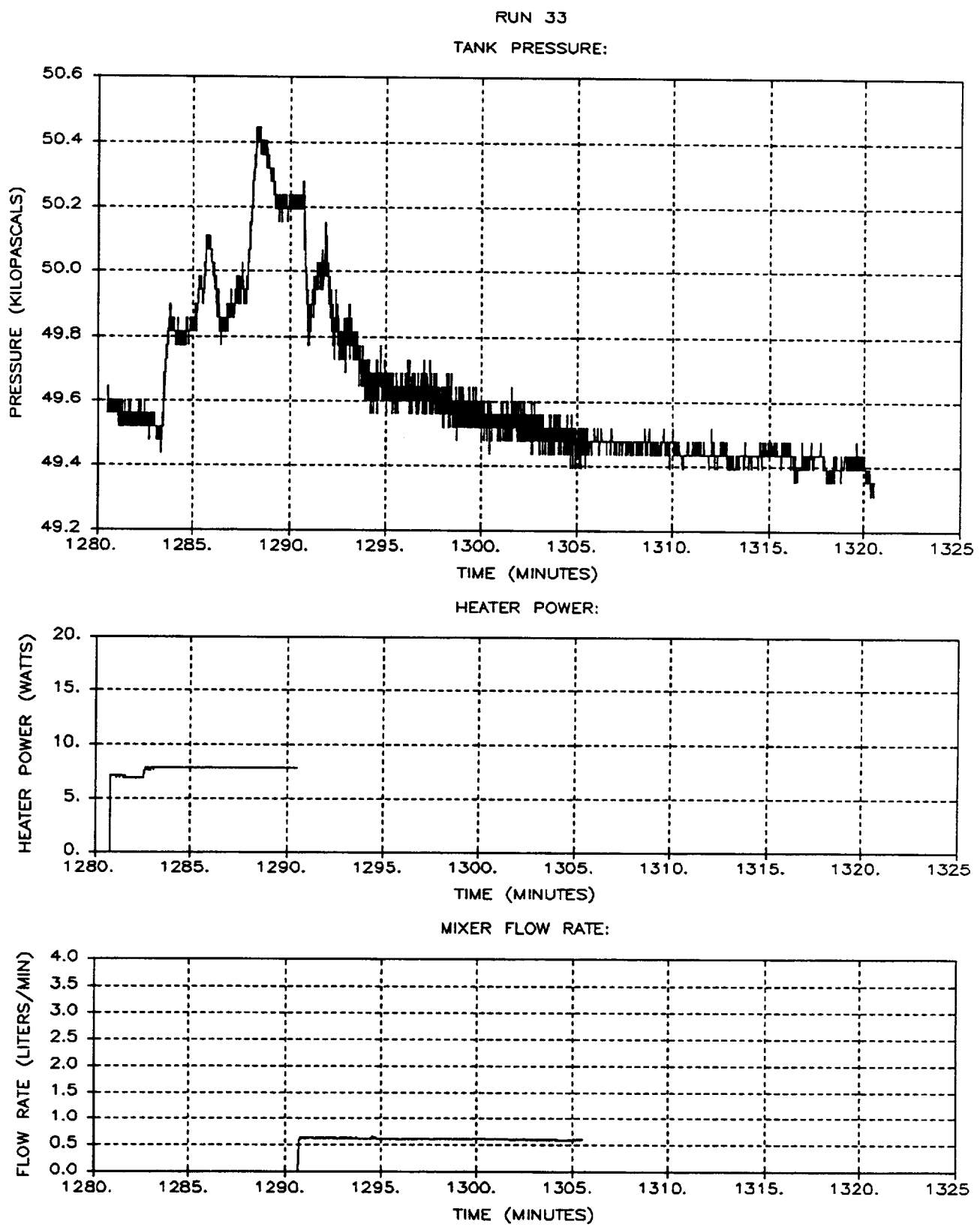


Figure A-71: Run 33 Pressure, Heater Power, and Flow Rate
A-72

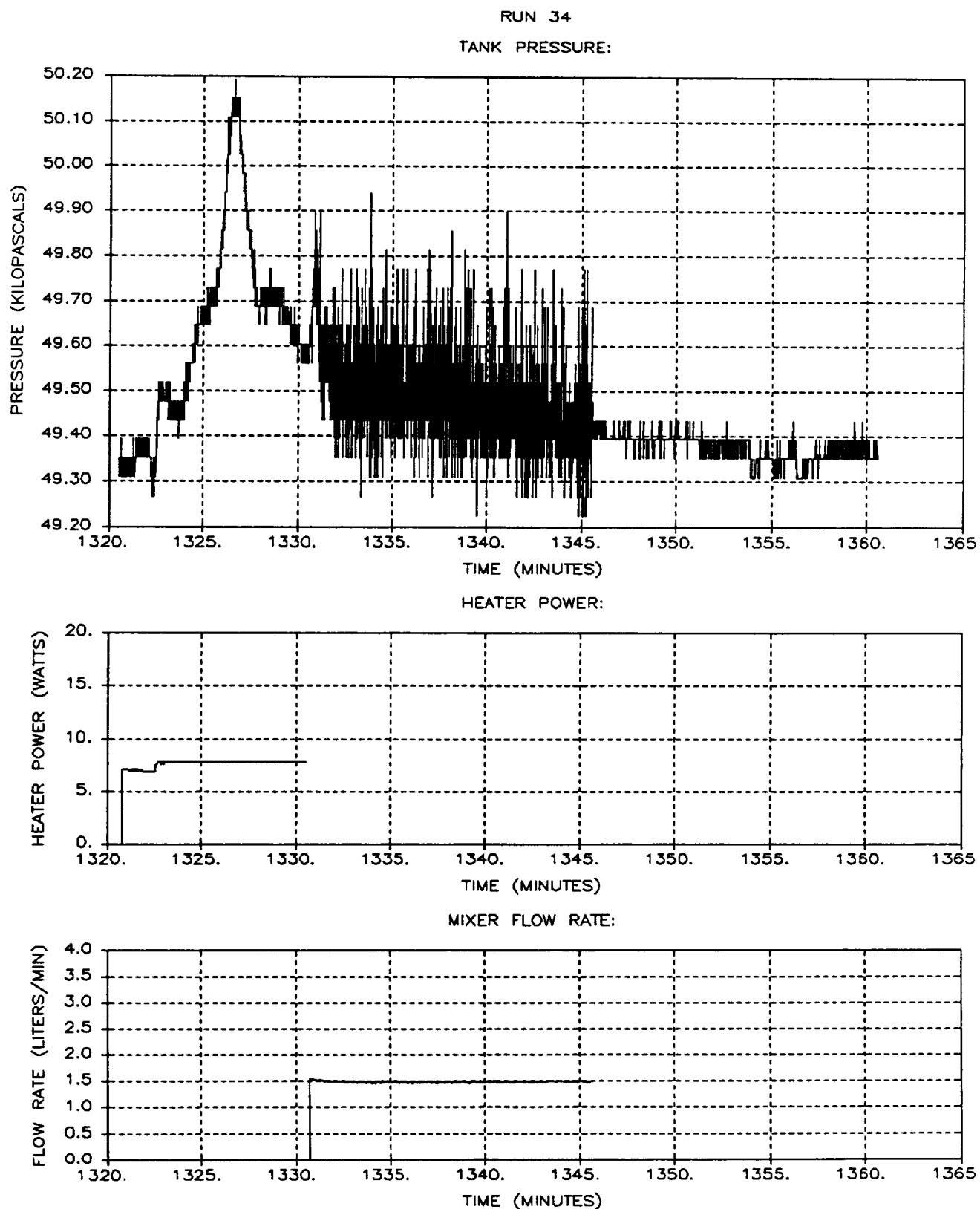


Figure A-72: Run 34 Pressure, Heater Power, and Flow Rate
A-73

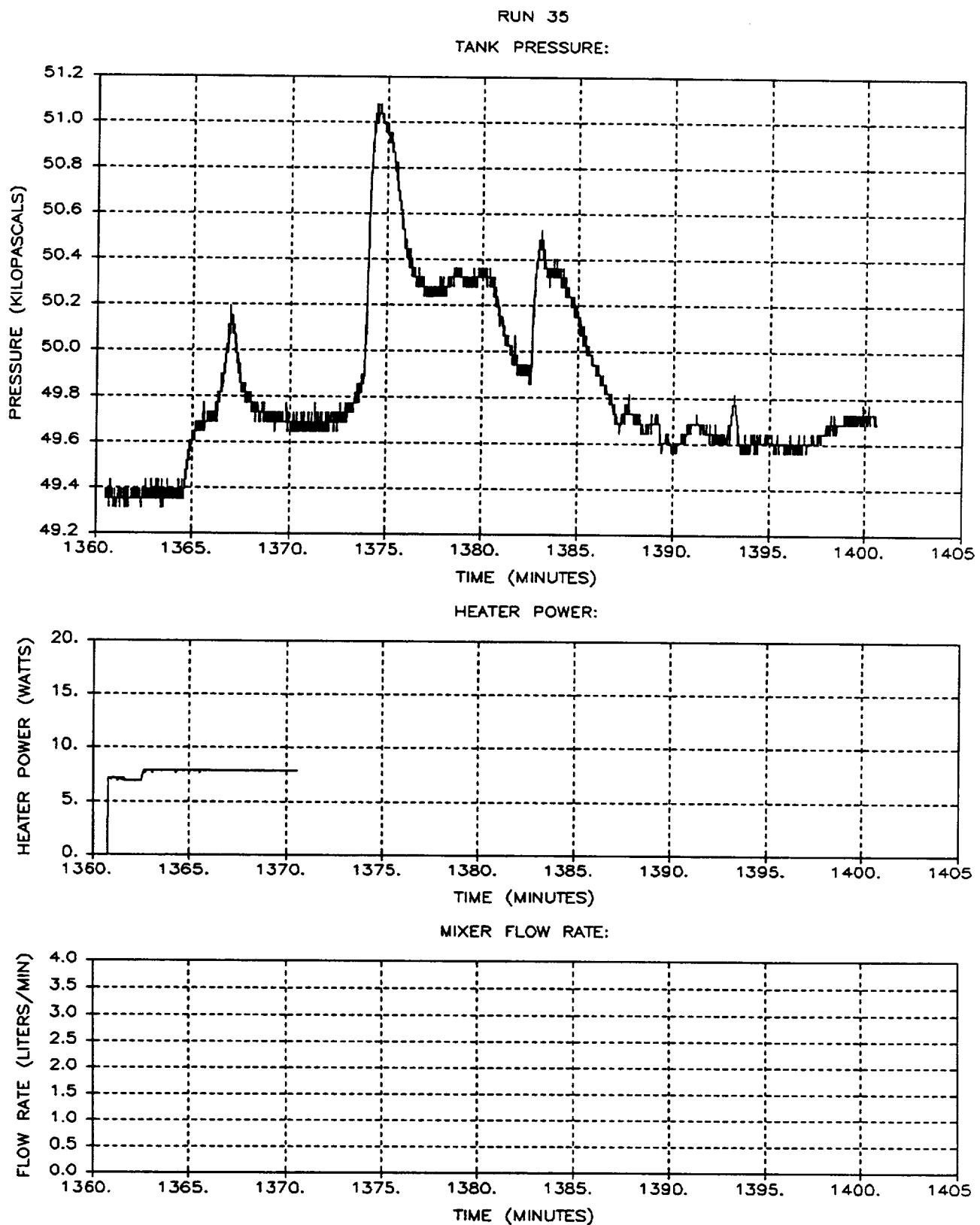


Figure A-73: Run 35 Pressure, Heater Power, and Flow Rate

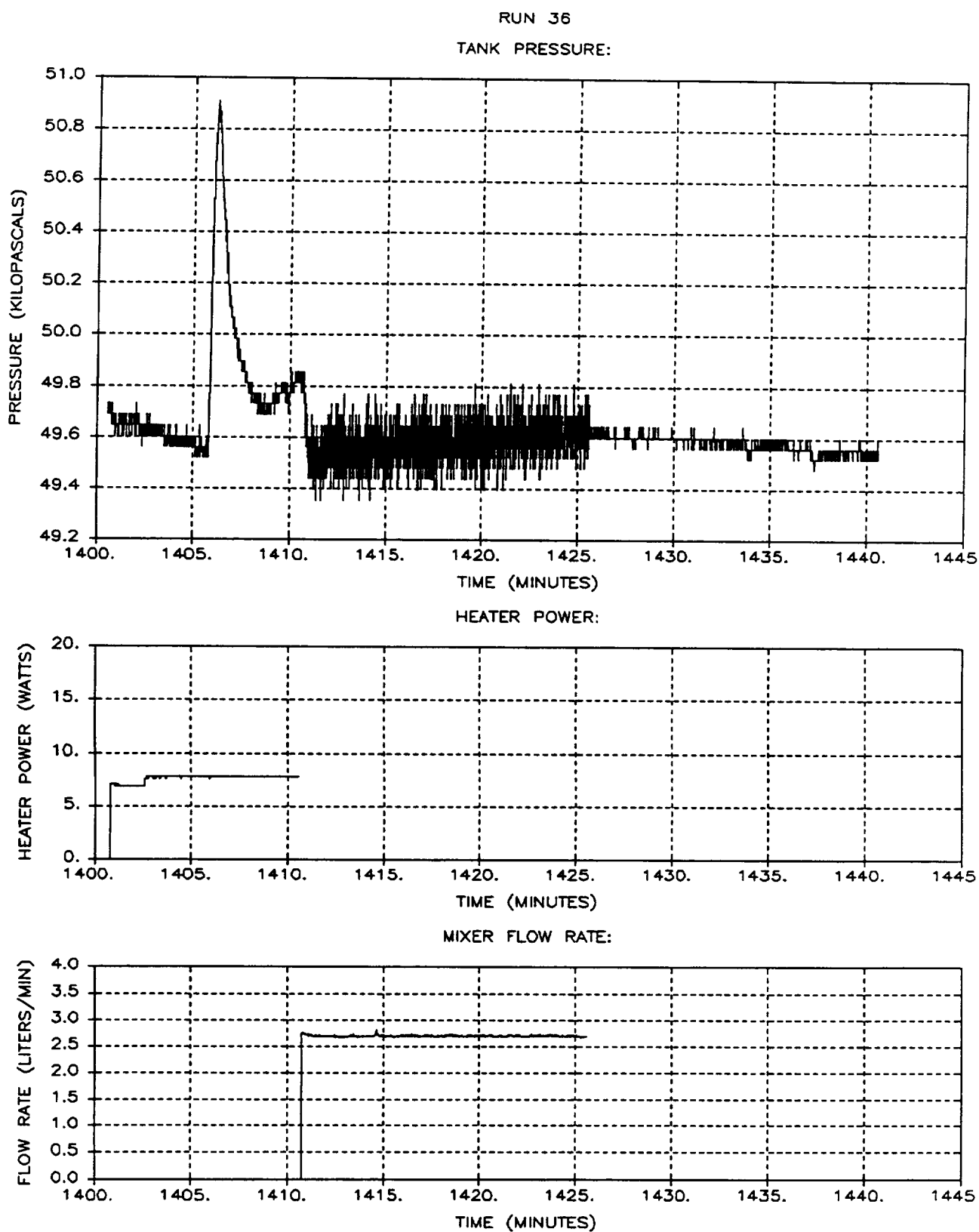
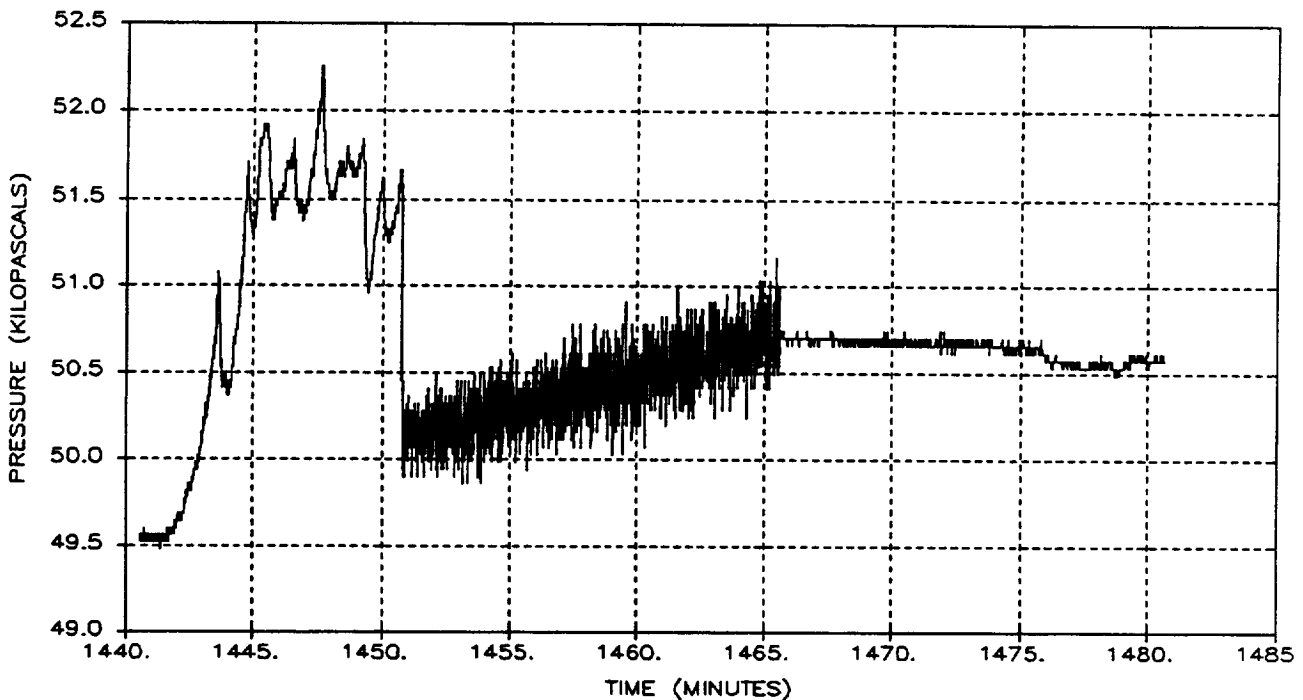


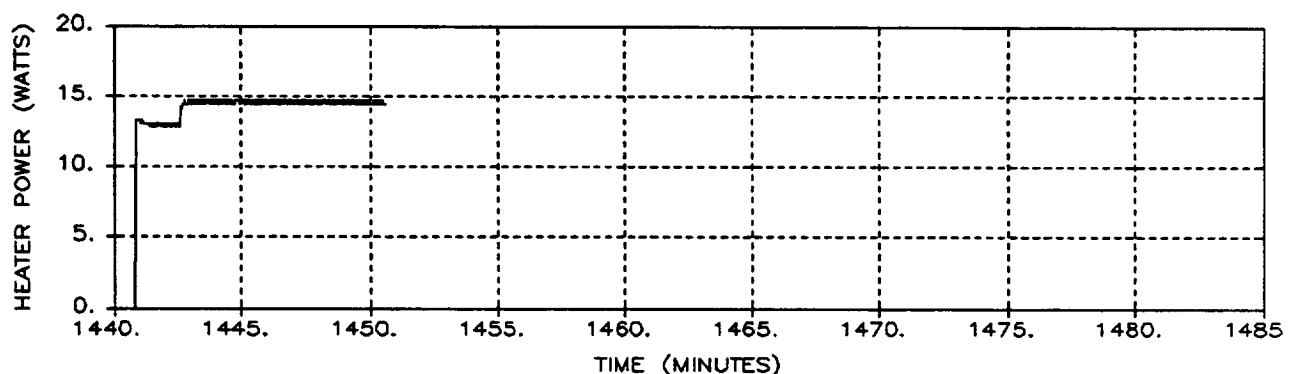
Figure A-74: Run 36 Pressure, Heater Power, and Flow Rate
A-75

RUN 37

TANK PRESSURE:



HEATER POWER:



MIXER FLOW RATE:

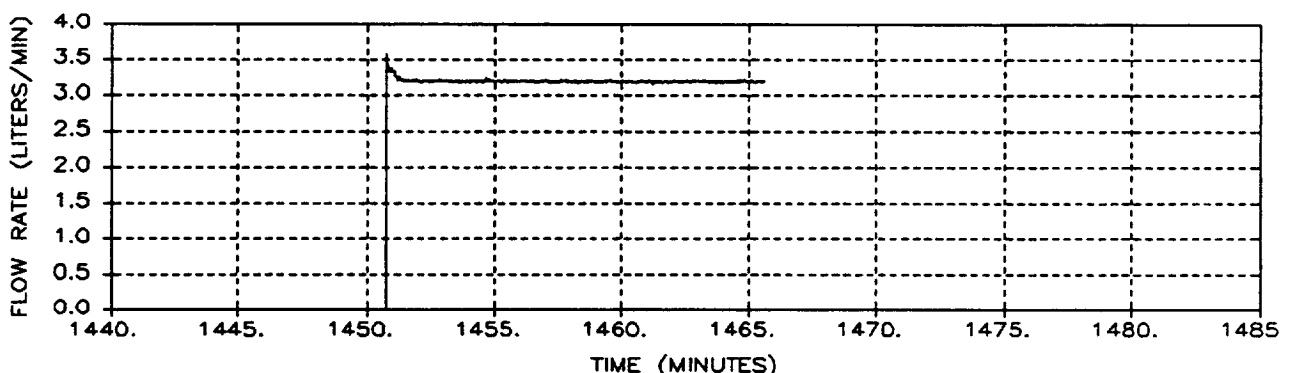
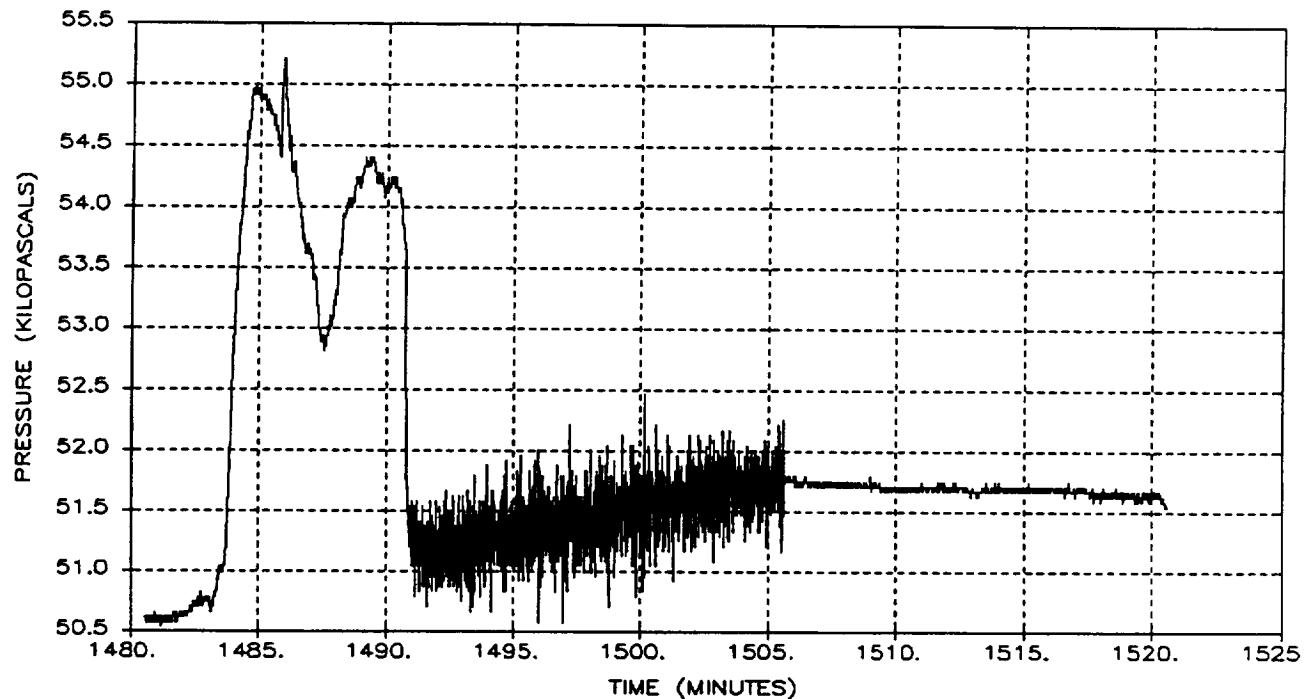
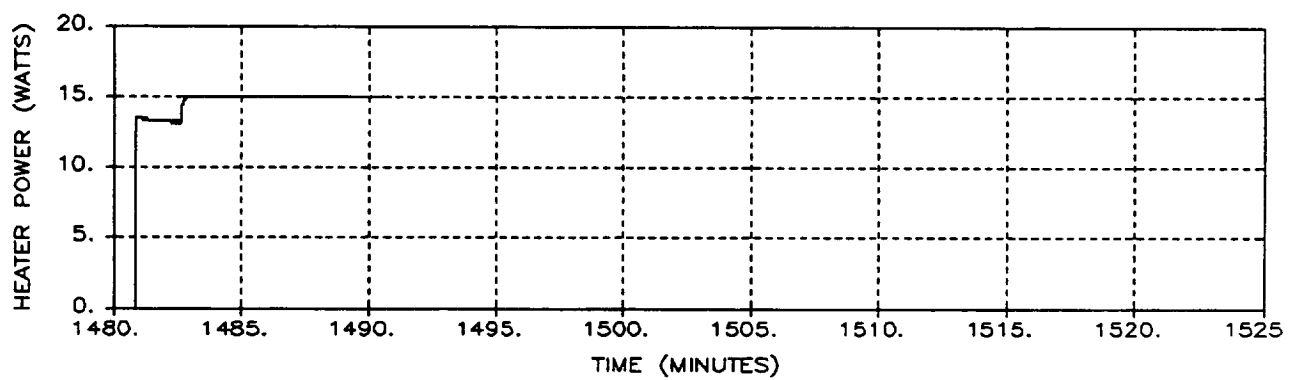


Figure A-75: Run 37 Pressure, Heater Power, and Flow Rate

RUN 38
TANK PRESSURE:



HEATER POWER:



MIXER FLOW RATE:

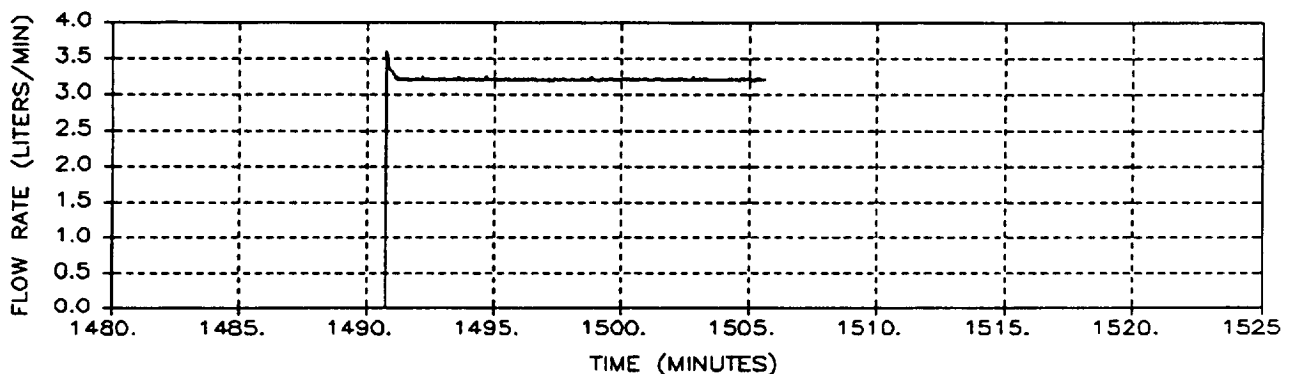


Figure A-76: Run 38 Pressure, Heater Power, and Flow Rate
A-77

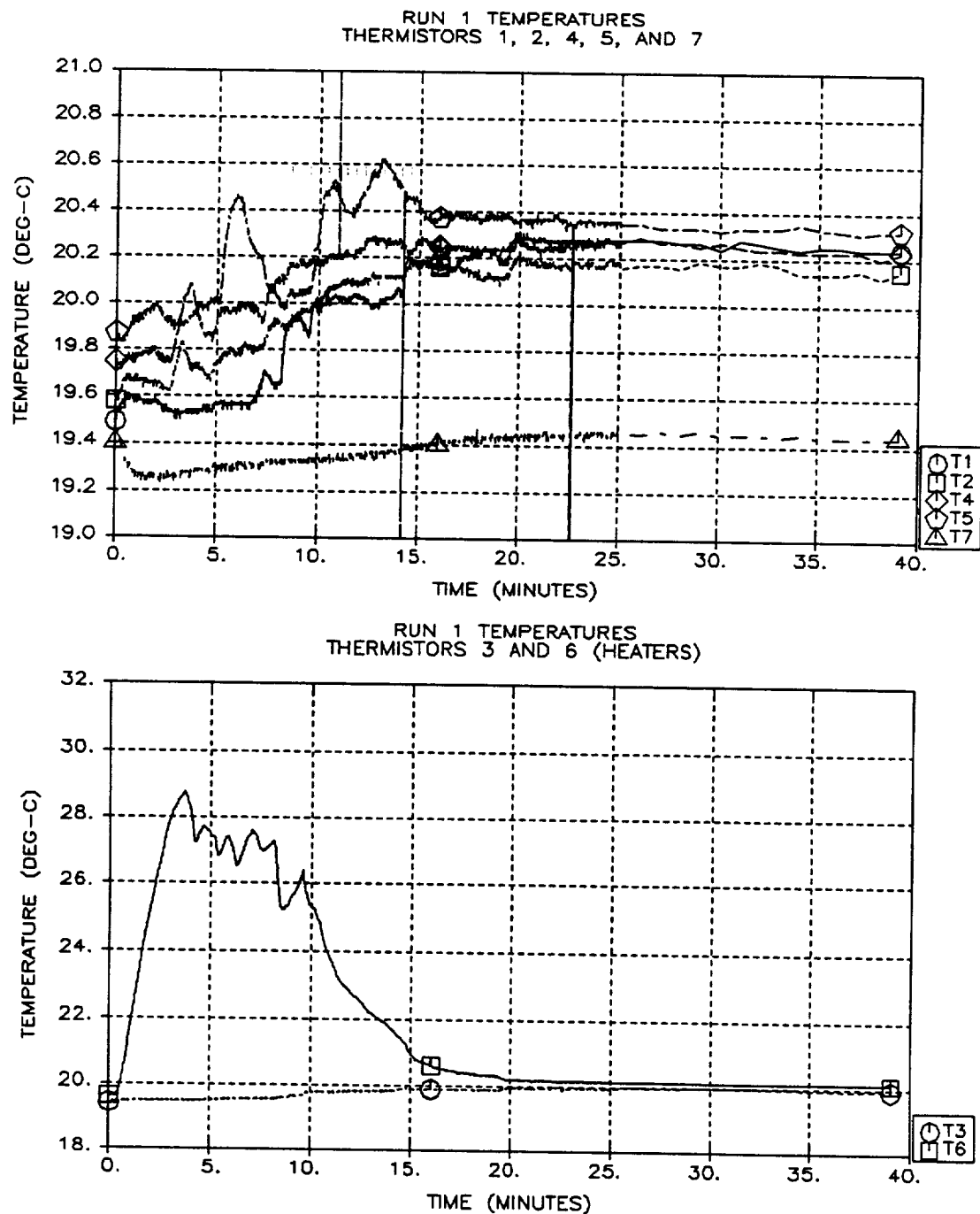


Figure A-77: Run 1 Temperatures
A-78

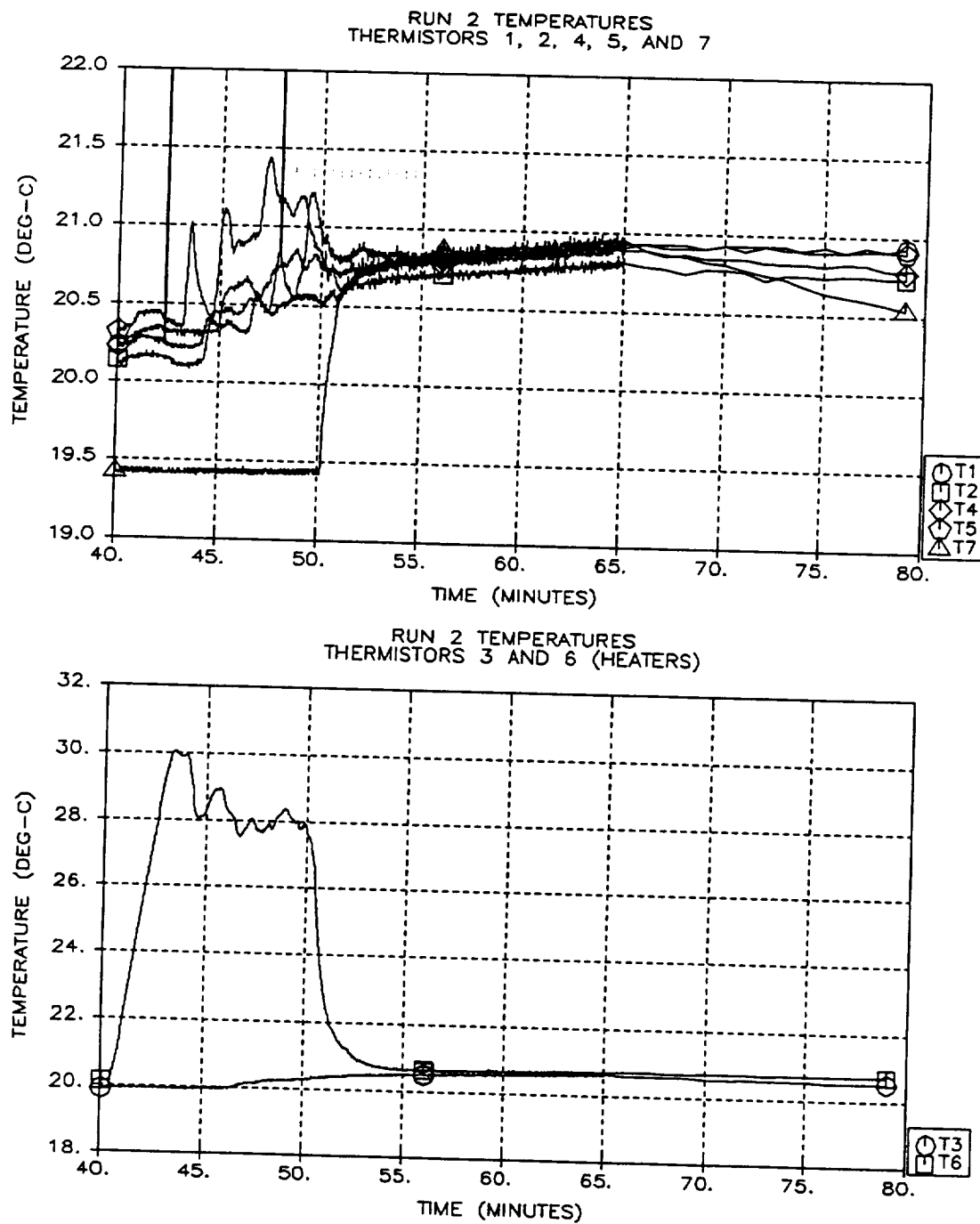
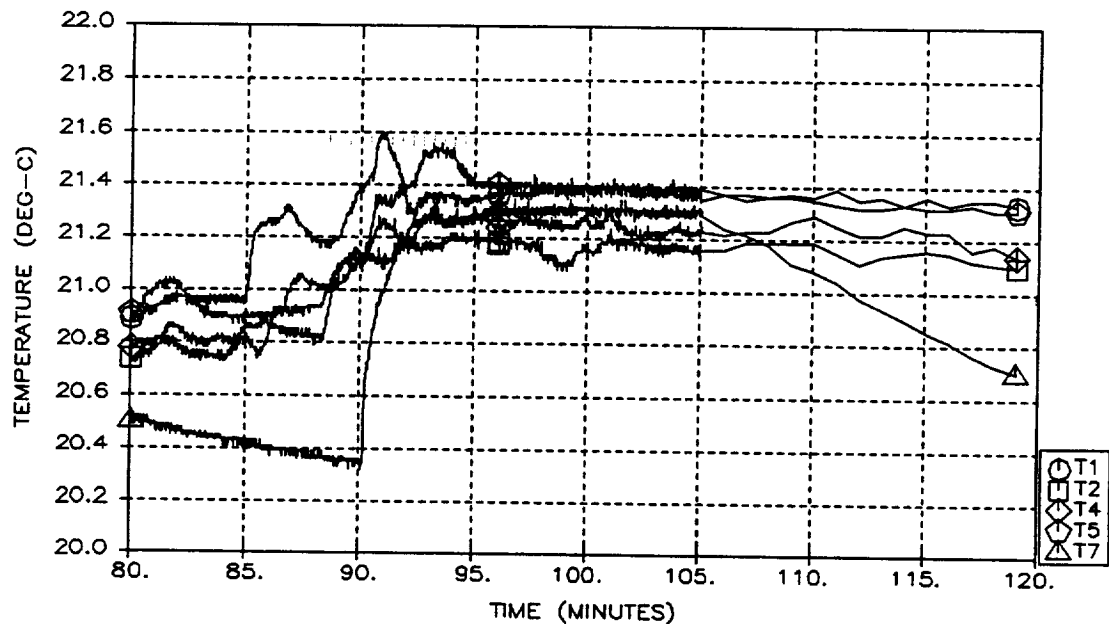


Figure A-78: Run 2 Temperatures
A-79

RUN 3 TEMPERATURES
THERMISTORS 1, 2, 4, 5, AND 7



RUN 3 TEMPERATURES
THERMISTORS 3 AND 6 (HEATERS)

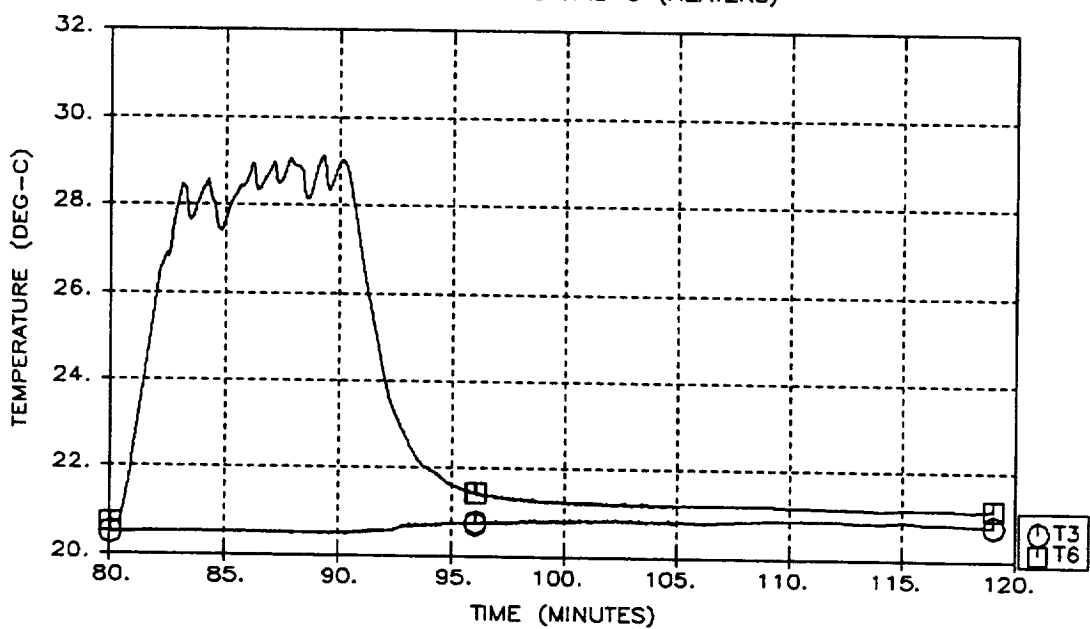
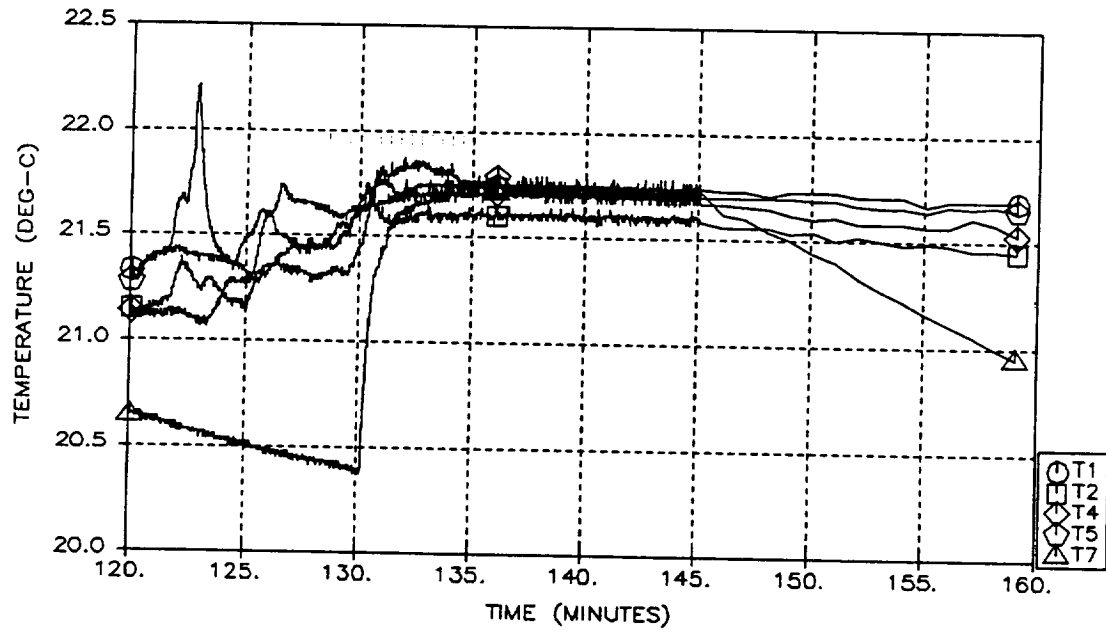


Figure A-79: Run 3 Temperatures
A-80

RUN 4 TEMPERATURES
THERMISTORS 1, 2, 4, 5, AND 7



RUN 4 TEMPERATURES
THERMISTORS 3 AND 6 (HEATERS)

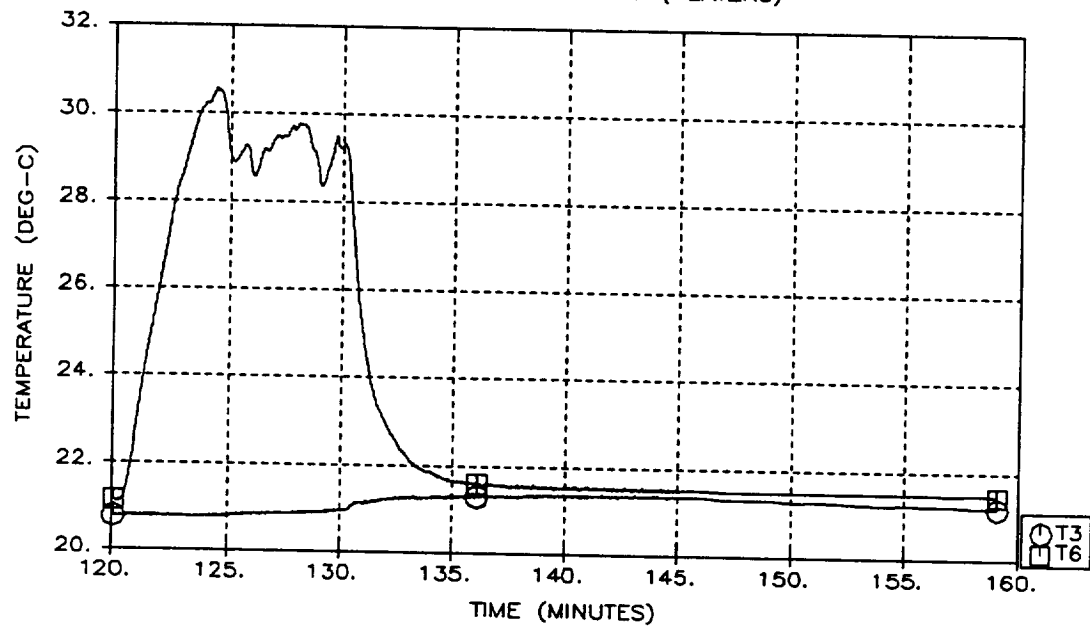


Figure A-80: Run 4 Temperatures
A-81

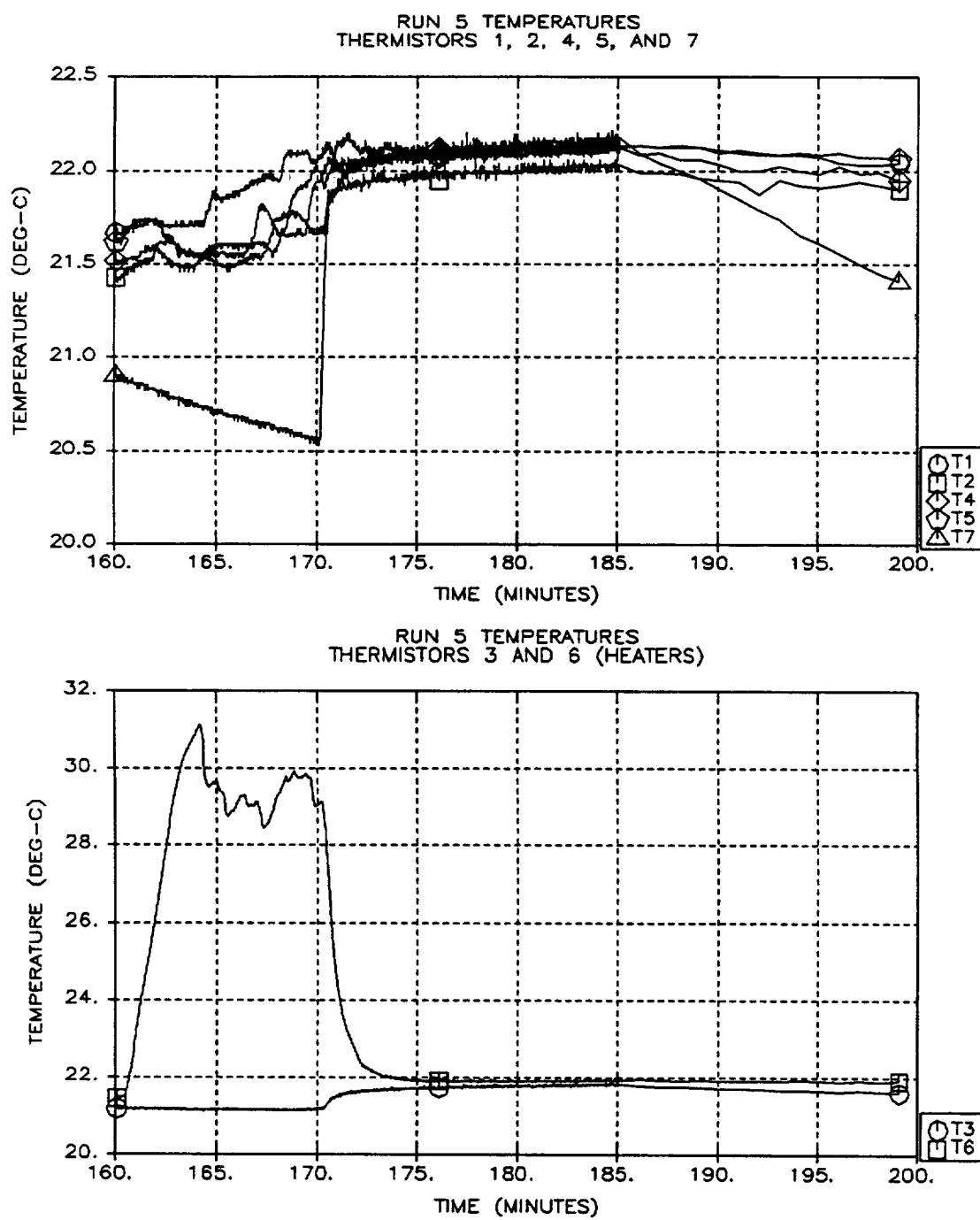
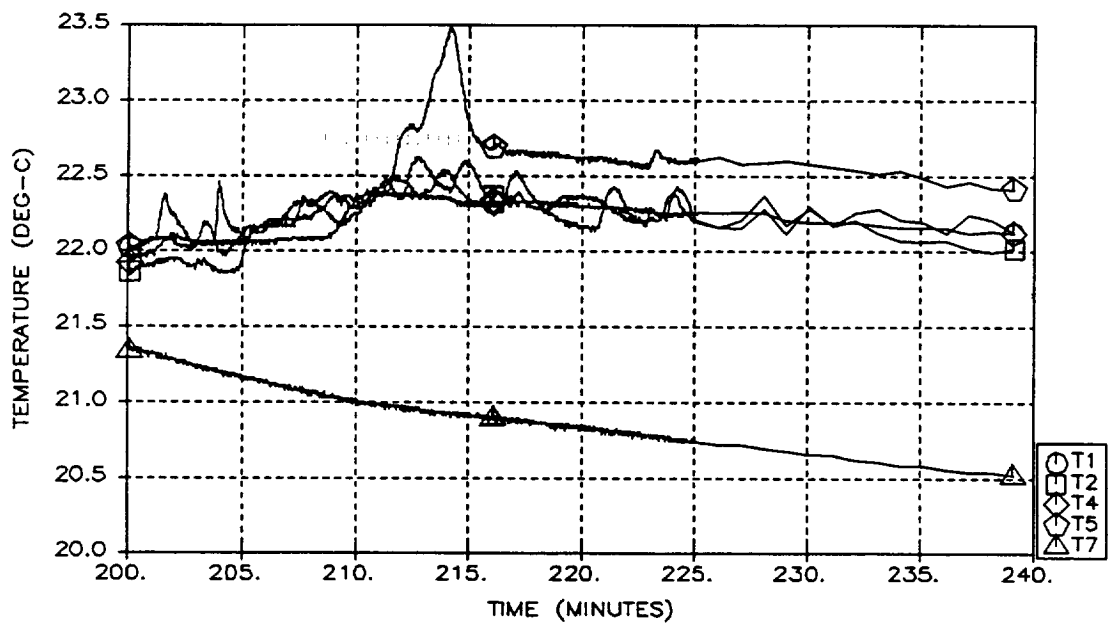


Figure A-81: Run 5 Temperatures
A-82

RUN 6 TEMPERATURES
THERMISTORS 1, 2, 4, 5, AND 7



RUN 6 TEMPERATURES
THERMISTORS 3 AND 6 (HEATERS)

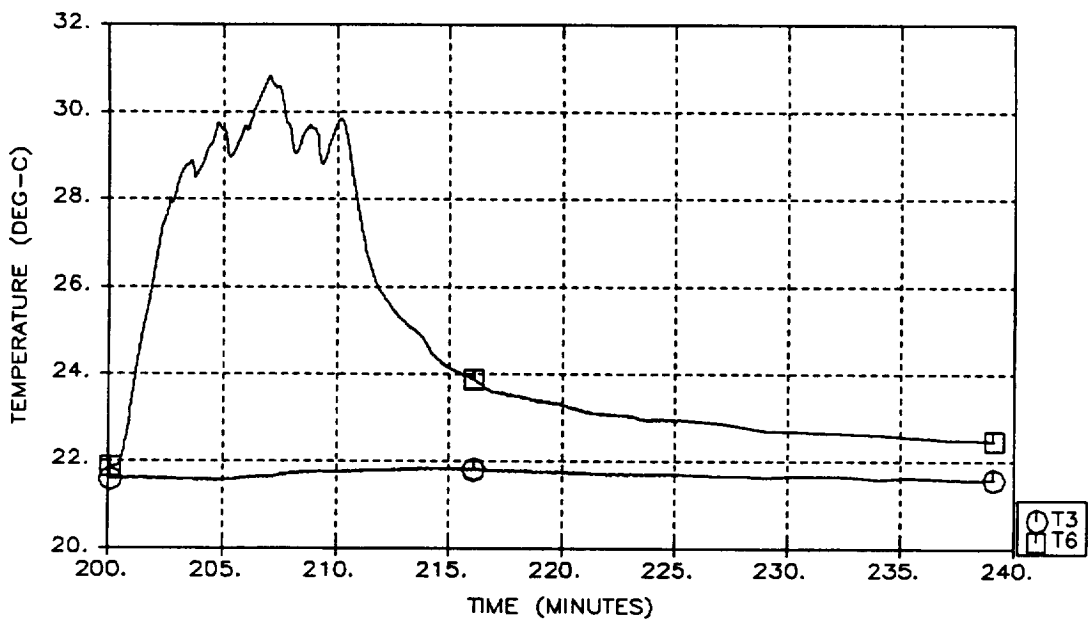
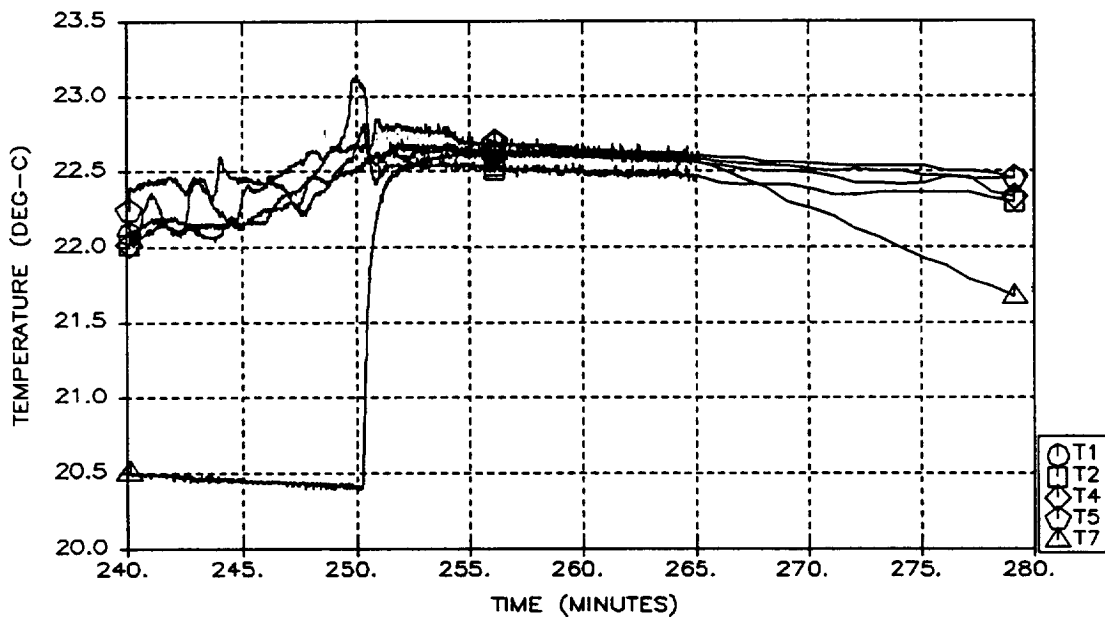


Figure A-82: Run 6 Temperatures
A-83

RUN 7 TEMPERATURES
THERMISTORS 1, 2, 4, 5, AND 7



RUN 7 TEMPERATURES
THERMISTORS 3 AND 6 (HEATERS)

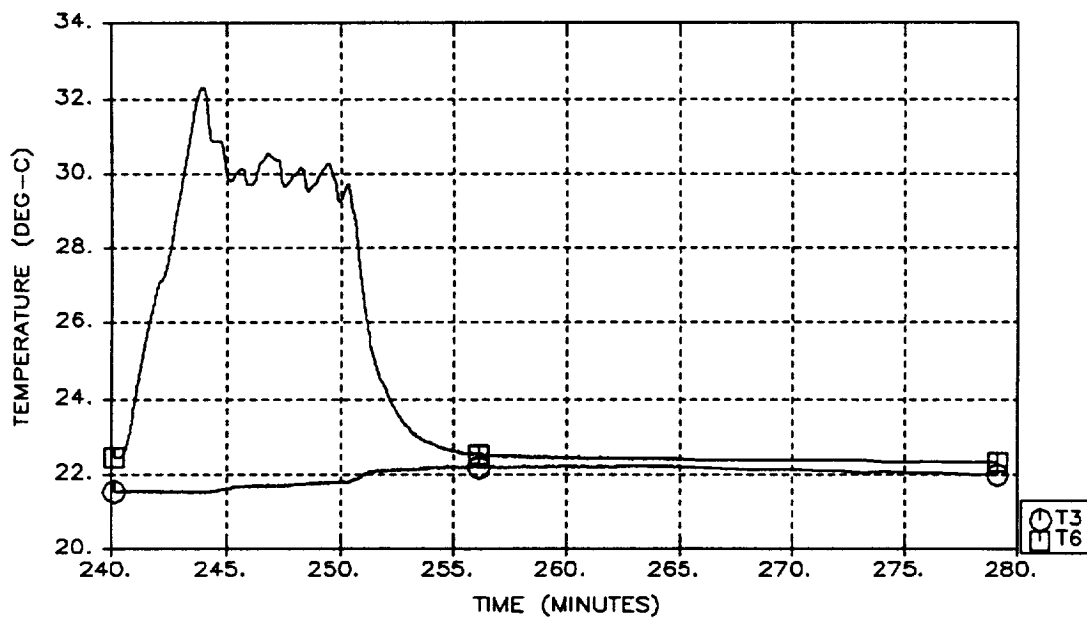
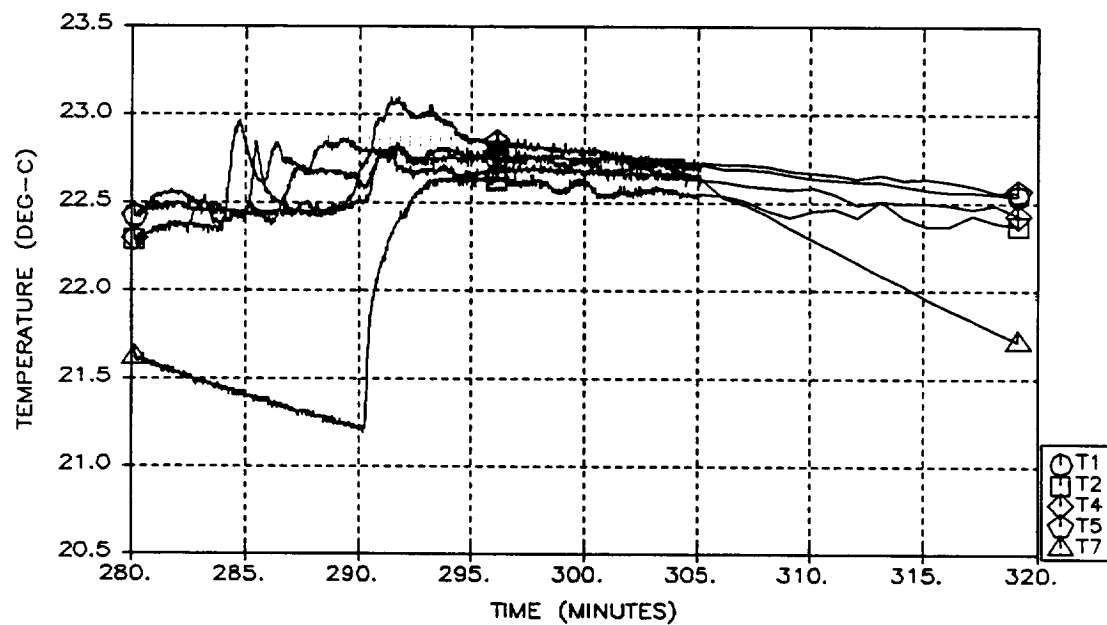


Figure A-83: Run 7 Temperatures
A-84

RUN 8 TEMPERATURES
THERMISTORS 1, 2, 4, 5, AND 7



RUN 8 TEMPERATURES
THERMISTORS 3 AND 6 (HEATERS)

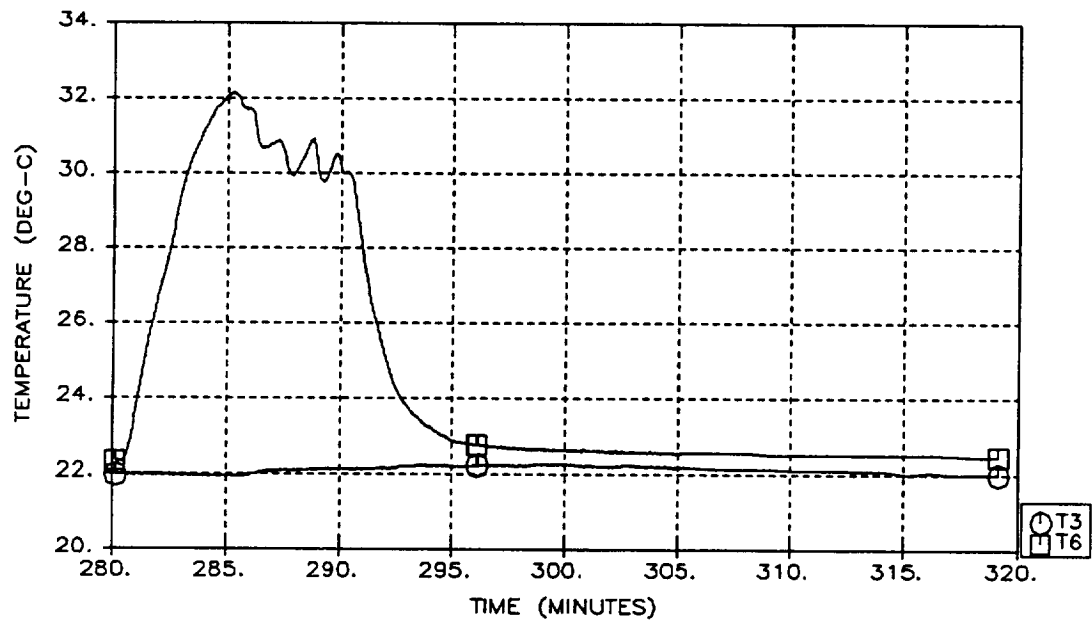
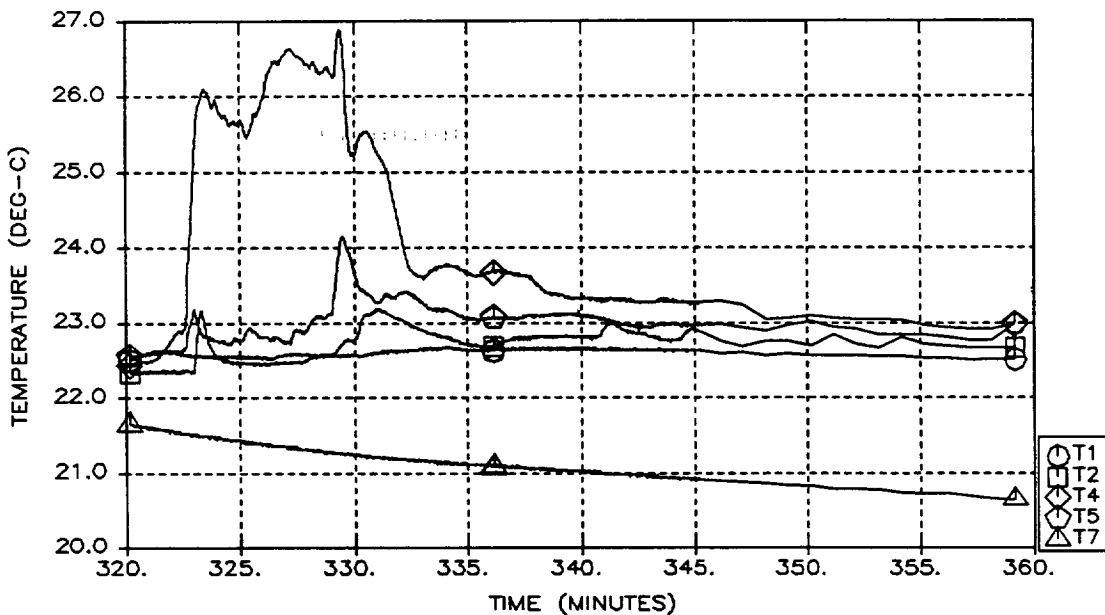


Figure A-84: Run 8 Temperatures
A-85

RUN 9 TEMPERATURES
THERMISTORS 1, 2, 4, 5, AND 7



RUN 9 TEMPERATURES
THERMISTORS 3 AND 6 (HEATERS)

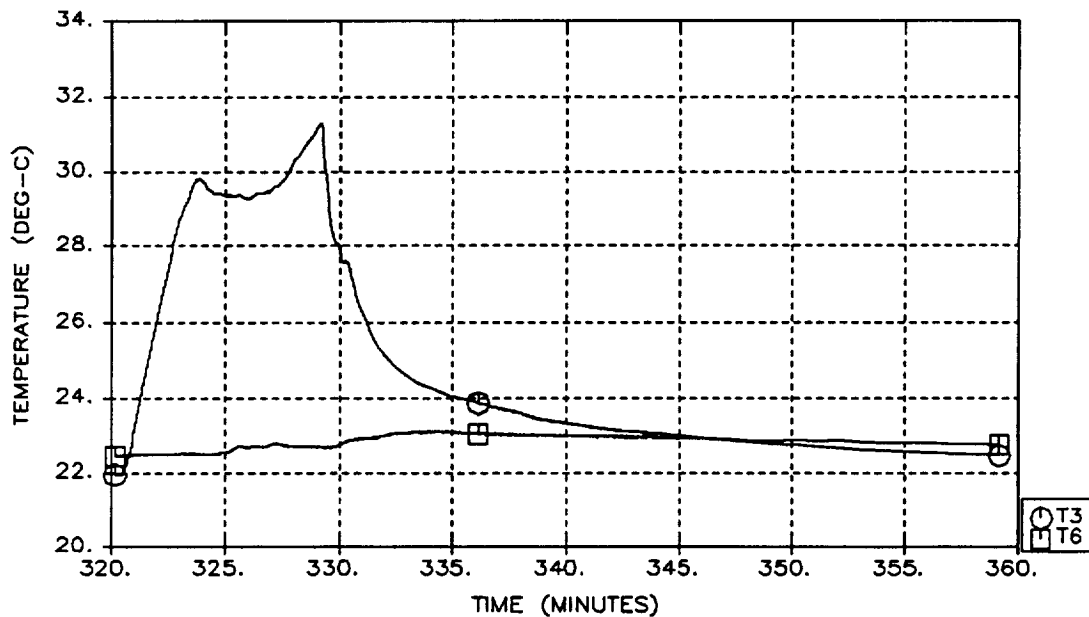
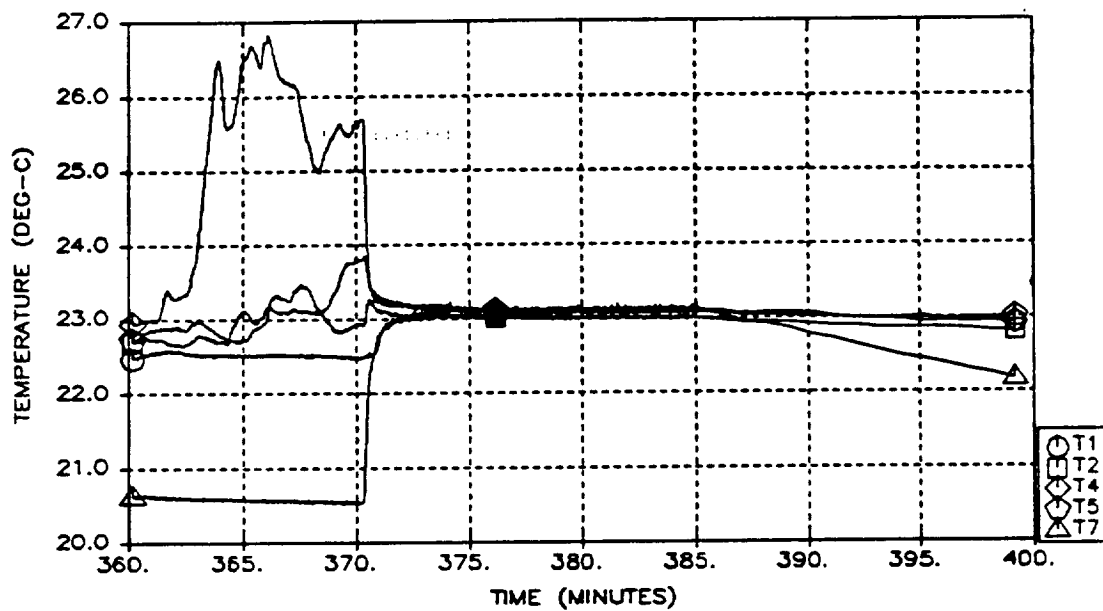


Figure A-85: Run 9 Temperatures
A-86

RUN 10 TEMPERATURES
THERMISTORS 1, 2, 4, 5, AND 7



RUN 10 TEMPERATURES
THERMISTORS 3 AND 6 (HEATERS)

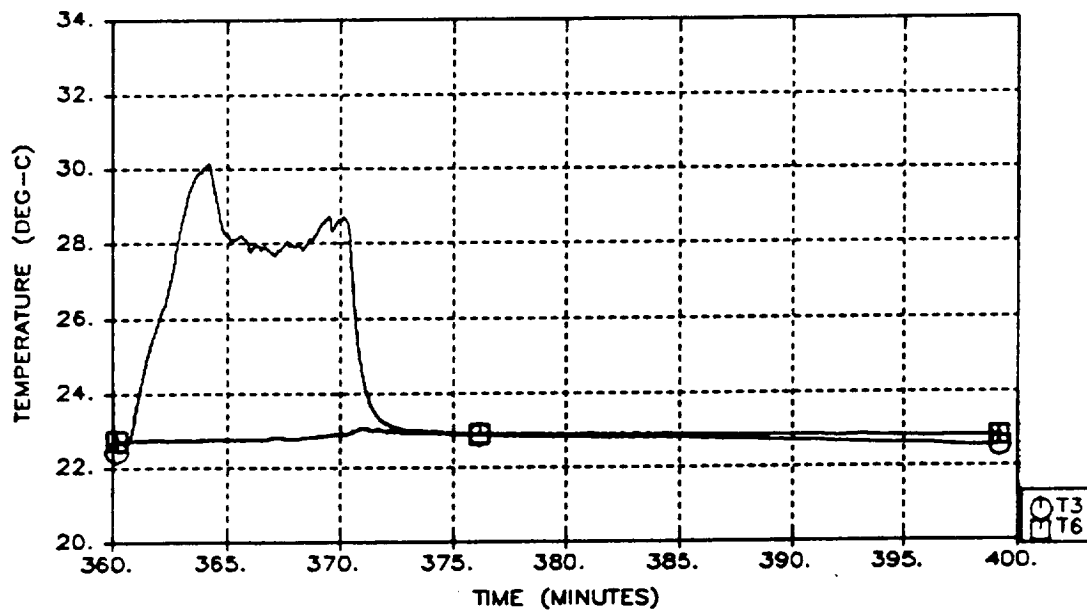
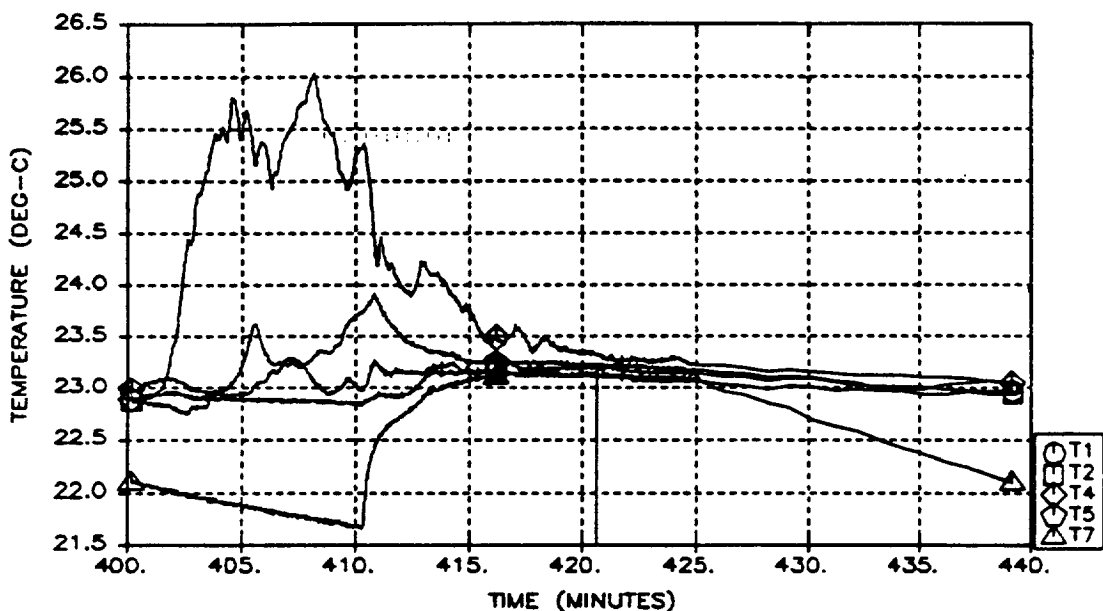


Figure A-86: Run 10 Temperatures
A-87

RUN 11 TEMPERATURES
THERMISTORS 1, 2, 4, 5, AND 7



RUN 11 TEMPERATURES
THERMISTORS 3 AND 6 (HEATERS)

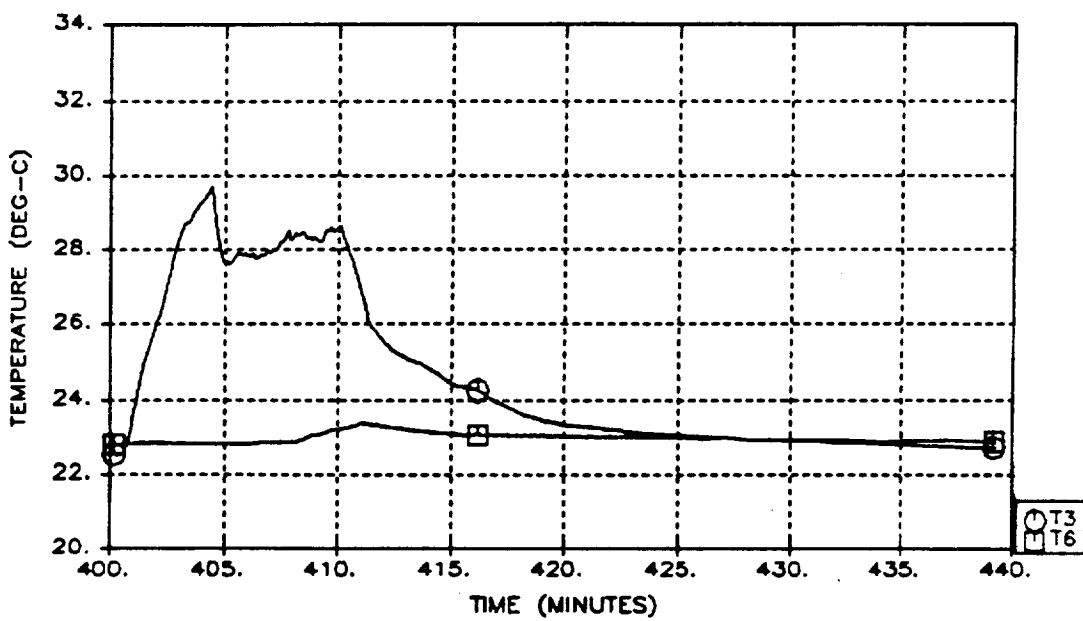
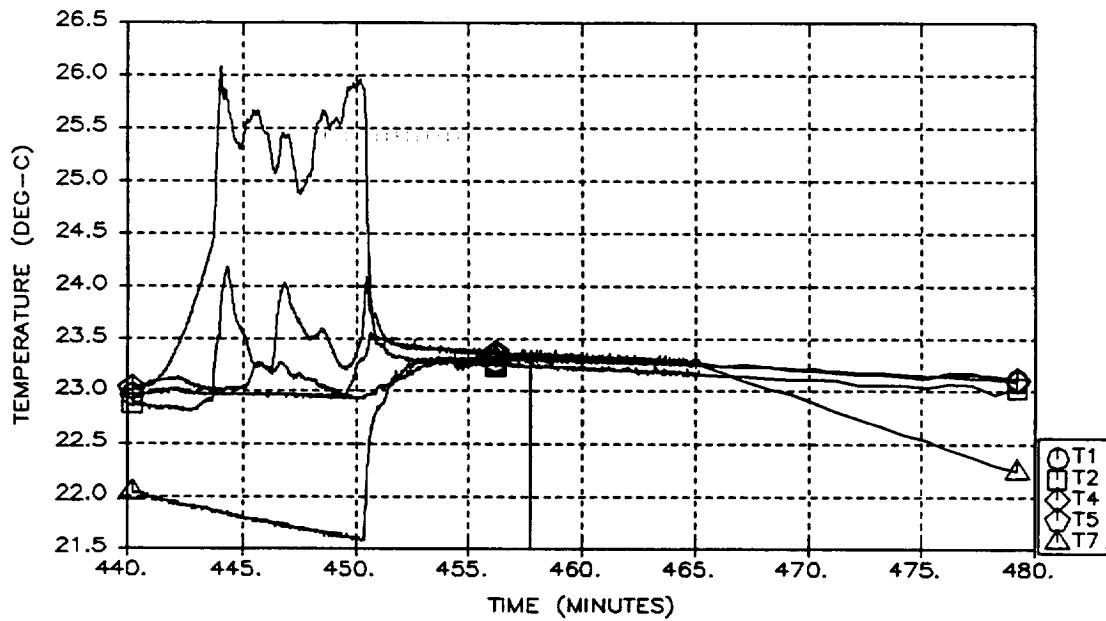


Figure A-87: Run 11 Temperatures
A-88

RUN 12 TEMPERATURES
THERMISTORS 1, 2, 4, 5, AND 7



RUN 12 TEMPERATURES
THERMISTORS 3 AND 6 (HEATERS)

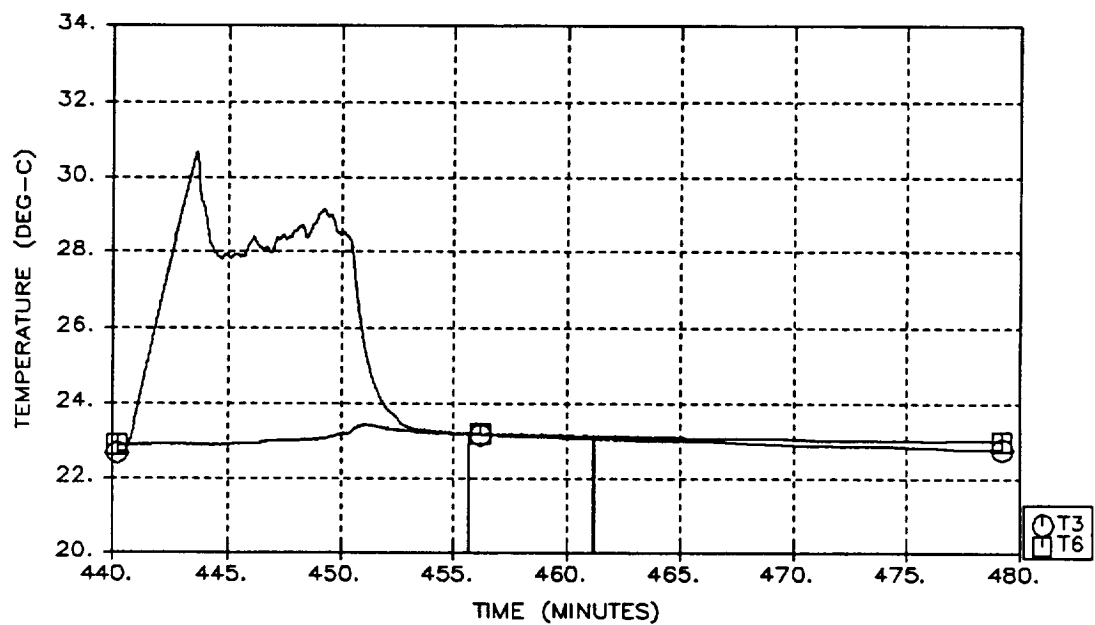
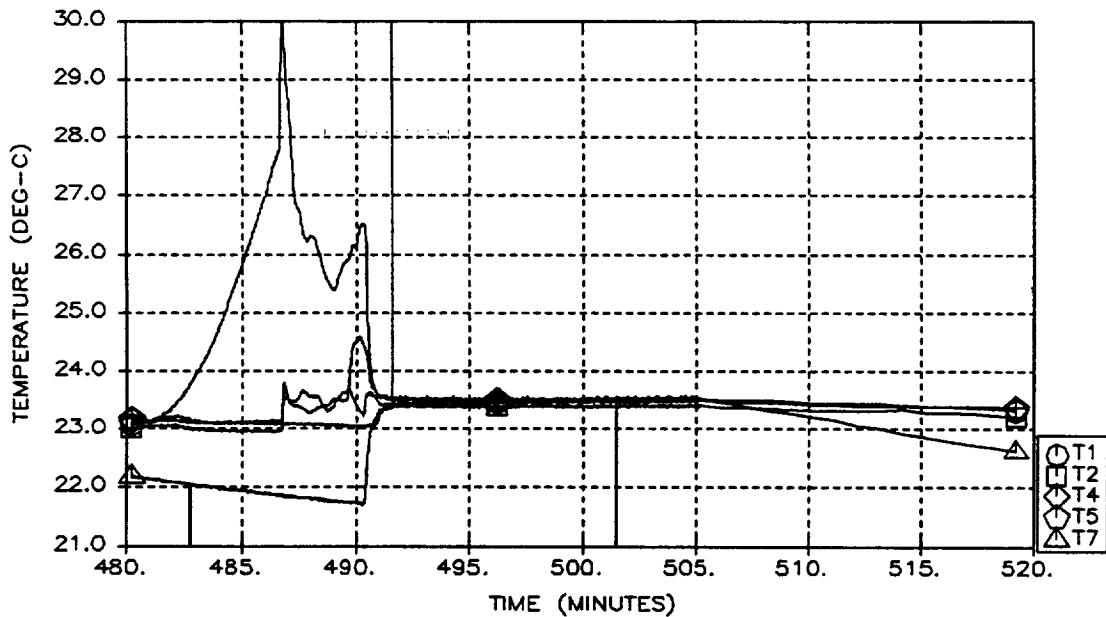


Figure A-88: Run 12 Temperatures
A-89

RUN 13 TEMPERATURES
THERMISTORS 1, 2, 4, 5, AND 7



RUN 13 TEMPERATURES
THERMISTORS 3 AND 6 (HEATERS)

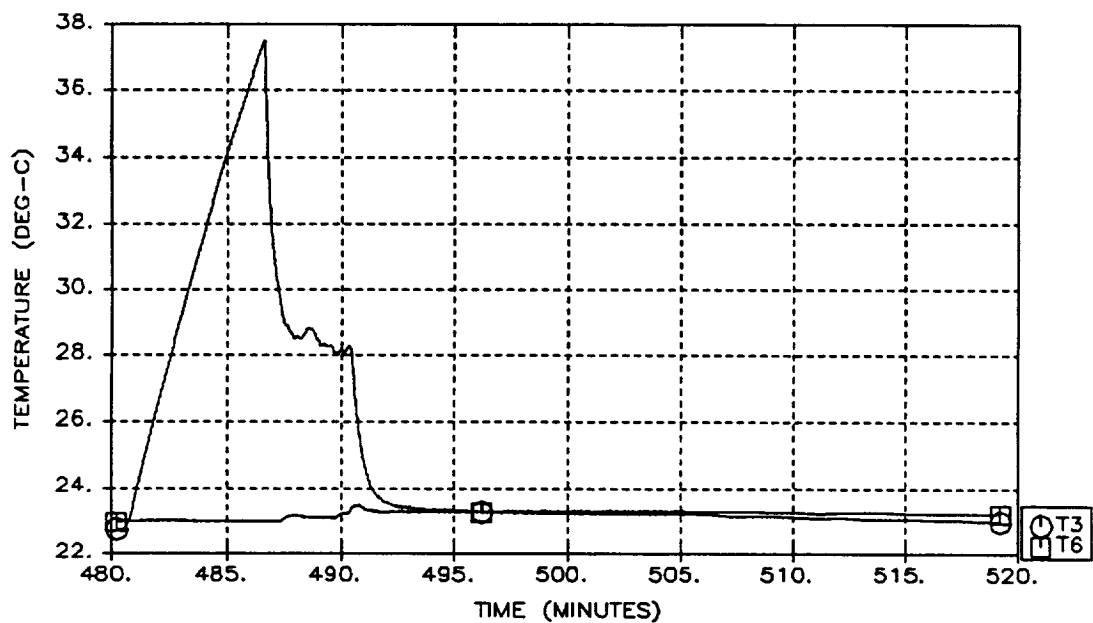
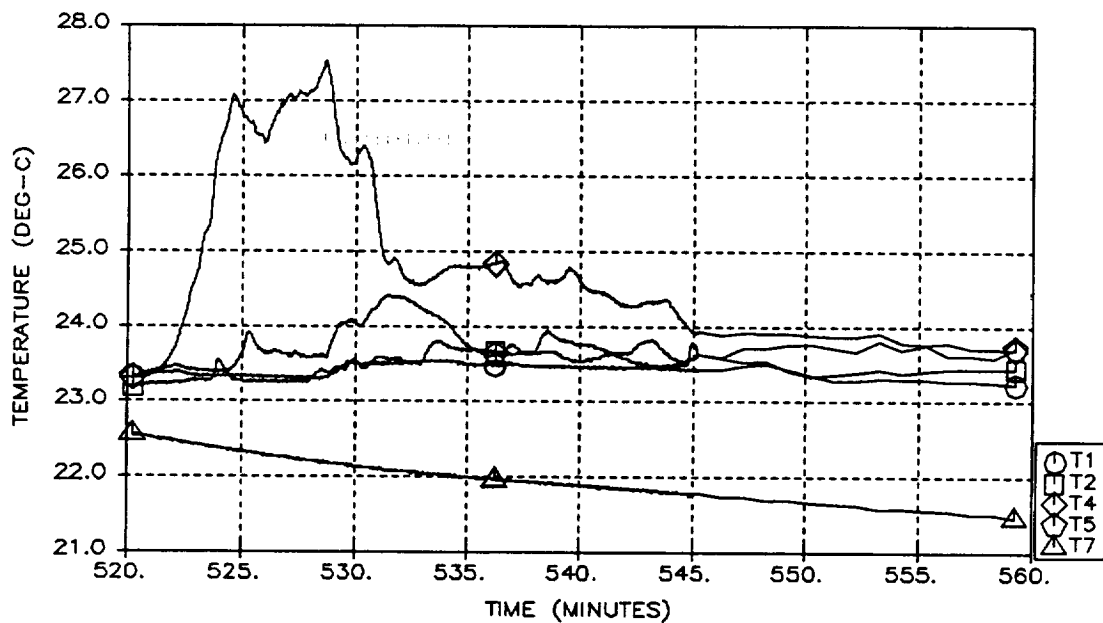


Figure A-89: Run 13 Temperatures
A-90

RUN 14 TEMPERATURES
THERMISTORS 1, 2, 4, 5, AND 7



RUN 14 TEMPERATURES
THERMISTORS 3 AND 6 (HEATERS)

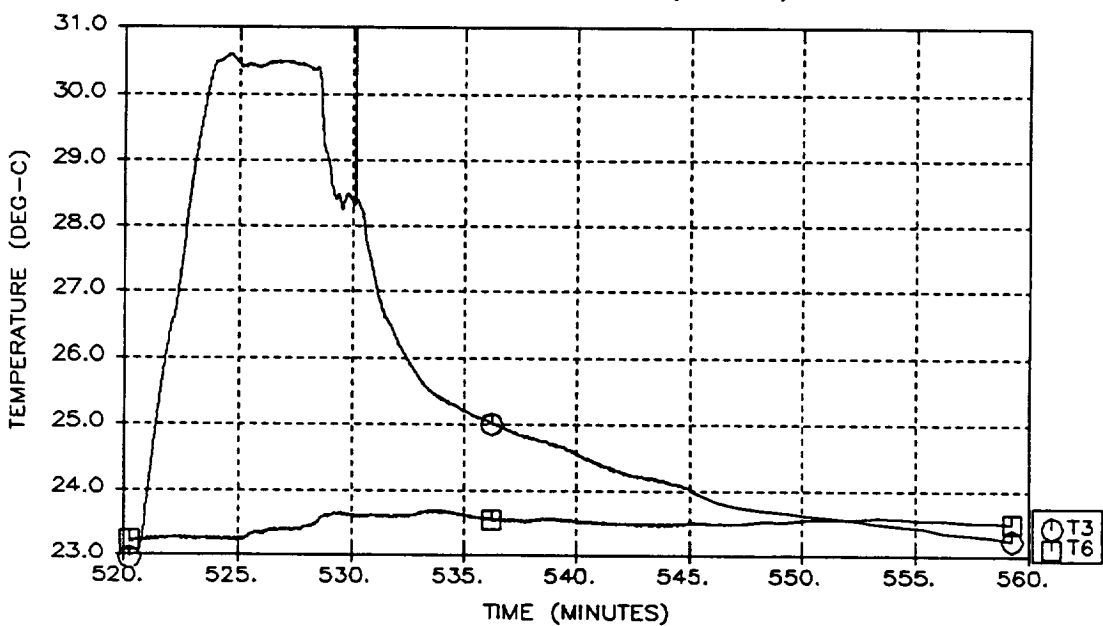
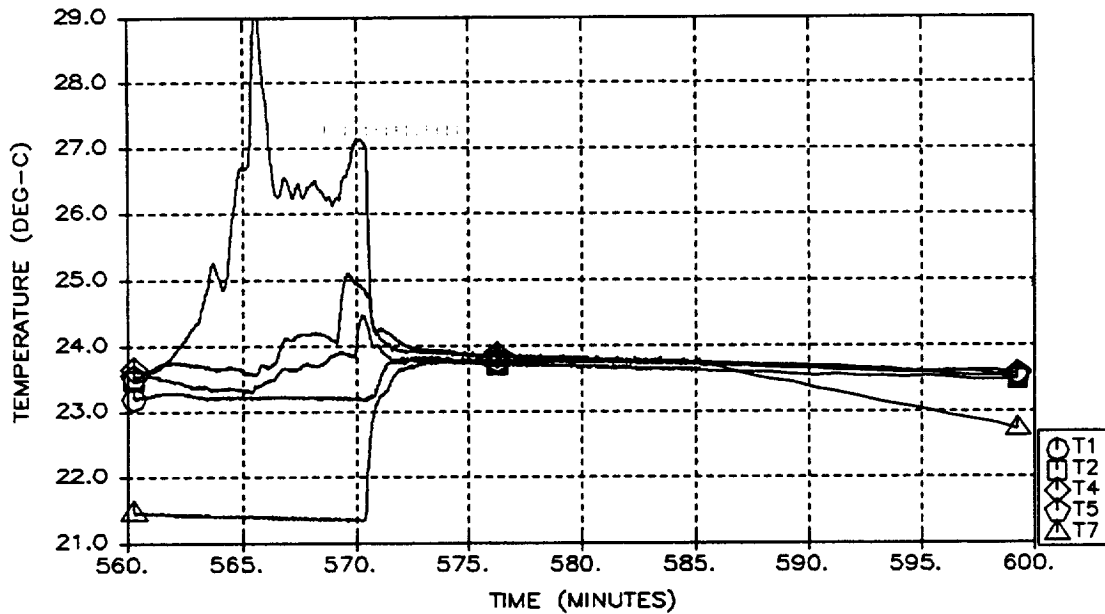


Figure A-90: Run 14 Temperatures
A-91

RUN 15 TEMPERATURES
THERMISTORS 1, 2, 4, 5, AND 7



RUN 15 TEMPERATURES
THERMISTORS 3 AND 6 (HEATERS)

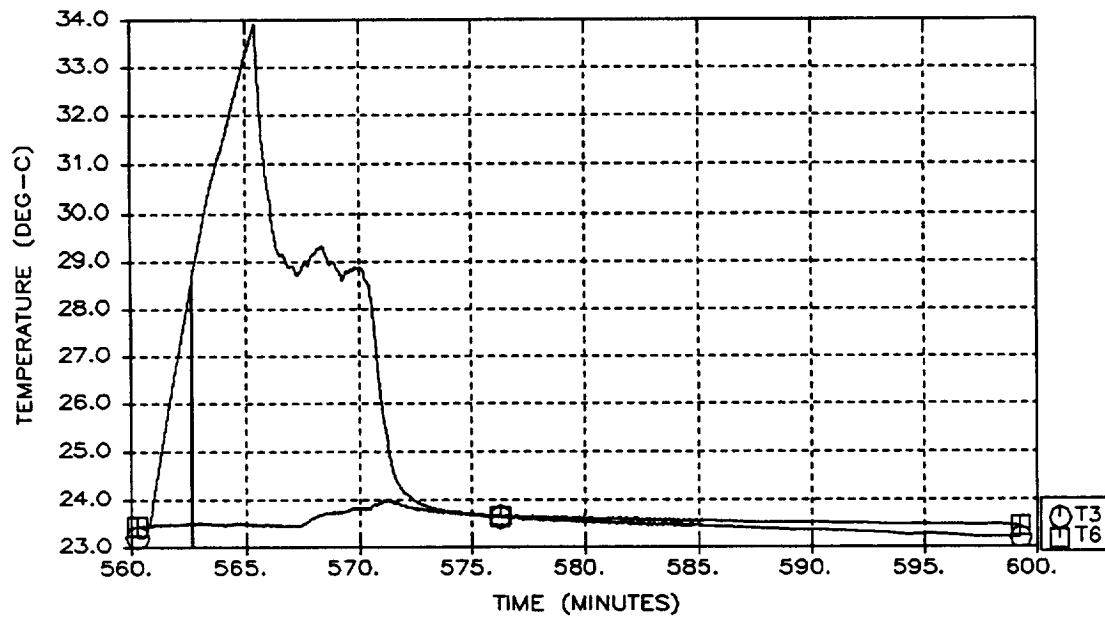


Figure A-91: Run 15 Temperatures
A-92

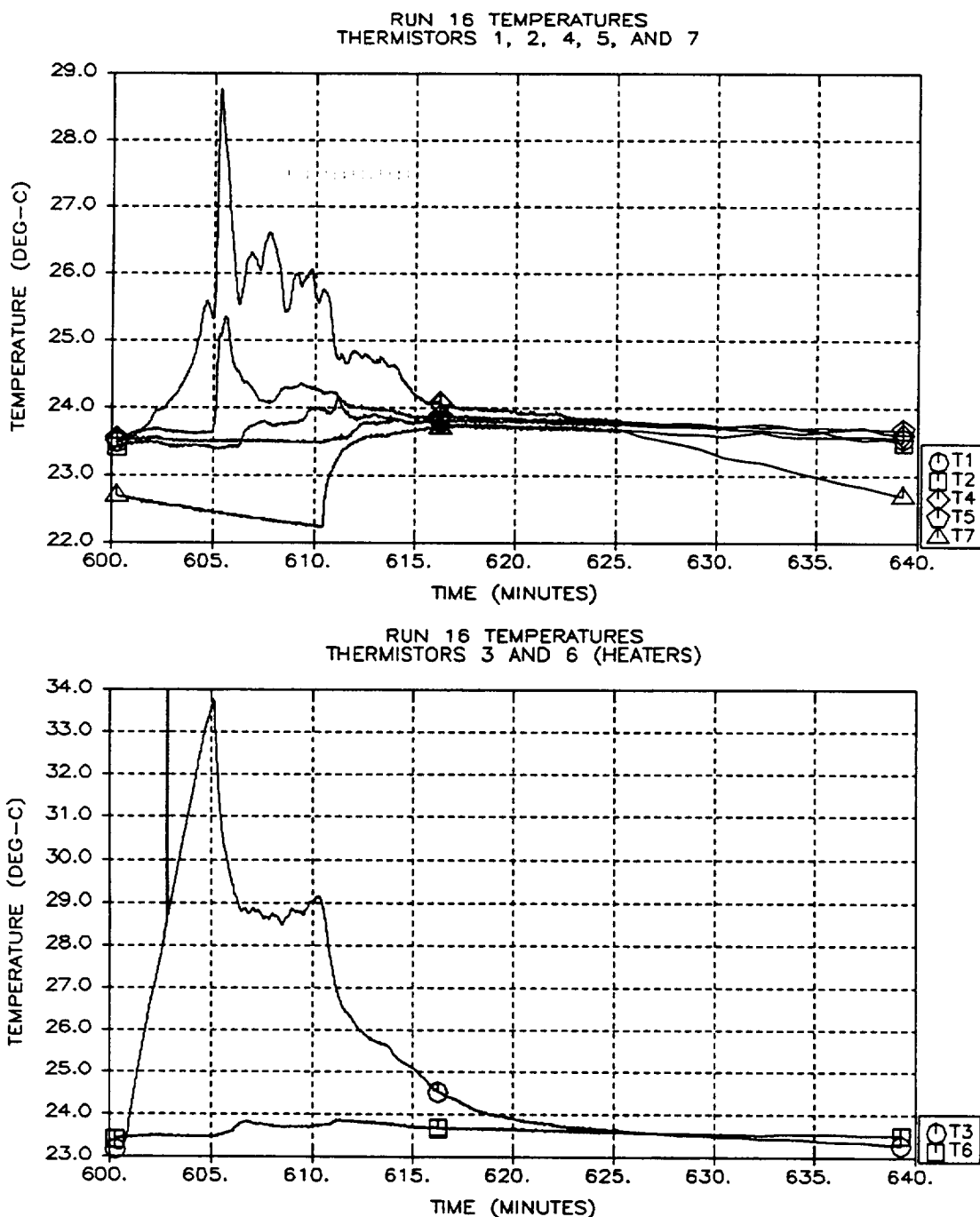
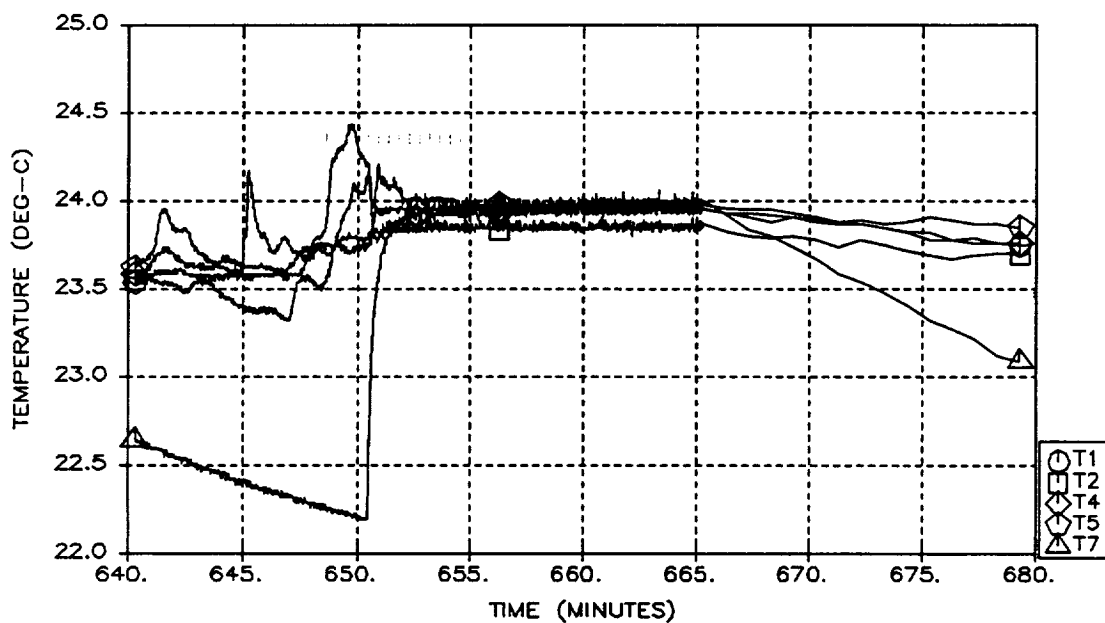


Figure A-92: Run 16 Temperatures
A-93

RUN 17 TEMPERATURES
THERMISTORS 1, 2, 4, 5, AND 7



RUN 17 TEMPERATURES
THERMISTORS 3 AND 6 (HEATERS)

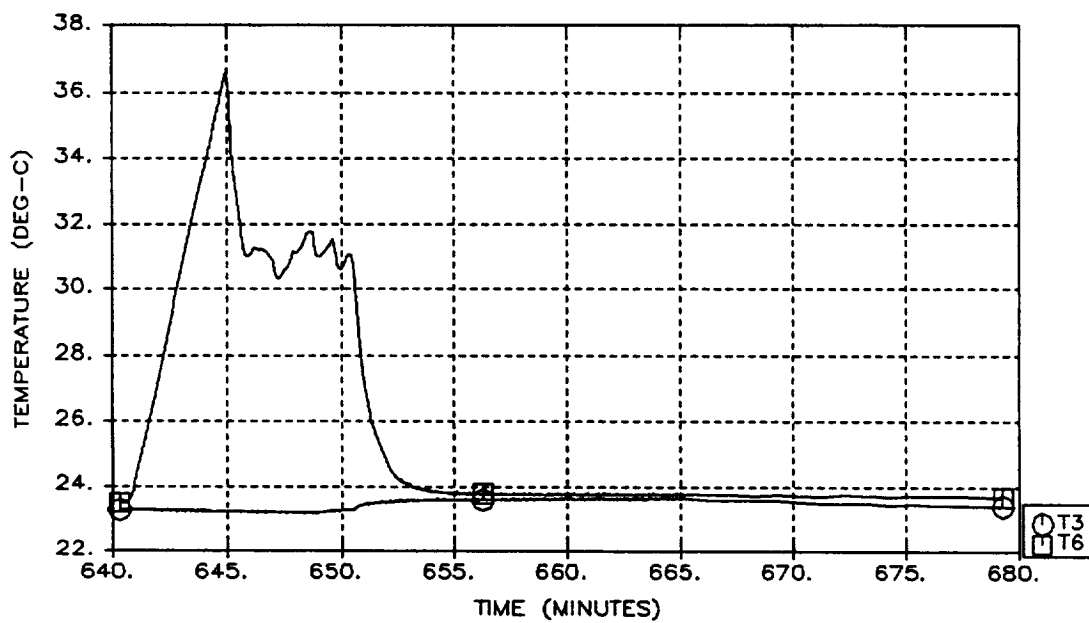
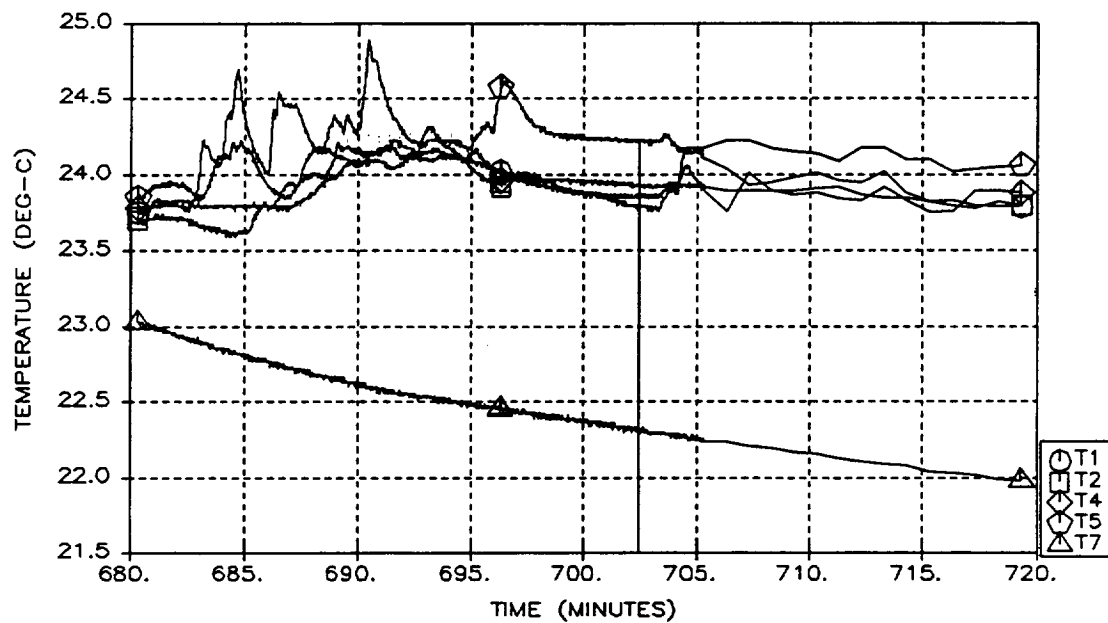


Figure A-93: Run 17 Temperatures
A-94

RUN 18 TEMPERATURES
THERMISTORS 1, 2, 4, 5, AND 7



RUN 18 TEMPERATURES
THERMISTORS 3 AND 6 (HEATERS)

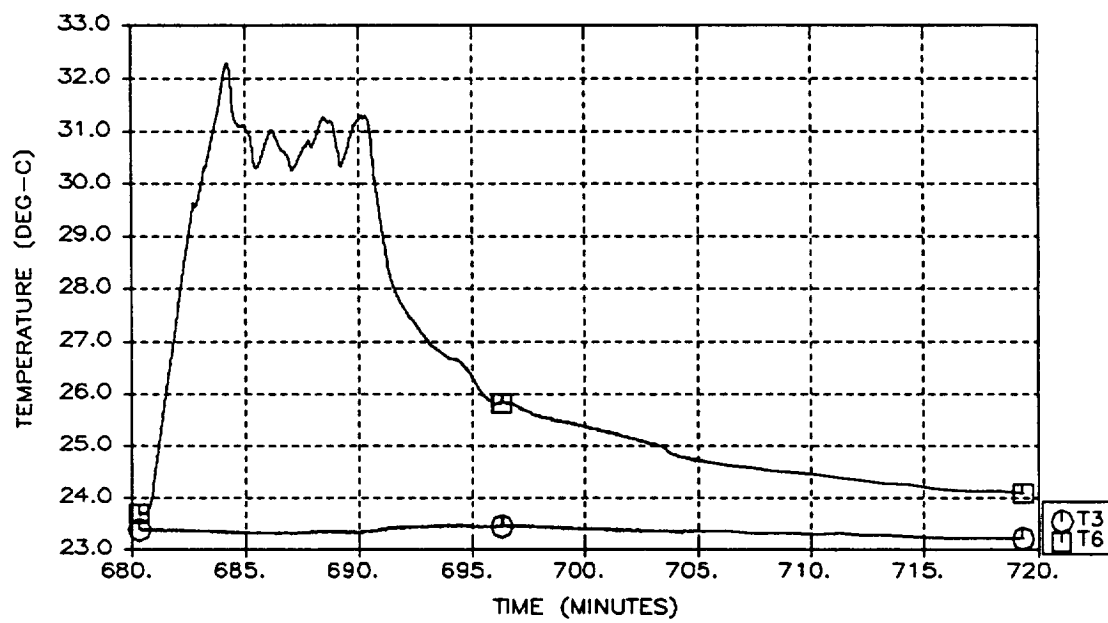
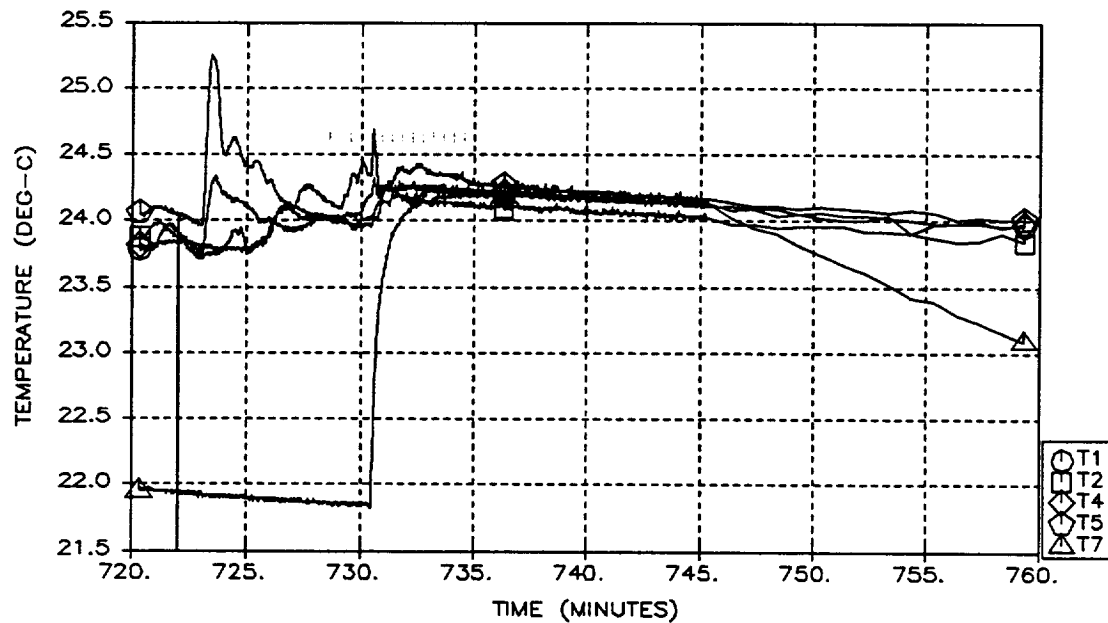


Figure A-94: Run 18 Temperatures
A-95

RUN 19 TEMPERATURES
THERMISTORS 1, 2, 4, 5, AND 7



RUN 19 TEMPERATURES
THERMISTORS 3 AND 6 (HEATERS)

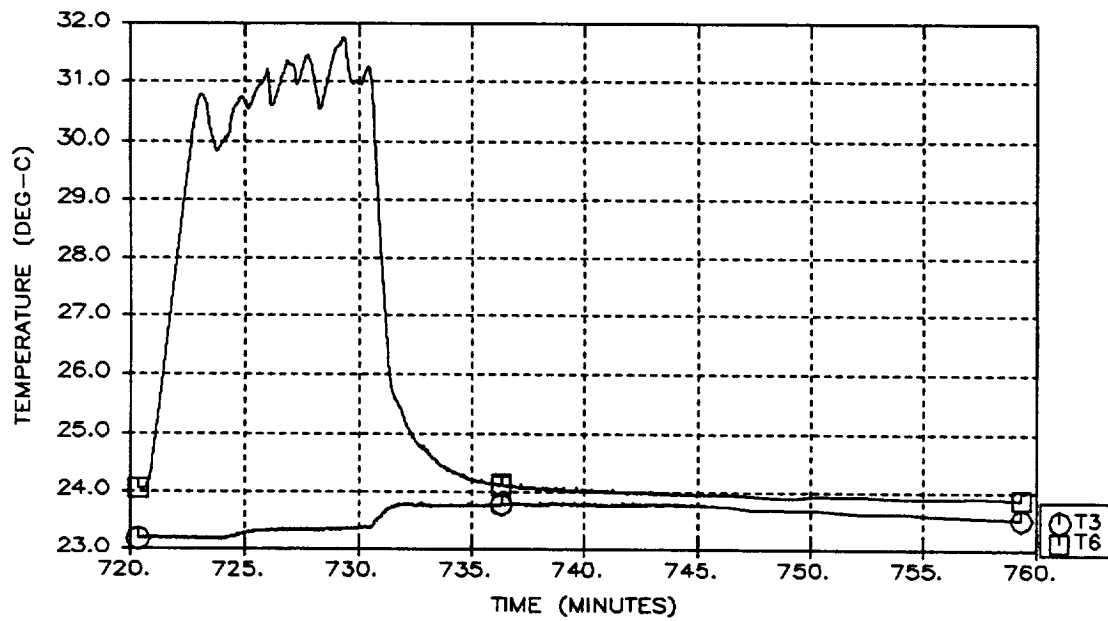
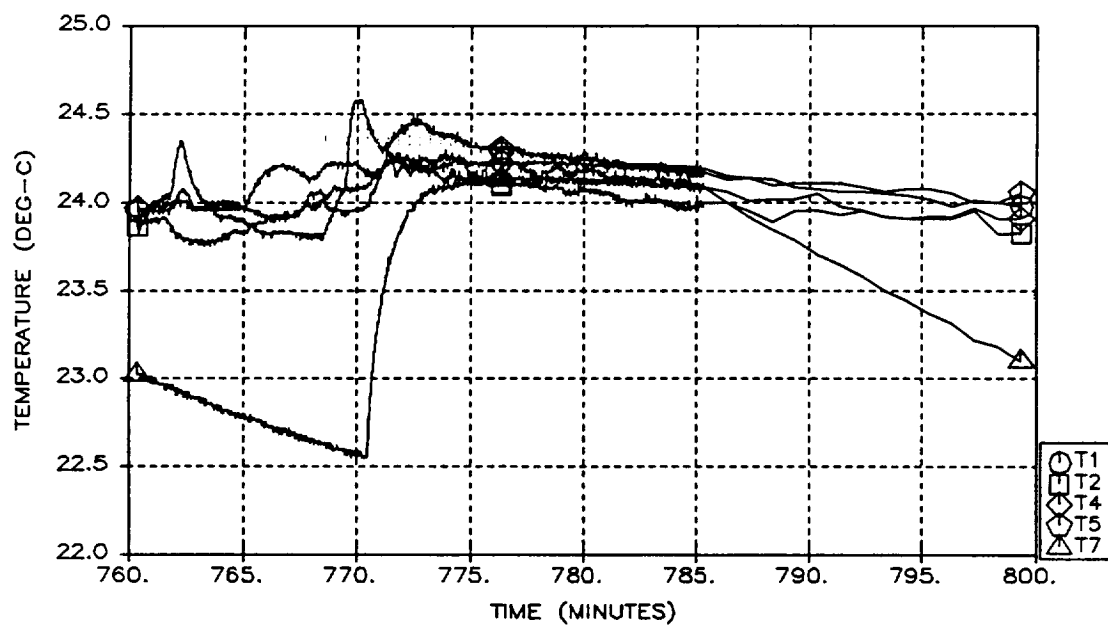


Figure A-95: Run 19 Temperatures
A-96

RUN 20 TEMPERATURES
THERMISTORS 1, 2, 4, 5, AND 7



RUN 20 TEMPERATURES
THERMISTORS 3 AND 6 (HEATERS)

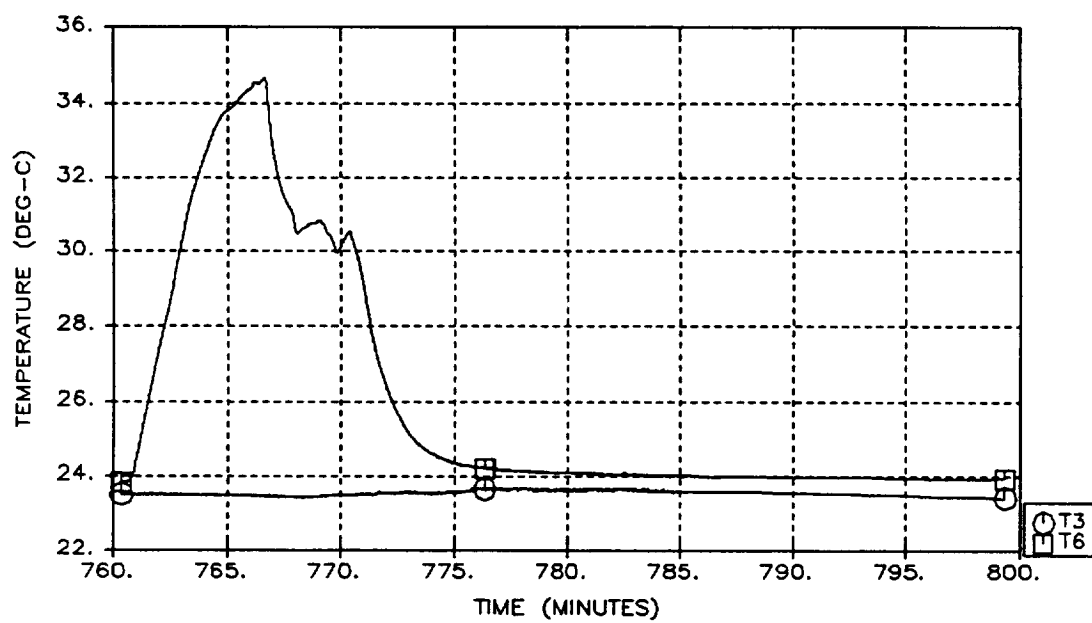
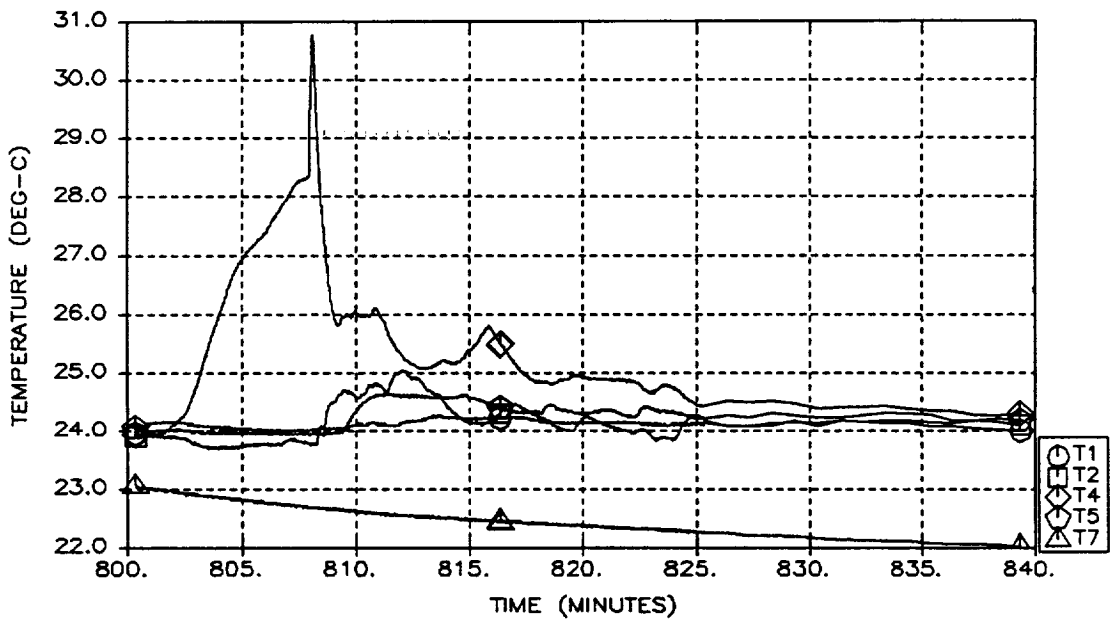


Figure A-96: Run 20 Temperatures
A-97

RUN 21 TEMPERATURES
THERMISTORS 1, 2, 4, 5, AND 7



RUN 21 TEMPERATURES
THERMISTORS 3 AND 6 (HEATERS)

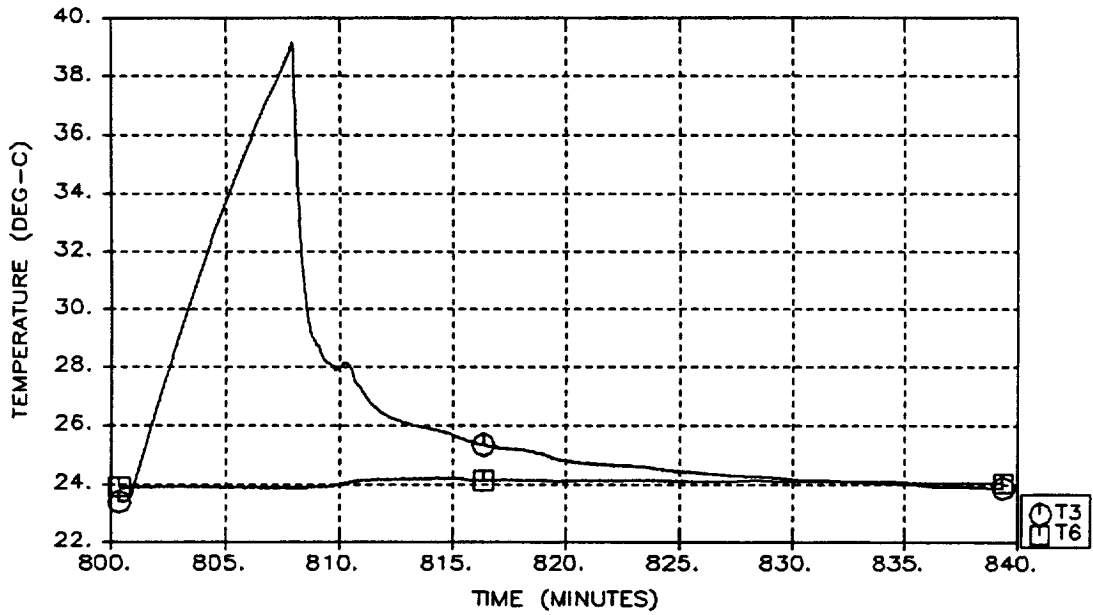
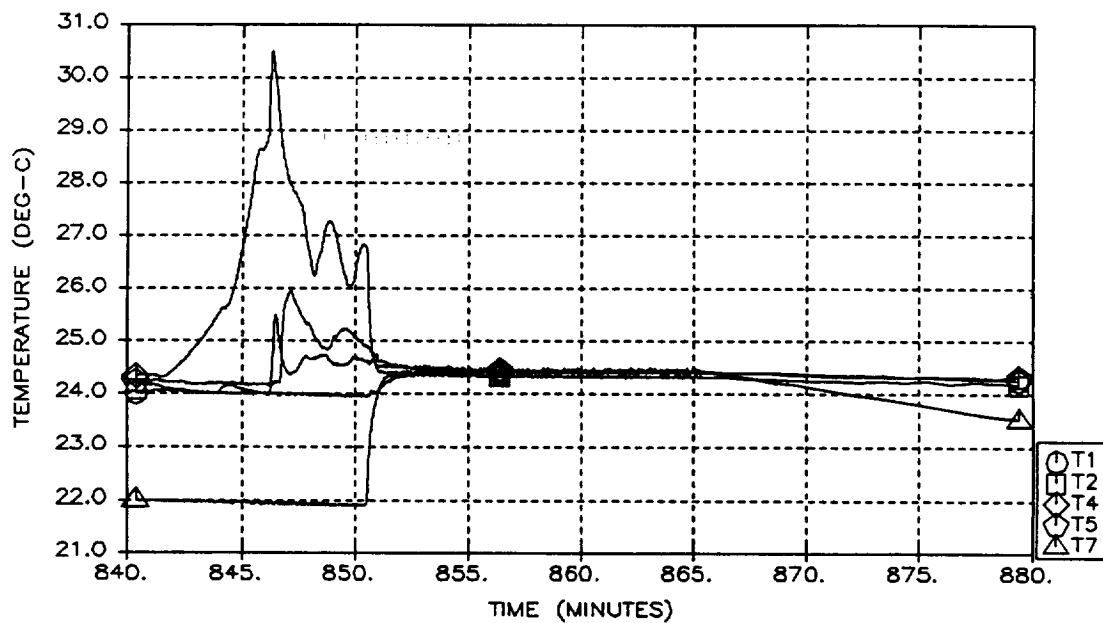


Figure A-97: Run 21 Temperatures
A-98

RUN 22 TEMPERATURES
THERMISTORS 1, 2, 4, 5, AND 7



RUN 22 TEMPERATURES
THERMISTORS 3 AND 6 (HEATERS)

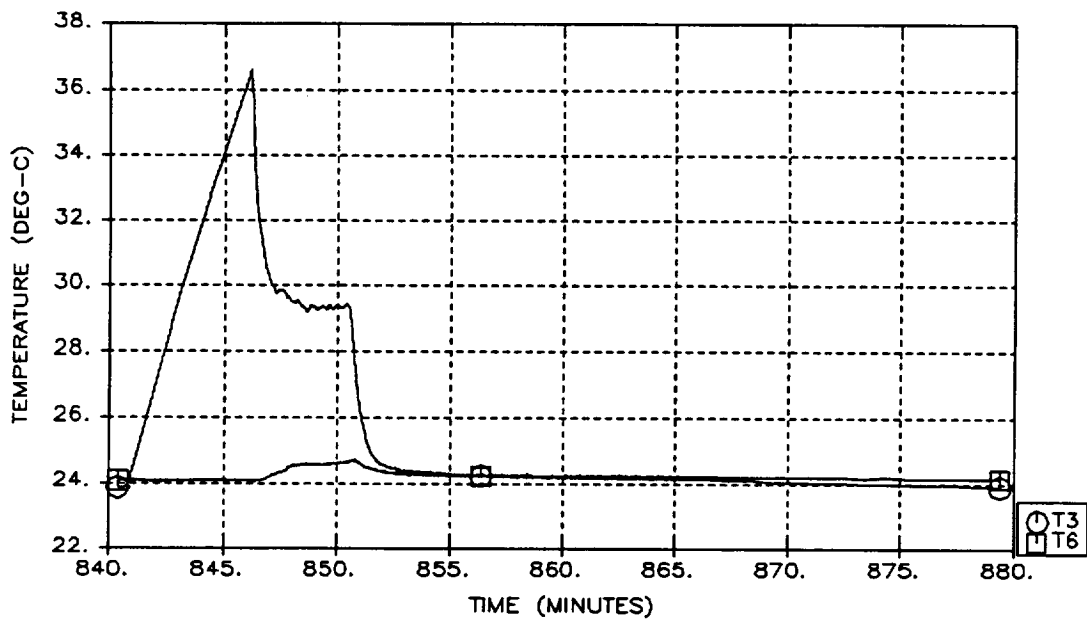
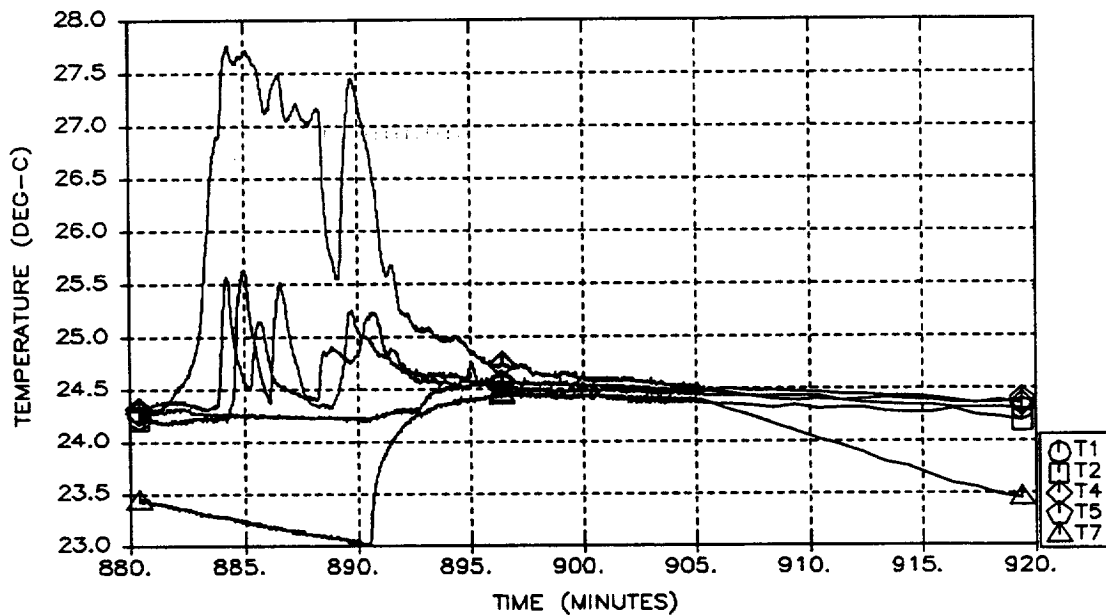


Figure A-98: Run 22 Temperatures
A-99

RUN 23 TEMPERATURES
THERMISTORS 1, 2, 4, 5, AND 7



RUN 23 TEMPERATURES
THERMISTORS 3 AND 6 (HEATERS)

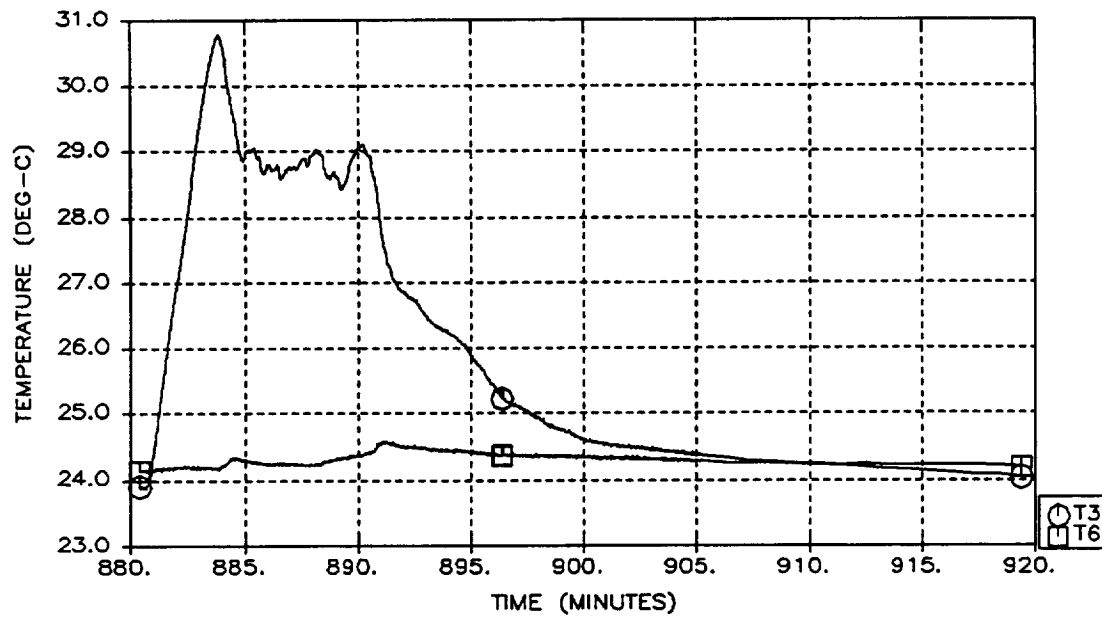
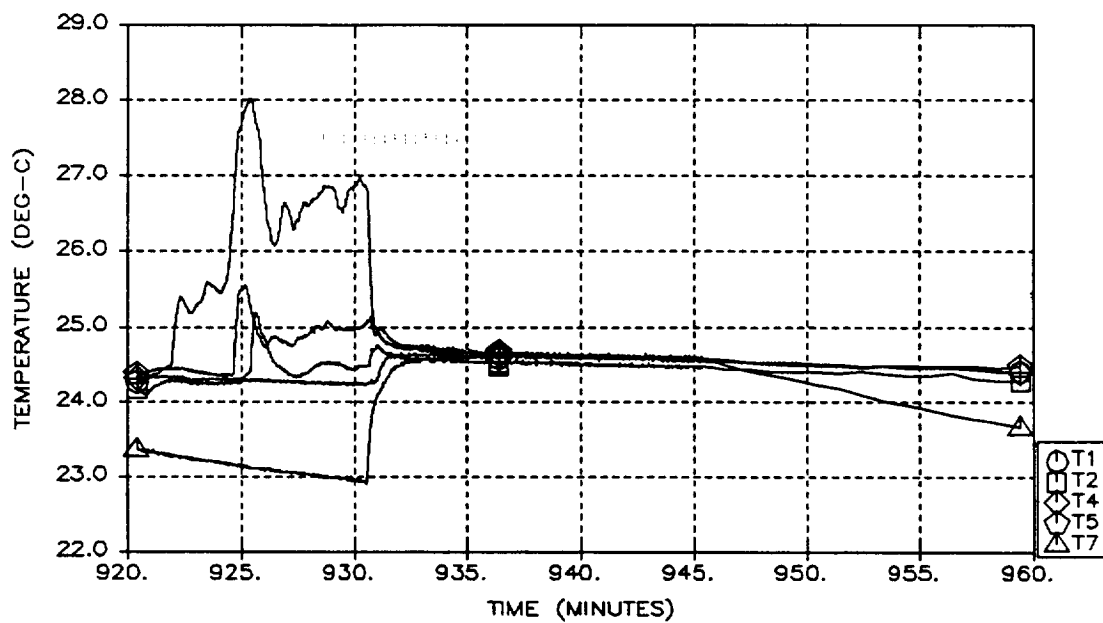


Figure A-99: Run 23 Temperatures
A-100

RUN 24 TEMPERATURES
THERMISTORS 1, 2, 4, 5, AND 7



RUN 24 TEMPERATURES
THERMISTORS 3 AND 6 (HEATERS)

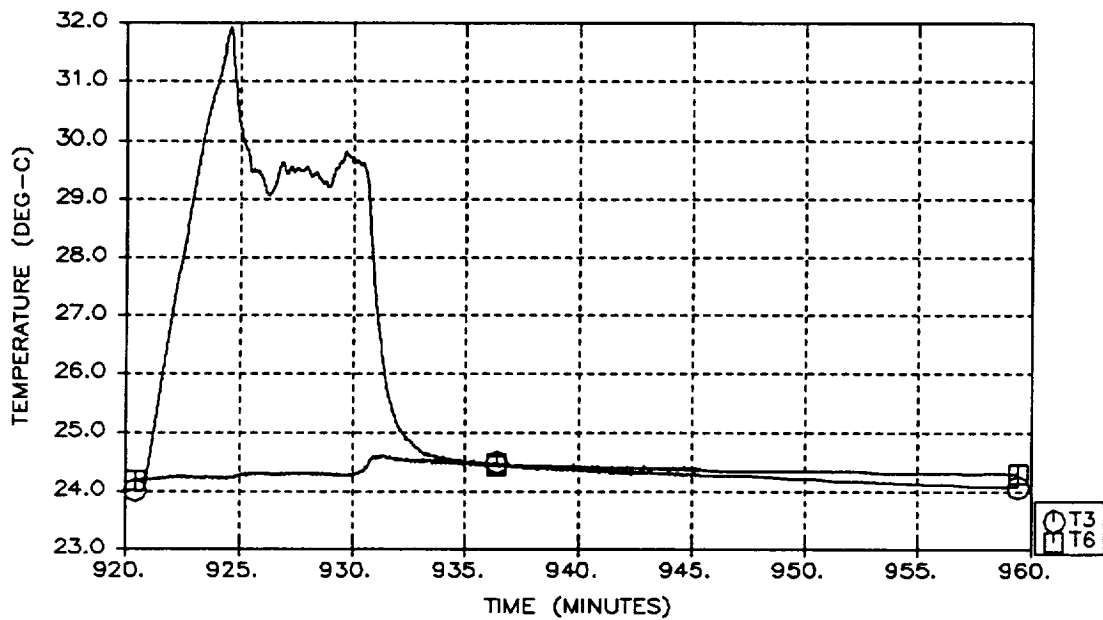
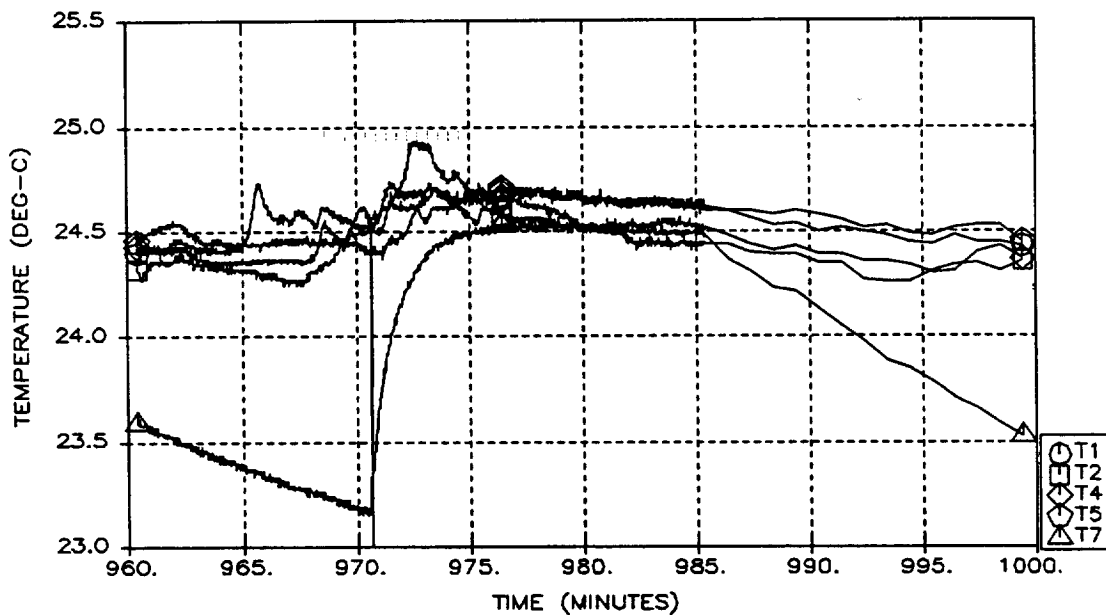


Figure A-100: Run 24 Temperatures
A-101

RUN 25 TEMPERATURES
THERMISTORS 1, 2, 4, 5, AND 7



RUN 25 TEMPERATURES
THERMISTORS 3 AND 6 (HEATERS)

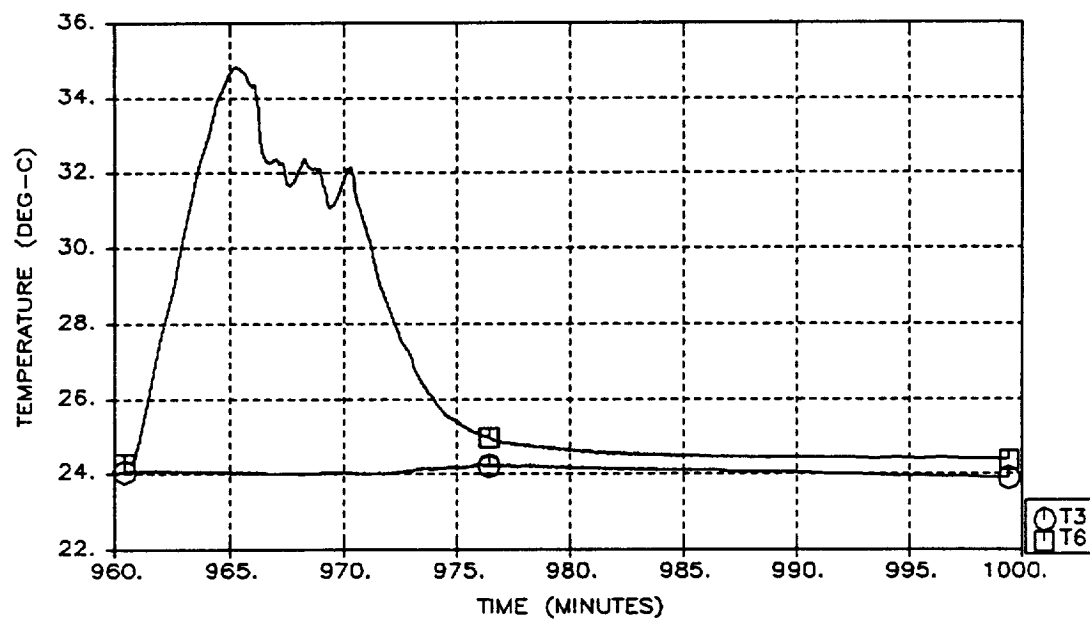
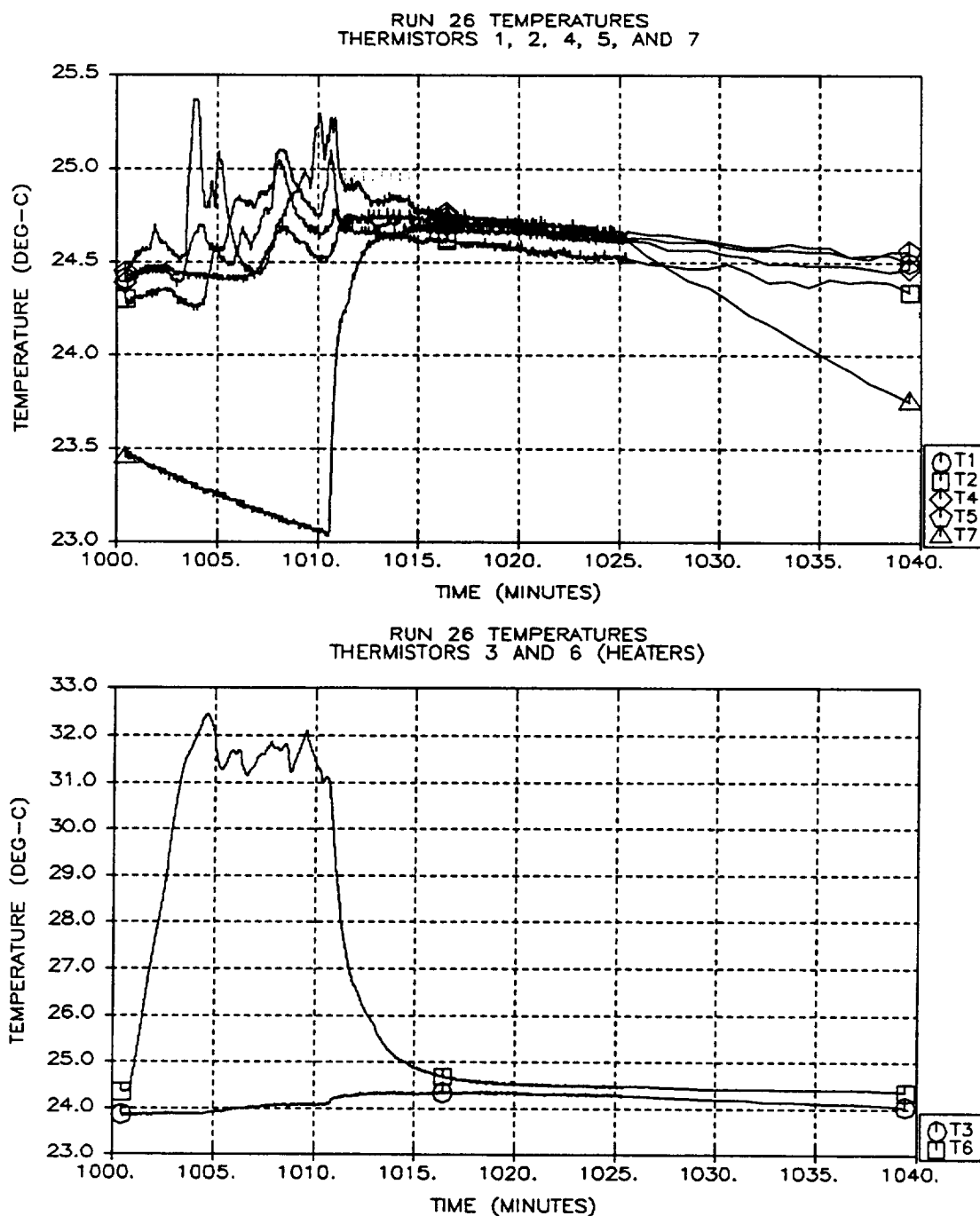
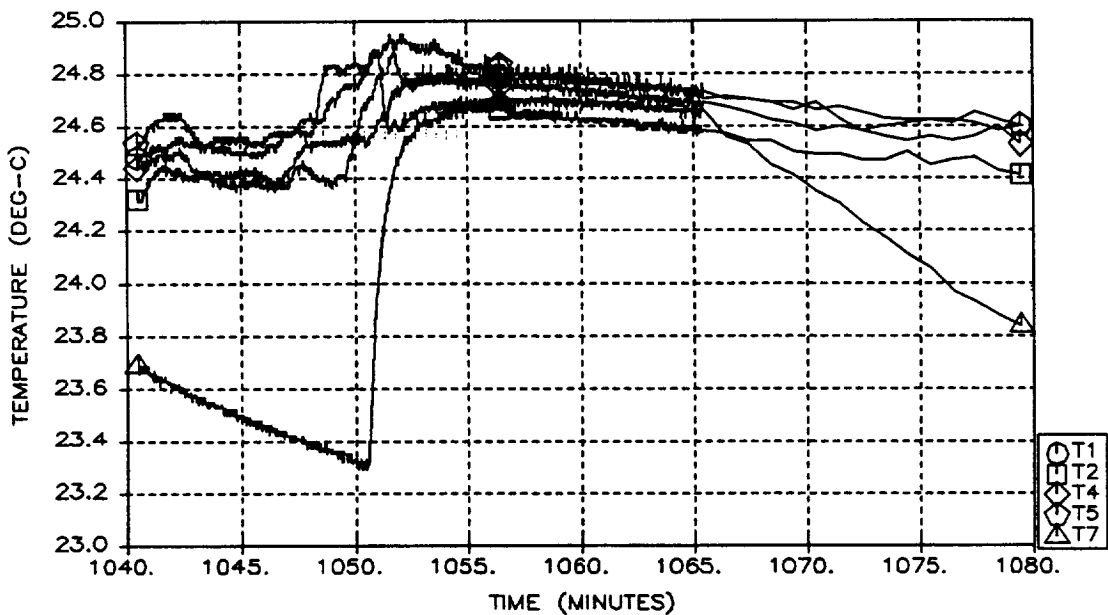


Figure A-101: Run 25 Temperatures
A-102



*Figure A-102: Run 26 Temperatures
A-103*

RUN 27 TEMPERATURES
THERMISTORS 1, 2, 4, 5, AND 7



RUN 27 TEMPERATURES
THERMISTORS 3 AND 6 (HEATERS)

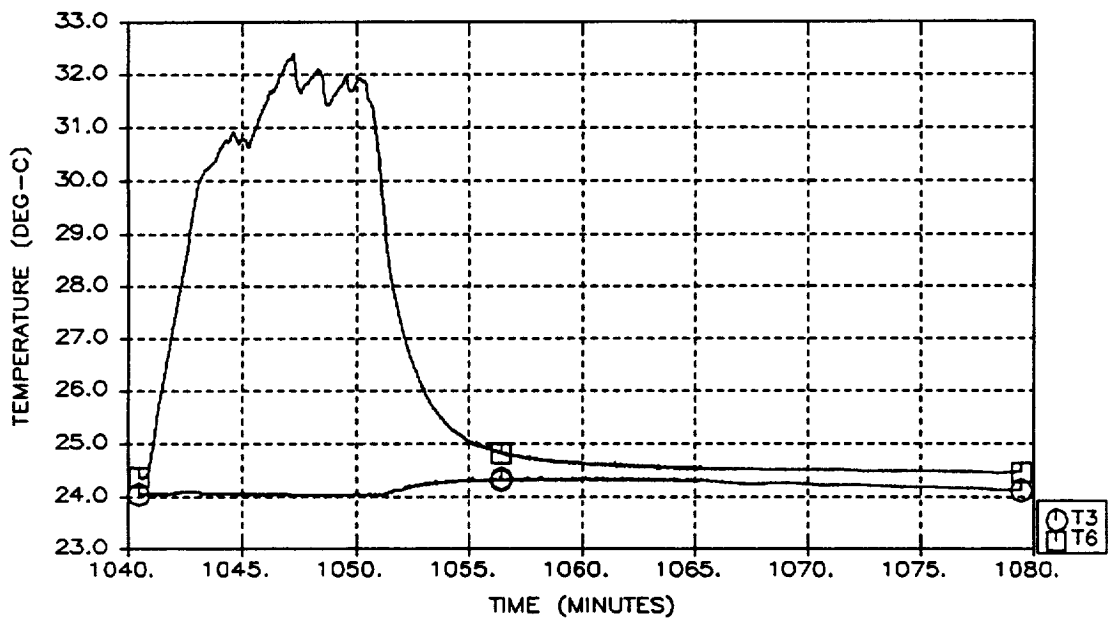
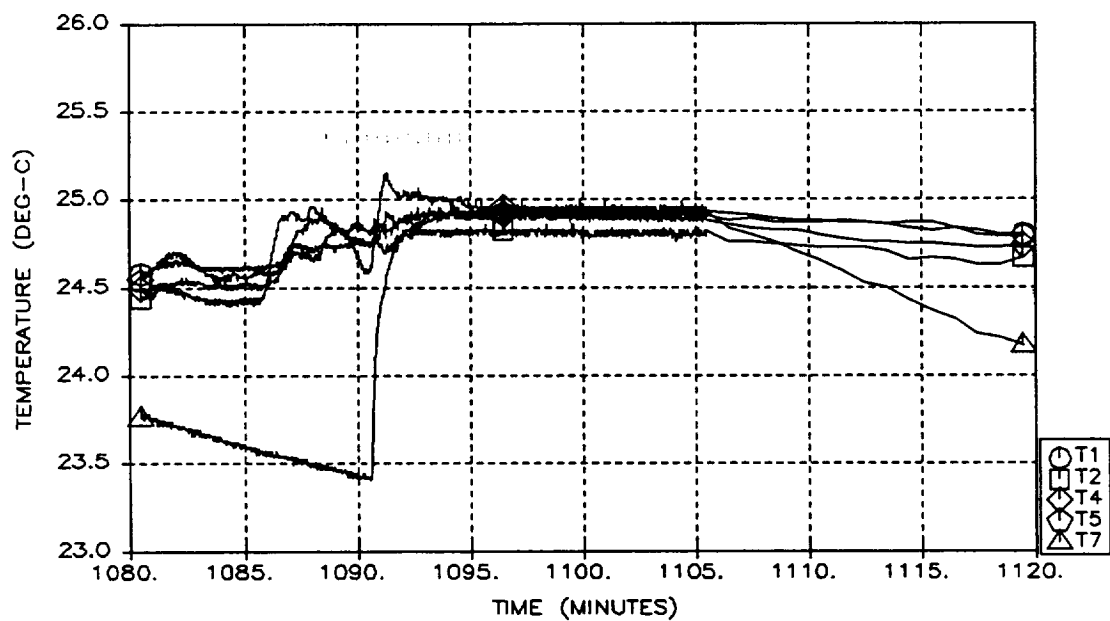


Figure A-103: Run 27 Temperatures
A-104

RUN 28 TEMPERATURES
THERMISTORS 1, 2, 4, 5, AND 7



RUN 28 TEMPERATURES
THERMISTORS 3 AND 6 (HEATERS)

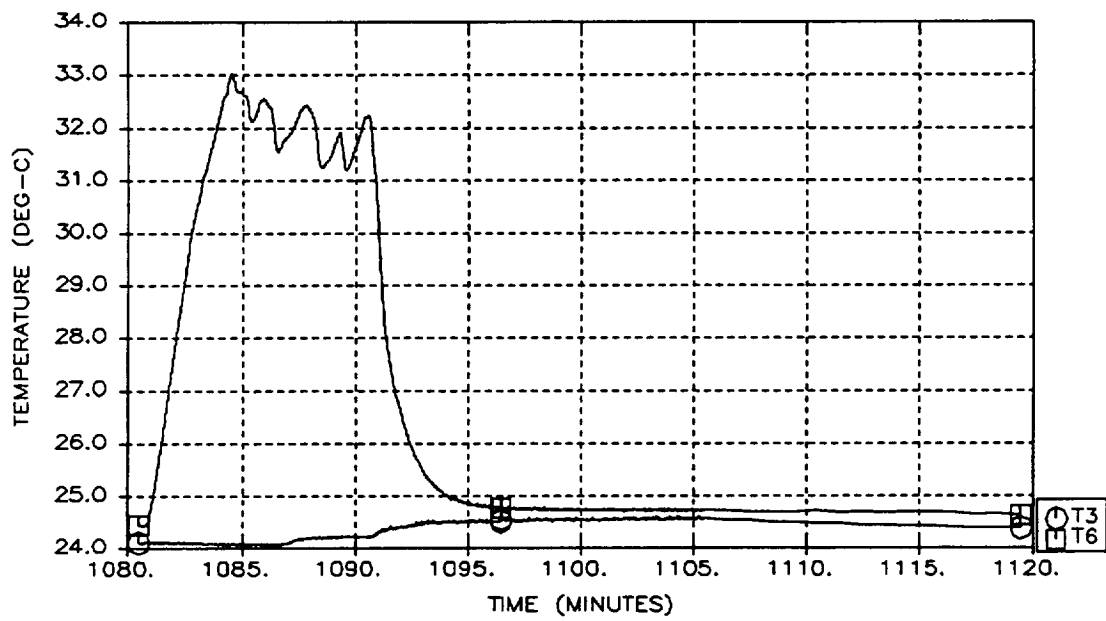
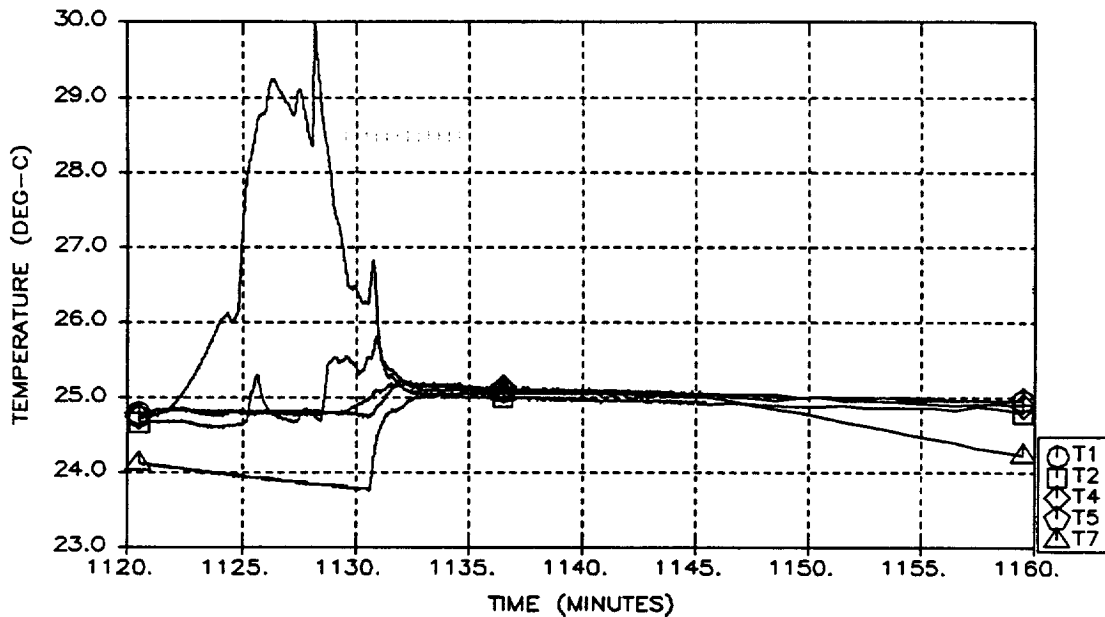


Figure A-104: Run 28 Temperatures
A-105

RUN 29 TEMPERATURES
THERMISTORS 1, 2, 4, 5, AND 7



RUN 29 TEMPERATURES
THERMISTORS 3 AND 6 (HEATERS)

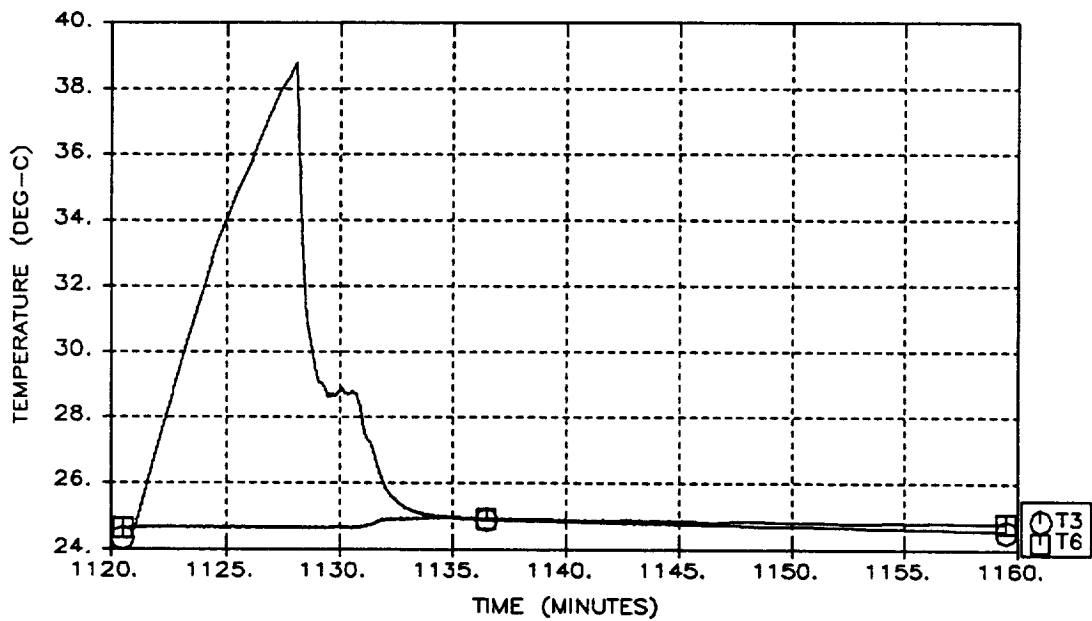
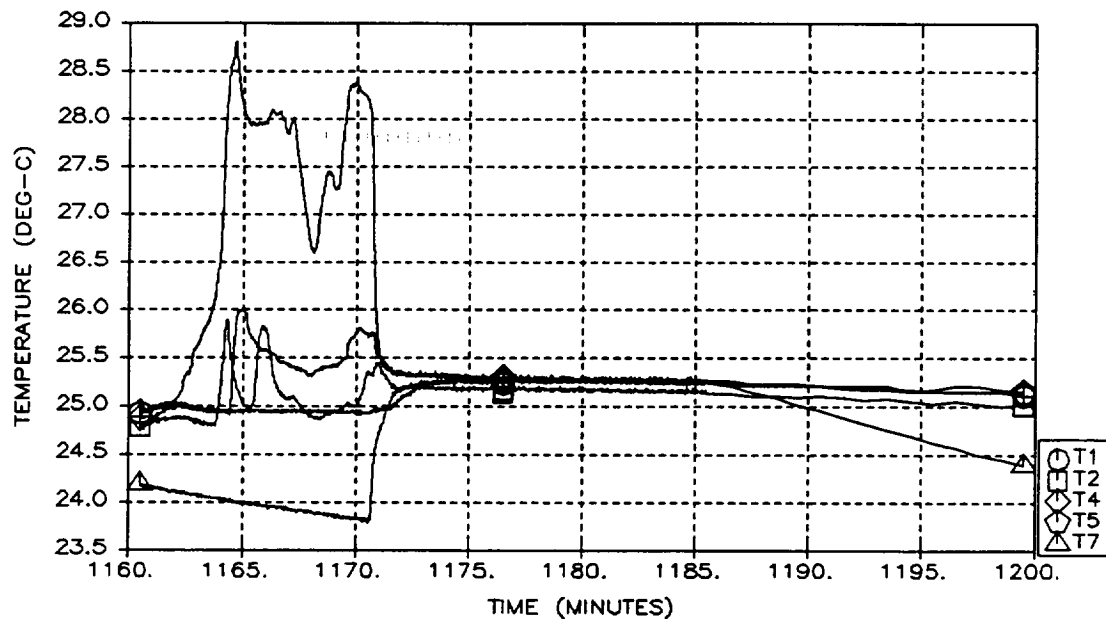


Figure A-105: Run 29 Temperatures
A-106

RUN 30 TEMPERATURES
THERMISTORS 1, 2, 4, 5, AND 7



RUN 30 TEMPERATURES
THERMISTORS 3 AND 6 (HEATERS)

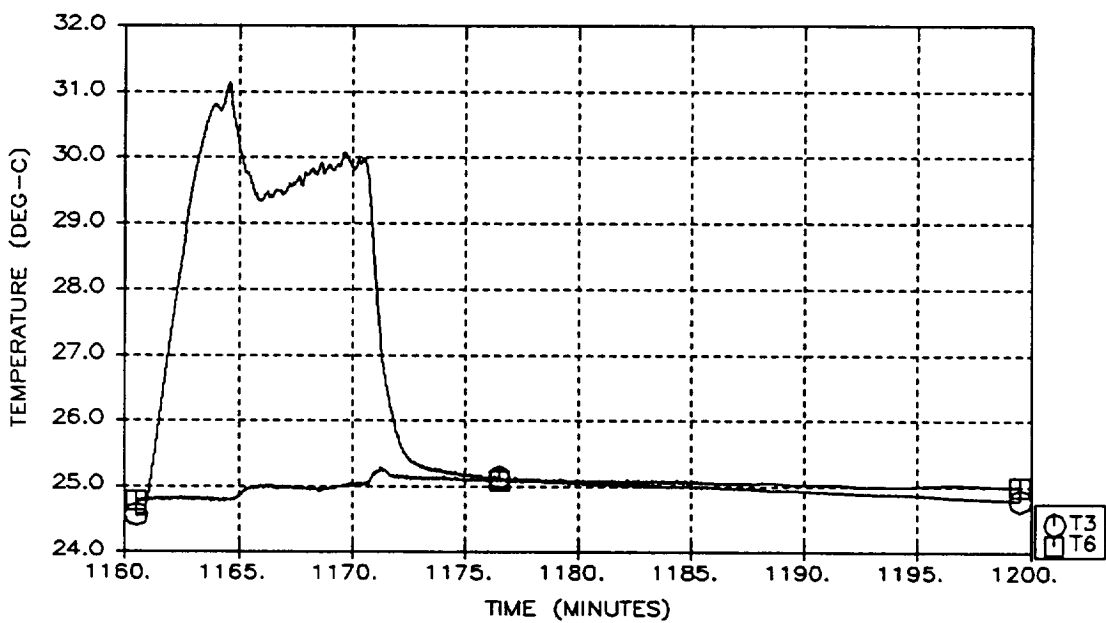
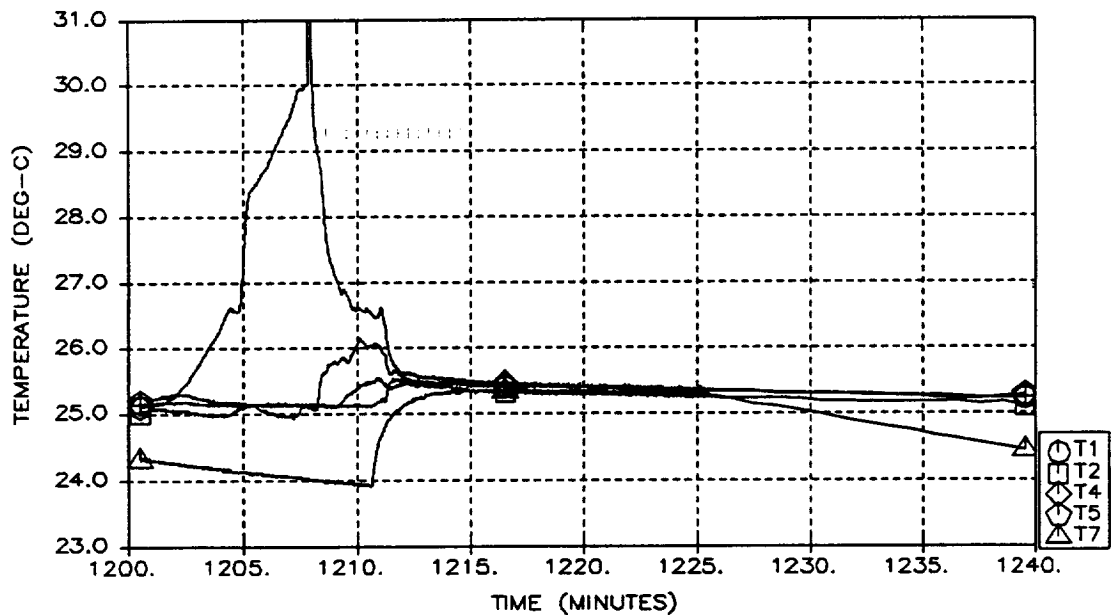


Figure A-106: Run 30 Temperatures
A-107

RUN 31 TEMPERATURES
THERMISTORS 1, 2, 4, 5, AND 7



RUN 31 TEMPERATURES
THERMISTORS 3 AND 6 (HEATERS)

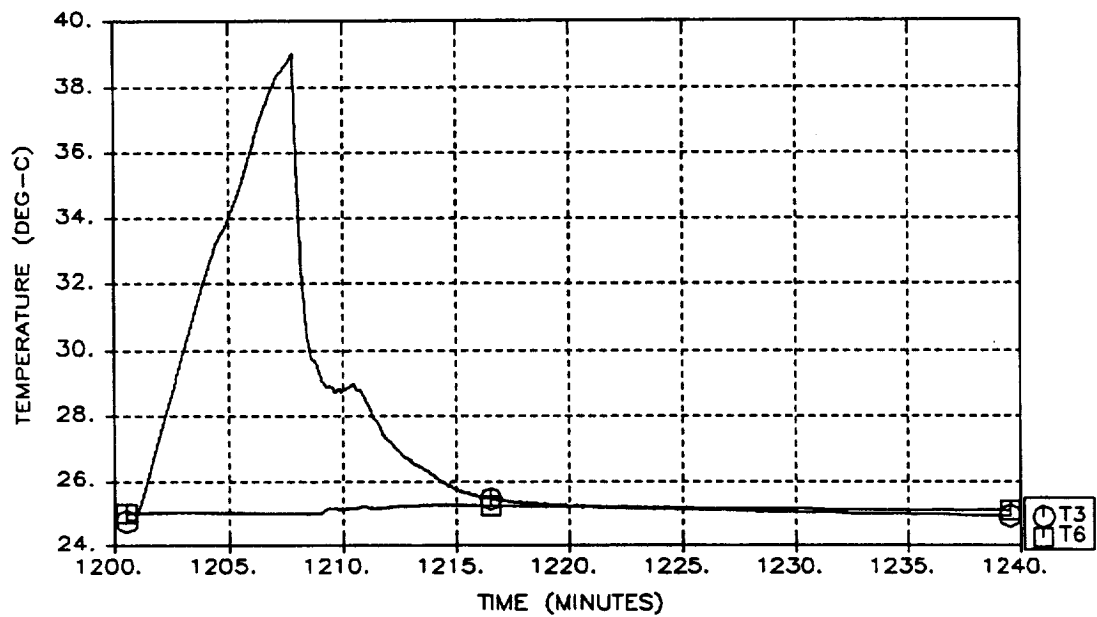
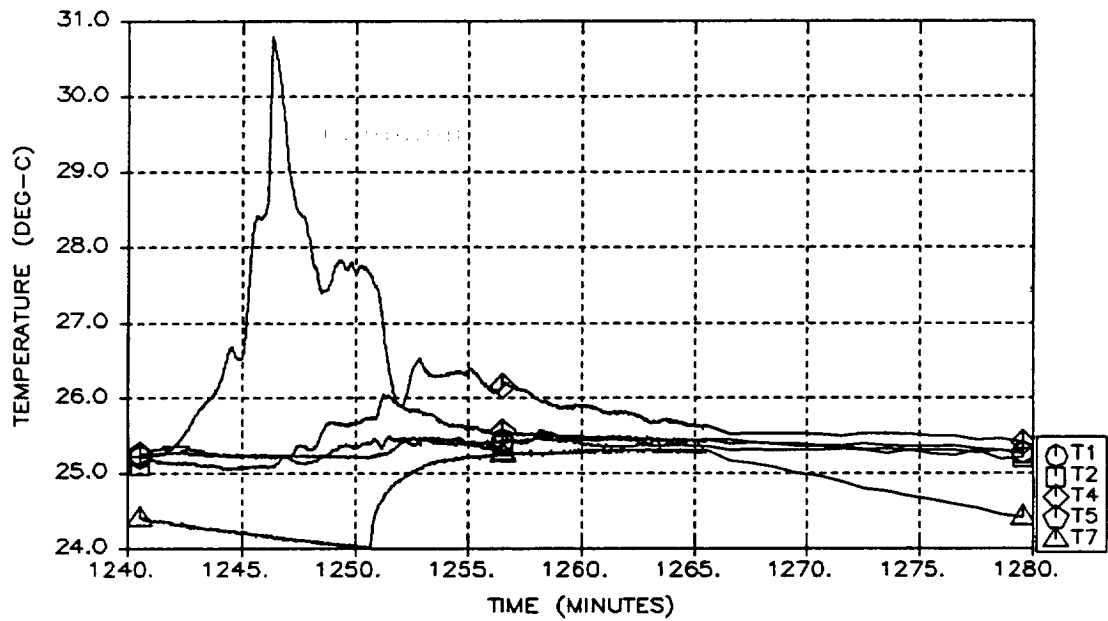


Figure A-107: Run 31 Temperatures
A-108

RUN 32 TEMPERATURES
THERMISTORS 1, 2, 4, 5, AND 7



RUN 32 TEMPERATURES
THERMISTORS 3 AND 6 (HEATERS)

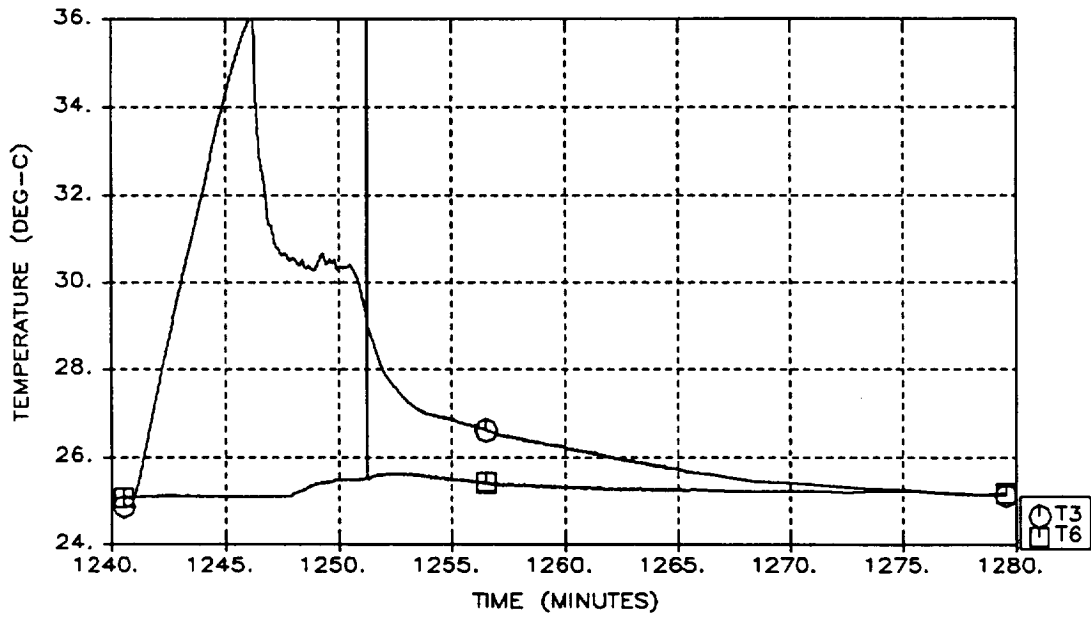
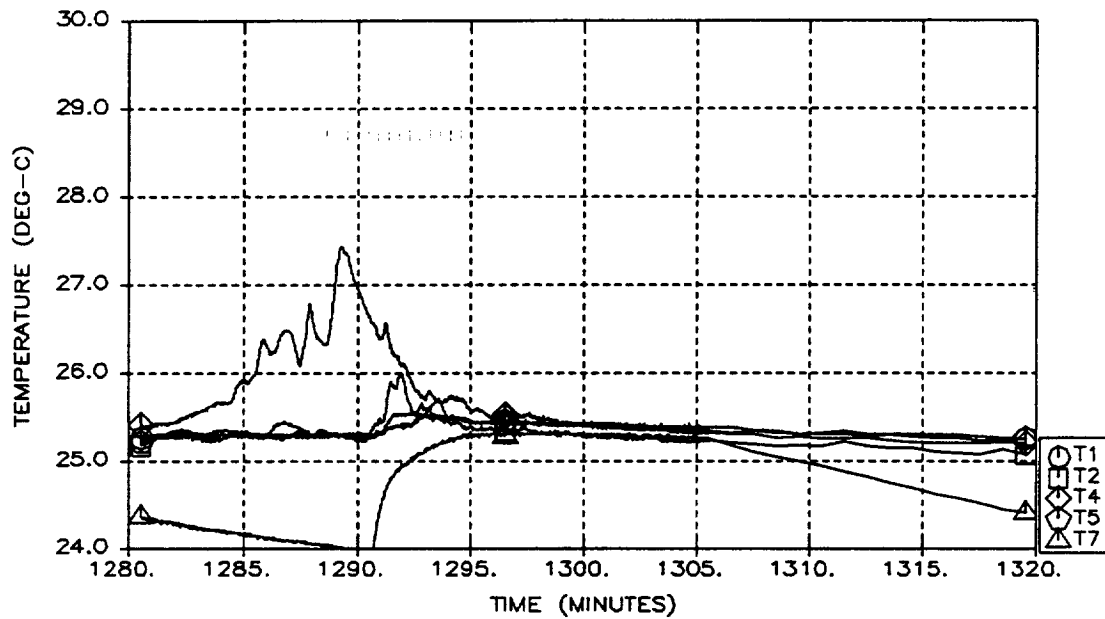


Figure A-108: Run 32 Temperatures
A-109

C-3

RUN 33 TEMPERATURES
THERMISTORS 1, 2, 4, 5, AND 7



RUN 33 TEMPERATURES
THERMISTORS 3 AND 6 (HEATERS)

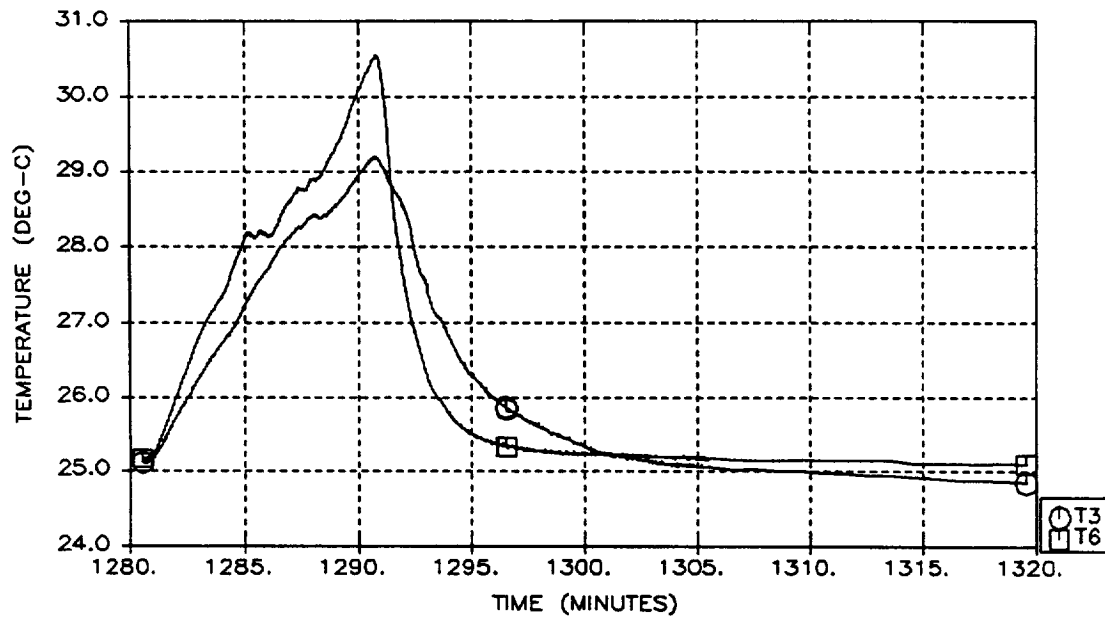
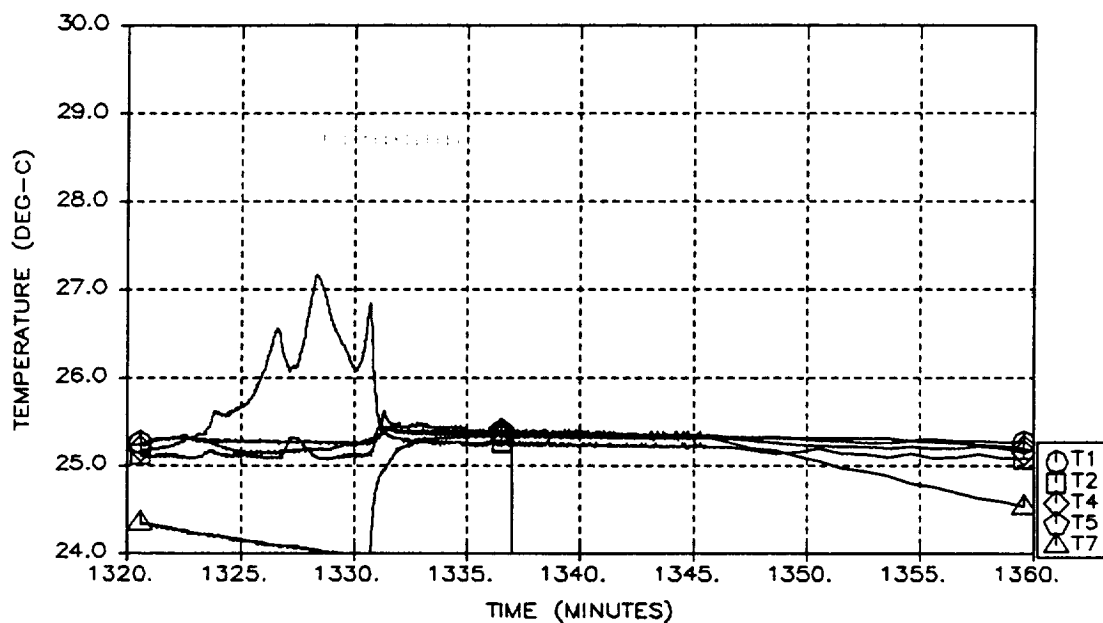


Figure A-109: Run 33 Temperatures
A-110

C-3.

RUN 34 TEMPERATURES
THERMISTORS 1, 2, 4, 5, AND 7



RUN 34 TEMPERATURES
THERMISTORS 3 AND 6 (HEATERS)

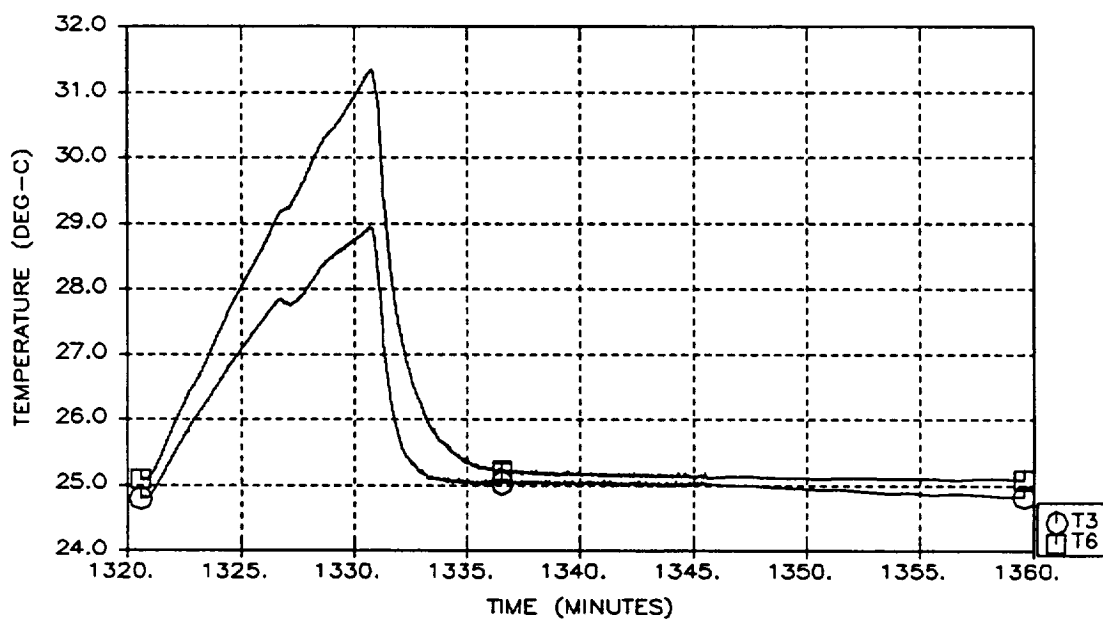
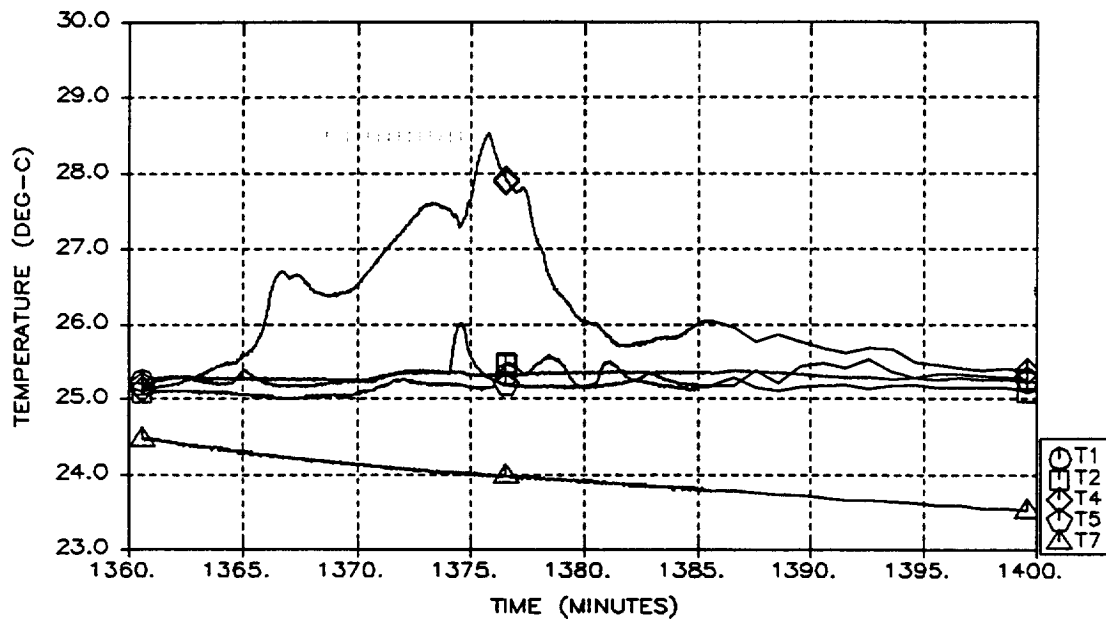


Figure A-110: Run 34 Temperatures
A-111

RUN 35 TEMPERATURES
THERMISTORS 1, 2, 4, 5, AND 7



RUN 35 TEMPERATURES
THERMISTORS 3 AND 6 (HEATERS)

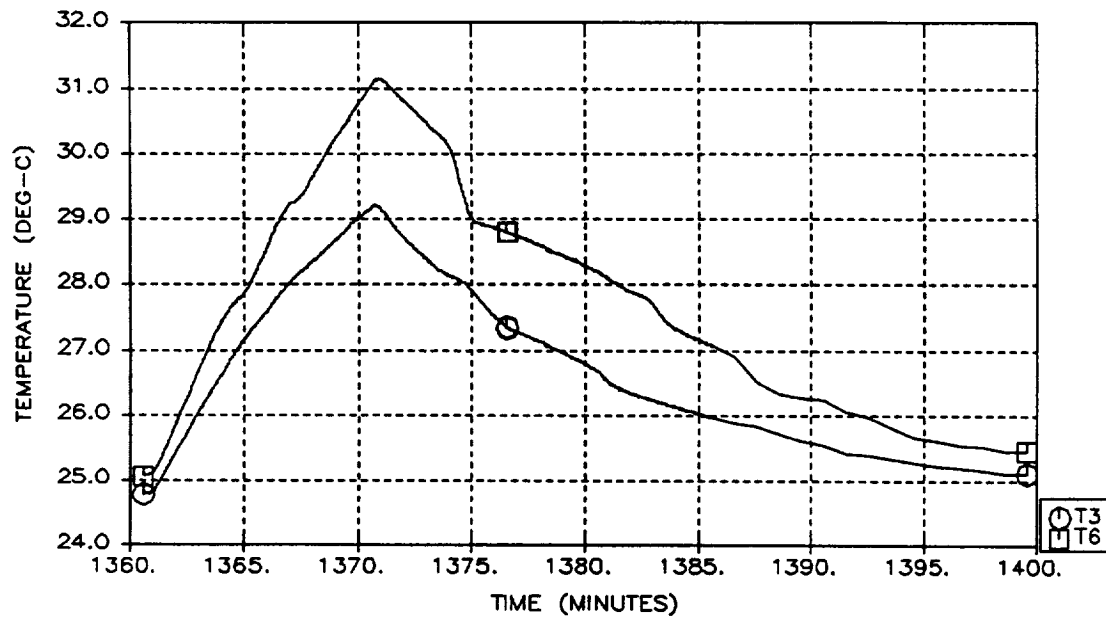
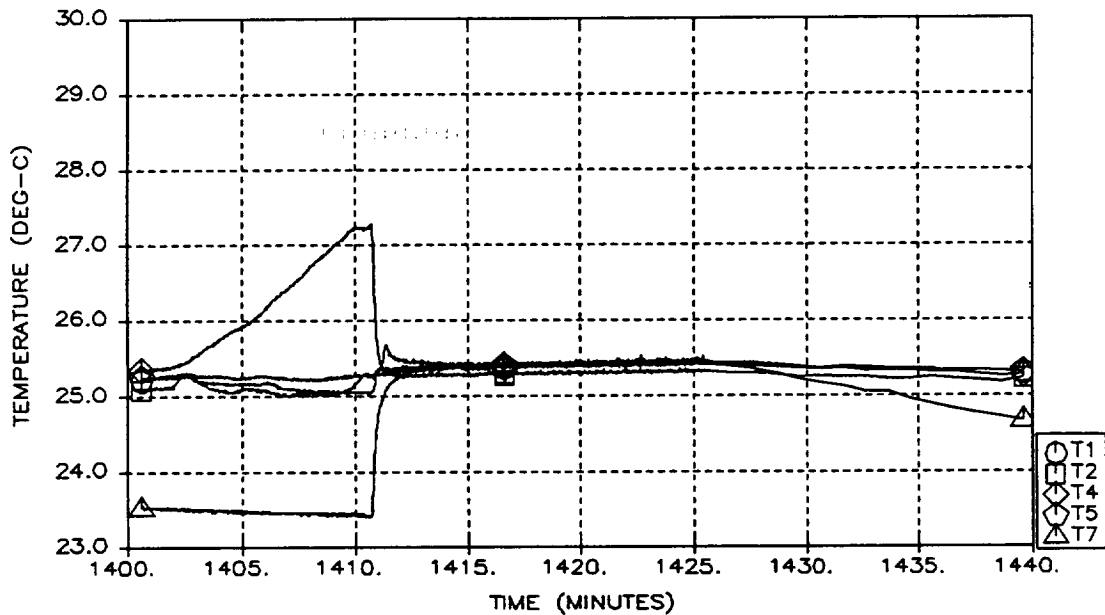


Figure A-111: Run 35 Temperatures
A-112

RUN 36 TEMPERATURES
THERMISTORS 1, 2, 4, 5, AND 7



RUN 36 TEMPERATURES
THERMISTORS 3 AND 6 (HEATERS)

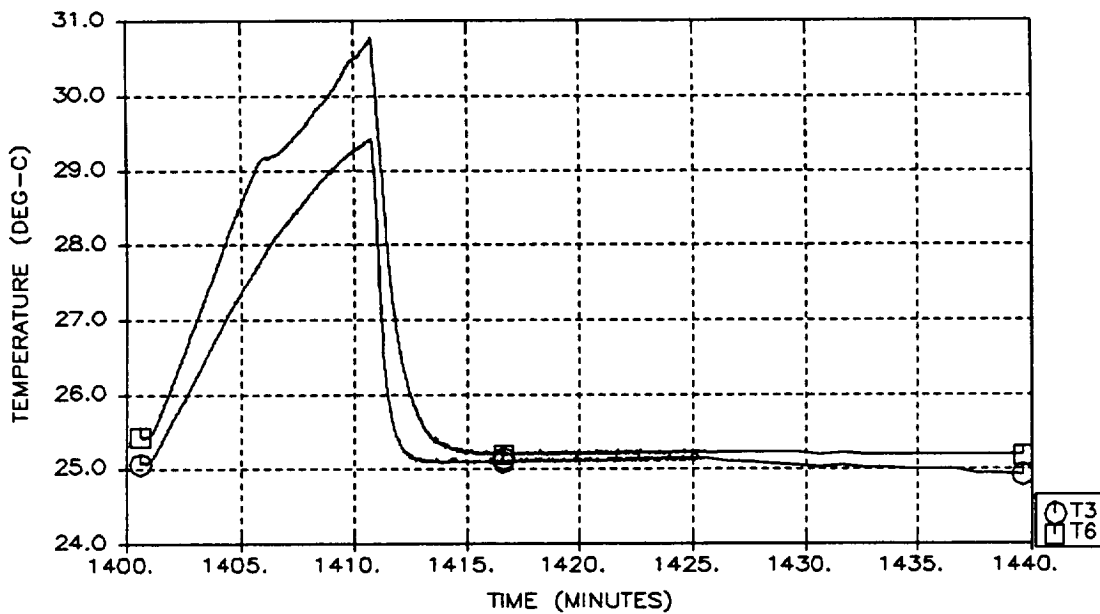
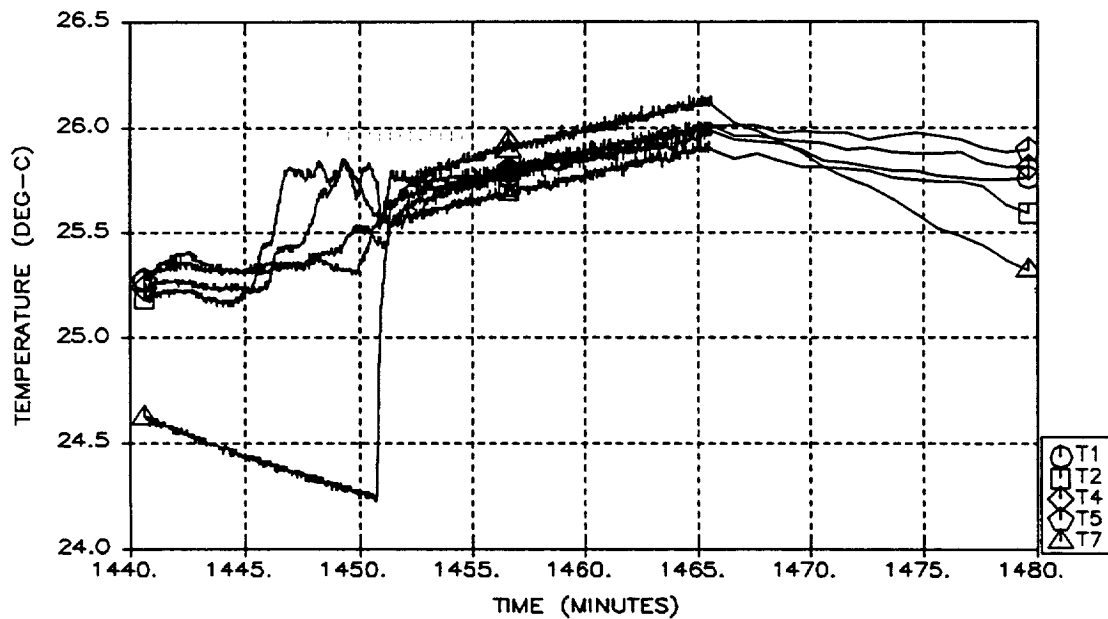


Figure A-112: Run 36 Temperatures
A-113

RUN 37 TEMPERATURES
THERMISTORS 1, 2, 4, 5, AND 7



RUN 37 TEMPERATURES
THERMISTORS 3 AND 6 (HEATERS)

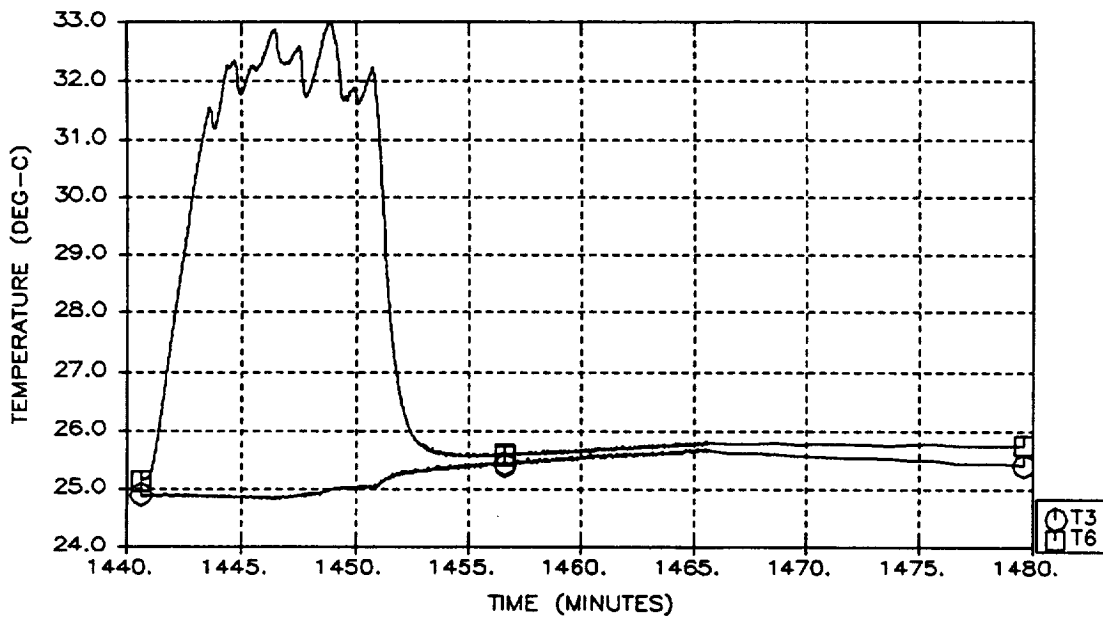
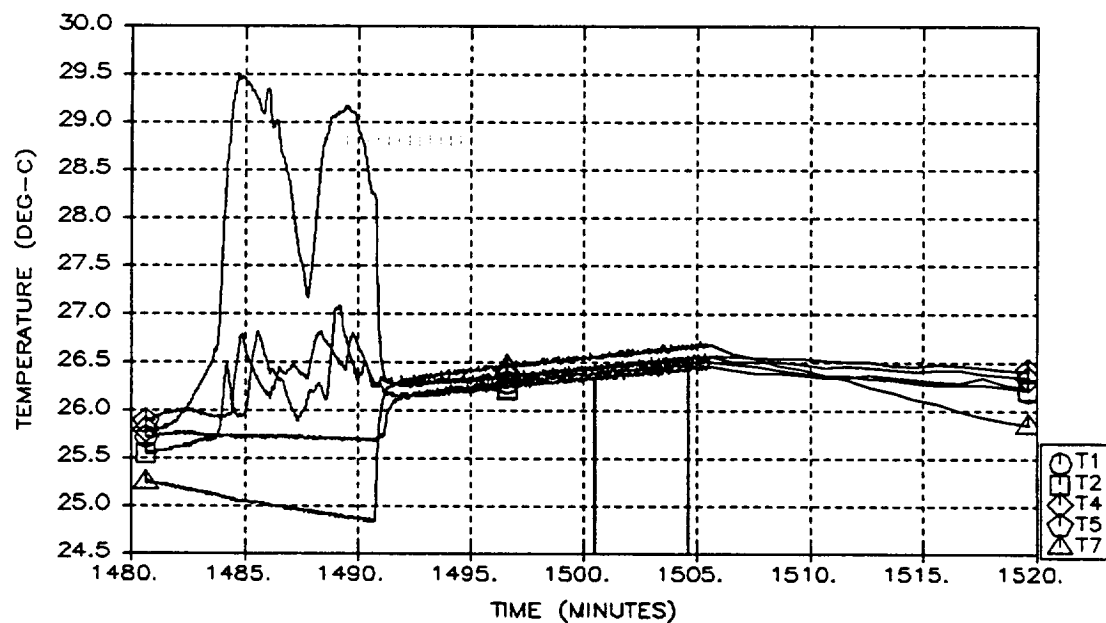


Figure A-113: Run 37 Temperatures
A-114

RUN 38 TEMPERATURES
THERMISTORS 1, 2, 4, 5, AND 7



RUN 38 TEMPERATURES
THERMISTORS 3 AND 6 (HEATERS)

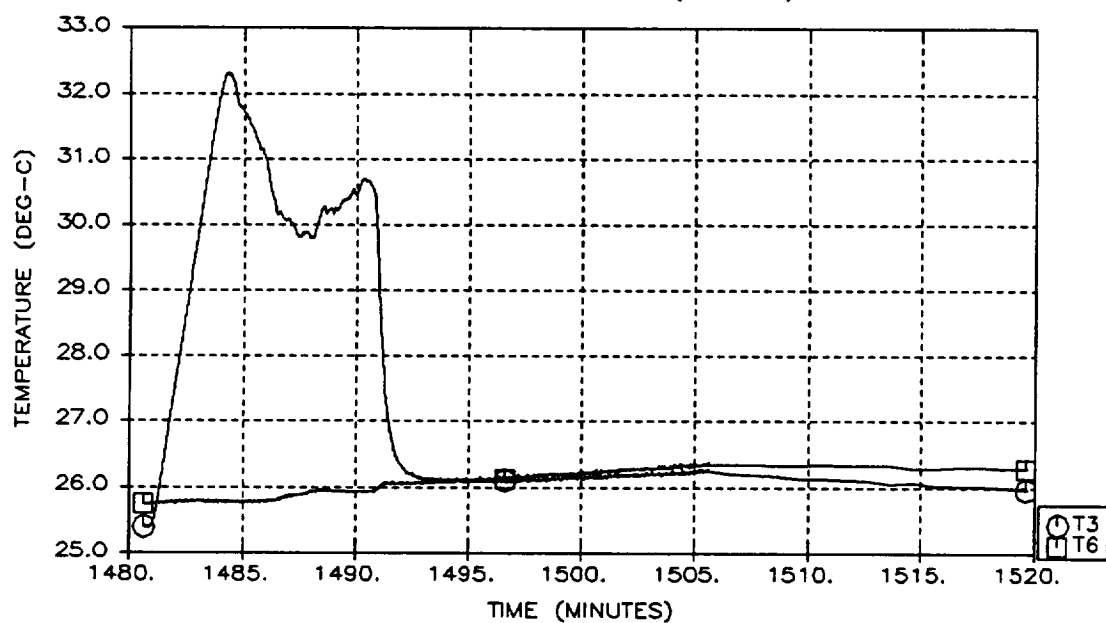


Figure A-114: Run 38 Temperatures
A-115

Videotape Supplement

A videocassette supplement to this document is available through the NASA Lewis Research Center videotape library. Much of the data returned by this experiment is best seen in this format as the still photographs reproduced in this report cannot convey the information that a motion picture can. The video supplement consists of two 2-hour tapes containing the complete data set. Each test run is identified in a preceding title slate by its run number, and a timer display is superimposed that corresponds with the time values in the digital data.

The videotape supplement is available on loan from NASA by sending the request shown below to:

NASA Lewis Research Center
Video Department (Mail Stop 5-2)
21000 Brookpark Road
Cleveland, OH 44135

Date _____

Please send one loan copy of Film Supplement to report NASA CR-191012

Technical Film TF-_____; Lewis Video 93-219

in the following format (check one):

3/4 in. U-Matic tape; 1/2 in. VHS tape; 16 mm film

Name of organization _____

Street number _____

City and State _____ Zip code _____

Attn: Mr./Ms. _____

Title _____ Telephone (____) _____

Place
stamp
here

NASA Lewis Research Center
Video Department (Mail Stop 5-2)
21000 Brookpark Road
Cleveland, OH 44135

REPORT DOCUMENTATION PAGE

*Form Approved
OMB No. 0704-0188*

Public reporting burden for this collection of information is estimated to average 1 hour per response, including the time for reviewing instructions, searching existing data sources, gathering and maintaining the data needed, and completing and reviewing the collection of information. Send comments regarding this burden estimate or any other aspect of this collection of information, including suggestions for reducing this burden, to Washington Headquarters Services, Directorate for Information Operations and Reports, 1215 Jefferson Davis Highway, Suite 1204, Arlington, VA 22202-4302, and to the Office of Management and Budget, Paperwork Reduction Project (0704-0188), Washington, DC 20503.

1. AGENCY USE ONLY (Leave blank)			2. REPORT DATE March 1993		3. REPORT TYPE AND DATES COVERED Final Contractor Report		
4. TITLE AND SUBTITLE Tank Pressure Control in Low Gravity by Jet Mixing			5. FUNDING NUMBERS WU-589-01-2C				
6. AUTHOR(S) Michael D. Bentz							
7. PERFORMING ORGANIZATION NAME(S) AND ADDRESS(ES) Boeing Defense and Space Group P.O. Box 3999 Seattle, Washington 98124-2499			8. PERFORMING ORGANIZATION REPORT NUMBER E-(None)				
9. SPONSORING/MONITORING AGENCY NAMES(S) AND ADDRESS(ES) National Aeronautics and Space Administration Lewis Research Center Cleveland, Ohio 44135-3191			10. SPONSORING/MONITORING AGENCY REPORT NUMBER NASA CR-191012				
11. SUPPLEMENTARY NOTES Project Manager, Richard H. Knoll, NASA Lewis Research Center, (216) 433-2419.							
12a. DISTRIBUTION/AVAILABILITY STATEMENT [REDACTED]			12b. DISTRIBUTION CODE [REDACTED]				
Date for general release: March 1995 Subject Category 28							
13. ABSTRACT (Maximum 200 words) <p>The Tank Pressure Control Experiment (TPCE) is a space experiment developed to help meet the need for a critical aspect of cryogenic fluid management technology: control of storage tank pressures in the absence of gravity by forced-convective mixing. The experiment used a 13.7-liter tank filled to a constant 83% level with refrigerant 113 at near-saturation conditions to simulate the fluid dynamics and thermodynamics of cryogenic fluids in space applications. The objectives of TPCE were to characterize the fluid dynamics of axial jet-induced mixing in low gravity, to evaluate the validity of empirical mixing models, and to provide data for use in developing and validating computational fluid dynamic models of mixing processes. TPCE accomplished all of its objectives in flight on Space Shuttle Mission STS-43 in August of 1991. The range of flow patterns photographed generally confirmed a prior correlation based on drop tower tests. A closed-form equation derived from a simple thermodynamic model was found to provide a first-order prediction of the pressure reduction time as a function of mixer parameters, tank size, and fluid thermophysical properties. Low-energy mixing jets were found to be effective and reliable at reducing thermal non-uniformities, promoting heat and mass transfer between the phases, and reducing tank pressure.</p>							
14. SUBJECT TERMS Cryogenic fluid management; Pressure control; Mixing; Low gravity; Boiling; Condensation				15. NUMBER OF PAGES 212 16. PRICE CODE A10			
17. SECURITY CLASSIFICATION OF REPORT Unclassified		18. SECURITY CLASSIFICATION OF THIS PAGE Unclassified		19. SECURITY CLASSIFICATION OF ABSTRACT Unclassified		20. LIMITATION OF ABSTRACT Unlimited	





